Understanding and simulating wind-induced vibrations of iced vertical cables

Theoretical moddeling and experimental studies

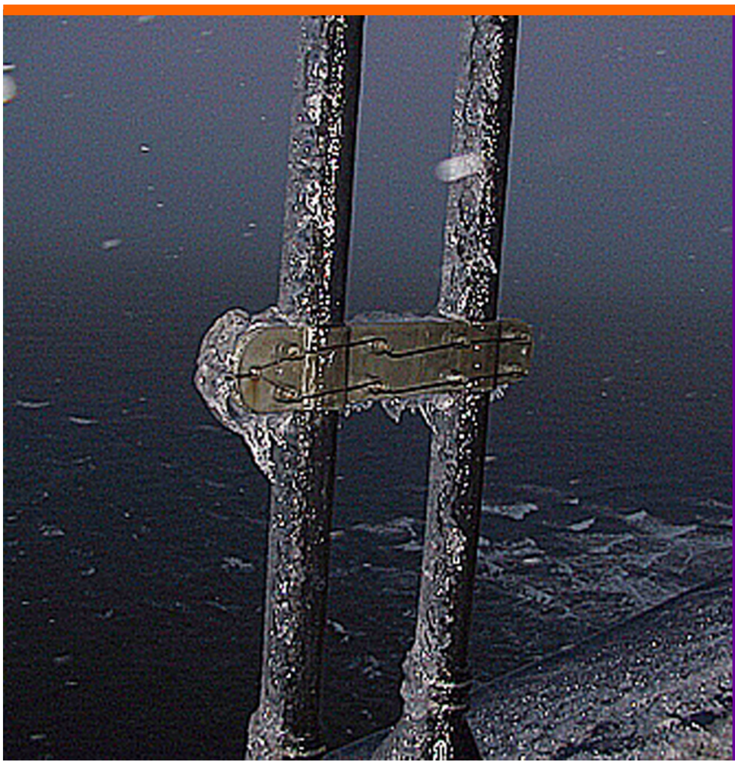

Henrik Gjelstrup

PhD Thesis

Department of Civil Engineering

2011

DTU Civil Engineering Report R-235 (UK)
March 2011

DTU Civil Engineering
Department of Civil Engineering

Understanding and Simulating Wind-Induced Vibrations of Iced Vertical Cables

Theoretical modelling and Experimental studies

Henrik Gjelstrup

PhD thesis

Department of Civil Engineering
Technical University of Denmark
2011

Understanding and Simulating Wind-Induced Vibrations of Iced Vertical Cables
Theoretical modelling and Experimental studies
Copyright © 2011 by Henrik Gjelstrup
Printed by DTU Tryk
Department of Civil Engineering
Technical University of Denmark
ISBN: 9788778773159
ISSN: 1601-2917

Preface

So how did a wedding, a trip on an airplane, and Greece turn out to be a thesis on cable vibration? For the risk of using a old quote then “It’s a long story”, but it will suffice to say that life have its ups and downs, twist and curves and if you look at the scenery you pass on your way through life you might be on the right spot on the right time.

One once told me “You are a try’er” and another put in “Then you can make it far”. This thesis is a testament to these two quotes and I suggest that all who dream about something should pursue it. By doing so, you will make you own fate and just as important your own luck.

* * *

Kongens Lyngby, December, 2010

Henrik Gjelstrup.

Acknowledgments

I would like to thank the following parties for making it possible to publish this thesis.

COWI A/S for helping founding the research project.

Storebælt A/S for providing data and money needed for experiments.

Femern A/S for providing money needed for experiments.

NRC in Ottawa, Canada for making some of the research possible through a corporative research program.

FORCE Technology for the use of their wind tunnel, which made it possible to finalize the experimental studies.

I would like to thank Holger Koss and Jacob Wittrup Schmidt for helping me with some of the illustrations presented in this thesis and Allan Larsen for giving relevant input the work presented

Also I would like to thank Holger Koss and Christos T. Georgakis for generally helping with the thesis.

Abstract

On March 29, 2001, the Great Belt East Bridge exhibited large-amplitude hanger vibrations having elliptical orbits for wind speeds of between 16 - 18m/s. Vibration amplitudes were in the order of 2m in the across-wind direction and 0.6m along-wind. The vibrations of the hangers were not a first, but in this case a very thin ice accretion on the hangers had been observed. The hypothesis is that thin ice deposits can significantly change the aerodynamic properties of a bridge cable, so as to lead - under certain conditions - to large amplitude vibrations. As such, the main focus of this work has been to determine the effect of ice on the aerodynamic stability of bridge hangers, whilst creating the theoretical and experimental background for the evaluation of any similarly observed vibrations on other structures. To this end, a new 3 degree-of-freedom quasi-steady galloping instability model has been developed, where the 3 degrees-of-freedom consist of movement in the cross-sectional plane of a cable and rotation around the shear centre of the cable. Furthermore, based on this model, an aerodynamic instability criterion has been suggested, which can predict galloping instability and estimate the needed damping for the avoidance of the instability. The model has been validated through wind tunnel experiments, which consist of three experimental series. The first series focuses on the formation and shape of thin ice accretions, the second series is focused on the determination of the aerodynamic force coefficients for carefully selected ice shapes, as observed in the first experimental series and the third series are passive-dynamic tests of selected models. Finally, an online database with all collected research papers has been made.

Resumé(Danish)

På Storebælt broen den 29. marts 2001, blev der observeret kabel svingninger med store amplituder med elliptiske baner for vindhastigheder på mellem 16 – 18 m/s. Amplituder var i størrelses orden 2 meter på tværs af vindretningen og 0,6 meter i vindretningen. Dette er ikke de første kabel svingninger der er observeret på Storbælt broen, men i dette tilfælde blev der også observeret et tyndt lag is på hængerne. Hypotesen er, at dette tynde lag is, under bestemte betingelser, kan signifikant ændre den aerodynamiske form af bro kabler og der igennem føre til kabel svingninger med store amplituder. I lyset af dette har fokus for the præsenterede arbejde i denne afhandling været på at identificere de aerodynamiske effekter der opstår på grund af dette tynde lag af is på et kabel. Dette har resulteret i udviklingen af en ny quasi-steady ustabilitetsmodel model med 3 frihedsgrader, hvor de 3 frihedsgrader består af bevægelse i tværsnits-planet for et kabel og rotation omkring ”shear centre” af kablet. Desuden bruges denne ustabilitetsmodel model i udviklingen af et ny aerodynamisk ustabilitet kriterium der også er blevet foreslået. Dette ustabilitetskriterium kan forudsige kabel svingninger og estimere den nødvendige dæmpning for at undgå disse svingninger. Dette ustabilitetskriterium er blevet valideret gennem vindtunnel eksperimenter, som består af tre dele; Første del fokuserer på dannelse og former af tynde overisninger af kabler. Anden del handler om at finde aerodynamiske kraftkoefficienter for omhyggeligt udvalgte is profiler der er fundet i første del. Tredje del omhandler dynamiske forsøg med nogle få udvalgte modeller. Tilslut er der oprettet en online database der indeholder alle papers der er samlet under denne PhD.

Table of Contents

I Extended Summary 1

1. Introduction 3
  1.1. General Considerations 3
  1.2. Thesis Outline 3
    1.2.1. Overall Structure 3
    1.2.2. Foundation and Motivation for this Work 4
    1.2.3. Motivation and Goals 5
    1.2.4. Research Strategy and Method 5
    1.2.5. Scope and Original Contributions 6
2. Review of Wind-Induced Cable Vibrations 9
  2.1. General Categorization 9
    2.1.1. Vortex Induced Vibrations 10
    2.1.2. Wake Induced Vibrations 11
    2.1.3. Buffeting 11
    2.1.4. Rain-Wind Induced Vibration 12
    2.1.5. Galloping 13
    2.1.6. Ice Induced Vibration 13
    2.1.7. Drag Crisis 14
    2.1.8. Dry Inclined Cable Galloping 15
    2.1.9. Torsional Galloping 17
  2.2. Summary 18
3. Development of Theoretical Models 21
  3.1. General Approach to Development of Models 21
  3.2. Sectional Response Model 22
  3.3. Sectional Instability Model 26

3.4. Modal Response Model 28
4. Experimental Models and Equipment 31
4.1. Model Design 31
4.1.1. Types of Ice 31
4.1.2. Ice Shapes. 32
4.1.3. Choice of Ice Simulation Method 34
4.2. Wind Tunnels. 36
4.2.1. Altitude Icing Wind Tunnel Facility (AIWT) 36
4.2.2. Closed Circuit Wind Tunnel (CCWT) 37
4.3. Control Experiments in the CCWT. 45
4.3.1. Static Experiments 47
4.3.2. Dynamic Experiments 52
4.4. Summary 56
5. Experimental Campaign 59
5.1. Experiments with Ice Growth on Circular Cylinders 59
5.1.1. Experimental Setup 59
5.1.2. Documentation of Ice Accretions Surface Contour. 65
5.1.3. Summary of Results 66
5.1.4. Comments on Main Findings 73
5.2. Simulated Ice Experiments in the CCWT 74
5.2.1. Models Used in Experiments 74
5.2.2. Static Rig 77
5.2.3. Dynamic Rig 86
5.2.4. Comments on Main Findings. 90
6. Application of Theory and Experiments 93
6.1. Comparisons of Results 93
6.2. Comments on Main Findings. 96
7. Summary and Conclusion 99

7.1. Summary 99
7.1.1. Theory 99
7.1.2. Experiments 99
7.1.3. Comparison of Theory and Experiments 99
7.1.4. Knowledge Sharing 100
7.2. Conclusion 100
8. Future Work 103
8.1. Experiments and Theory 103
9. Bibliography 105
II Appended Papers **113**

Appendix A: Vibrations on the Great Belt East Bridge Hangers and Weather Data

Appendix B: Smooth and Turbulent Wind Velocity Profiles

Appendix C: Displacements of D-Section in Smooth and Turbulent Flow (I_X~7%)

Appendix D: Ice Shapes Obtained from Experiments at NRC

Appendix E: Subtest Programs from Icing Tests performed at NRC

List of abbreviations

AIWT - Altitude Icing Wind Tunnel facility.

CCWT - Closed Circuit Wind Tunnel.

COG - Centre Of Gravity.

DS - Droplet Size, ie. diameter of the droplets of water.

DOF - Degrees-Of-Freedom.

EOM - Equations Of Motions.

H - Horizontal.

LWC - Liquid Water Content.

MMI - Mass Moment of Inertia.

NRC - National Research Council.

Orien - Orientation.

STD - Standard Deviation.

V - Vertical.

List of symbols

A_{ice} = integrated cross-sectional area.

$x, \dot{x}, \ddot{x}$ = displacement, velocity and acceleration.

$y, \dot{y}, \ddot{y}$ = displacement, velocity and acceleration.

$\theta, \dot{\theta}, \ddot{\theta}$ = structural rotation, angular velocity and acceleration.

α_0 = steady wind angle of attack.

β = angle of rotation, relative wind.

ϕ = wind angle of attack, cable length axis.

μ = dynamic viscosity.

C_L = aerodynamic force coefficients for lift.

C_D = aerodynamic force coefficients for drag.

C_M = aerodynamic force coefficients for moment.

C_{sxx} = structural damping in x direction.

C_{syy} = structural damping in y direction.

$\mathrm{C}_{s\theta\theta}$ = structural damping in θ direction.

C_a = aerodynamic damping.

C_s = structural damping.

C_T = total damping, $C_s + C_a$.

C_{accr} = general accretion coefficient.

D_{cable} = cable diameter.

F_L = lift force.

F_D = drag force.

F_θ = moment force.

$(\;)_R$ = relative.

t = time in seconds.

F_x = aerodynamic for in the x direction.

F_y = aerodynamic for in the y direction.

F_θ = aerodynamic for in the θ direction.

f_c = eigenfrequency of cable.

f_v = vortex shedding frequency.

f_G = frequency with high gust wind energy.

$H_0 - H_6$ = coefficients from 6th order eigenvalue problem.

$\boldsymbol{D}_0 - \boldsymbol{D}_5$ = Hurwitz determinant.

m_{accr} = accreted ice mass.

m_{appr} = water mass in the approaching airflow.

m = mass of cable.

J = rotational inertia about COG.

ρ = fluid density.

ρ_{ice} = density of ice.

R_δ = radial distance, length determining rotational velocity.

Re = Reynolds number.

St = Strouhal number.

U = mean wind velocity.

U_R = relative wind velocity.

U_{PR} = projected relative vertical wind velocity.

U_p = projected relative horizontal wind velocity.

U_{NR} = normal projected relative wind velocity.

U_A = along axis wind velocity.

ψ = $\alpha_o + \theta$.

φ = $\gamma_0 + \theta$.

γ_0 = angle offset for mass centre.

L_e = mass centre offset.

D_{mean} = mean cross sectional diameter perpendicular to the flow for all rotations of the model.

D_{max} = maximum cross sectional diameter perpendicular to the flow for all rotations of the model.

D_i = cross sectional diameter perpendicular to the flow for a given rotation of the model.

$D_{section}$ = height of wind tunnel test section.

D = cylinder diameter.

k_x = structural stiffness in x direction.

k_y = structural stiffness in y direction.

k_θ = structural stiffness in θ direction.

X = direction in coordinate system.

Y = direction in coordinate system.

Z = direction in coordinate system.

δ = angle for defining radial distance, R_δ.

(X_G, Y_G) = centre of gravity.

T_{air} = air temperature.

Part I

Extended Summary

Chapter 1

1. Introduction

1.1. General Considerations

Engineers and architects have always looked for way to improve the quality of life and to continually push the limits in structural design. This search have made it possible to design ever longer, taller and lighter structures, which means that structural vibrations, due to wind are becoming increasingly problematic. This has led to an ever-growing need for a clear understanding of the mechanisms behind these vibrations.

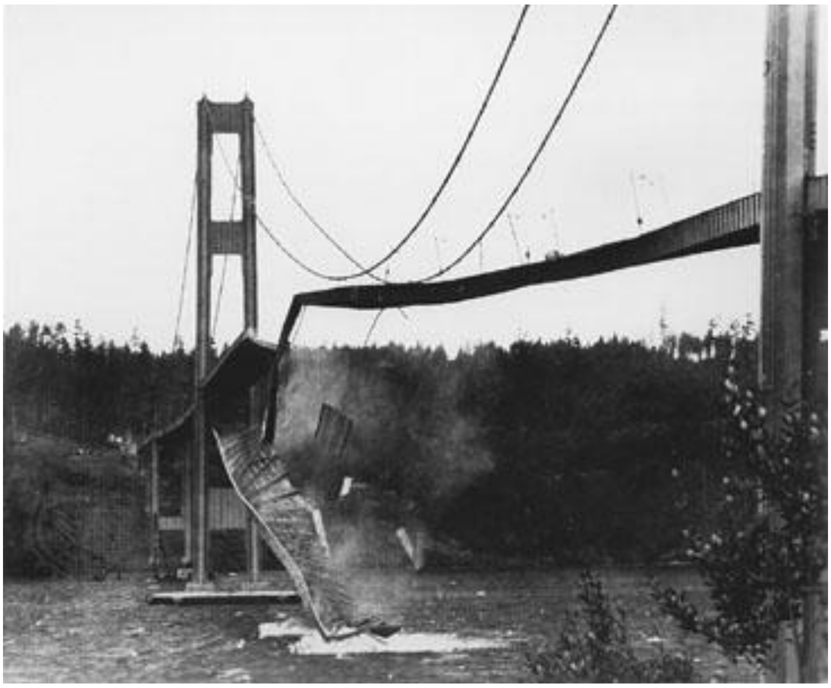

Figure 1. Tacoma Narrows Bridge collapse[1].

---

[1] http://egretsnest.wordpress.com/2007/08/02/gephyrophobia/

In the wake of the Tacoma Narrows Bridge collapse (Figure 1) and over the last six decades, extensive research has been undertaken in the field of bridge aerodynamics. It would be fair to state that the knowledge obtained in this field of research has allowed for the safe global design of the current long-span bridges in relation to wind induced forces. Numerical calculation, wind tunnel facilities, site testing and the diligent application of developed aerodynamic principles, have all played their part in this achievement. Nonetheless, there still remain numerous troubling vibrations on long-span bridges, of which cable vibrations seem to remain the least understood.

Several cable excitation mechanisms have been identified and fair level of research towards comprehending these has been undertaken. Excitation mechanisms are currently broadly grouped into two forms: those attributable to the wind and those which are the consequence of some other form of end loading, i.e. structurally induced. Of the wind induced mechanisms, those involving rain and/or ice seem to generate the largest cable vibration amplitudes. Yet, for vertical cables, as shown in Figure 2, the overall picture remains confused. There is no definitive understanding and description of these excitation mechanisms.

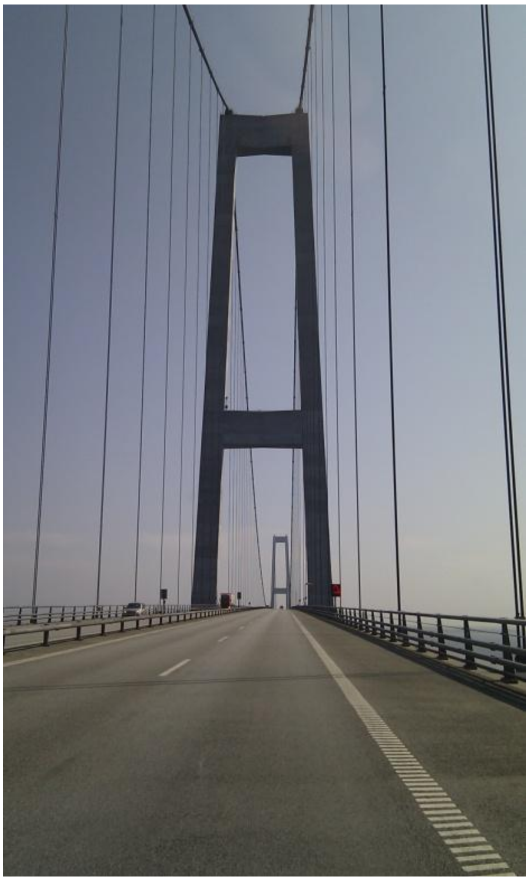

Figure 2. Hangers of the Great Belt East Bridge.

In an attempt to understand the cable excitation mechanisms, researchers have focused mainly on horizontal or inclined cables, as these are the prevalent type on cable-supported structures and tend to have lengths several times those found on vertical-cable supported structures. Lately, more reports of vertical cable vibrations have been published and the requirement for more focus on excitation mechanisms leading to vertical cable vibrations is more apparent. In addition, the clearer understanding of the behavior of vertical cables would immediately lead to the improved design of hangers for long-span suspension bridges, which are frequently subjected to various forms of cable excitations.

1.2. Thesis Outline

1.2.1. Overall Structure

This thesis can be divided into two main parts. Part I is an introduction, where the motivation and background for this research and the major findings and conclusions are presented. Part II is a collection of submitted papers which describe the research in greater detail.

In Part I the motivation and the vibration event which generated the foundation for this research is introduced. It also contains a short overview of the different known causes of wind induced cable vibration as of today. The experimental equipment and experiments made for verification of reliability of this test equipment is presented. Finally the main findings and conclusions are presented.

Part II contains the papers which explain the research in greater detail. The collection of papers consists of three conference papers and three papers submitted to journals. Whenever one of these papers is cited in Part I, the full paper can be looked up in Part II.

Finally, all references to the research papers gathered on the subject of wind induced cable vibration have been published in an online database. It is the idea that the database should be used as a quick reference point to cable vibration. The database is located at www.cabledynamics.dk/login.aspx. Please contact Henrik Gjelstrup on h_gjel@yahoo.dk for login information.

1.2.2. Foundation and Motivation for this Work

The history of cable mechanics goes back as far as the fifteenth-century where Leonardo da Vinci made sketches which anticipated cable mechanic theory which was first developed in 1586, [1].

A lot has happened since then and today a fairly good understanding of cables and their behavior has been established, making it possible to model and predict most vibration events, but the underlying mechanism are still unclear, which calls for a continuation of research within this area.

A special case within the cable behavior is vibrations due to ice accretion. This group of vibrations has received a lot of attention with respect to electrical transmission lines. The references [2-6] are just a few selected papers on the subject of electrical transmission lines vibration due to ice.

Lately, cables on bridges have received more attention due to greater awareness of bridge owners regarding cable vibrations on their bridge. References [7-9] shows selected papers, which list bridges with cable vibrations. With respect to vibration in bridge cables due to ice, little or no published research exists.

A vibration event recorded and observed on the Great Belt East Bridge, March 28. 2001 was the initiating factor and the foundation for this work. Displacements with amplitudes of two meters were recorded and pictures of the cable were taken, see Figure 3. Besides visual inspection this was the first documentation that ice was present under the vibration events which were seen in the winter half year. A preliminary description of the vibration event is given in [8].

COWI A/S decided in collaboration with DTU-BYG to start up a research project to study the possible effects of ice on vertical cable. This decision was made on the evidence, which was present during this vibration event and in conjunction with earlier records of vibration events and weather data. The data does not prove that ice was the initiating factor but insinuated that ice might be present at most of the events, see appendix A.

Figure 3. Iced Hanger of the Great Belt East Bridge.

1.2.3. Motivation and Goals

The motivations for this research is founded in the attempt to understand cable vibration and through this knowledge to make bridges safer and better in future designs rather than fixing vibration problems after the bridge has been built.

The overall aim of the research is to explain cable instabilities due to ice accretions. An ideal way to approach this problem would be to perform wind tunnel tests to study ice accretion and to measure load coefficients on cable models with reproduced ice accretions. Furthermore a theoretical model should be developed, which in conjunction with results from wind tunnel experiments can be used to predict cable instability and the needed damping necessary to prevent instability. Such a theoretical model would be a good addition to help understand the previous mentioned cable vibration on the Great Belt East Bridge hangers. Finally, the creation of an online database with references to papers related to cable vibration would provide industry and academia a faster way to knowledge on cable dynamics.

1.2.4. Research Strategy and Method

The strategy of the research was to concentrate on a single cable. First, a theoretical model was developed to get at better understanding of the underlying physics. Secondly, tests on how ice is formed on the cable were studied in a wind tunnel capable to produce the required atmospheric conditions. Thirdly, wind tunnel tests on simulated ice shapes were carried out to find aerodynamic forces on the cable and the cable displacements. The aerodynamic force coefficients resulting from the wind tunnel test should be used in the theoretically model in an attempt to explain the possible cable vibrations found from the wind tunnel test on the simulated ice shapes. Finally, all papers accumulated during the research presented in this thesis, will be made available in the form of references in an online database, which will be accessible by industry and academia.

The method used to derive the theoretical model is based on the changes in the aerodynamic forces acting on the cable. These changes can arise from either Reynolds number effects and/or from the different angles of attack of the approaching wind on the cable. The method was chosen due to the assumption that no other external force than the wind was applied to the cable under the vibrations events recorded at the Great Belt East Bridge.

1.2.5. Scope and Original Contributions

In this section the scope and the original contributions are summed up for the research presented in this thesis.

Scope

The scope of the thesis is to develop an instability model based on a sectional responds model of a thinly ice cable subjected to wind loading. The thesis also contains a summary of known mechanisms which contributes to aerodynamic instabilities of cables and other slender structures. Finally, the literature which has been used in the research presented in this thesis is published in an online reference library providing a quick access to the most current knowledge in iced cables and the research done in this area of interest.

Original Contributions

The original contributions presented in this thesis are split in to two areas, namely a theoretical part and an experimental part.

Theoretical

For the theoretical part the focus is mainly on the development of the 3-DOF instability model. The original contribution in this model are the inclusion of the torsional degree of freedom and also the analytical solution to the stability problem. The analytical solution is obtained using the Routh-Hurwitz stability criterion and the equation of motion is developed by using the Euler–Lagrange equations.

Experimental

In the experimental part, the original contributions are split in to two parts; The first part lies in icing experiments at temperatures ranging from -5°C to -1°C and relative low wind speeds ranging from 10m/s to 30m/s. The experiments show the formation of ice on two circular cylinders with different diameters and orientation which was varied from horizontal and vertical.

The second part of the experiments lies in finding aerodynamic force coefficients and dynamic responses for a circular cylinder with simulated ice shapes. The simulated ice shape is made up by replicas of selected from the ice shapes partly obtained in part one of above mention experimets or numerically obtained ice shapes. Finally, some generic ice shapes were also included in the experiments. All the different ice shapes were produced by rapid prototyping and the experiments were performed at temperatures significantly higher the zero.

Chapter 2

2. Review of Wind-Induced Cable Vibrations

2.1. General Categorization

The main part of cable vibrations research has so far been focused on horizontal or inclined cables. Through cable vibrations research, and research on structural dynamics in general, a sub-group of vibrations phenomena, which are related to aerodynamic forces has been identified. In order to get a better understanding of the driving mechanism behind the vibration event that initiated this research, it was deemed necessary to get an overview of the different known types of cable vibration and their origin

In the following section different vibrations types of cable vibrations, which are related to change in aerodynamic forces, are briefly described. The given definitions will allow for associating a vibration to a specific category or vibration type. Furthermore, the given descriptions provide references for further reading on specific vibration phenomenon.

The different types of vibration described in the following sections are:

- Vortex Induced Vibration.
- Wake Induced Vibration.
- Buffeting.
- Rain/Wind Induce vibration.
- Galloping.
- Ice Induced Vibration.
- Drag Crisis.
- Dry Inclined Cable Galloping.
- Torsional Galloping

2.1.1. Vortex Induced Vibrations

Vortex induced vibrations are caused by the shedding of vortices from alternating sides of the cable, which is shown in Figure 4. If the eigenfrequency for the first lower modes (f_c) and the vortex shedding frequency (f_v) are equal or close, large cable displacement can be observed oscillating transverse to the wind direction (resonant excitation).

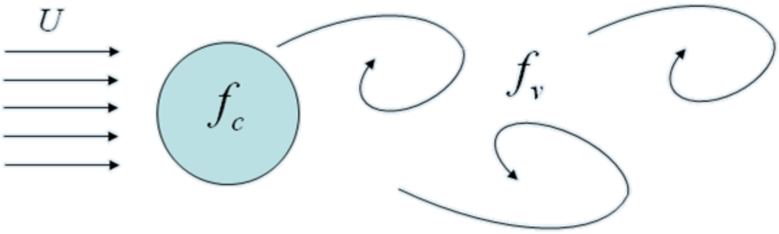

Figure 4. Vortex Shedding from a Circular Cable.

The vortex shedding frequency (f_v) depends on the wind speed and the diameter of the cable. This vortex shedding wind speed can be found by looking at the Strouhal number (St), which is equal to the vortex shedding frequency (f_v) multiplied by the cable diameter (D_{cable}) and divided by the wind speed, eq. (2.1). In general St for vortex shedding, on circular cables, is in the range 0.18 to 0.2. Knowing this relationship and the eigenfrequency for the cable makes it possible to predict the wind speed where resonant excitation will happen ($f_c = f_v$)

$$St = \frac{f_v D_{cable}}{U} \tag{2.1}$$

A sub-section of this kind of vibration also has an alternative name originating from ancient Greece. This alternative name is Aeolian vibrations and is named after the Greek god of all the winds. The Greeks used this vibration phenomenon when creating the Aeolian harp, which plays music by itself, if wind is blowing over the strings of the harp. The harp has strings with equal tension but different diameters, which according to (2.1) can produce different audible frequencies. In ancient Greece, this would be considered as if the harp was playing a melody by itself.

For conductors in electrical transmission lines, the frequency of these Aeolian vibration has been reported to be between 3-150 Hz and cause peak-to-peak oscillations of 0.01-1.00 cable diameter [10].

2.1.2. Wake Induced Vibrations

The driving force for this type of vibration originates from the wake turbulence behind a body upstream of the considered cable as shown in Figure 5. The wake turbulence can either be random or exhibit a distinct regular character from vortex shedding as described in section 2.1.1. The wake induced vibration might be large if the shedding frequency, f_v, is close or equal to the cable eigenfrequency, (f_c).

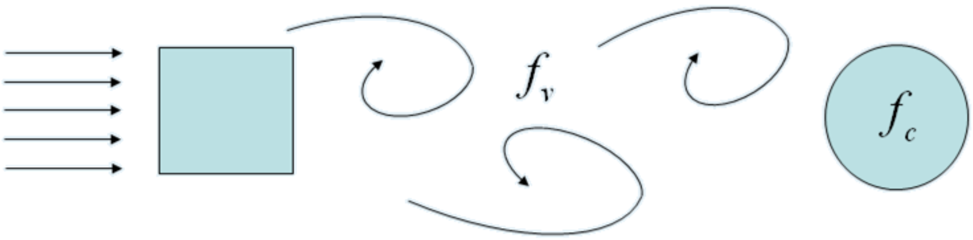

Figure 5. Wake Induced Vibration of Cable.

2.1.3. Buffeting

The term “Buffeting” refers to a random vibration problem caused by wind gusts from the turbulence in the wind. Looking at the power spectrum of turbulent winds shows the frequency where most of the winds energy is located, which is given as f_G in Figure 6. f_G is also the most likely frequency at which the wind will excite the cable in the vibration mode which is call buffeting. The amplitude of cable displacement due to buffeting is general not high, but structural fatigue damage may occur.

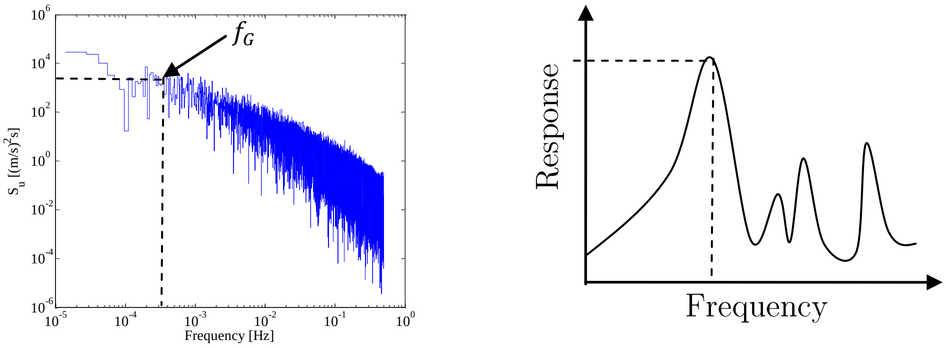

Figure 6. Wind Power Spectrum(left) and Illustrative Frequency/Responds Plot(right).

2.1.4. Rain-Wind Induced Vibration

Rain/Wind induced vibration is a relative new category for a previously unknown vibration phenomenon. The phenomenon was first correctly identified in 1986 (Written in Japanese, published in English in 1988, [11]), where experiments on inclined cable subjected to rain and wind was performed. Today it is assumed that 95% of all vibrations observed on cable-stayed bridges can be attributed to the phenomenon of Rain/Wind induced vibration, [12]. The mechanism behind this type of cable instability originates from two water rivulets, which run along the cable axis, as shown by experiments performed by Hikami and Shiraishi, [11]. Figure 7 shows such a case, and it is seen that the cable loses its symmetry, which in turn may lead to instability due to the changes in the aerodynamic forces.

Matsumoto et al. performed experiments with a simulated water rivulet, using the assumption that only the upper water rivulet is responsible for Rain/Wind induced vibrations, [13, 14]. They found that the instability due to rain could happen for this one upper rivulet only. One could ask if this is the total picture or if more experiments on cables with two rivulets, [15], should be performed in the future to verify assumption of Matsumoto et al.

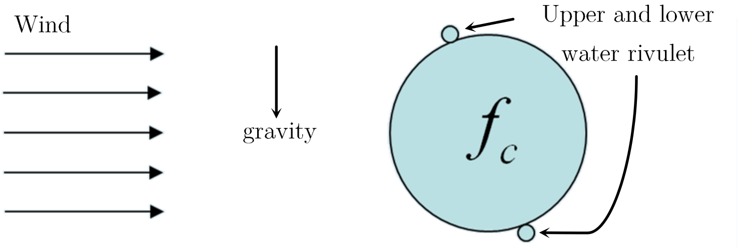

Figure 7 Rain/Wind Induce Vibration

Research on this type of instability is ongoing, and a comprehensive summary of what research already performed in this area is listed by Caetano in [12].

2.1.5. Galloping

The term "Galloping" is usually used for a one degree-of-freedom motion perpendicular to the flow. The motion or cross-wind vibration is sustained by a force component acting in the direction of the motion, which results from the oscillating flow angle of attack, α. The change in this force is primarily associated to the lift force, $\mathrm{F_L}$, which oscillates in relation to the change in α, see Figure 8.

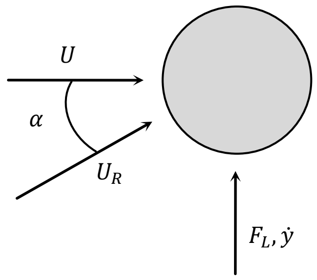

Figure 8 Relative wind, $\boldsymbol{U_R}$, on galloping cable

The underlying physics were first reported in 1932, where Jacob Pieter Den Hartog's(1907-1989), [16] research in this area led to the Den Hartog's criterion (eq. (2.2)), which predicting motion instability based on statically obtained wind forces.

$$C_D + \frac{dC_L}{d\alpha} < 0 \tag{2.2}$$

where C_L and C_D is the aerodynamic lift and drag force coefficients respectively and α is the wind angle of attack.

2.1.6. Ice Induced Vibration

The research that led to the above mention Den Hartog's criterion was initiated due to vibration problems on electrical transmission cables where sleet (wet snow) had accumulated. This is however only one kind of ice/snow case which can initiate cable vibrations. Examples of instabilities due to ice are reported in the following papers, [2-4, 17, 18]

2.1.7. Drag Crisis

The phenomenon called drag crisis occurs due to a sudden drop in the drag force. This drop is well known for circular structures appearing within the critical range of Reynolds numbers, which is 2x10^5 to 8x10^5 for at smooth cylinder, [12, 19]. The phenomenon of drag crises was first described in 1981, by the criterion shown in equation (2.3), [20].

$$\frac{dC_D}{dRe}\mathrm{Re} + 2C_D < 0 \tag{2.3}$$

where Re is the Reynolds number and C_D is the drag force coefficient for the cylinder.

Using the Great Belt East Bridge hangers as an example to the application of the criterion, where the diameter is ~0.11 meters, we could expect to see instability for wind velocities between ~30 m/s to ~110 m/s if the hanger surface is smooth, as defined in [19]. This may not be a correct assumption as the surface of the hanger probably would have a higher roughness then the one which is characterized as smooth. This roughness will shift the critical range towards lower Reynolds numbers. In other words the instability might occur at lower wind speeds which is illustrated in Figure 9 and discussed in [12, 19].

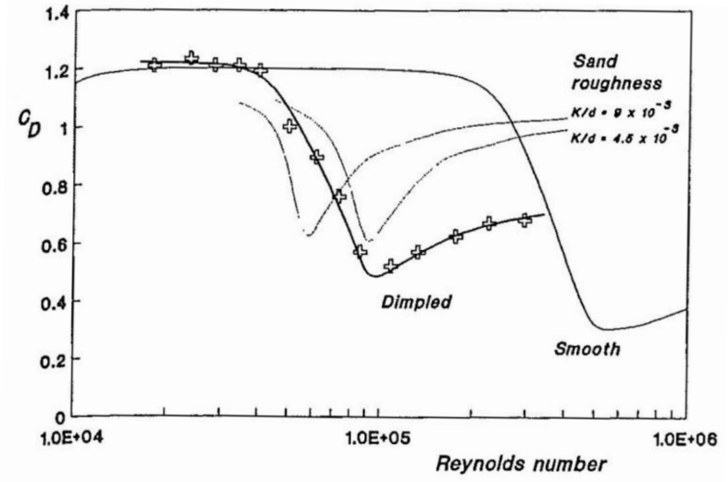

Figure 9. Drag-Variation due to Difference in Roughness, [21].

Several bridges have been identified to be prone to this type of instability, and some of them are discussed in the following papers, [12, 22, 23].

2.1.8. Dry Inclined Cable Galloping

Vibrations on cable stay bridges have been observed in situation where no rain or ice is present [24-26]. The particular conditions for developing cross-flow lift forces as prerequisites for galloping derives from the inclined orientation of the cable to the incoming wind for a non-rotating cable this angle is ϕ, see Figure 10. This phenomenon has been defined as dry inclined cable galloping, and has recently been attributed to a change in the aerodynamic forces acting on the cable by Larose et al., [27], in wind tunnel experiments on a dry cable model. The wind tunnel tests showed that cable stays are subject to an asymmetric lift, [27]. Especially for a wind angle of attack in the area of $\phi = 60°$, where $\theta_c = 0°$, (See Figure 10 for angle definition).

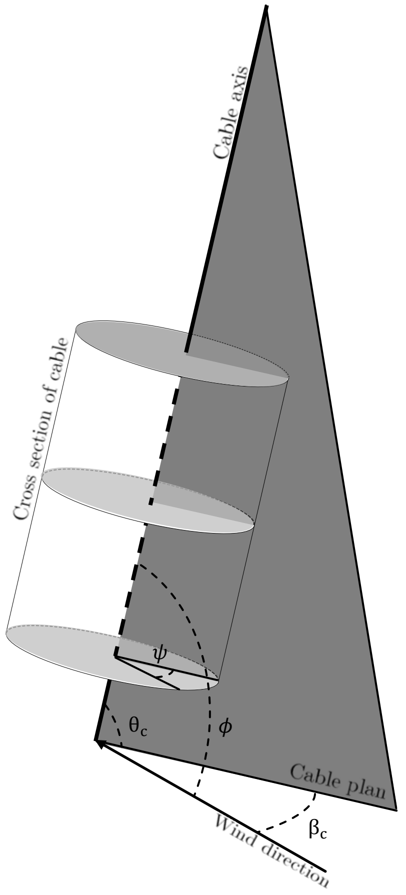

θ_c = cable inclination angle

$\psi = \alpha_0 + \theta$.

ϕ = wind angle of attack, cable length axis. (cable/wind plan).

β_c = wind/cable yaw angle

$\cos(\phi) = \cos(\beta_c)\cos(\theta_c)$.

Figure 10. Angles of Attack on an Inclined Cable.

The aerodynamic force coefficients published by Larose et al. are presented in Figure 11, were θ_c for all test was zero. It is seen that the cable will experience a significant absolute raise in lift and a small drop in the drag force for a wind angle of attack in the area of $\phi = 60°$. Using the Den Hartog criterion, mentioned in chapter 2.1.5, in conjunction with the lift and drag forces shown in Figure 11, results in a fulfilled Den Hartog criterion, which in turn means that the cable is prone to galloping. This result can obviously never happen for at vertical cable unless the topology of the surrounding area makes it possible for the wind to have a wind angle of attack of about $\phi = 60^\circ$ in relation to a vertical cable ($\theta_c = 90^\circ$).

In the period 2004 to 2008 a 2-DOF model was developed which could explain all of the above mentioned instability types in relation to change in the aerodynamic force coefficients drag and lift, [28-36]. In this model lift and drag is a function of Reynolds number, wind angle of attack and the wind's skew angle in relation to the cable.

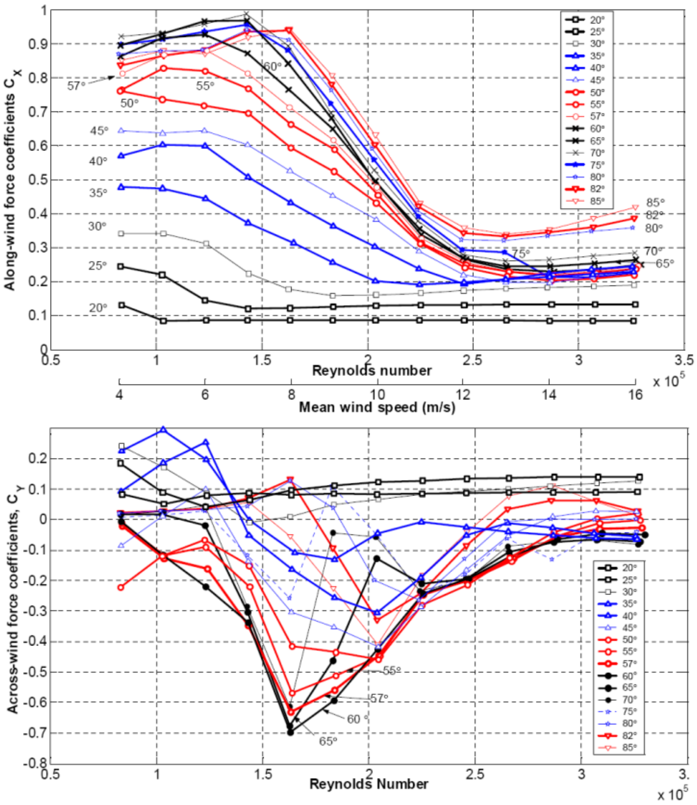

Figure 11. Drag(C_x) and Lift(C_y) Curve depending of wind angle of attack, ϕ, [27].

This 2-DOF model focuses on the effect of aerodynamic damping, C_a defined in equation (2.4), which is used in conjunction with the equations defined in equations (2.5) and (2.6). Instability can occur if $C_s - C_a < 0$, where C_s is the structural damping.

$$C_a = \mu * \frac{\text{Re}}{4} * ((G - J)B + (H + J)) \tag{2.4}$$

$$G = \begin{bmatrix} g(C_D) & -g(C_L) \\ g(C_L) & g(C_D) \end{bmatrix} \qquad H = \begin{bmatrix} h(C_D) & -h(C_L) \\ h(C_L) & h(C_D) \end{bmatrix}$$

$$J = \begin{bmatrix} \frac{dC_L}{d\alpha} & \frac{dC_D}{d\alpha} \\ -\frac{dC_D}{d\alpha} & \frac{dC_L}{d\alpha} \end{bmatrix} * \frac{1}{\sin(\phi)} \qquad B = \begin{bmatrix} \cos(2 * \alpha) & \sin(2 * \alpha) \\ \sin(2 * \alpha) & -\cos(2 * \alpha) \end{bmatrix} \tag{2.5}$$

$$g(C_D) = C_D * \left(2 * \sin(\phi) - \frac{1}{\text{Sin}(\phi)}\right) + \frac{dC_D}{d\text{Re}} * \text{Re} * \sin(\phi) + \frac{dC_D}{d\phi} * \cos(\phi)$$

$$g(C_L) = C_L * \left(2 * \sin(\phi) - \frac{1}{\sin(\phi)}\right) + \frac{dC_L}{d\text{Re}} * \text{Re} * \sin(\phi) + \frac{dC_L}{d\phi} * \cos(\phi)$$

$$h(C_D) = g(C_D) + 2 * \frac{C_D}{\sin(\phi)} \tag{2.6}$$

$$h(C_L) = g(C_L) + 2 * \frac{C_L}{\sin(\phi)}$$

2.1.9. Torsional Galloping

Torsional galloping has received special attention within the electrical transmission line community. This is due to a number of vibration events, where the wind was perpendicular to the transmission line and the occurring vibration could not be explained by either galloping or drag crisis. The following papers give examples of field observation and wind tunnel tests of torsional instability, [3, 4, 17, 37-41]. In 1981 a method for calculating the aerodynamic damping due to torsion, was proposed by splitting the structural and the aerodynamic damping up in separate parts, [3]. It was found that the criterion seen in equation (2.7) should be fulfilled if torsion was going to initiate instability for a cable with wind perpendicular to its length axis.

$$\frac{dC_M}{d\alpha} < 0 \tag{2.7}$$

where $\frac{dC_M}{d\alpha}$ is the gradient of the moment coefficients with respect to the wind angle of attack. Applying this approach in experiments showed that torsional movement of a single cable could initiate galloping, [3].

2.2. Summary

In the category of wind induced galloping we have several sub-categories, which each has its own special case analysis tool. In 2008 a theory which include almost all sub-categories was developed, [33, 34]. It can explain Den Hartog galloping, Wind/Rain induced vibration, Drag crisis, and Dry inclined cable galloping, but lacks the last sub-category of torsional galloping.

In relation to the research presented in this thesis and the above review of known vibration types it was decided to add the torsional degree of freedom to the previous mentioned 2D model in order to get a more complete picture of the mechanism causing to the previous mentioned vibration event on the Great Belt East Bridge. Such a model, including all of the galloping cases mentioned in the previous paragraph and including torsional galloping, was developed. This model and the theory is presented in three papers in Part II, [8, 42, 43], and is summarized in Chapter 3.

Chapter 3

3. Development of Theoretical Models

3.1. General Approach to Development of Models

The following chapter describes the development of the theoretical models, which are a part of the work presented in thesis. The models are based on a sectional approach to the development of a response model, from which the instability model is derived. Finally, an extension for the response model into modal coordinates has been developed.

- Theoretical Models
    - Sectional Response Model
    - Modal Response Model
    - Sectional Instability Model

The definition of the coordinate system which is used for deriving the models is shown in Figure 12. X is positive in the downstream direction, Y is positive in the upwards direction and rotation is positive in the clockwise direction around the Z-axis.

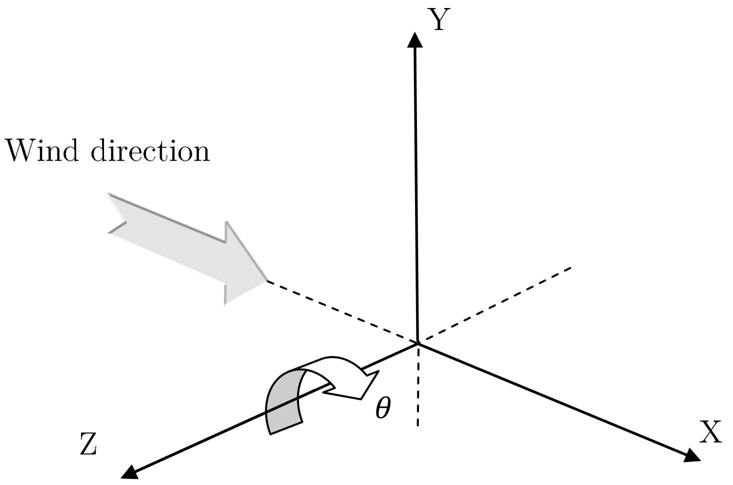

Figure 12. Sign Convention for Model Coordinate System.

3.2. Sectional Response Model

The theoretical model is based on a section model approach where a cross-sectional view of this section model is shown in Figure 13.

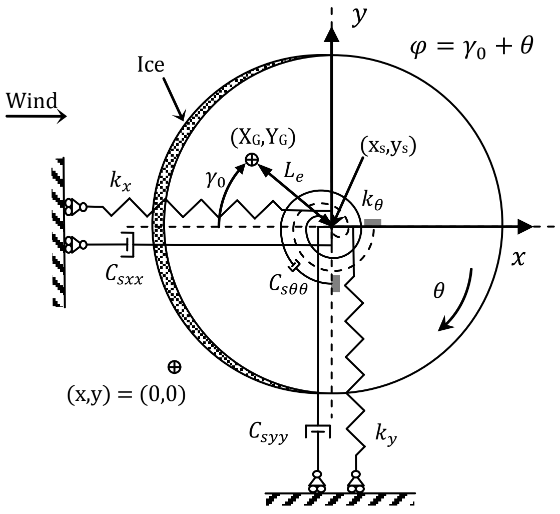

x = displacement direction.

y = displacement direction.

θ = rotation direction.

γ_0 = angle offset for mass centre.

L_e = mass centre offset.

k_x = structural stiffness in x direction.

k_y = structural stiffness in y direction.

k_θ = structural stiffness in Θ direction.

C_{sxx} = structural damping in x direction.

C_{syy} = structural damping in y direction.

$C_{s\theta\theta}$ = structural damping in Θ direction.

(X_G,Y_G) = mass centre.

(x,y) = origo of the coordinate system

(x_s,y_s) = shear centre(centre of cable)

Figure 13. Definition of Section Based System.

The origo of the coordinate system (0,0) is defined as the location were the cable is at rest, meaning that it could be the location of the cable centre when the cable is subjected to no wind force or it could be a location for the cable centre which is defined by a statically displacement due to a mean wind force.

The section model has 3-DOF, which are the displacements in the x- and y-direction and rotation around the shear centre of the model. It can also be seen that the mass centre/center of gravity (COG) of the model is different from the shear centre, due to the ice and the related eccentricity of mass. This in turn leads to a coupling of all three degrees-of-freedom. The section model has been approached as a cable section with a thin ice accretion. An isometric view of the section model is shown in Figure 14.

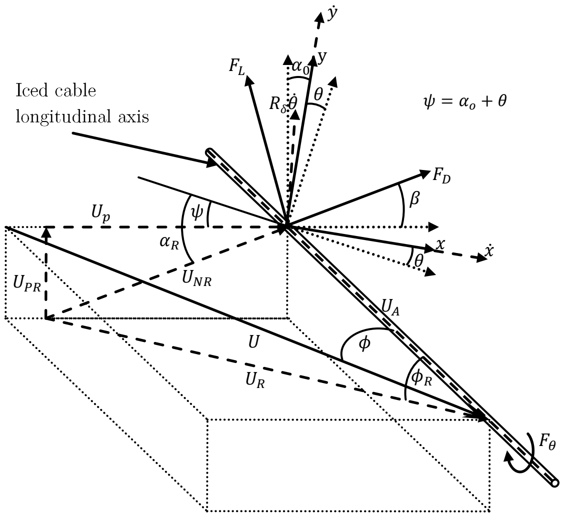

$x, \dot{x}$ = displacement, velocity.
$y, \dot{y}$ = displacement, velocity.
α_0 = steady wind angle of attack
$\theta, \dot{\theta}$ = structural rotation, angular velocity.
α_R = wind angle of attack, cable surface.
β = angle of rotation, relative wind.
ϕ = wind angle of attack, cable length axis.
F_L = lift force.
F_D = drag force.
F_θ = moment force.
R_δ = length determining rotational velocity.
U = mean wind velocity.
U_R = relative wind velocity.
U_{PR} = projected relative vertical wind velocity.
U_p = projected relative horizontal wind velocity.
U_{NR} = normal projected relative wind velocity.
U_A = along axis wind velocity.
ψ = $\alpha_o + \theta$

Figure 14. Schematic Model of Cable Section with Ice Accretion.

A close-up of the cross-sectional view of the model with projected wind velocities and the related displacements in x, y and θ direction is shown in Figure 15.

As introduced before the theoretical model is based on a section model approach for a bluff body. For this model it is assumed that the bluff body is a straight and rigid 2-D section model, and that the stiffness of the spring supports of the model is constant for all degrees-of-freedom, i.e. stiffness does not change with respect to movement in x and y or rotation about the structural axis (θ). Also, it is assumed that the structural damping force is proportional to velocity and that the wind velocity U is constant. Furthermore, it is assumed that the rotational velocity can be represented by a cross-sectionally dependent radial length times the radial rotation velocity $(R_\delta \dot{\theta})$, that quasi-steady assumptions apply, and that gravitational forces do not influence the model. Finally, it is assumed that the cable is at rest at the initiation of any motional instability.

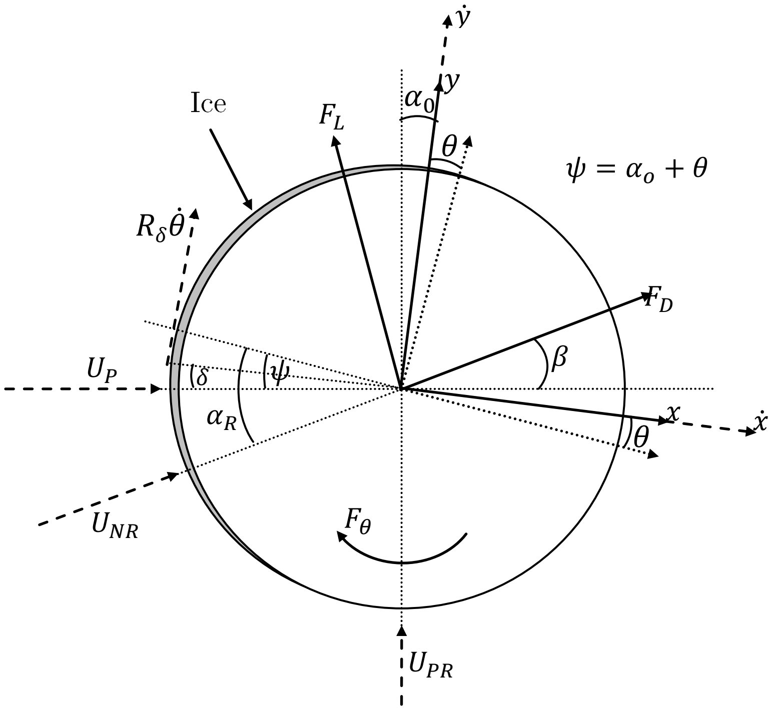

Figure 15. Analytical Model of Cable Section with Ice Accretion.

Both vertical and rotational motions of the cable section cause a variation in the wind angle of attack along the body, i.e. a positive rotational velocity induces a down-draft upwind of the centre of rotation and an up-draft downwind of the centre of rotation seen with Figure 13 as reference for up and down. A negative rotational velocity will create the opposite effect. The rotational velocity is approximated by the motion of a reference point defined in polar coordinates by the radial distance R_δ and angle δ, as shown in Figure 15. The length R_δ is not directly related to characteristic points of the bluff body's geometry or of the flow field, [1]. It is rather a variable used to adjust the aerodynamic model output to the observed instabilities. However, it has been found that the length and the angle is the same for structures with similar geometry. For example, for the torsional instability of rectangles about their centroid, R_δ has been approximated to half the distance between the centroid and the body's leading edge under the respective angle of attack [44]. Another example is torsion about flutter of airfoils where R_δ is chosen to give the angle of attack at a point three-quarters of the way back from the leading edge, [1].

Using these assumptions it should be possible to expand the application of this model to any geometry of a prismatic bluff body subjected to aerodynamic forces, as long as quasi-steady theory holds true.

In the following the notation for time dependent variables given as $x(t), y(t)$ and $\theta(t)$ are denoted x, y and θ. Derivatives with respect to time are written as $(\mathrm{d}/\mathrm{dt})x = \dot{x}$ and $(\mathrm{d}^2/\mathrm{dt}^2)x = \ddot{x}$. This notation is used to write up the equation of motions, which are given in equations (3.1) - (3.3). The full explanation on deriving the equation are shown in [43].

$$m\ddot{x} + C_{sxx}\dot{x} + k_x x + mL_e\big(cos(\varphi)\,\dot{\theta}^2 + sin(\varphi)\,\ddot{\theta}\big) = F_x \tag{3.1}$$

$$m\ddot{y} + C_{syy}\dot{y} + k_y y + mL_e\big(-sin(\varphi)\,\dot{\theta}^2 + cos(\varphi)\,\ddot{\theta}\big) = F_y \tag{3.2}$$

$$J\ddot{\theta} + C_{s\theta\theta}\dot{\theta} + k_\theta \theta + mL_e\big(sin(\varphi)\,\ddot{x} + cos(\varphi)\,\ddot{y} + L_e\ddot{\theta}\big) = F_\theta \tag{3.3}$$

where, C_{sxx} is the structural damping in the x direction, C_{syy} is the structural damping in the y direction and $C_{s\theta\theta}$ is the structural damping in the θ direction, L_e is the length to the mass centre from the point of rotation, $\varphi = \gamma_0 + \theta$ (see Figure 13). F_x, F_y and F_θ are the aerodynamic forces in the x direction, y direction and for torsion respectively. These can be written as:

$$F_x = \frac{1}{2}\rho U_R^2 D(C_D(\alpha_R, \mathrm{Re}_R, \phi_R)\, cos(\alpha_R) + C_L(\alpha_R, \mathrm{Re}_R, \phi_R)\, sin(\alpha_R)) \tag{3.4}$$

$$F_y = \frac{1}{2}\rho U_R^2 D(C_L(\alpha_R, \mathrm{Re}_R, \phi_R)\, cos(\alpha_R) - C_D(\alpha_R, \mathrm{Re}_R, \phi_R)\, sin(\alpha_R)) \tag{3.5}$$

$$F_\theta = \frac{1}{2}\rho U_R^2 D^2 C_M(\alpha_R, \mathrm{Re}_R, \phi_R) \tag{3.6}$$

where, $\alpha_R = (\psi + \beta)$, Re_R =Relative Reynolds number, ϕ_R = Relative wind angle of attack, cable length axis, ρ = fluid density, U_R = Relative fluid velocity, D =

Characteristic length of section (diameter for circular models), C_D = Drag coefficient, C_L = Lift coefficient and C_M = Moment coefficient.

Below are shown the velocities acting on the section model of the iced cable and used in the expressing U_R which are a part of equations (3.4)-(3.6).

$$U_R = \sqrt{(U_A^2 + U_{NR}^2)} \tag{3.7}$$

$$U_A = U\, cos(\phi) \tag{3.8}$$

$$U_{NR} = \sqrt{(U_P^2 + U_{PR}^2)} \tag{3.9}$$

$$U_P = U \sin(\phi) - \dot{x}\, cos(\psi) - \left(\dot{y}\, sin(\psi) + R_\delta \dot{\theta}\, sin(\delta)\right) \tag{3.10}$$

$$U_{PR} = -\left(\dot{y}\, cos(\psi) + R_\delta \dot{\theta}\, cos(\delta)\right) + \dot{x}\, sin(\psi) \tag{3.11}$$

The different relative and projected wind velocities shown above can be seen on Figure 14.

3.3. Sectional Instability Model

To develop the instability model the full set of nonlinear equation mention above, has to be linearized. This linearization is obtained by applying a Taylor expansion to the aerodynamic forces results in a static wind force in all three directions and a dynamic force, which is equal to a Jacobian matrix (C_a, equation (3.12)) multiplied with the velocity in the three directions, $\boldsymbol{C_a}\dot{Z}$, where $\dot{Z} = \left[\dot{x}, \dot{y}, \dot{\theta}\right]'$.

$\boldsymbol{C_a}$ is the aerodynamic damping matrix as given in equation (3.12). The values of the aerodynamic damping matrix $\boldsymbol{C_a}$ are calculated for small initial displacements $(\theta \ll 1)$. For the full solution of $\boldsymbol{C_a}$, see [43].

$$\boldsymbol{C_a} = -\begin{bmatrix} \dfrac{\partial F_x}{\partial \dot{x}} & \dfrac{\partial F_x}{\partial \dot{y}} & \dfrac{\partial F_x}{\partial \dot{\theta}} \\ \dfrac{\partial F_y}{\partial \dot{x}} & \dfrac{\partial F_y}{\partial \dot{y}} & \dfrac{\partial F_y}{\partial \dot{\theta}} \\ \dfrac{\partial F_\theta}{\partial \dot{x}} & \dfrac{\partial F_\theta}{\partial \dot{y}} & \dfrac{\partial F_\theta}{\partial \dot{\theta}} \end{bmatrix}_{\dot{x}=\dot{y}=\dot{\theta}=0} \tag{3.12}$$

Furthermore, it is assumed that all higher order terms in the equations of motions (EOM) are negligible. These assumptions are based on the instant where a vibration event is initiated on the body which is at rest. Equation (3.13) gives the total damping matrix containing both structural and aerodynamic damping.

$$\boldsymbol{C_T} = \boldsymbol{C_s} + \boldsymbol{C_a} = \begin{bmatrix} C_{sxx} & 0 & 0 \\ 0 & C_{syy} & 0 \\ 0 & 0 & C_{s\theta\theta} \end{bmatrix} + \begin{bmatrix} C_{axx} & C_{axy} & C_{ax\theta} \\ C_{ayx} & C_{ayy} & C_{ay\theta} \\ C_{a\theta x} & C_{a\theta y} & C_{a\theta\theta} \end{bmatrix} = \begin{bmatrix} C_{xx} & C_{xy} & C_{x\theta} \\ C_{yx} & C_{yy} & C_{y\theta} \\ C_{\theta x} & C_{\theta y} & C_{\theta\theta} \end{bmatrix} \quad \textbf{(3.13)}$$

It is possible to estimate the stability of the 3-DOF system by using the assumptions mention above and by rewriting the equations of motions (equations. (3.1)-(3.3)) into state space and solving the obtained eigenvalue problem.

By solving the eigenvalue problem for this linearized system of equations it is possible to estimate the aerodynamic stability of a bluff body subjected to aerodynamic forces. The eigenvalue problem produces a 6th order polynomial, which can be solved either analytically or numerically.

Analytically the eigenvalue problem can be solved by using the Routh-Hurwitz stability criterion, [45]. The Routh-Hurwitz stability criterion states that a system of equations is stable if the Real part of all the Routh-Hurwitz stability criterion coefficients is greater than zero. Applying the Routh-Hurwitz stability criterion results in 13 coefficients (7 from the polynomial, $(H_0 - H_6)$, and 6 from the Hurwitz determinant, $(\boldsymbol{D_0} - \boldsymbol{D_5})$), which can be found analytically. Through this approach it possible to make a parametric study of the various input variables used in the instability model. See appendix B for the full expression of $(H_0 - H_6)$ and $(\boldsymbol{D_0} - \boldsymbol{D_5})$. The full solution to the 7 coefficients from the polynomial, $(H_0 - H_6)$, and 6 coefficients from the Hurwitz determinant, $(\boldsymbol{D_0} - \boldsymbol{D_5})$ can be seen in ref. [43].

In summary, the criterion for aerodynamic stability, with respect to change in the aerodynamic forces, H_0 to H_6 and D_0 to D_5 should be greater the zero to avoid instability.

3.4. Modal Response Model

In order to estimate the displacements of a cable in its full length, equations (3.1)-(3.3) can be rewrite into modal coordinates. The modal coordinates are obtained by inserting $z(t,s) = Z(t)\sin(i\pi s/L_0), z = x, y, \theta$ and $Z = X, Y, \Theta$ into equations (3.1)-(3.3). Furthermore, the equations are multiplied by $\sin(i\pi s/L_0)$ for the use of sinusoidal orthogonality, which is used when integrating over s from zero to L_0. Using this approach the displacements in model coordinates are obtained as shown in equations (3.14)-(3.16).

The corresponding equations of motion in modal coordinates are:

$$m\ddot{X} + C_s\dot{X} + k_sX = \frac{2}{L_0}\int_0^{L_0} F_{XX}\,\sin\left(\frac{i\pi s}{L_0}\right)ds \tag{3.14}$$

$$m\ddot{Y} + C_s\dot{Y} + k_sY = \frac{2}{L_0}\int_0^{L_0} F_{YY}\,\sin\left(\frac{i\pi s}{L_0}\right)ds \tag{3.15}$$

$$J\ddot{\Theta} + C_\theta\dot{\Theta} + k_\theta\Theta = \frac{2}{L_0}\int_0^{L_0} F_{\Theta\Theta}\,\sin\left(\frac{i\pi s}{L_0}\right)ds \tag{3.16}$$

where s is the system line for the cable, running from 0 to the full length of the cable (L_0), $\frac{2}{L_0}\int_0^{L_0} F_{XX}\sin\left(\frac{i\pi s}{L_0}\right)ds$, $\frac{2}{L_0}\int_0^{L_0} F_{YY}\sin\left(\frac{i\pi s}{L_0}\right)ds$ and $\frac{2}{L_0}\int_0^{L_0} F_{\Theta\Theta}\sin\left(\frac{i\pi s}{L_0}\right)ds$ are the dynamic components of the aerodynamic forces for the i^{th} mode in the respective directions. The cable deflection should be taken into account when applying wind force coefficients to the modal response model, i.e. change of wind angle of attack.

Chapter 4

4. Experimental Models and Equipment

The following chapter will discuss the considerations regarding the chosen method of simulating ice on the cable model. Verification tests of the used equipment are also shown where possible.

4.1. Model Design

In order to choose the best method of simulating the ice accretion on a vertical hanger cable, different approaches were considered, as explained in the following chapter. A short introduction to the different types of ice is also presented.

4.1.1. Types of Ice

Normally ice is classified in 3 groups, which are shown in Figure 16. The three groups are hard rime, soft rime and glaze ice. A fourth form is wet snow or sleet, which is not ice but falls in the same group of solid water accretion on cables. These groupings of ice are related to air temperature ranges as described below.

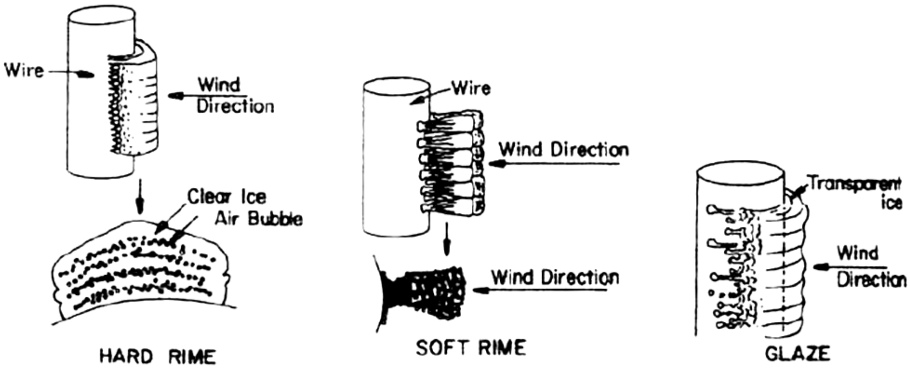
Wire
Wind Direction
Clear Ice
Air Bubble
HARD RIME
Wire
Wind Direction
Wind Direction
SOFT RIME
Transparent ice
Wind Direction
GLAZE

Figure 16. Different Type of Ice, [46].

Apart from air temperature the ice formation depends on the water vapor in the air (droplet size and distribution density) and wind speed, which can be summarized to the local weather condition. Hard rime is formed from freezing cloud or fog droplets for temperatures around -2 °C to -8 °C. Soft rime is formed in very high levels of relative humidity (above 90%) for temperatures below -8 °C. Glaze ice is formed from freezing rain, cloud or fog for temperatures around -0 °C. Sleet is formed by wet snow in temperatures around -1 °C to 2 °C. The corresponding density and other adherence properties are listed in Table 1.

Table 1. Different Types of Ice Accretions.

Types of accretion	Temperature [°C]	Density [kg/m^3]	Adherence
Hard rime	-2 °C to -8 °C.	600-900	Strong
Soft rime	< -8 °C	Less than 600	Poor
Glaze	~ -0 °C	900-920	Excellent
sleet	-1 °C to 2 °C	300-700	fair

4.1.2. Ice Shapes.

The selected shapes of thin ice accretions are based on wind tunnel experiments presented in [47] and summarized in section 5.1. The ice shapes are also partially based on previously made experiments performed by Lozowski et al., [48].

Figure 17 shows the obtained results of ice accretion for different wind speeds and different Liquid Water Content(LWC). Liquid water content in air is generally, given in values of water mass per volume air [g/m^3]. A value of 0.4 for LWC is assumed to represent the water present under the ice accretion mention in relation to the vibration event on the Great Belt East Bridge hangers. This choice was made by combining the experiments performed by Lozowski et al., [48], and the theoretical work done in the area of thermodynamics in relation to icing cylinders, [49]. Finally values of LWC = 0.44 in Strato-cumulus clouds has been reported [50]. A Strato-cumulus cloud belongs to a class of clouds characterized by large dark, rounded masses, usually in groups, lines, or waves. These clouds are often seen at either the front or tail end of a weather front so they may indicate forthcoming storms.

From the experiments and the theoretical work it is possible to see that a LWC greater than 0.4 has little consequence for the ice formation when the temperature is just below zero. Figure 18 shows an analytical calculation of the limit of LWC vs. air speed at which the surface temperature rises to 0°C due to thermodynamic effects. It is seen that for at temperature of -5°C the maximum LWC is approximately 0.4. If LWC is higher, then the unfrozen fraction of water may shed away with the airflow or freeze at the back side of the cylinder (runback icing), or may be partly incorporated into a spongy ice structure similar to hail growth, [51].

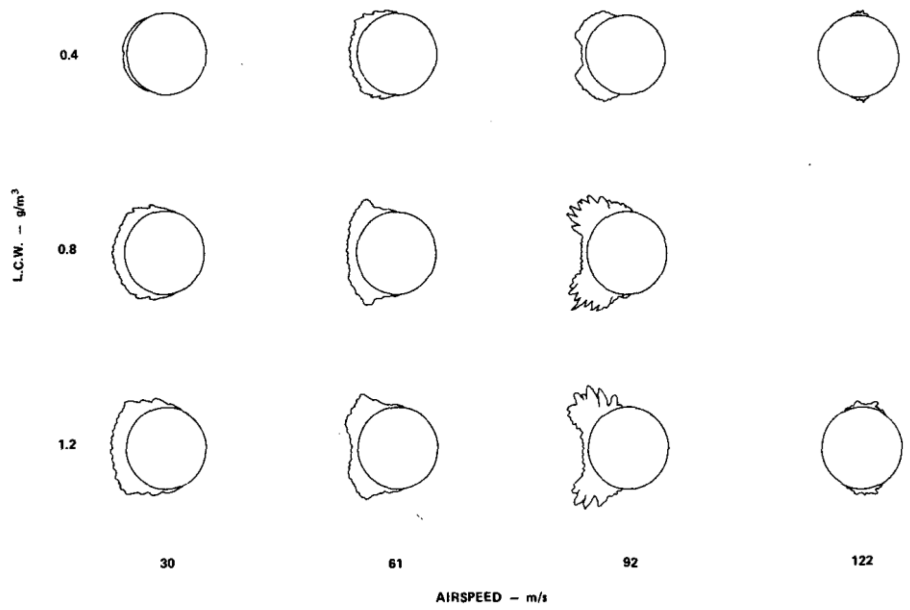

Figure 17. Ice Accretions for a Cylinder in Icing Experiments at -5°C, [48].

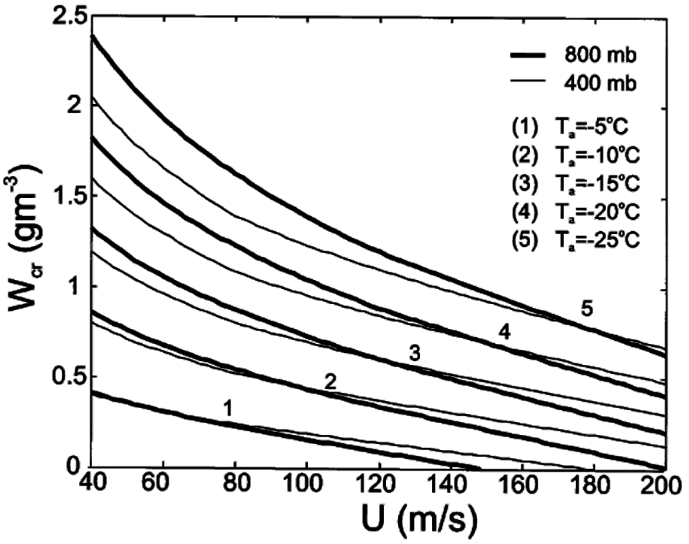

Figure 18. Critical LWC at which the surface temperature rises to 0°C, [49].

For the performed experiments, which simulate the assumed meteorological conditions present at the vibration event on the Great Belt East Bridge, it is assumed that neither runback icing nor spongy ice structure effects are present, and that the ice is formed due to a LWC in the air surrounding the cable similar that of a Strato-cumulus cloud.

The formation of ice has received a considerable amount of attention within the aircraft and electrical transmission line community due to the problem of ice on aircraft wings and transmission lines. The research within these areas is split in to two focus areas. One area concentrates on experiments, [48, 52-57], and another attempts to simulate the ice formation numerically, [58-60]. However, the conditions under which the ice accretion observed on the Great Belt East Bridge falls outside the region of interest for this community. There is therefore a need for wind tunnel tests, which will cover this unmapped region of icing in high temperature, ranging from -5° to -1° and relatively low wind speeds.

4.1.3. Choice of Ice Simulation Method

There are several ways of simulating ice, ranging from applying a layer of paint to making water solidify on the surface of the model.

The method of how to simulate ice should be chosen so it would be easy to shift between different sizes of the ice accretion. The ice should also have a well defined geometry to enable the possibility of comparison between different experiments. This constrain makes it difficult to use real ice in wind tunnels where the air temperature can't be lowered below freezing point because thawing will happen during the test. Cooling elements could be placed inside the cable model, which will have the advantage of a relative stable and defined geometry of the ice.

The following paragraphs list advantages and obstacles of different ways to simulate ice accretion

First option, Paint:

> A section of the cable circumference where the ice is simulated should preferable be spray painted to get at smooth surface, [19]. One drawback of this method is that it can limit the shapes which can be tested.

Second option, Silicon:

The mold used for producing the silicon "ice" could be made from real ice, found in nature or obtained in wind tunnel tests, which would imprint the same roughness to the silicon and then in turn to the cable model. However, this approach have the drawback that every ice shape, which have to tested, will require a mold.

Third option, Real Ice:

This would give the most correct data, but it would be practically impossible to experimentally reproduce the same ice shape hence comparisons of the results obtained from these tests would be virtually impossible.

Fourth option, Rapid prototyping:

Rapid Prototyping (RP) would allow for generating complex ice accretion shapes. Coating the RP models with pain or varnish will make it possible to have some control over the surface smoothness. This combination allows for a fast and relative cheap way of testing complex shapes of ice accretions.

The final choice of production method fell on rapid prototyping due to the speed, versatility and relative low cost of this method.

4.2. Wind Tunnels.

This section describes the different wind tunnels which have been used in the experiments performed in the frame of the presented research work. Validation experiments of wind tunnels and the used equipment is also shown, where possible.

4.2.1. Altitude Icing Wind Tunnel Facility (AIWT)

The ice accretion tests were performed in the AIWT at the National Research Council (NRC) Institute for Aerospace Research in Ottawa, Canada. The test section of the wind tunnel is 0.57mx0.57m and the overall design and capability of the facility is described in detail in [61]. Figure 19 shows a sketch of the altitude icing wind tunnel facility at NRC.

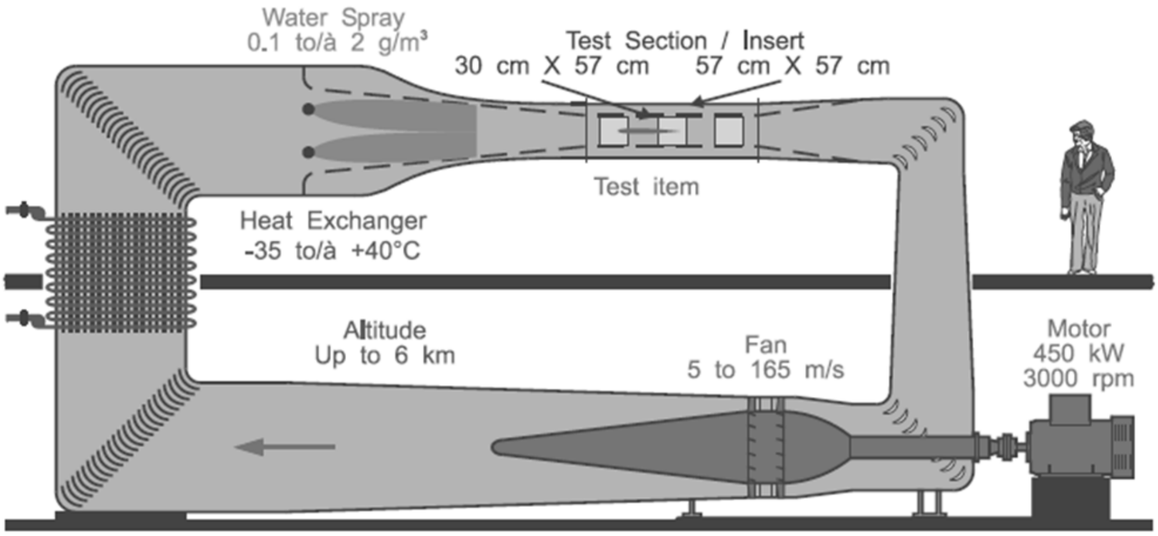
Water Spray
0.1 to/à 2 g/m³
Test Section / Insert
30 cm X 57 cm
57 cm X 57 cm
Test item
Heat Exchanger
-35 to/à +40°C
Altitude
Up to 6 km
Fan
5 to 165 m/s
Motor
450 kW
3000 rpm

Figure 19. Sketch of Icing Wind Tunnel Facility at the NRC Institute for Aerospace Research.

The water which is sprayed into the air flow is distributed by 6 spraybars which each have 11 spray nozzles. In the experiments only 4 of the 6 spraybars were activated, namely spraybars B2 to B5, Figure 20. On these spraybars only 5 nozzles were used to distribute the water, namely N1, N4, N6, N8 and N11. A schematic drawing of the configuration is shown in Figure 20.

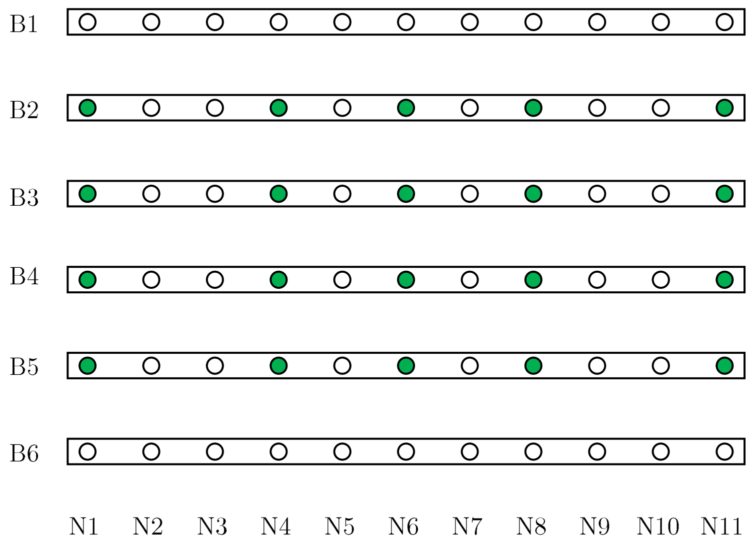

Figure 20. Spraybars and Spray Nozzles in NRC Wind Tunnel, ● Indicates Active Nozzles.

Wind Profile Measurements.

A mapping of the wind profiles was not possible in the AIWT, but a thorough categorization of the AIWT can be found in [61].

4.2.2. Closed Circuit Wind Tunnel (CCWT)

The closed circuit wind tunnel used for the aerodynamic force and dynamic experiments is situated at FORCE Technology, Lyngby. The definition of the coordinate system in the wind tunnel is chosen to coincide with the definition for the derived theoretical model and is shown in Figure 21. The drag is measured in the x-direction, lift is measured in the y-direction and moment is measured around the z-direction.

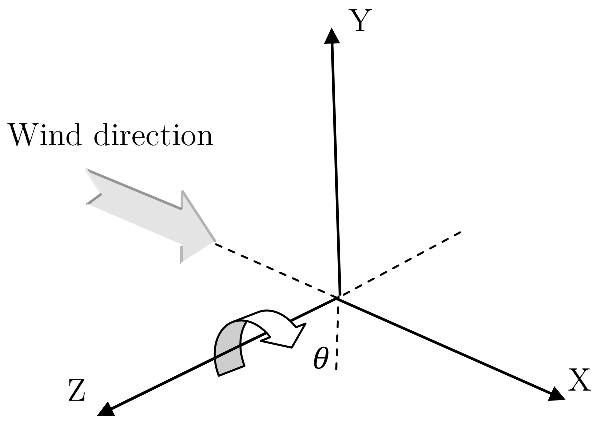

Figure 21. Sign Convention in Wind Tunnel.

FORCE Technology's Closed Circuit Wind Tunnel (CCWT) is shown in Figure 22 and Figure 23 below. This tunnel is mainly used to perform experiments in uniform flow. By installing special grids upstream of the working section, varying turbulence intensities can be created in the initially laminar flow.

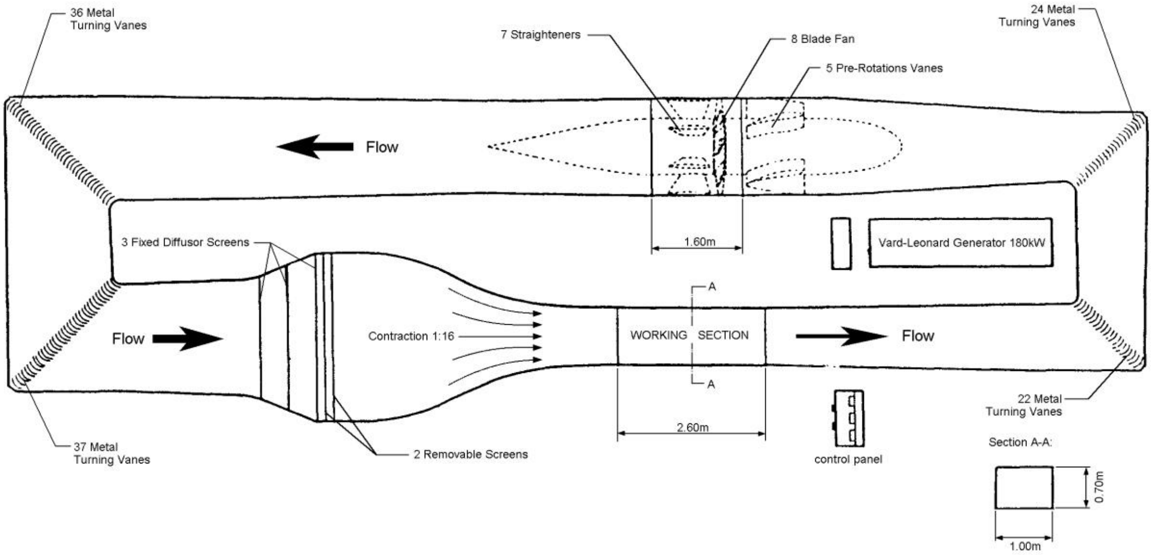
36 Metal Turning Vanes
7 Straighteners
8 Blade Fan
5 Pre-Rotations Vanes
24 Metal Turning Vanes
Flow
1.60m
Vard-Leonard Generator 180kW
3 Fixed Diffusor Screens
A
Flow
Contraction 1:16
WORKING SECTION
Flow
A
2.60m
22 Metal Turning Vanes
Section A-A:
0.70m
1.00m
control panel
37 Metal Turning Vanes
2 Removable Screens

Figure 22. Sketch of the Close Circuit Wind Tunnel at FORCE.

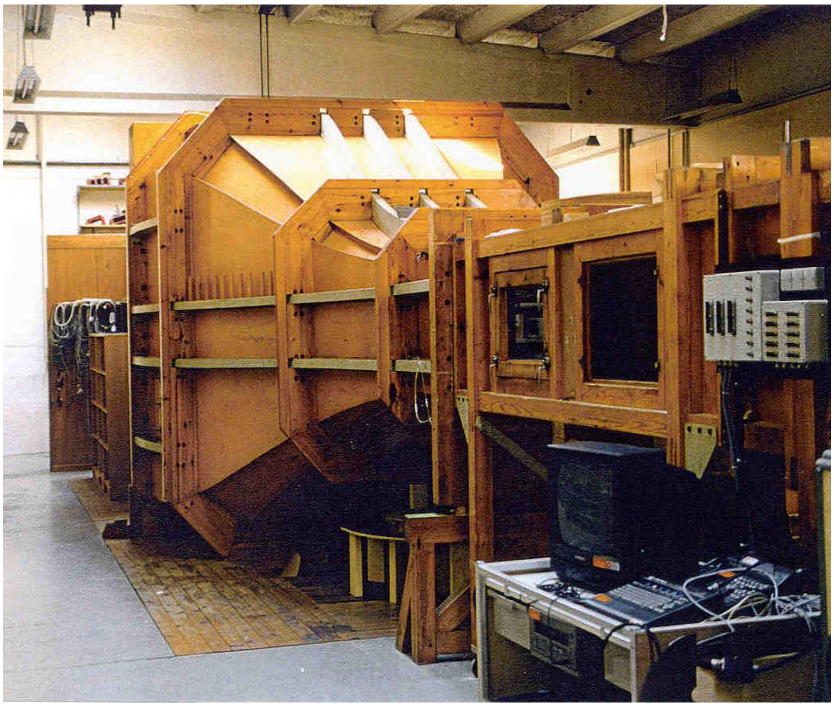

Figure 23. View on Test Section of the CCWT at FORCE.

The high flow speed of up to 60m/s allows for investigation of a variety of fluid dynamical problems at high Reynolds numbers. Small-scale models, section models or ships and buildings, are tested to identify forces, surface pressures or to observe the flow field around the respective body.

The working section is completely exchangeable and a number of different types are available. Dimensions of the exchangeable test section of the Closed Circuit Wind-Tunnel used for the experiments presented within this thesis can be seen Table 2

Table 2. Dimensions of the Test Section.

Length	2.60m
Width	1.00m
Height	0.70m

Wind Profile Measurements.

Due to asymmetry and the wall friction to which all wind tunnels are subjected to in more or less degree, it was found necessary to map the wind profile of the wind tunnel velocity range of the planned experiments. The mapping of the wind profile was carried out at 5 different heights in order to have a detailed picture of the velocity profile both a static and dynamic model is subjected too.

Position of Wind Profiles

The following summarize the different levels and setups for the measured wind profiles in smooth flow. A total of 5 profiles located at different heights, were measured along the width of the wind tunnel.

The smooth and turbulent wind profiles was measured in 28 and 26 points across the wind tunnel section, respectively. All points were repeated at 5 heights, named H1-H5, and at 7(smooth) and 5(turbulent) wind speeds to be able to fully document the Reynolds effects on the wind profile. The profiles where mapped for both smooth(I_X<1%) and turbulent(I_X=7%) flow conditions

For the smooth flow profiles, Table 3 list wind speeds which were used in the tests.

Table 3. Wind Speeds at which the Profile was Measured for Smooth Flow.

20 m/s	25 m/s	30 m/s	35 m/s	40 m/s	50 m/s	60 m/s

The position of the points used in measuring the smooth flow profiles are listed in Table 4, where the points are found by measuring from side 2 and towards side 1 of the wind tunnel, see Figure 24.

Table 4. Positions Measured, Starting from Side 2 for Smooth Flow.

Point	1	2	3	4	5	6	7	8	9	10	11	12	13	14
Position [mm]	12	19	26	33	40	47	54	61	68	75	122	232	342	452
Point	15	16	17	18	19	20	21	22	23	24	25	26	27	28
Position [mm]	562	672	782	892	925	932	939	946	953	960	967	974	981	988

Table 5 shows the wind speeds for the turbulent flow profiles and the position of the points used in measuring the turbulent flow profiles are listed in Table 6, where the points are found by measuring from side 2 and towards side 1 of the wind tunnel, see Figure 24.

Table 5. Wind Speeds at which the Profile was Measured for Turbulent Flow.

20 m/s	25 m/s	30 m/s	35 m/s

Table 6. Positions Measured, Starting from Side 2 for Turbulent Flow

Point	1	2	3	4	5	6	7	8	9	10	11	12	13
Position [mm]	9	16	23	30	37	44	51	58	63	72	116	226	336
Point	14	15	16	17	18	19	20	21	22	23	24	25	26
Position [mm]	667	777	887	931	938	945	952	959	966	973	980	987	944

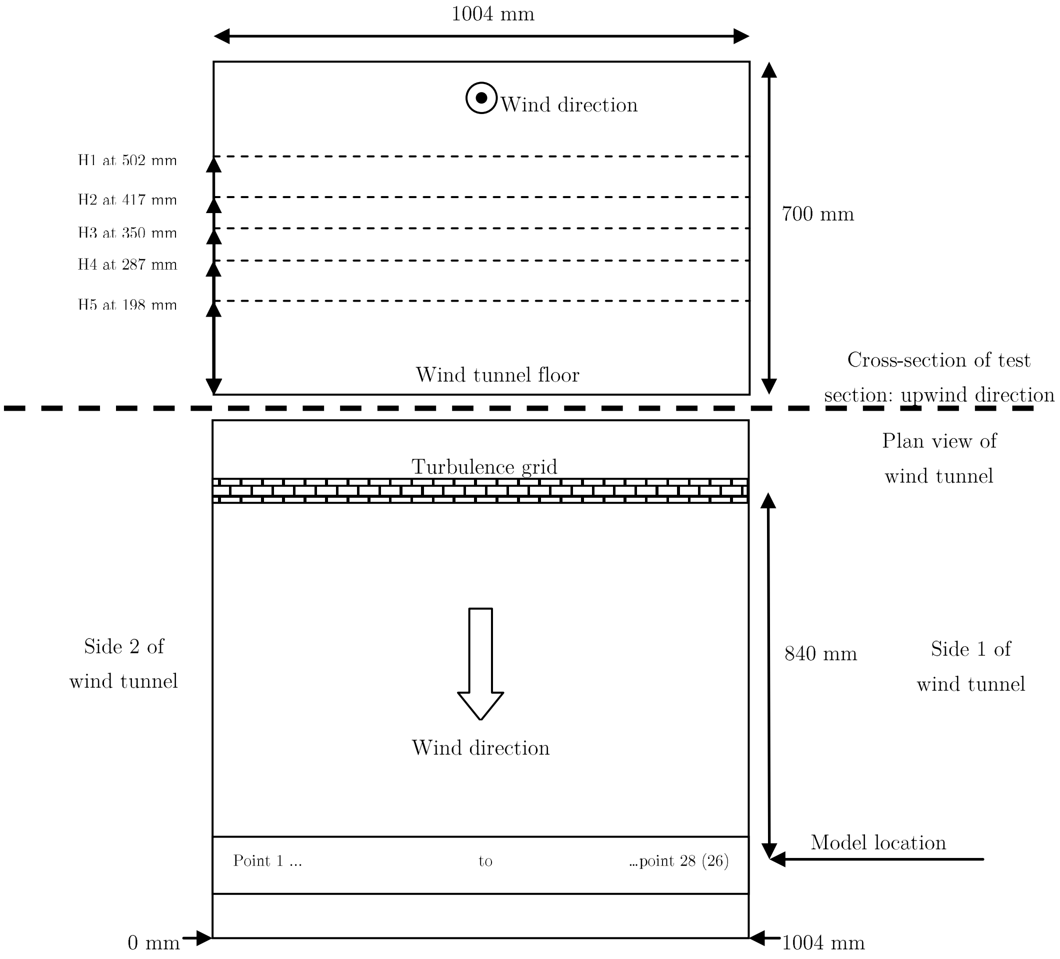
1004 mm
Wind direction
H1 at 502 mm
H2 at 417 mm
H3 at 350 mm
H4 at 287 mm
H5 at 198 mm
700 mm
Wind tunnel floor
Cross-section of test section: upwind direction
Plan view of wind tunnel
Turbulence grid
Side 2 of wind tunnel
840 mm
Side 1 of wind tunnel
Wind direction
Model location
Point 1 ...
to
...point 28 (26)
0 mm
1004 mm

Figure 24. Different Levels and Position for the Profile Measured in The Wind Tunnel.

Figure 26 shows a picture of the grid used to generate turbulence in the experiments for turbulent flow. The grid is located upstream of the model at a distance of 0.84m, Figure 24. The dimensions of the turbulence grid can be seen in Figure 25. Here A and B are the length and width of the square hole in the grid and C is the width of the wooden bars making up the grid.

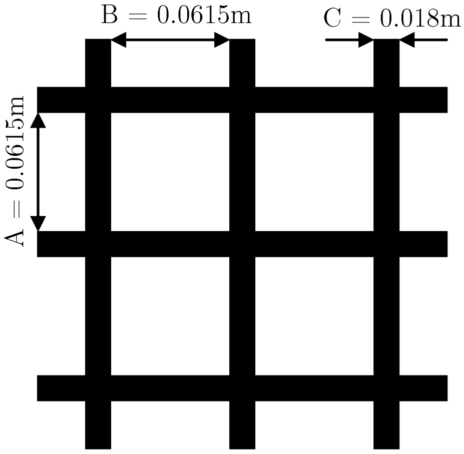

Figure 25. Dimensions of Turbulence Grid.

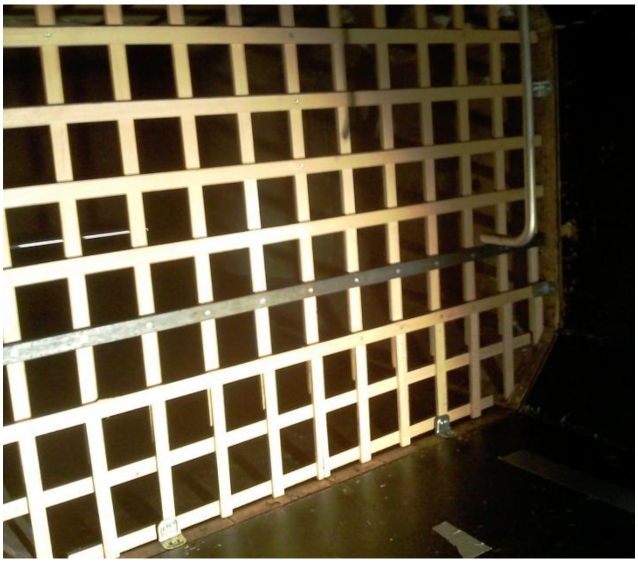

Figure 26. Picture of Turbulence Grid and Pitot Tube Location.

All the above defined wind profiles were mesured by hotwire anamometry. Figure 27 shows the sign converntion used for the measurements.

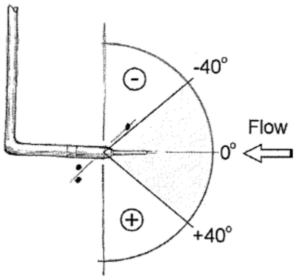

Figure 27. Sign Convention for Flow Angle.

Figure 28 shows plots for all the wind velocity profiles found for smooth flow collected at each of the five different levels H1 – H5 for a given wind speed. Figure 29 shows similar plots for all the wind velocity profiles found for turbulent flow conditions. For more detailed plots each of the wind profiles, see Appendix B.

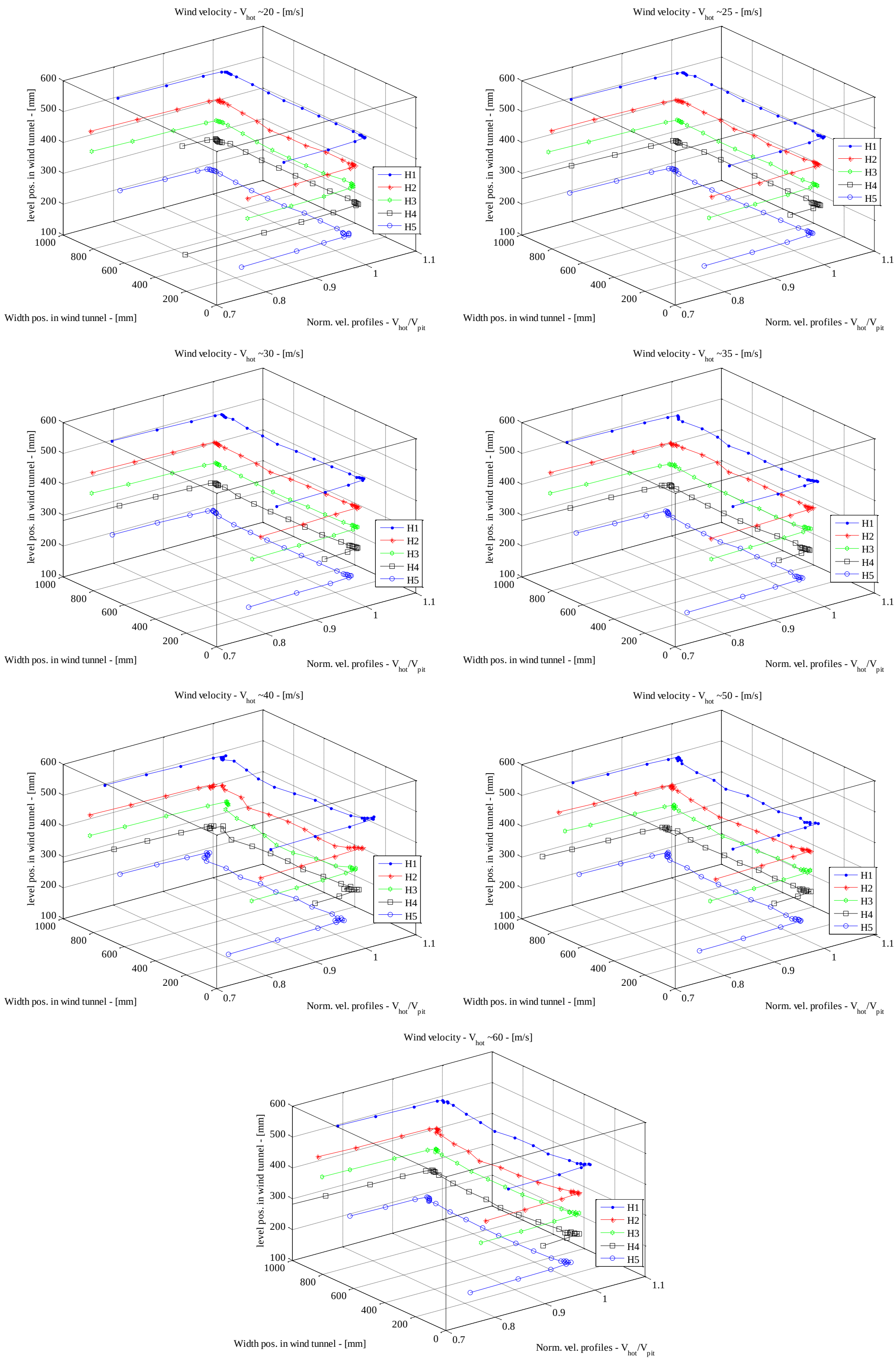

Figure 28. Wind Velocity Profiles for Smooth Flow.

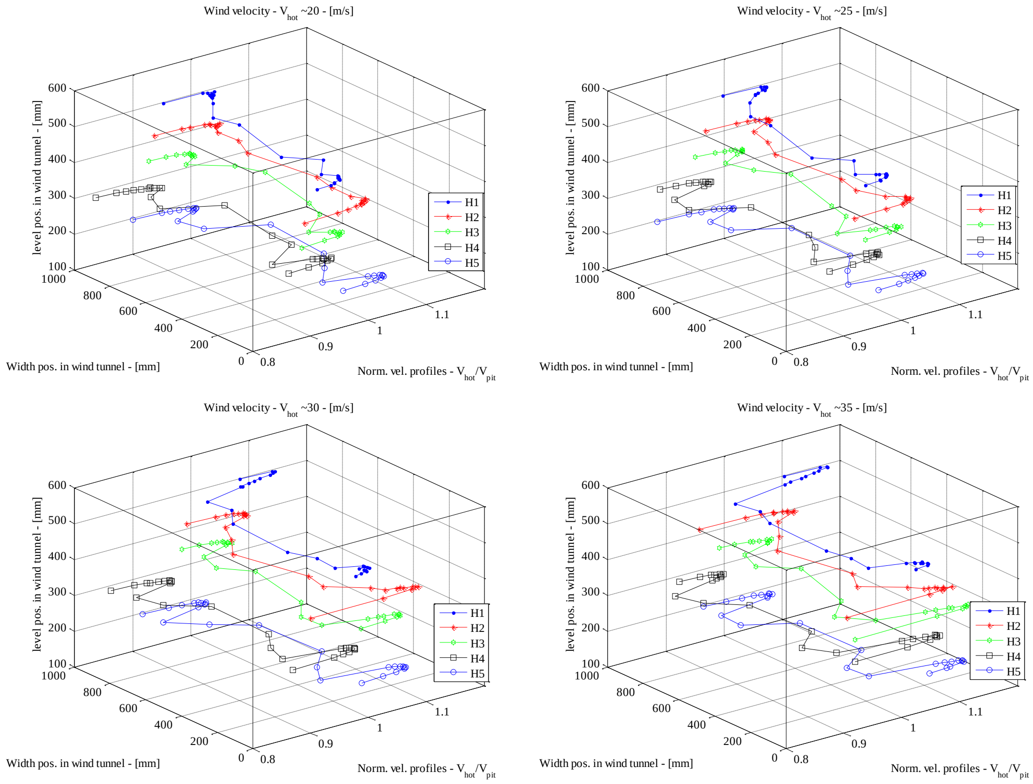

Figure 29. Wind Velocity Profiles for Turbulent Flow (7%).

4.3. Control Experiments in the CCWT.

In order to verify the accuracy of the wind tunnel and of the experimental equipment, it was decided to run a set of control experiments. The first set of experiments focused on the static aerodynamic forces to allow comparison of force coefficients. It was decided to test a D-section due to the well known and documented aerodynamic instability of that shape. The dimension of the D-section model, which was used in the experiments, is shown in Figure 30.

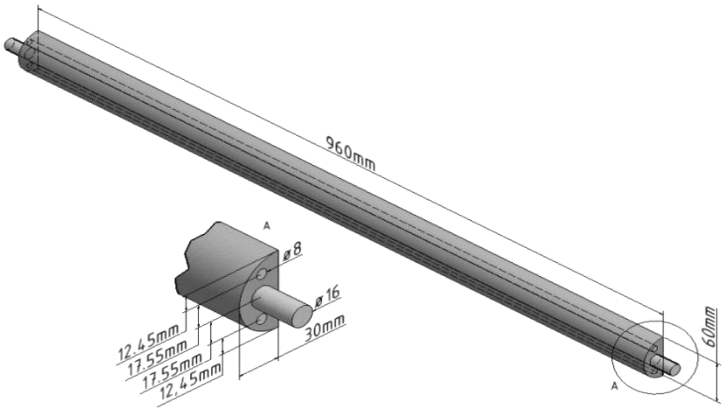

Figure 30. Dimension of D-section Control Model.

Figure 31 shows the sign convention used for the D-section wind tunnel test. Lift (L) is measured positive in the upwards direction, Drag (D) is measured positive in the flow direction and the Moment (M) is measured positive the clockwise direction around the centre of rotation.

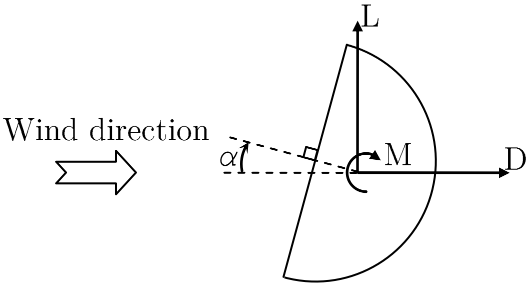

Figure 31. Sign Convention for D-section Test.

Figure 32 shows a picture of the D-section mounted in the wind tunnel with smooth flow.

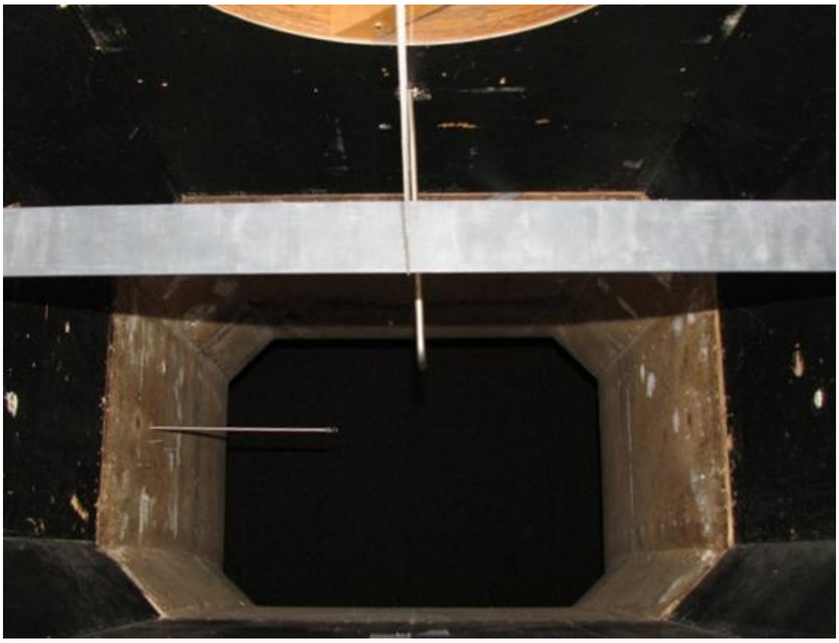

Figure 32. D-section Model Mounted in Wind Tunnel, Smooth Flow.

Figure 33 shows a picture of the D-section mounted in the wind tunnel with turbulent. The turbulence grid generates a turbulent intensity of 7%.

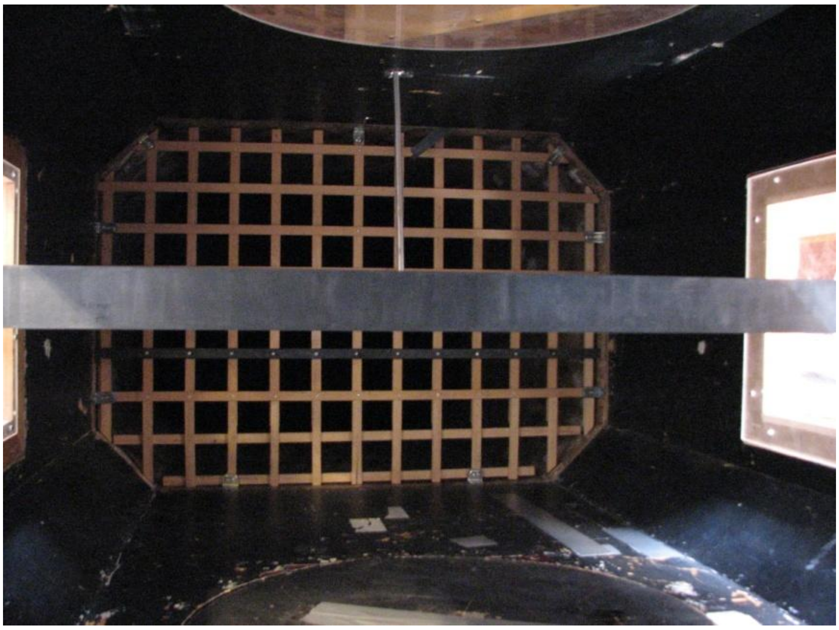

Figure 33. D-section Model Mounted in Wind Tunnel, Turbulent Flow

4.3.1. Static Experiments

Values for force coefficients found in literature and used in a comparison of the results denoted Gjelstrup, can be found the following papers, [62-65].

Figure 34 shows a comparison of 6 drag coefficients curves found for a D-section subjected to smooth flow. It is seen that there is a high degree of variation in the ranges of $\alpha = 0°$ to $25°$ and from $\alpha = 135°$ to $180°$. This could be contributed to Reynolds number effects, how smooth the flow is or differences in the D-section model itself.

Looking at the two curves denoted Gjelstrup for Reynolds numbers of $5\text{x}10^5$ and $9\text{x}10^5$ in Figure 34 indicates that the Reynolds number effects has little effect on the C_D curves for the D-section in the two ranges of α. This suggests that the flow turbulence or the model geometry has the greatest effect on the C_D curves in those two wind angles of attack ranges.

Figure 35 shows the C_D curves for the D-section found from turbulent flow. Here the experiments denoted Gjelstrup shows that the C_D increases in the wind angle of attack ranging between $\alpha = 0°$ to $40°$, seen in relation to the smooth flow results. This is in contrast to the experiments performed by Novak et al., [62], who showed that the C_D decrease in those same ranges. The differences between the two experiments are the level of turbulence, the results denoted Gjelstrup were obtain with a turbulence intensity of I_X=7% whereas Novak et al., [62], used I_X=11%. This difference does not seem to have a large effect in the wind attack ranges of $\alpha = 45°$ to $130°$.

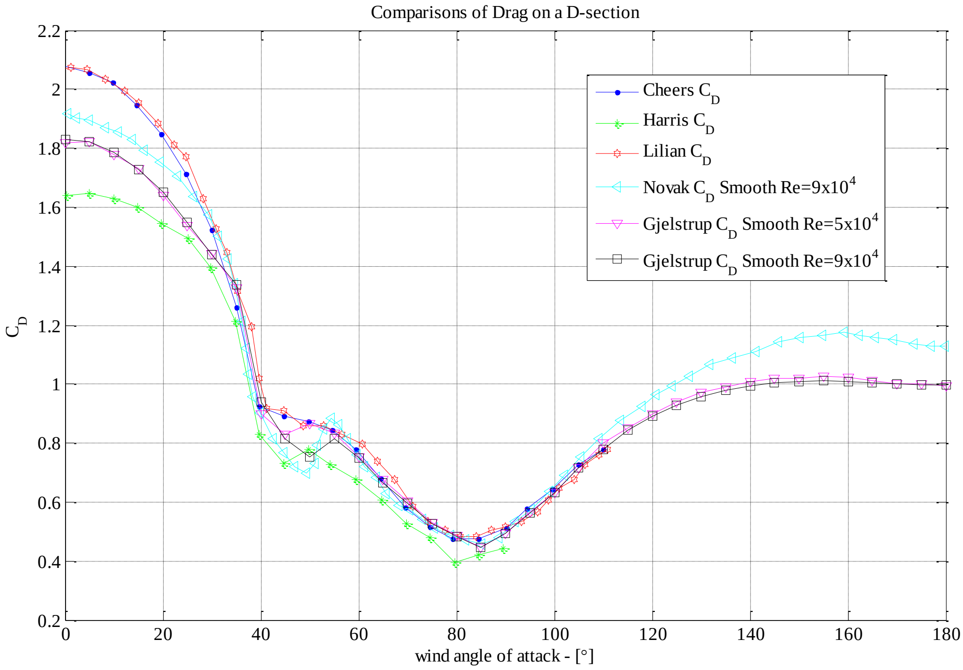

Figure 34. Comparison of Drag for D-section model in Smooth Flow.

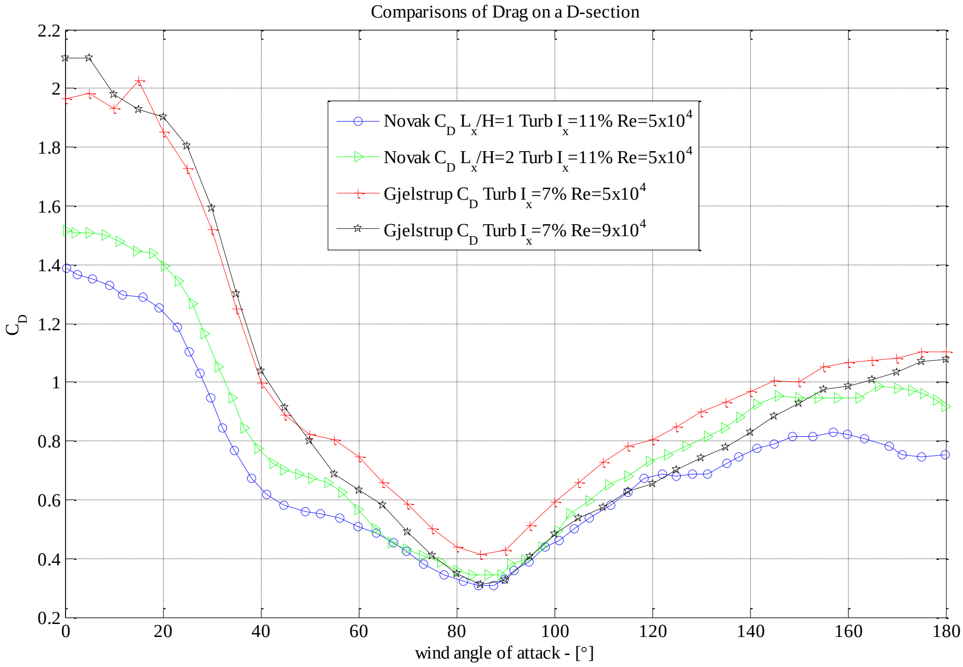

Figure 35. Comparison of Drag for D-section model in Turbulent Flow.

For the wind angle ranges $\alpha = 0°$ to $25°$ and from $\alpha = 135°$ to $180°$, it can be seen that the D-section model has a relative sharp transition from the straight side to the curved side. It is well known that turbulence shifts the vortex shedding velocity, [19], and combining this with the other indications it is concluded that the difference in the C_D curves is mostly caused by differences in the turbulence intensity.

For smooth flow it is seen that the lift coefficients C_L does not seem to be as dependent on the turbulence as was observed for the C_D curves. C_L curves are compared and shown in Figure 36. It is seen that there is good agreement between all six experiments. However, there are some differences around a wind angle of attack of $\alpha = 45°$ and $\alpha = 90°$, which rather characteristic angles seen in relation to the model geometry.

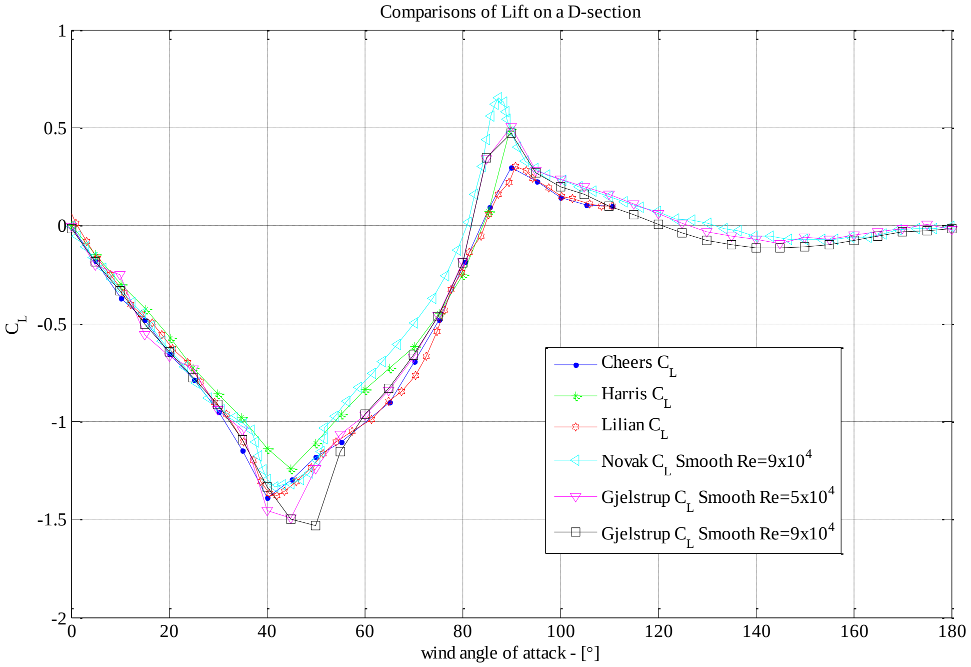

Figure 36. Comparison of Lift for D-section model model in Smooth Flow.

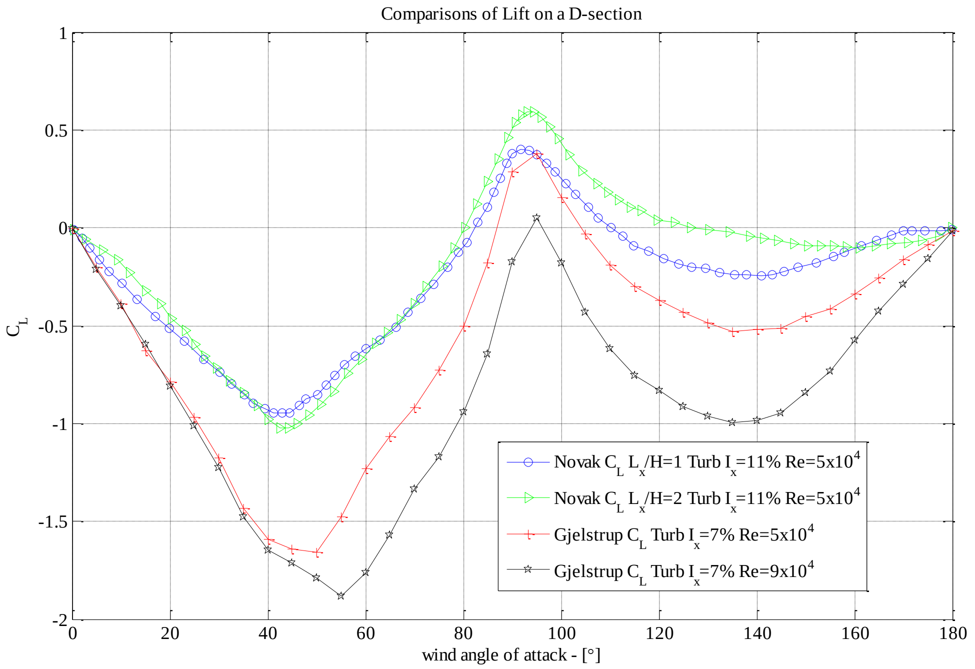

Figure 37. Comparison of Lift for D-section model model in Turbulent Flow.

Figure 37 shows the effect of turbulence on the C_L curves. It is seen that the lift force becomes Reynolds number depended and that there is a significant difference between results obtain by Novak et al., [62], and the results denoted Gjelstrup.

The combination of turbulence and the Reynolds number effects could explain the difference that can be observed in the C_L curves around a wind angle of attack of $\alpha = 45°$ and $\alpha = 90°$. A slight difference in the turbulence and wind speed could shift the C_L curves either up or down.

Figure 38 shows the found moment coefficient, C_M, derived from the experiments. Here it is seen that there is a good agreement between the experiments compared in the figure. The C_M curves do not appear to be sensitive to small differences in the turbulence intensity of the wind velocity profile, just as it was observed for the C_L curves. Figure 39 shows the found C_M curves for turbulent flow and as for the C_L curves it is seen that the turbulence intensity affects the aerodynamic moment.

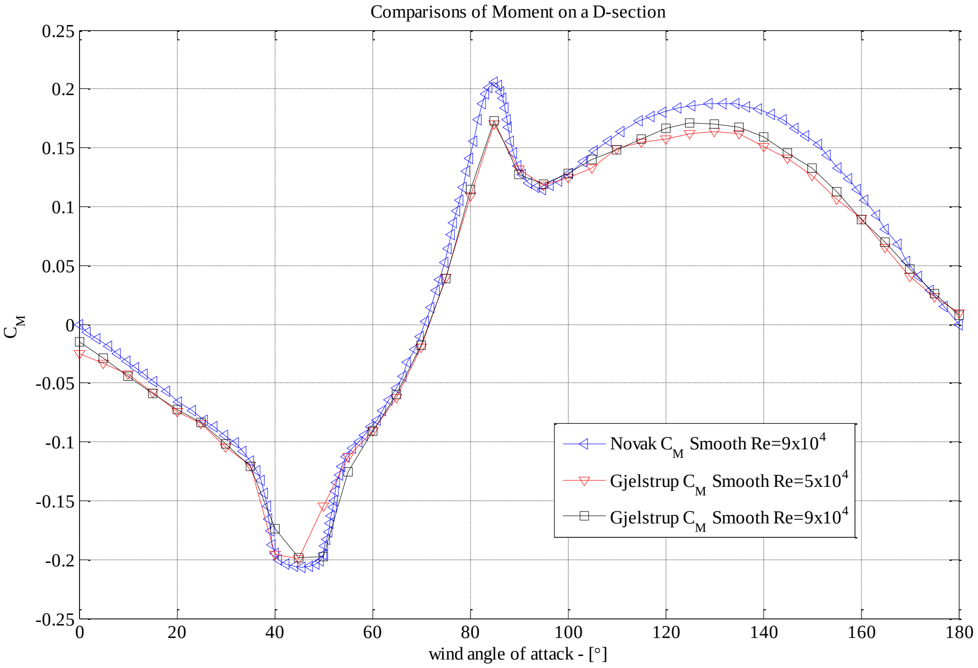

Figure 38. Comparison of Moment for D-section model model in Smooth Flow.

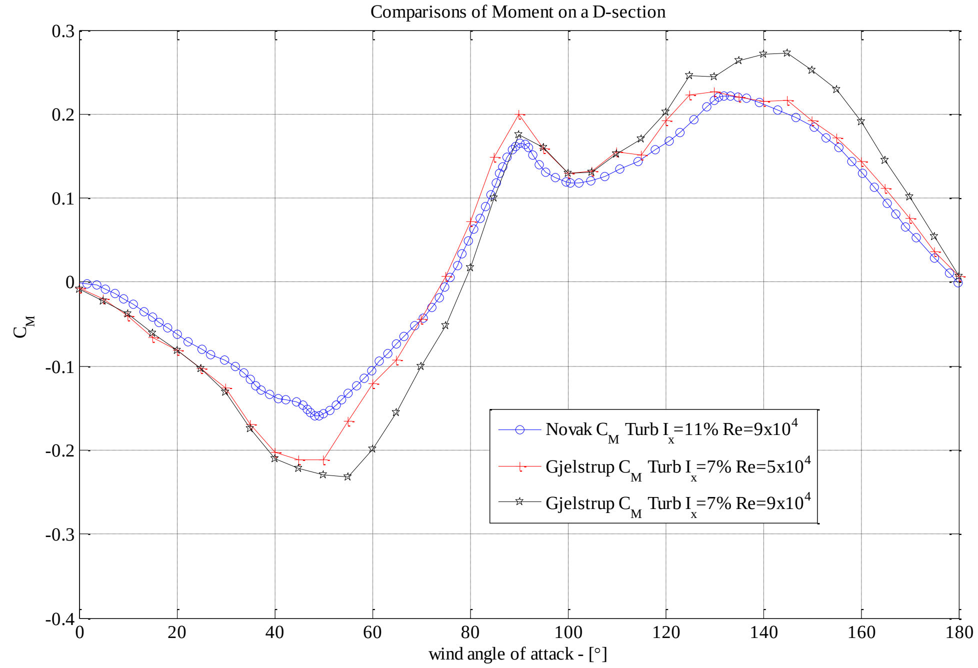

Figure 39 Comparison of Moment for D-section model in Turbulent Flow

4.3.2. Dynamic Experiments

The second set of tests was conducted in a dynamic rig with 2-DOF, vertical and torsional. Here, one subset with tuned frequencies $(f_v = f_t)$ and two subsets with detuned frequencies $(f_v \neq f_t)$ were tested. Iso-plots of the mean displacements are provied appendix C.

Table 7. Model Parameters for Dynamic Tests

Frequency configuration		Tuned	Detuned	Detuned
Model weight	[kg]	6.2	6.2	6.2
Vertical freq. (f_v)	[Hz]	6.48	6.48	6.48
Torsional freq. (f_t)	[Hz]	6.50	11.8	4.466
Damping vertical	% of critical	0.08	0.08	0.08
Damping Torsion	% of critical	0.13	1.47	0.13
Mass moment of inertia	[$\text{kg} \cdot \text{m}^3/\text{m}$]	0.16	0.07	0.68

To verify the static and the dynamic test, a comparison of the lift and moment coefficients was made. Figure 40a shows the static C_L for U=12.5m/s, smooth flow and the C_L obtained from the dynamic tests. C_L from the dynamic tests is found by using the spring stiffness of the test rig in conjunction with at the mean displacement in the vertical direction for every angle. Likewise, Figure 40b shows the static C_M plotted in the same figure as C_M found from the dynamic tests with U=12.5m/s, smooth flow. Similar plots is shown in Figure 41 for U=22.5m/s.

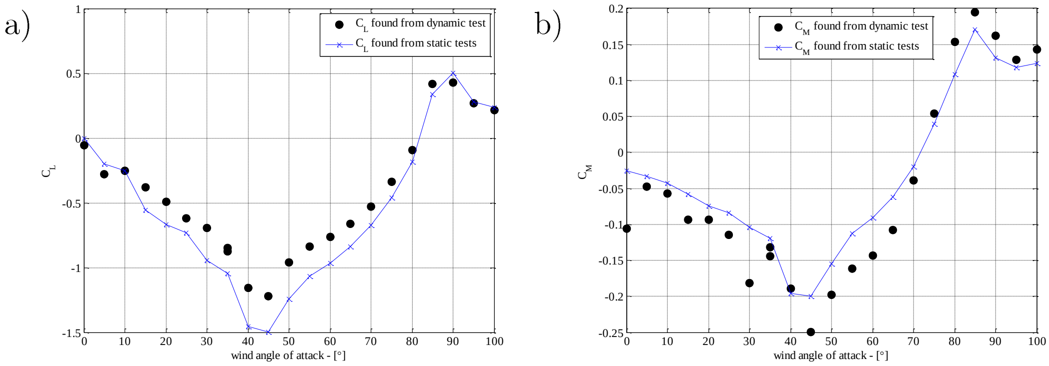

Figure 40. a) Dynamic C_L vs. Static C_L for U=12.5m/s, Smooth Flow, b) Dynamic C_M vs. Static C_M for U=12.5m/s, Smooth Flow.

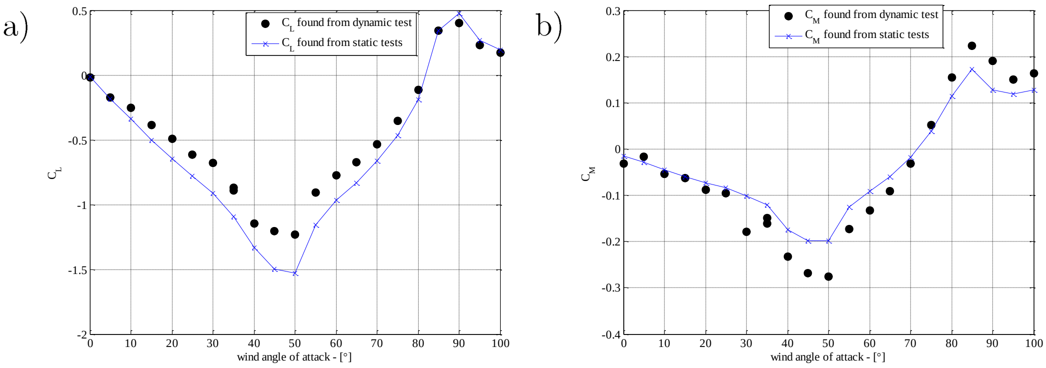

Figure 41. a) Dynamic C_L vs. Static C_L for U=22.5m/s, Smooth Flow, b) Dynamic C_M vs. Static C_M for U=22.5m/s, Smooth Flow.

It is seen, that for U=12.5m/s, smooth flow, there is a good agreement for both C_L and C_M when comparing the statically and dynamically found force coefficients.

In a similar plot for turbulent flow with U=12.5m/s it is seen that the difference between static and dynamic force coefficients is greater than for smooth flow, see Figure 42. Comparing this particular turbulent flow seems to suggest that results found on the basis of quasi-static theory should be used with some caution, or that the added stiffness origination from the drag wires of the rig, which adds stiffness to the system as the vibration amplitudes grows, is the cause of the observed difference, in the force coefficients.

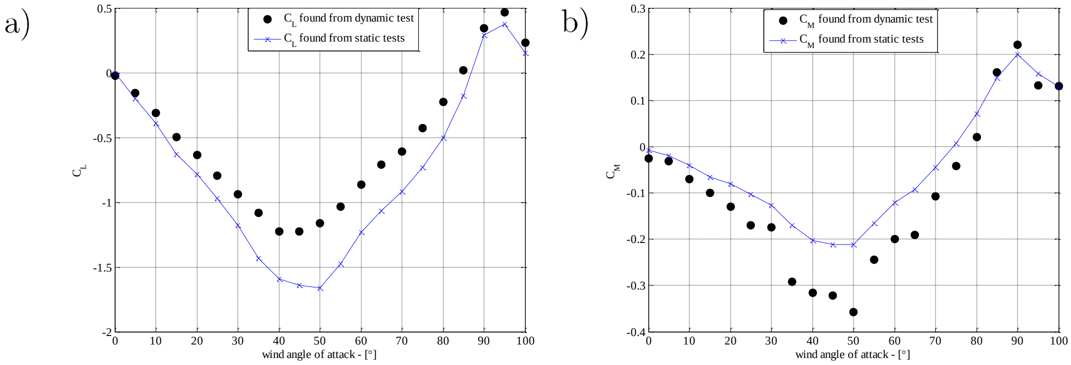

Figure 42. a) Dynamic C_L vs. Static C_L for U=12.5m/s, Turbulent Flow (7%), b) Dynamic C_M vs. Static C_M for U=12.5m/s, Turbulent Flow (7%).

Looking at the force coefficients found from the dynamic experiments for smooth and turbulent flow, shows that the deviation from the static test is related to the size of the force acting on the model.

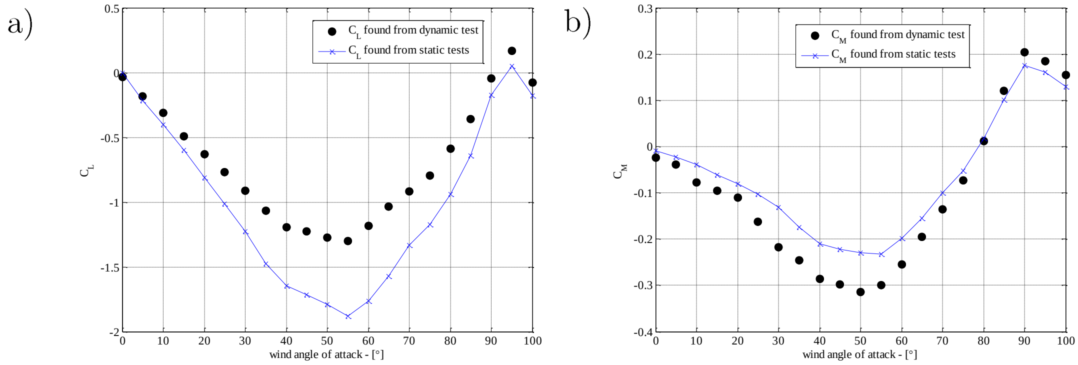

Figure 43. a) Dynamic C_L vs. Static C_L for U=22.5m/s, Turbulent Flow (7%), b) Dynamic C_M vs. Static C_M for U=22.5m/s, Turbulent Flow (7%).

Tests with detuned vertical and torsional frequencies were also performed. Two set of detuned frequencies are shown below, where the first set has a torsional and vertical frequency of $f_t = 11.8$ and $f_v = 6.48$ respectively and the second set has $f_t = 4.66$ and $f_v = 6.48$. The plots shown in Figures 44 – 47 displays a comparison between the aerodynamic force coefficients, C_L and C_M, found from the dynamic and static experiments. The detuned experiments were carried out in smooth flow for wind speeds of 12.5 m/s and 22.5m/s.

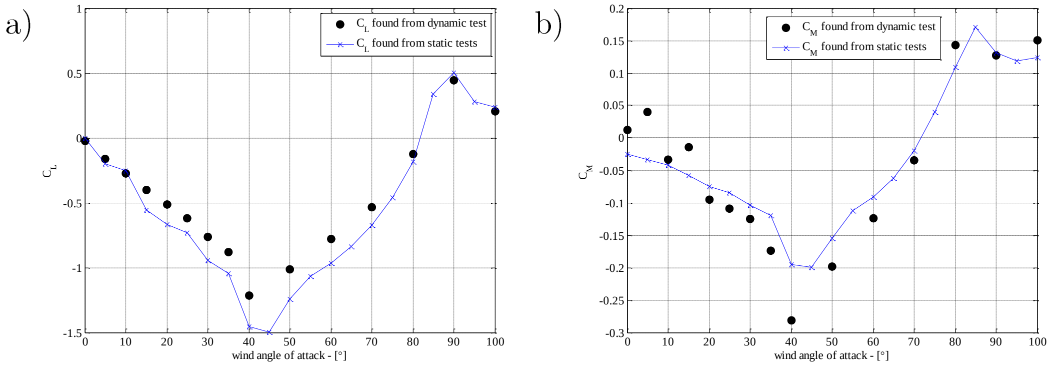

Figure 44. a) Dynamic C_L vs. Static C_L for U=12.5m/s, Smooth Flow, b) Dynamic C_M vs. Static C_M for U=12.5m/s, Smooth Flow, f_t = 11.8hz, f_h = 6.48.

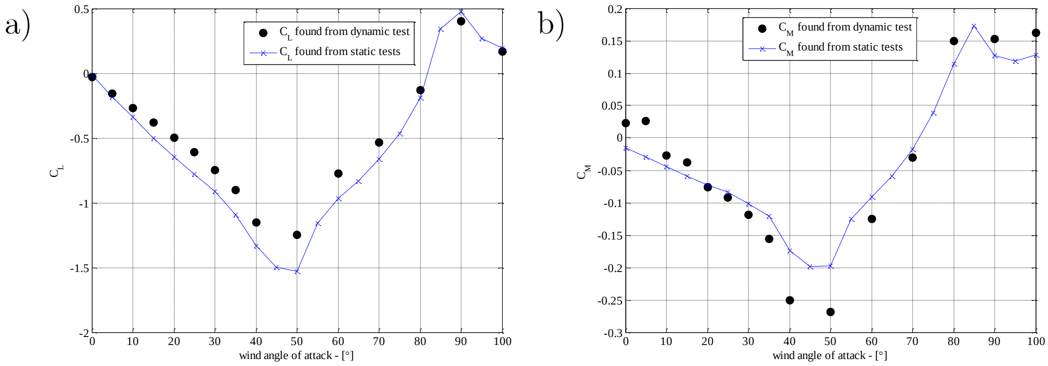

Figure 45. a) Dynamic C_L vs. Static C_L for U=22.5m/s, Smooth Flow, b) Dynamic C_M vs. Static C_M for U=22.5m/s, Smooth Flow, f_t = 11.8hz, f_h = 6.48.

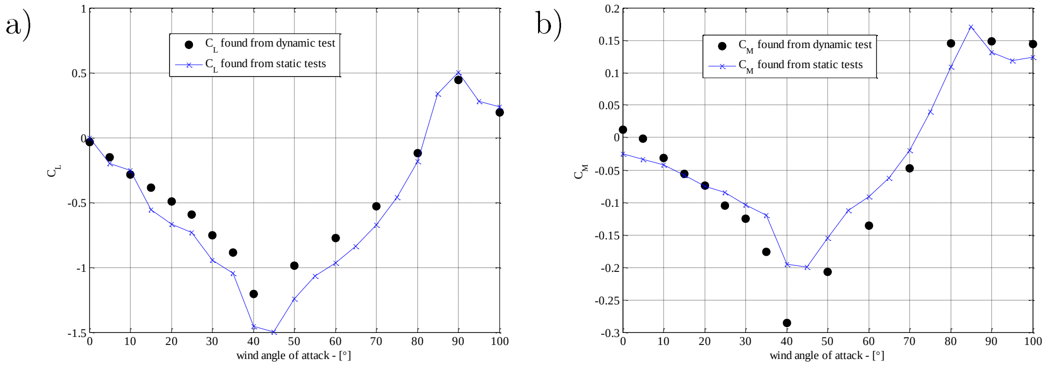

Figure 46. a) Dynamic C_L vs. Static C_L for U=12.5m/s, Smooth Flow, b) Dynamic C_M vs. Static C_M for U=12.5m/s, Smooth Flow, f_t = 4.66hz, f_h = 6.48.

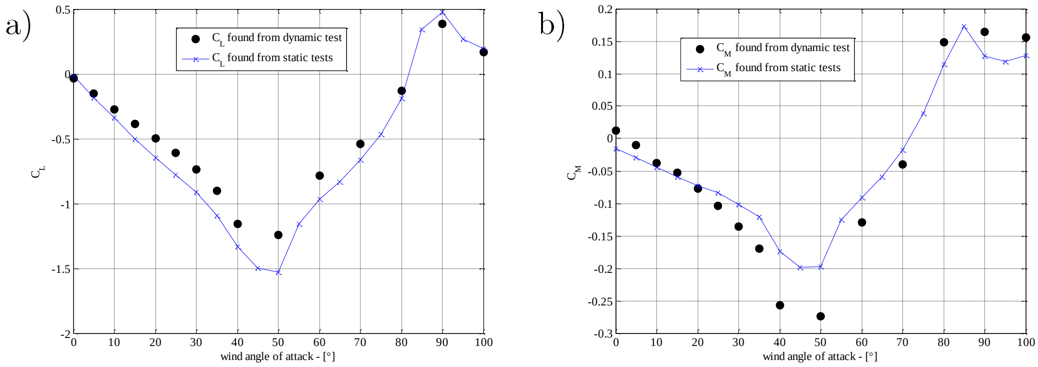

Figure 47 a) Dynamic C_L vs. Static C_L for U=22.5m/s, Smooth Flow, b) Dynamic C_M vs. Static C_M for U=22.5m/s, Smooth Flow, f_t = 4.66hz, f_h = 6.48

4.4. Summary

Through the examination of different types of ice and varies way of producing simulated ice, the choice of method for simulating ice was decided to be rapid prototyping due to the relative low cost and speed of producing models and finally the versatility of this method.

An introduction to the different wind tunnels and experimental equipments used in the work presented in this thesis has been made. For the AIWT no verification experiments have been performed but a thorough categorization of the AIWT can be found in [61]. For the CCWT a series of verification experiments has been performed on the used equipment, including a mapping of the wind tunnel flow field. The verification experiments show good agreement with data found in literature.

Chapter 5

5. Experimental Campaign

The following section describes the experiments performed. The experiments consist of a test series of ice accretion on circular cylinders of different diameter and orientation. Using the results from these experiments in conjunction with availeble literature data, several ice shapes were selected for reproduction in rapid prototyping and testing in a static and dynamic rig.

5.1. Experiments with Ice Growth on Circular Cylinders

The following section describes the icing experiments performed in the Altitude Icing Wind Tunnel Facility at the NRC Institute for Aerospace Research in Ottawa, Canada. It also describes the procedure used in documenting the results which was obtained during the experiments. For an in-depth description of the experiments see refs. [47] and [66].

5.1.1. Experimental Setup

The experimental setup of the tests is illustrated in Figure 48, where the setup shows the small cylinder mounted horizontally in the wind tunnel. The icing of the cylinders was recorded by two fixed mounted cameras. A mini-cam and a normal size video camera were used. Additionally, some tests have been recorded with a high definition camera mounted on a tripod.

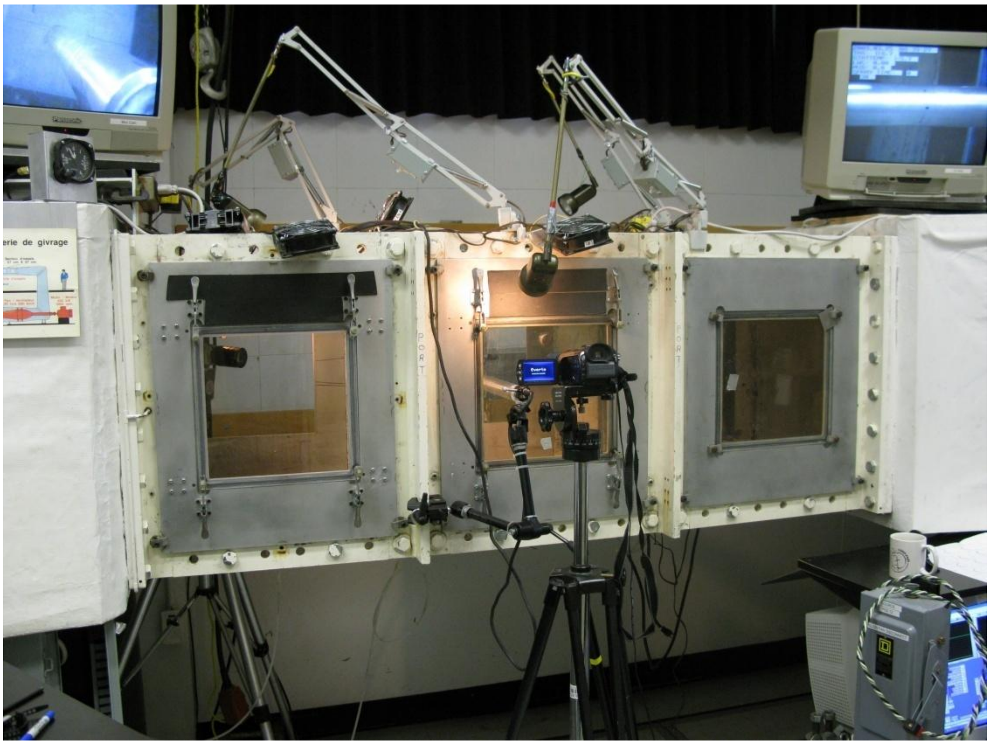

Figure 48. Outside View on the Test section of the High-Altitude Icing Wind Tunnel. The flow passes in the direction from the left to the right.

The experiments were performed under different configurations of temperature, wind speed, water droplet size, exposure time, cylinder diameter, and cylinder orientation. The total test program consists of 46 experiments which are listed in Table 8.

Table 8. Test program for Ice Shapes Experiments Performed at NRC, Ottawa Canada. Here "Orien." is short for Orientation and "H" and "V" is short for Horizontal and Vertical respectively.

#	LWC	U	DS	T_{air}	$Test_{time}$	D	Orien.	#	LWC	U	DS	T_{air}	$Test_{time}$	D	Orien.
[-]	[g/m^3]	[m/s]	[µm]	[ºC]	[min]	[cm]	[-]	[-]	[g/m^3]	[m/s]	[µm]	[ºC]	[min]	[cm]	[-]
1	0.4	10	50	-5	15	3.81	H	24	0.4	30	20	-5	30	3.81	H
2	0.4	10	50	-5	10	3.81	H	25	0.4	20	50	-3	30	3.81	H
3	0.4	10	30	-5	10	3.81	H	26	0.4	20	50	-2	30	3.81	H
4	0.4	10	10	-5	10	3.81	H	27	0.4	20	50	-1	30	3.81	H
5	0.4	10	50	-5	15	3.81	H	28	0.4	20	50	-1	60	3.81	H
6	0.4	10	50	-4	10	3.81	H	29	0.4	20	50	-3	10	8.9	H
7	0.4	10	50	-3	10	3.81	H	30	0.4	20	50	-3	30	8.9	H
8	0.4	10	50	-2	10	3.81	H	31	0.4	20	50	-2	10	8.9	H
9	0.4	10	50	-1	10	3.81	H	32	0.4	20	50	-2	30	8.9	H
10	0.4	10	50	-5	30	3.81	H	33	0.4	20	50	-1	30	8.9	H
11	0.4	20	50	-5	10	3.81	H	34	0.4	20	50	-3	10	8.9	V
12	0.4	20	50	-4	10	3.81	H	35	0.4	20	50	-3	30	8.9	V
13	0.4	20	50	-3	10	3.81	H	36	0.4	20	50	-2	10	8.9	V
14	0.4	20	50	-2	10	3.81	H	37	0.4	20	50	-2	30	8.9	V
15	0.4	20	50	-1	10	3.81	H	38	0.4	20	50	-1	30	8.9	V
16	0.4	30	50	-5	10	3.81	H	39	0.4	10	50	-1	30	8.9	V
17	0.4	30	50	-4	10	3.81	H	40	0.4	10	50	-2	30	8.9	V
18	0.4	30	50	-3	10	3.81	H	41	0.4	20	50	-3	10	3.81	V
19	0.4	30	50	-2	10	3.81	H	42	0.4	10	50	-3	10	3.81	V
20	0.4	30	50	-1	10	3.81	H	43	0.4	20	50	-2	10	3.81	V
21	0.4	10	50	-5	60	3.81	H	44	0.4	20	50	-1	10	3.81	V
22	0.4	30	20	-5	5	3.81	H	45	0.4	10	50	-1	10	3.81	V
23	0.4	30	20	-5	10	3.81	H	46	0.4	10	50	-2	10	3.81	V

The configurations of the two cylinders are divided into two sub-groups, one horizontally and one vertically. Figure 49 shows the small cylinder in the vertical orientation, where it is mounted vertically in the centre of the wind tunnel, height wise, and mounted to the Plexiglas window with a bolt.

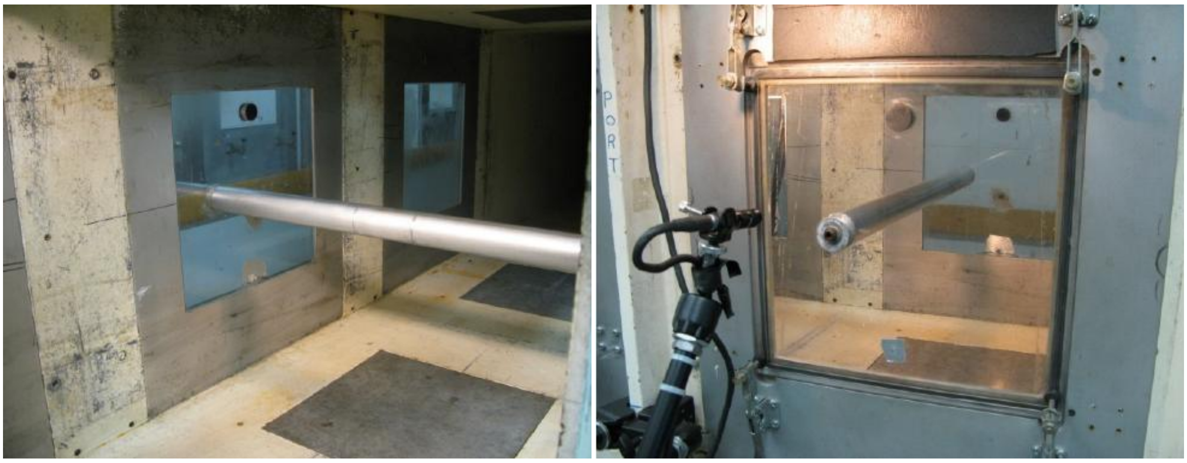

Figure 49. Small Cylinder in the Horizontal Orientation.

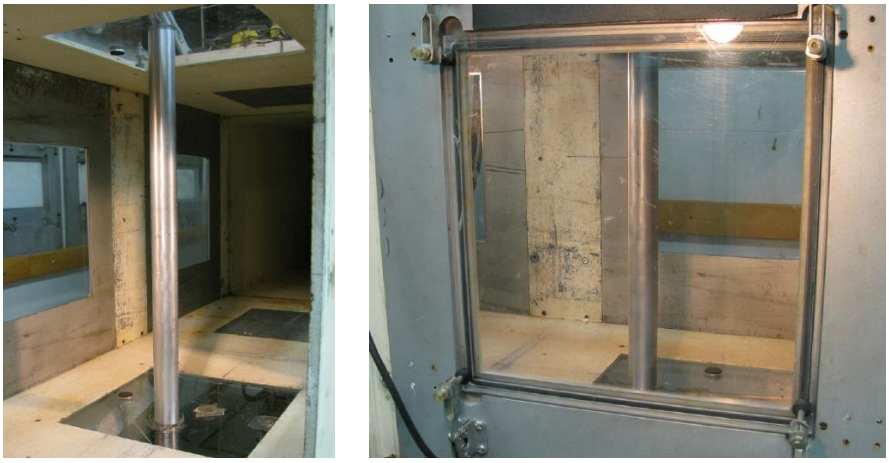

Figure 50. Small Cylinder in the Vertical Orientation.

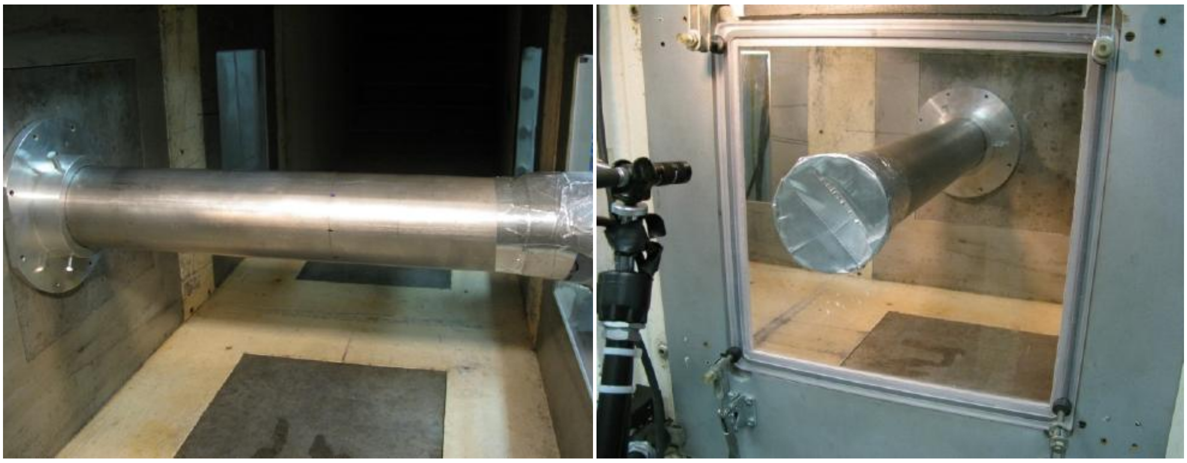

Figure 51. Big Cylinder in the Horizontal Orientation.

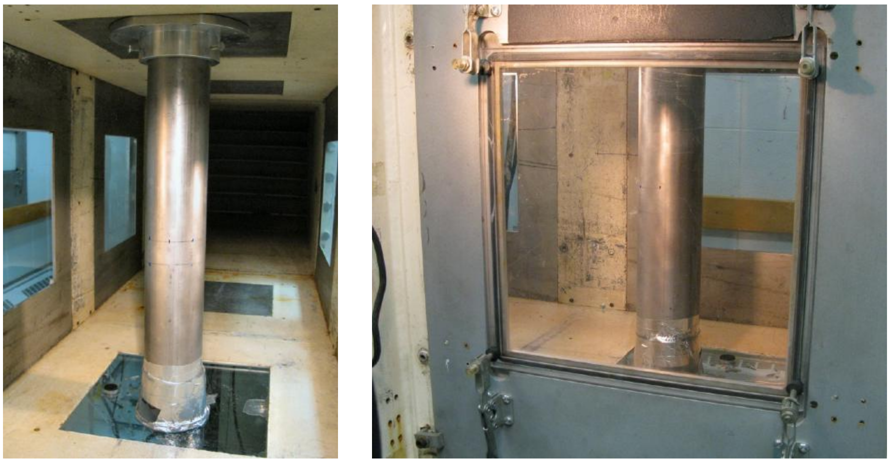

Figure 52. Big Cylinder in the Vertical Orientation.

In Figure 50 the small cylinder is presented in its vertical orientation, where the mounting on the Plexiglas for the horizontally orientation is reused. Figure 51 and Figure 52 shows the big cylinder mounted horizontally and vertically, respectively in the wind tunnel.

The small and large cylinder has a diameter of 3.81 cm and 8.90 cm respectively. Due to the limitations of the wind tunnel it was not possible to test the model in a 1:1 scale. A scaling of 1:2.89 and 1:1.24 were used, where different laws of scaling ice accretion are shown in refs. [67, 68]. Even though the icing experiments is planned based on metrological condition, which is assumed to be present at the Great Belt East Bridge vibration event, the main purpose of the experiments is to observed the formation of ice accretions. Furthermore the purpose of the experiments is also to try and reproduces the observed ice formation on the Great Belt East Bridge hanger for later use in wind tunnel experiments with simulated ice accretions.

The blockage and projected areas perpendicular to the flow for the two cylinder used in the experiments are listed in Table 9. For the large cylinder, a blockage of 15.6% was obtained and should be taken into consideration when using the obtained data.

Table 9. Description of Mountings in the Wind Tunnel.

Item	projected area perpendicular to flow	blockage $A_i/A_{section}$
Test section cross-sectional area:	$A_{section} = 3249cm^2$	-
Small cylinder:	$A_{small} = 217.17cm^2$	$B_1 = 6.7\%$
Large cylinder:	$A_{large} = 507.3cm^2$	$B_2 = 15.6\%$

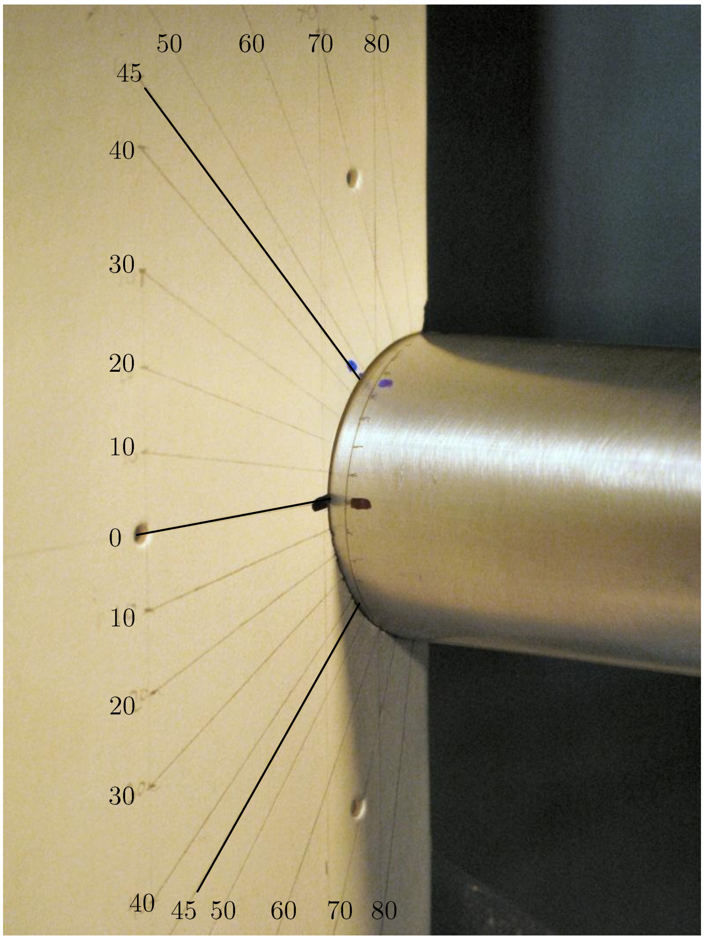

Figure 53. Angle Division of Small Cylinder.

A scale marking the circumferential angles has been applied on the cylinder surface for better identification of the ice accretion features locations. The circumference of both the small and the big cylinder has been divided into ranges to determine the angle step size. Based on visual inspection during the experiments the small cylinder has been divided angle step size of 10°, whereas for the big cylinder the step size was set to 45°. These divisions were used in order to obtain a more accurate description of the ice formation in relation to each cylinder and he position of specific ice features. Figure 53 shows a picture of the small cylinder with the angle division. The black dot indicates 0° and the blue dot indicates 45°.

5.1.2. Documentation of Ice Accretions Surface Contour.

Apart from pictures of the ice accretion which was done as a documentation of the ice formation over time, the final ice accretion was also traced. The tracing technique used for documenting the surface contour of the ice consists of three steps, Figure 54 and Figure 55.

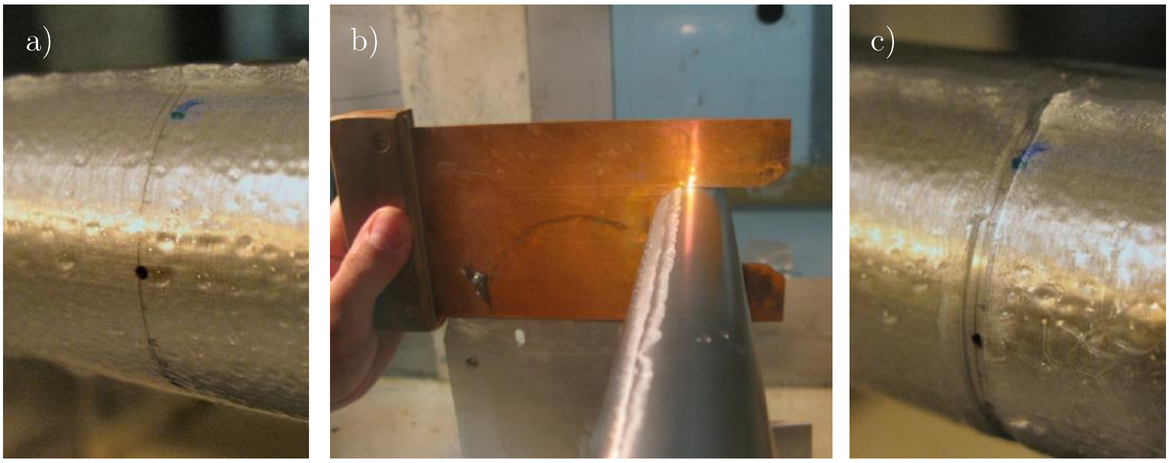

Figure 54. Melting of a Thin Slice in the Ice Accretion, a) Full Ice Accretion, b) Melting Slice of Ice, c) Melted Ice Slice.

Figure 54a shows the final ice accretion at the end of experiment number 9. This ice shape is then melted at the centre of the cylinder, which is shown in Figure 54b. The slice left by the melted ice is shown in a close-up picture, Figure 54c.

A piece of cardboard is then placed in the slice left by the melted ice, which is shown in Figure 55a. A pencil customized for this exact purpose is used to trace the surface contour of the ice accretion on this piece of cardboard, Figure 55b. The pencil has a 90° bend which makes it possible to drag the pencil over the surface of the ice while tracing the contour. Figure 55c shows the final traced surface contour, which have been retraced with ink due to the risk of erasing the pensile tracing.

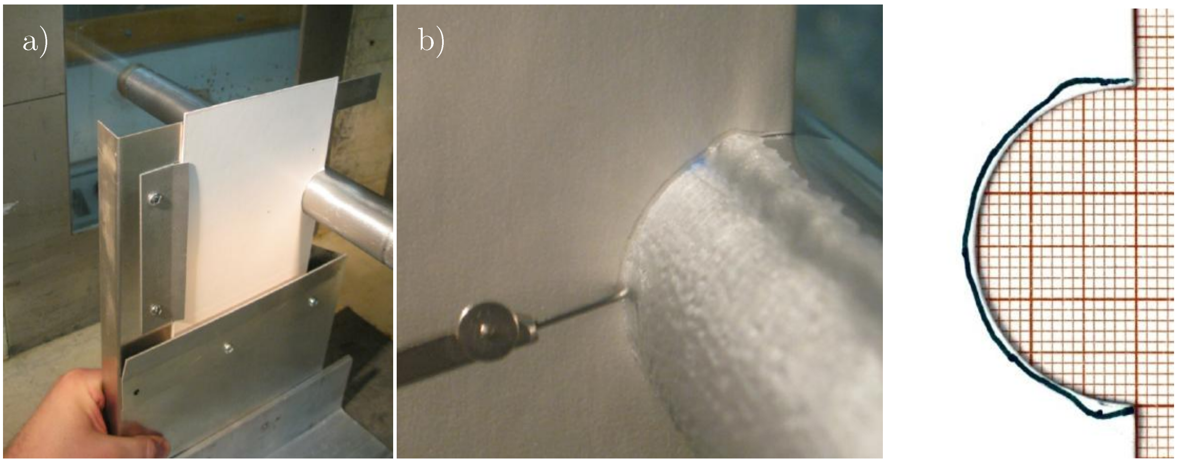

Figure 55. Tracing of Ice Accretions Surface (contour) a) Cardboard Place in Melted Slice of Ice, b) Tracing of Ice Surface Contour on Cardboard, c) Traced Surface Contour of Ice Accretion.

The drawback of this method is the clear shortcoming when it comes to catching the change of the ice shape over the length of the cylinder. Also capturing the structures of the ice surface smaller than the pencil used in the tracing may be problematic. In order to compensate for the lack of information on the changes in the surface structure of the ice over the length of the cylinder, a second cut where made. This melting cut was made 1/3 of the test section width from the wall. This second cut was only performed on the small horizontally mounted cylinder. Furthermore this method of tracing the ice can only capture the shape of the ice accretion for ± 90° around the stagnation point. Finnally, by tracing the surface of the ice accretion by this method, some of the fine surface details, especially with respect to roughness characteristics, are lost. The max resolution of the traced ice roughness is determined by the size of the used pen-devise, which in this case is 0.5mm.

5.1.3. Summary of Results

This section gives a summary of the results obtained in the experiments described above. A full descriptions of the result can be found in Gjelstrup et al., [47]

Accretion Coefficient

To study the overall ice accretion on the cylinder under different boundary conditions, an accretion coefficient, C_{accr}, is introduced, Eq. (5.1).

$$C_{accr} = \frac{m_{accr}}{m_{appr}} \tag{5.1}$$

This accretion coefficient is the ratio of the accreted ice mass, m_{accr}, defined in Eq. (5.2), at a particular time to the mass of water in the approaching airflow that passed the projected cross-flow area of the cylinder since the beginning of the test, m_{appr}.

$$m_{accr} = A_{ice} \cdot \rho_{ice} \tag{5.2}$$

In Eq. (5.2), A_{ice} is the integrated cross-sectional area of the accreted ice. The perimeter of the ice shape was determined with the shape tracing method mentioned above and later digitalized with a specially developed line-tracing program. The obtained data are used to integrate the area of the accreted ice to allow for further numerical analysis of the ice surface features. The density of the ice, ρ_{ice}, is set to 996kg/m^3.

$$m_{appr} = LWC \cdot D \cdot U \cdot t \tag{5.3}$$

The mass of water in the approaching airflow is defined in equation (5.3). Here, LWC is the Liquid Water Content in [g/m^3], D is the cylinder diameter, U the time averaged airflow speed in the test and t the time since water is introduced to the flow (exposure time).

The values of the accretion coefficient, C_{accr} are for lower time values between zero and one since the accreted ice mass cannot exceed the provided water mass. This is mainly valid for the first 10 to 30 minutes, where the cross-wind extension of the body, i.e. cylinder + accreted ice, is zero or negligible. At sixty minutes, significant accretion can change the crosswind dimension, which might lead to an increased adhesion of water droplets, leading to a $C_{accr} > 1$.

Over time, the surface roughness also increases significantly due to different shapes of ice accretion. The texture of the ice accretion multiplies the initial dry cylinder surface and creates additionally local turbulent wake flow behind large accreted ice structures leading to attachment of droplets due to sedimentation effects, which again can lead to $C_{accr} > 1$.

Generally, the surface boundary-layer is affected by the surface roughness. Increased roughness changes the flux in the boundary-layer flow and might in this respect also affect the accretion of droplets.

Test and Subtests Programs

The total test program has been separated in to 6 subtests programs provides the foundation for comparison between the test parameters. These subtest programs can be seen in appendix E or [47], where a comparison between the tests is sorted by time, temperature, droplet size, velocity, diameter and position.

Time

Figure 56 shows an ice accretion coefficient as a function of time. It is seen that the ice accretion coefficient has a tendency to approach a constant value when running over long time periods. This period also seems to be depended on droplet size of the water. This is seen in A2, which seems to have settled on a constant value for a relative short exposure time. A2 is a test series with a droplet size of 20 µm. This could suggest that ice accretions on the small cylinder may result into a more streamline form of the body cross-section, which guides the small droplets with low mass and inertia around the body, hence reducing the impact rate of droplets and consequently the growth.

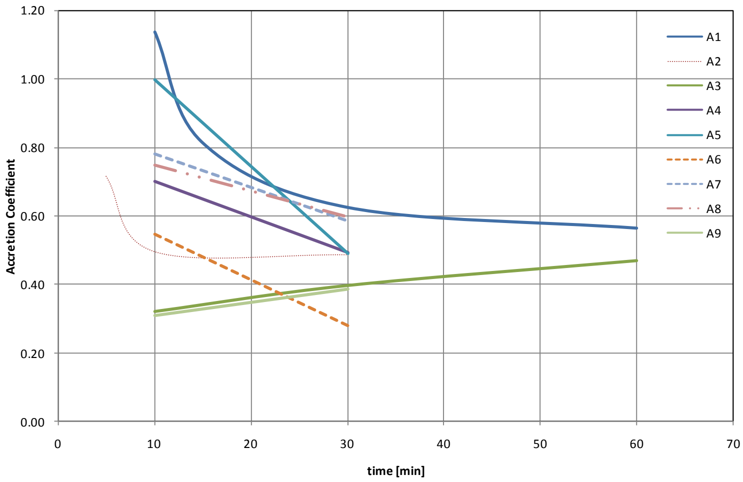

Figure 56. Plot of Accretion Coefficient as a Function of Time for Different Variations in Test Parameters.

Figure 57 shows an analysis of the stagnation line growth speed for the subtest program A. It is seen that the different subtest series show a tendency to reach a constant growth rate at higher exposure times. However looking at A6 in Figure 57 and comparing that to the result from Figure 56, it is seen that the stagnation line thickness seems to have been traced correctly. This in turn might suggest that the rest of the total area may have been traced in such a location that the found area could be treated as extreme point of either run 31 or run 32 or both. In either case, the test series A6 should be disregarded until comparative test has been made.

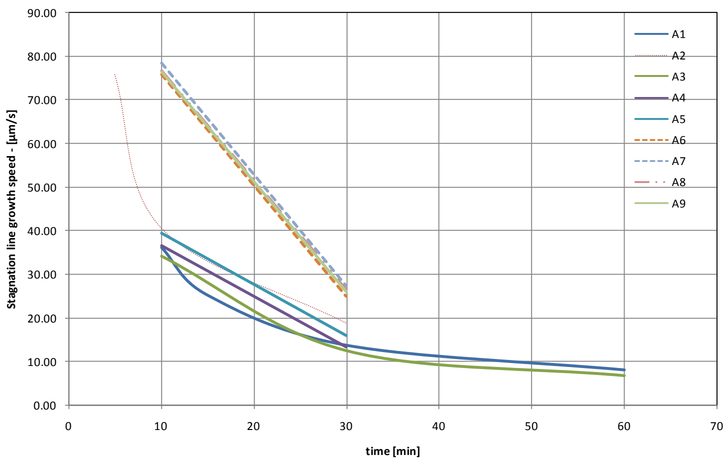

Figure 57. Plot of Stagnation Line Growth as a Function of Time for Different Variation in Test Parameters.

Temperature

Another parameter to analyze in the different developments of ice accretions are the correlation of symmetry. Splitting the accretion contour curve at the stagnation point or more exactly at 0° of the circumferential scale, into two parts makes it possible to make a comparison of the two parts to each other with respect to their geometric similarity. For this purpose the two curves are considered as function of the circumferential angle (0° - 90°). Calculating the correlation coefficient between theses two half's gives a first indication of how symmetric the accretion is. This aspect is in particular relevant for horizontal cylinders orientation, where gravity may influence the accretion process. A symmetry correlation of 1 would indicate identical ice accretion contour around the 0° position. For a more in-depth analysis of the symmetry, see [47].

Plotting the symmetry correlation as a function of temperature for all experiments in the test program shows that there is a high symmetry at low temperatures and relatively low symmetry at high temperatures as shown in Figure 58. It is furthermore seen that the range of which the correlation spans shift from a broad range to a more narrow range between -2°C to -3°C. This indication of a shift in span range is supported by visual observations during the experiments, where a significant change in the ice formation behavior was observed around this temperature range.

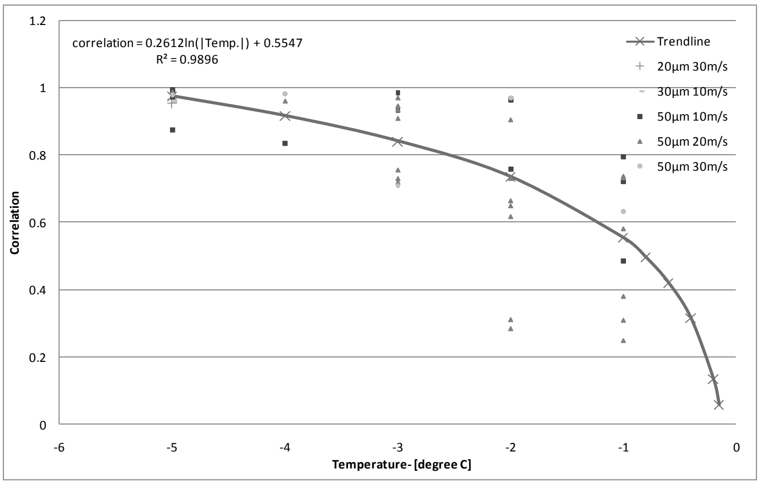

Figure 58. Symmetry Correlation for All Experiments as a Function of Temperature and Plotted in Grouped Velocities.

If the analysis focuses on the stagnation thickness, it is seen that there is a tendency for the stagnation growth speed to be higher at lower temperature. Plotting the stagnation growth speed as a non-dimensional number shows that the overall growth rate also is a linear function of the temperature, but has a relatively wide spread over different experiments as shown in Figure 60. This indicates that the growth rate is highly dependent on all the conditions present under each experiment, i.e. temperature, wind speed, time etc.

Similar, to the symmetry analysis of all experiments, discussed above, it is also possible to look at the horn location, shown in Figure 61. The horn location is defined as protrusion on the ice, which is illustrated in the traced accretion contour shown in Figure 59. In the following the horn location will be calculated by identifying the arc length along the circumference of the cylinder and dividing this length with the cylinder diameter.

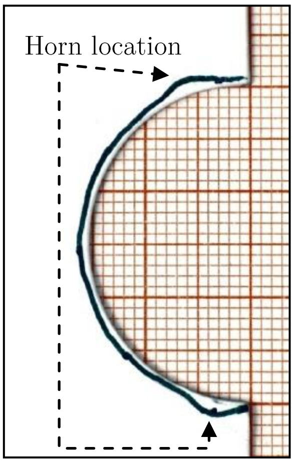

Figure 59. Example of horn location.

The horn location is for some ice accretions a subjective matter, which will introduce some spread in the location data. The overall trend of the data shows that the horn location has a tendency to move closer to the stagnation point as temperatures decreases. this is also observed by findings made by Szilder and Lozowski, [69]. This is most likely due to the fact that the lower temperature will freeze the water at a faster rate, which in turn shortens the distance of which the water will run back on the cylinder.

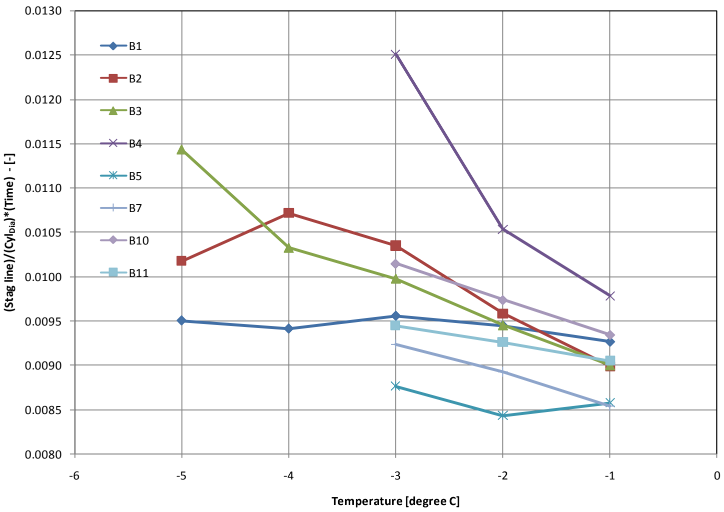

Figure 60. Plot of Stagnation Line Growth Coefficient as a Function of the Temperatures Test in the Wind Tunnel Experiments.

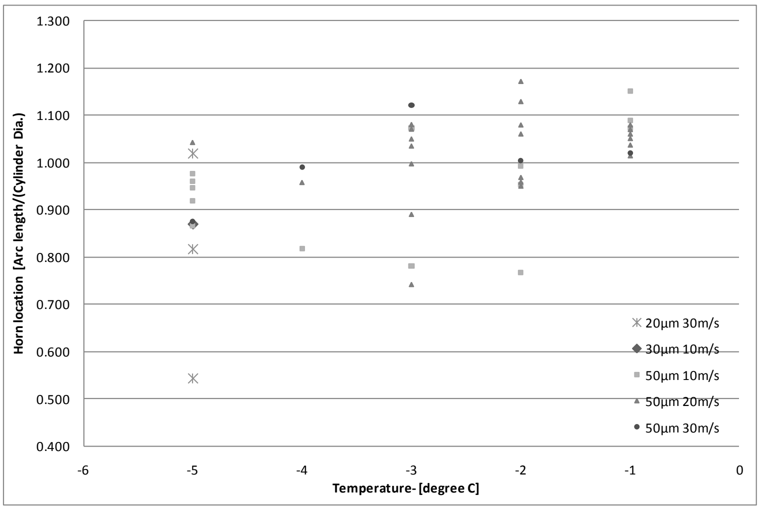

Figure 61. Horn Location for All Experiments as a Function of Temperature and Plotted in Grouped Velocities and Droplet Size.

Time

Information about the horn location can also be derived by looking at the total number of tests and sorting them according to time and droplet size. This reveals a tendency for the horn location to be a function of the droplet size, Figure 62. It is seen that the smaller the droplet size, the closer to the stagnation point the horns are located with respect to time and temperature. Similar to the air temperature the droplet size influences the solidification progress of a water droplet on the body surface. The dependency might be equal; hence the horn location position follows both parameters in a similar way.

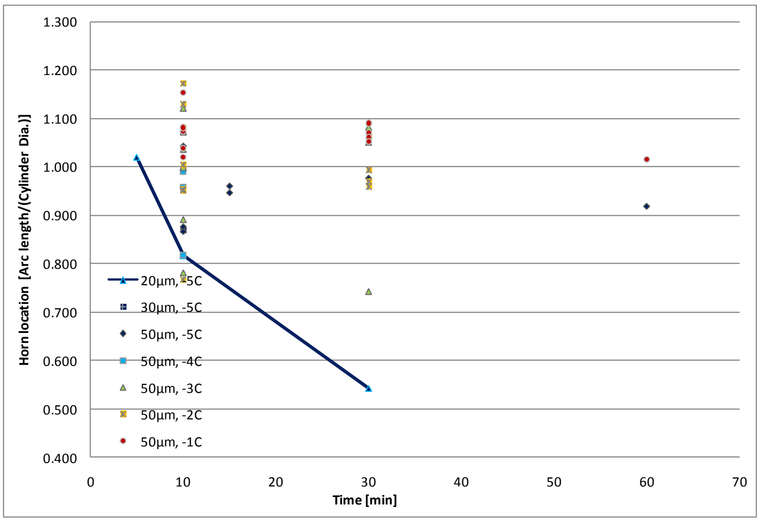

Figure 62. Horn Location for All Experiments as a Function of Time and Plotted in Grouped Droplet Sizes and Temperatures.

Wind Speed

One would suppose that variation in the wind velocity plays a significant role in predicting the possible ice shapes, which might occur. Unfortunately, in relation to the ice shape, it is difficult to accurately determine the horn locations dependency of wind speed from the experiments presented in this paper. Having said that, it seems that the higher the wind speed the smaller the spread of the horn location, Figure 63.

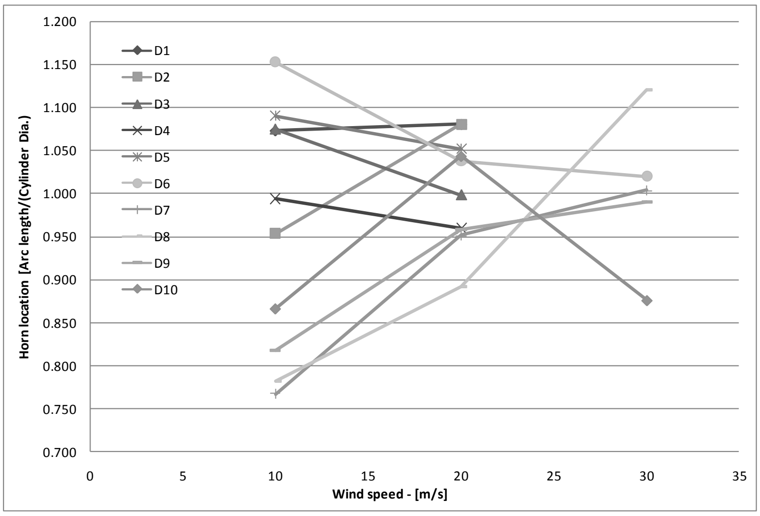

Figure 63. Horn Location for Sub-Series Test D.

Cylinder Diameter

The variation in the test setup for ice accretion dependency on the cylinder diameter is fairly small but nonetheless some information about the stagnation line growth speed is revealed. Figure 64 shows a comparison of the stagnation line growth coefficient. Here it is seen that the stagnation line growth speed decrease significantly the larger the cylinder. More tests with different cylinder diameter would be preferable in future test programs.

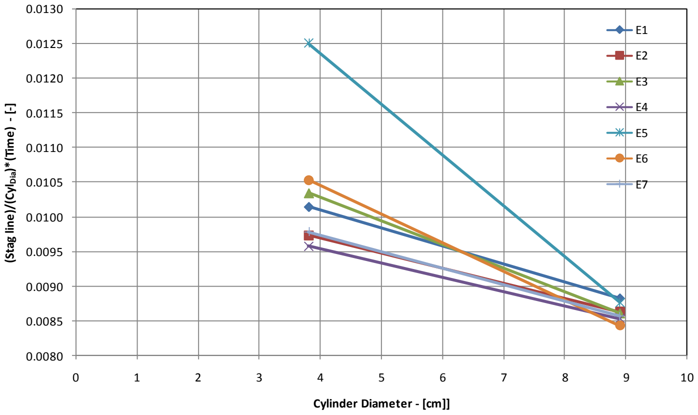

Figure 64. Stagnation Line Growth Coefficient Sub-Series Test E.

5.1.4. Comments on Main Findings

The main findings from the experiments are that the ice formation and shapes can partly be categorized by some distinct parameters, which are a function of time, temperature, wind speed, droplet size and other relevant parameters mention in the above section. The categorization is done by considering stagnation growth, horn location, symmetry and an ice accretion coefficient.

By this categorization of the parameters it is possible to get a good idea on how ice is formed at these relatively high temperatures and under the condition which was used in the experiments.

Using the data from the largest cylinder should only be done by taking the high blockage into account. With the present data obtained from this test series it is difficult to say what effect blockage will has on the formation of the ice shape in general. More tests on how blockage will influence the ice formation would be preferable in future experiments.

5.2. Simulated Ice Experiments in the CCWT

The following section describes the different experiments with ice accretions simulated by rapid prototype produced elements, which are fitted on the cable mode surface. A total of 6 different ice shapes was tested in a static rig and of these, 3 ice shapes were also tested in a dynamic rig. A detailed description of the experiments and their results are given in the references [66] and [70].

5.2.1. Models Used in Experiments

A list of the tested ice shapes and their resulting blockage during testing is presented in Table 10 and shown in Figure 65. The mean blockage is found by taking the mean diameter of the model, except for ice shape I, where the model was not tested for a large range of angles. Here the mean blockage is found by calculating the mean diameter perpendicular to the flow for the range of angles-of-attack tested instead.

The maximum blockage of each model is determined as the ratio between the maximum cable/ice diameter $D_{max} = 2r+t_{max}$ and the cross-sectional height of the tunnel. Corrections on the measured drag coefficients are made to account for the effect of tunnel blockage.The method used for blockage correction is presented by Dalton in [71], which is an improved correction based on an originally proposed correction by Allan & Vincenti [72].

Table 10. Ice shape and blockage for the prescribed wind tunnel tests

Ice shape	$D_{mean} = \text{mean}(D_i)$	$D_{max} = \max(D_i)$	Mean blockage $D_{mean} / D_{section}$	Max blockage $D_{max} / D_{section}$
I	7.56 cm	7.67 cm	10.78 %	10.96 %
II	7.20 cm	7.74 cm	10.29 %	11.06 %
III	7.14 cm	7.39 cm	10.20 %	10.56 %
IV	9.01 cm	9.29 cm	12.88 %	13.27 %
V	8.96 cm	9.13 cm	12.79 %	13.04 %
VI	7.07 cm	7.22 cm	10.10 %	10.31 %
VII	7.00 cm	7.00 cm	10.00 %	10.00 %

As mentioned above 6 different simulated ice models have been tested. A reference experiment on a circular cylinder has also been included in the test program (VII).

Due to the nature of ice, which melt at temperatures over 0°C, and the limitation of the available wind tunnel equipment in which the force test were carried out, it was decided to reproduce the ice accretions by rapid prototyping as described in section 4.1.3.

The ice accretion models were reproduced by rapid prototyping, and printed in the models axial direction in order to have the print lines of the rapid prototype model to run in the flow direction.

A cross sectional plot of the six models used in the experiments are shown in Figure 65, where the models are labeled in accordance with Table 10. All models I-VI were tested in the static rig and ice shape models labeled II, IV and V where additionally tested in the dynamic rig. Furthermore, the reference cylinder (ice shape VII) was also tested in both the dynamic and static rig.

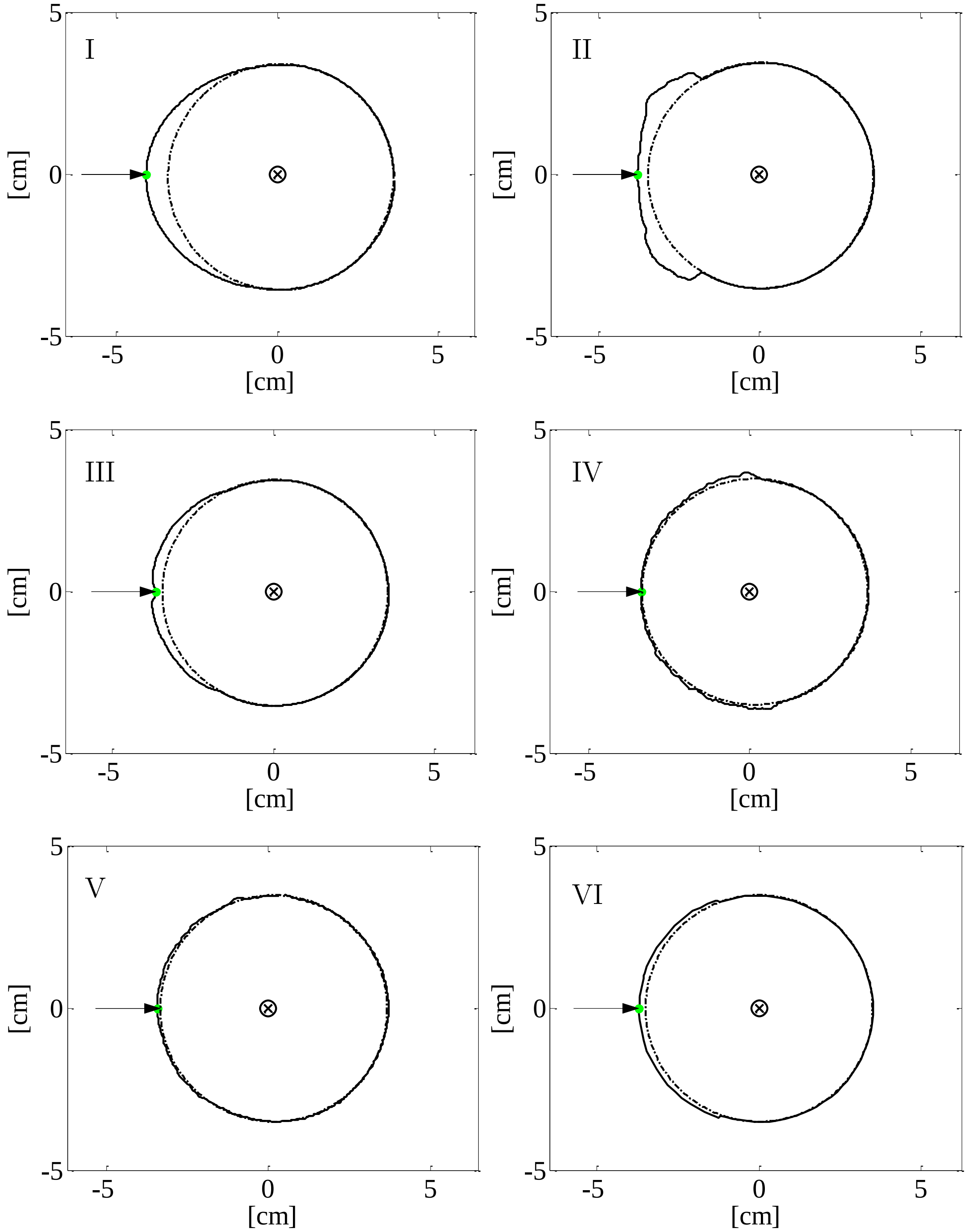

Figure 65. Ice accretion shapes according to icing conditions presented in Table 10. ⊗ indicates the center of the cylinder and "→" indicates the stagnation point of the section from which the 0° angle is defined. The positive change in wind angle-of-attack is counterclockwise. The dotted line illustrates the cylinder boundary behind the ice accretion. In all cases, the cylindrical section has a diameter of 70 mm.

5.2.2. Static Rig

This section describes the results obtained in the experiments carried out using the static rig. All the force coefficients reported in the following have been corrected with respect to the flow profiles presented in section 4.2.2. The correction method is shown in [47].

5.2.2.1. Reference Cylinder

A series of experiments on a reference cylinder was performed in order to determine how the drag coefficient varies within the tested wind speed range. Figure 66 shows the results obtained from the Reynolds experiments on the circular cylinder.

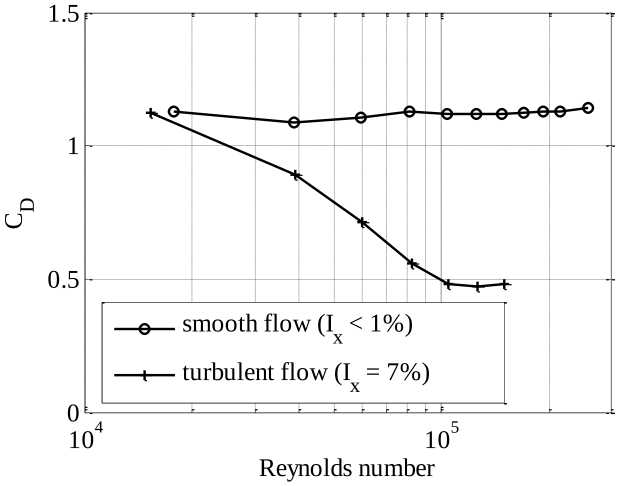

Figure 66. Reynolds Tests in Smooth and Turbulent Flow on a Circular Reference Cylinder (Ice shape VII).

5.2.2.2. Ice Shape I

A small series of experiments was performed in order to test the effect of the surface roughness and the results of these experiments are presented in Figure 67. The difference in surface roughness of the rapid prototype model has been obtained by testing the model with the inherited surface roughness. Another test where the surface had been coated with four layer of varnish to create a smooth surface was then performed. For the rough surface the printing of the simulated ice element leaves a relatively rough surface that was not explicitly measured using roughness measurement equipment, but that is visually and texturally equivalent to an ISO/FEPA grit designation of P150 or slightly higher. The smooth surface could be characterized a painted metal as shown in [19].

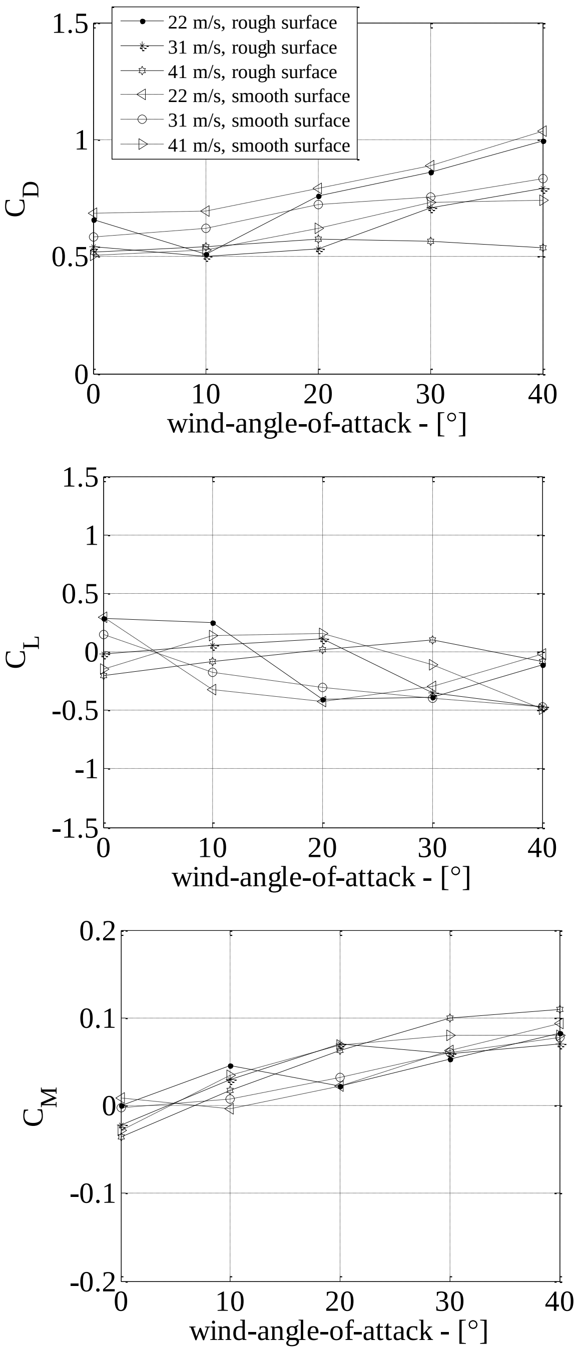

Figure 67. Static force coefficients for ice shape I, with varying model surface roughness

5.2.2.3. Ice Shape II

Figure 68 shows the results obtained for ice shape II. It is seen that the Reynolds effect is most profound for the turbulent flow.

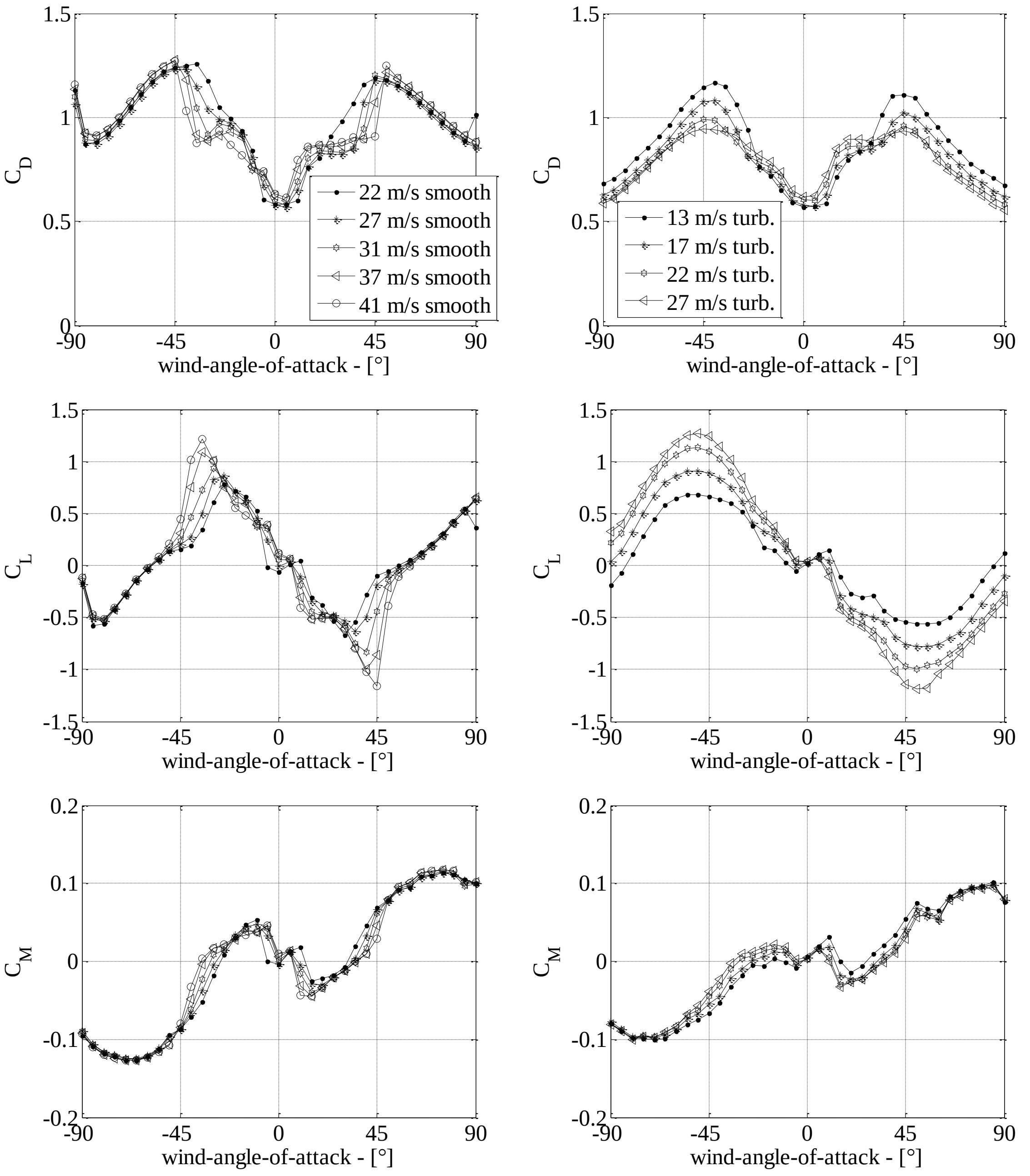

Figure 68. Static force coefficients for ice shape II: smooth flow (left) and turbulent flow (right)

5.2.2.4. Ice Shape III

Figure 69 shows the results obtained for ice shape III. It is seen that the Reynolds effect is most profound for the turbulent flow and especially for the lift force.

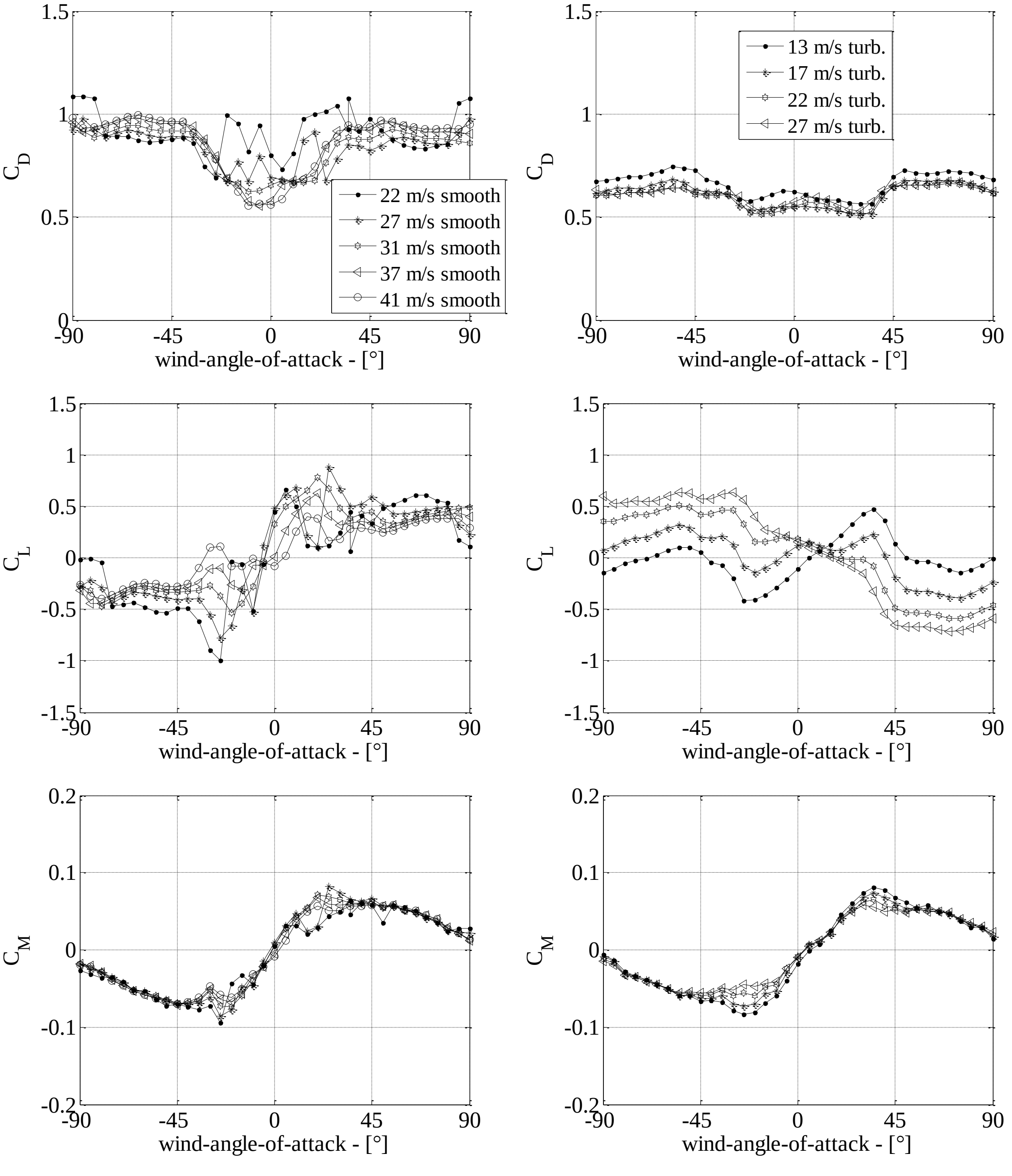

Figure 69. Static force coefficients for ice shape III: smooth flow (left) and turbulent flow (right)

5.2.2.5. Ice Shape IV

The results obtained for ice shape IV are presented in Figure 70. Here the same trend of greater Reynolds dependency for the turbulent flow is observed as well. However, there also seems to be that the Reynolds dependency for the drag force is following the critical range identified in Figure 66.

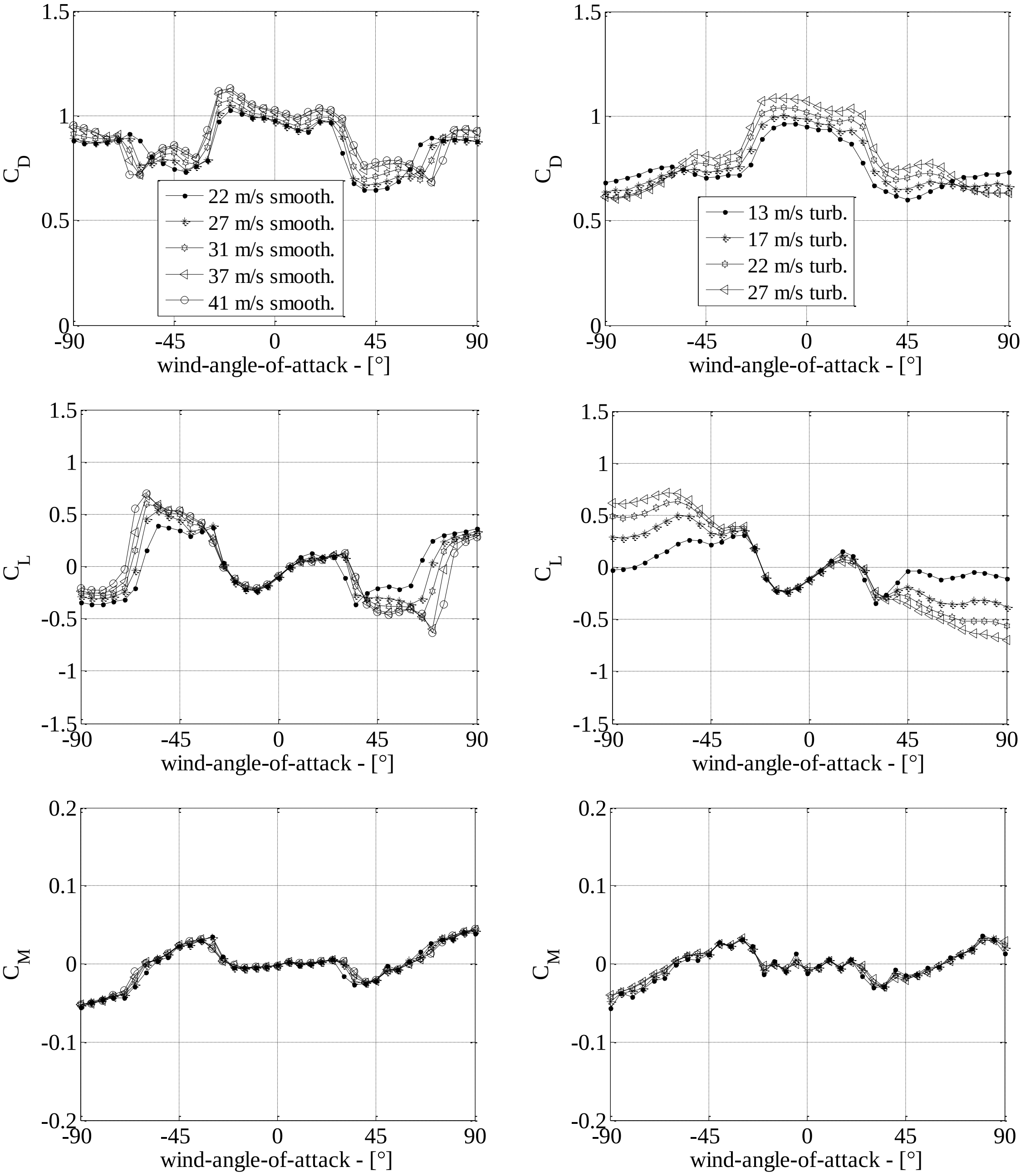

Figure 70. Static force coefficients for ice shape IV: smooth flow (left) and turbulent flow (right)

5.2.2.6. Ice Shape V

The results obtained for ice shape V are shown in Figure 71. Again the same trend of larger Reynolds dependency for the turbulent flow is seen, and likewise the drag force is following the critical range identified in Figure 66.

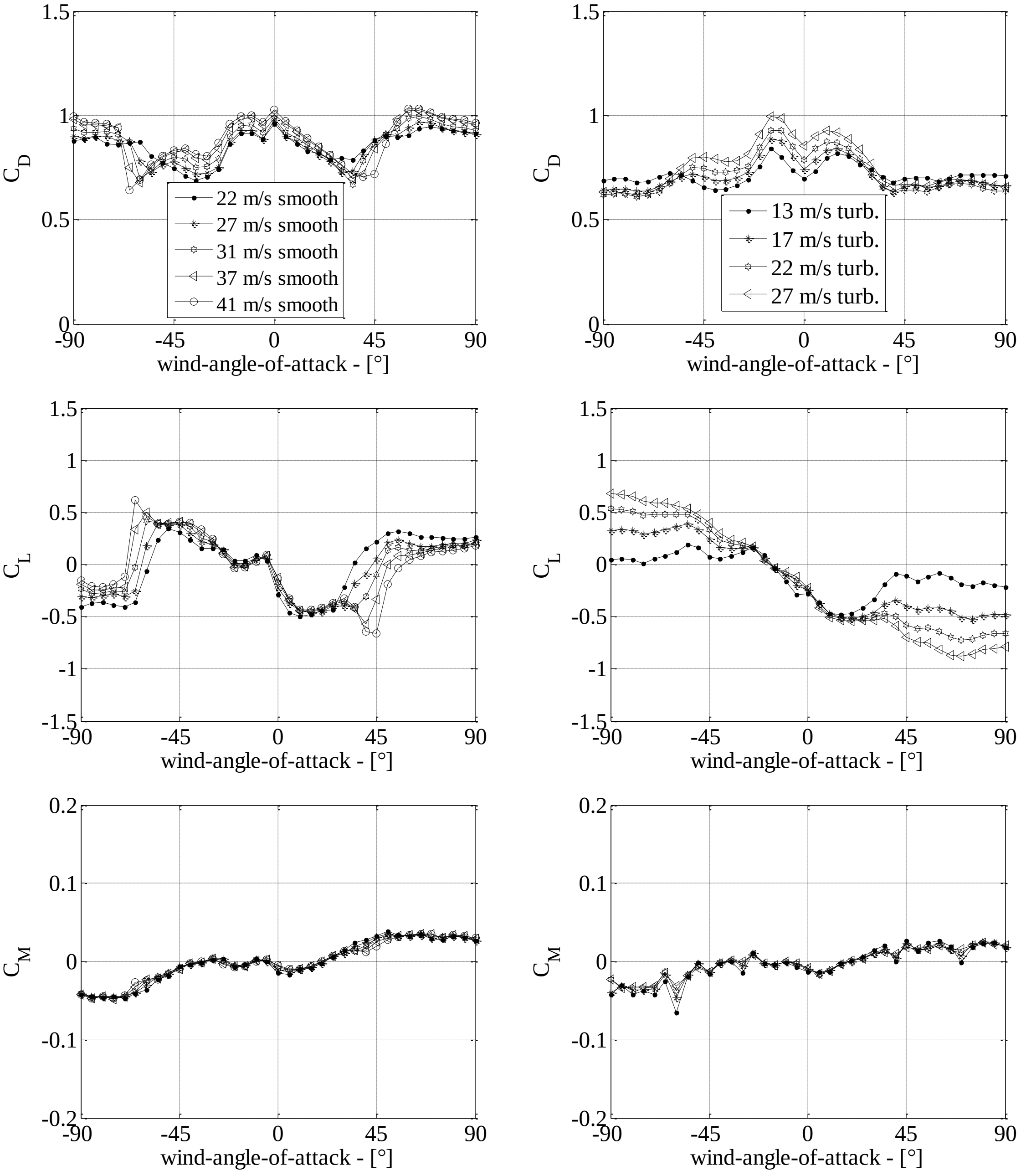

Figure 71. Static force coefficients for ice shape V: smooth flow (left) and turbulent flow (right)

5.2.2.7. Ice Shape VI

For ice shape VI, the force coefficients (Figure 72) exhibit Reynolds dependency for both smooth and turbulent flow, except for the C_M where Reynolds dependency is observed mainly in turbulent flow only for wind angles of attack in the range of 10° to 75°.

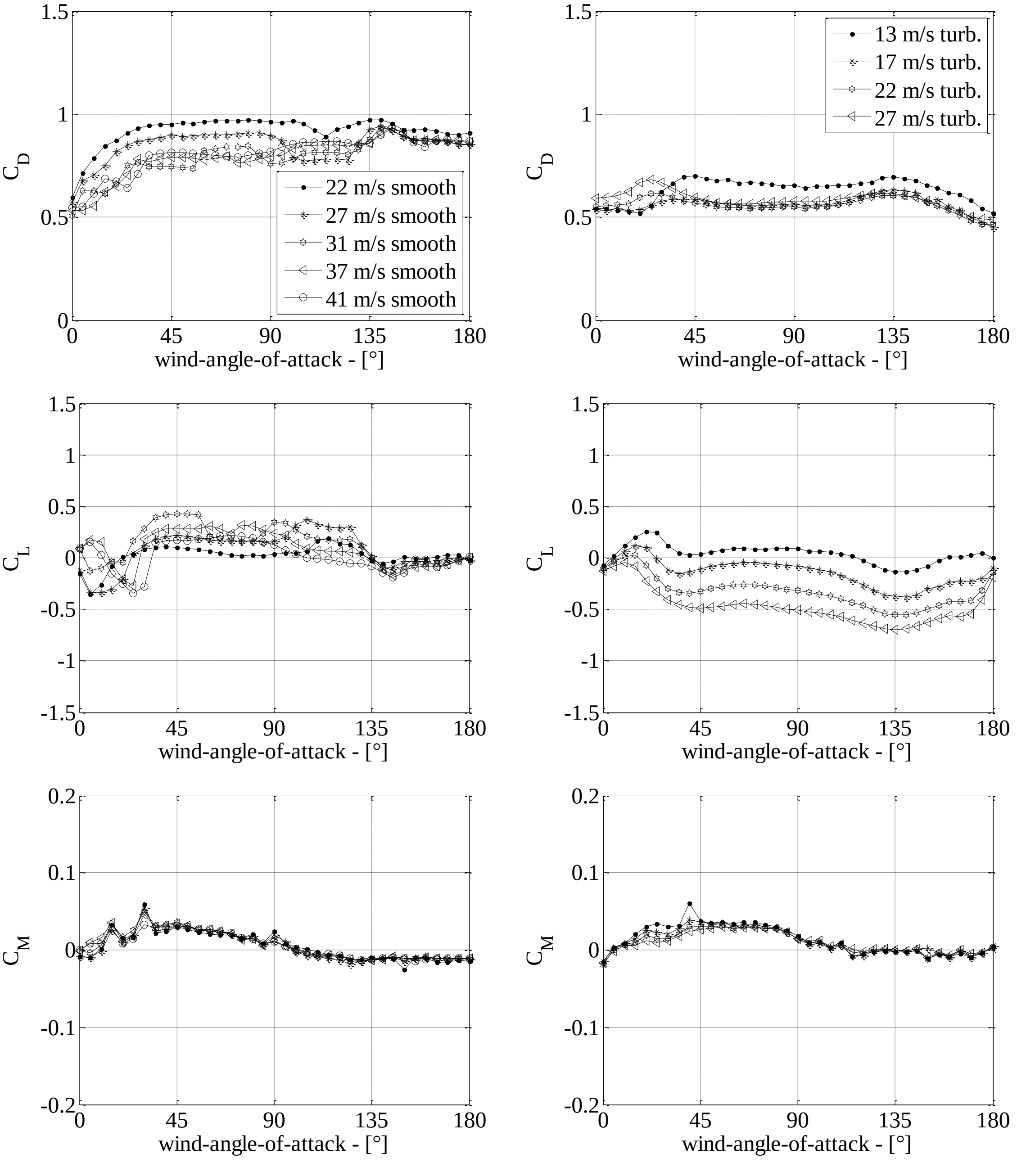

Figure 72. Static force coefficients for ice shape VI: smooth flow (left) and turbulent flow (right)

5.2.2.8. Hysteresis in Force Coefficients

Before using these models for further dynamic experiments, control check for hysteresis, in respect to wind velocity, where performed. Here hysteresis is defined as a noticeable change to the force coefficients for a particular wind angle-of-attack and velocity when testing the model in the wind tunnel and rotating it in one direction and then rotating it back in the opposite direction for varying wind velocities.

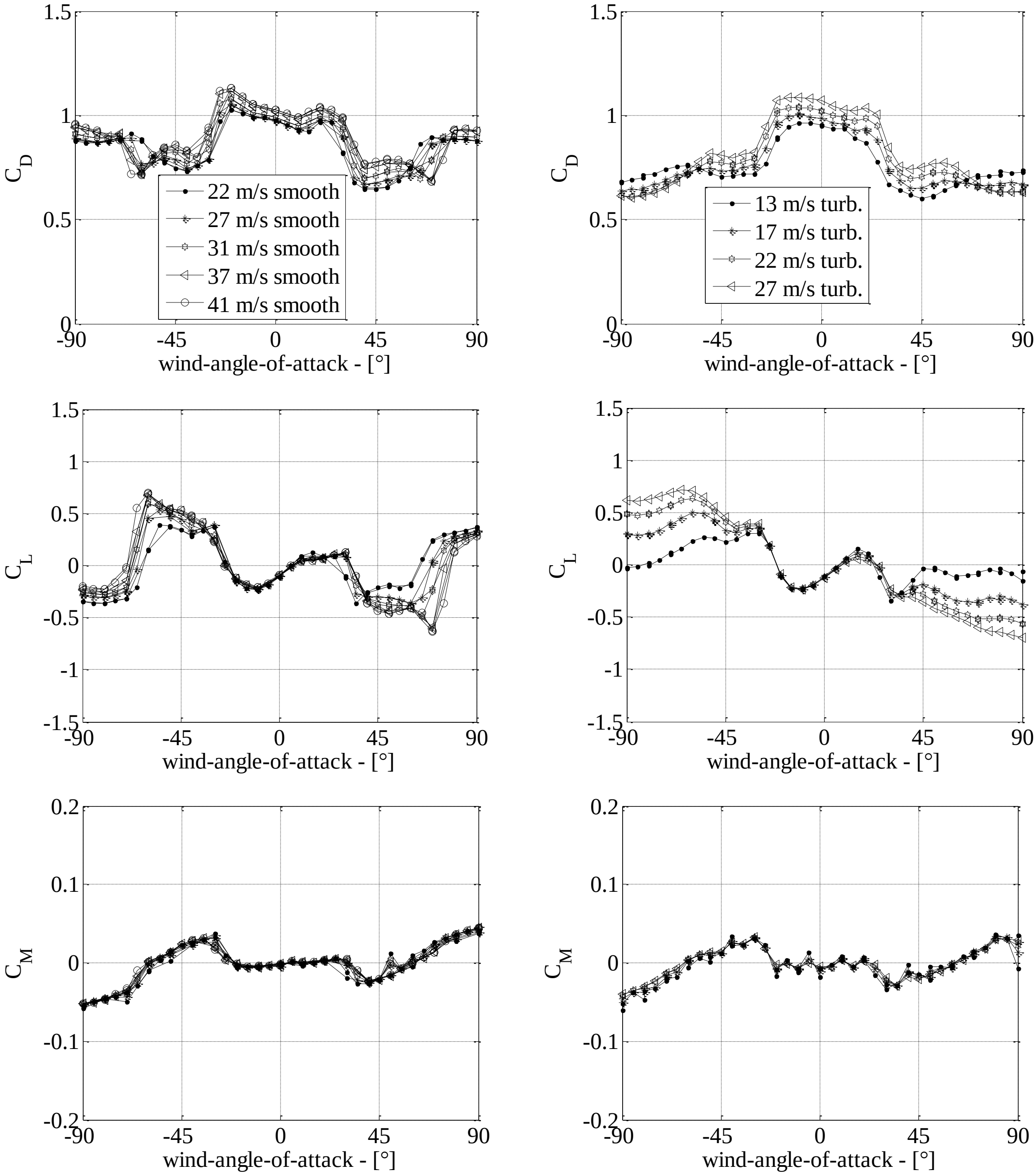

Figure 73. Hysteresis check for ice shape IV: smooth flow (left) and turbulent flow (right)

This set of experiments was carried out for shapes IV and V, for both smooth and turbulent flow. The model was rotated forward by 5° increments and back by 10° increments. These shape was choose due to the similarity of the ice shapes to that, which were observed on the Great Belt East Bridge hangers. Due to this similarity they were also chosen for test in the dynamic rig. The results of the hysteresis experiments are presented in Figure 73 and Figure 74. No significant hysteresis was observed for these two particular ice shapes.

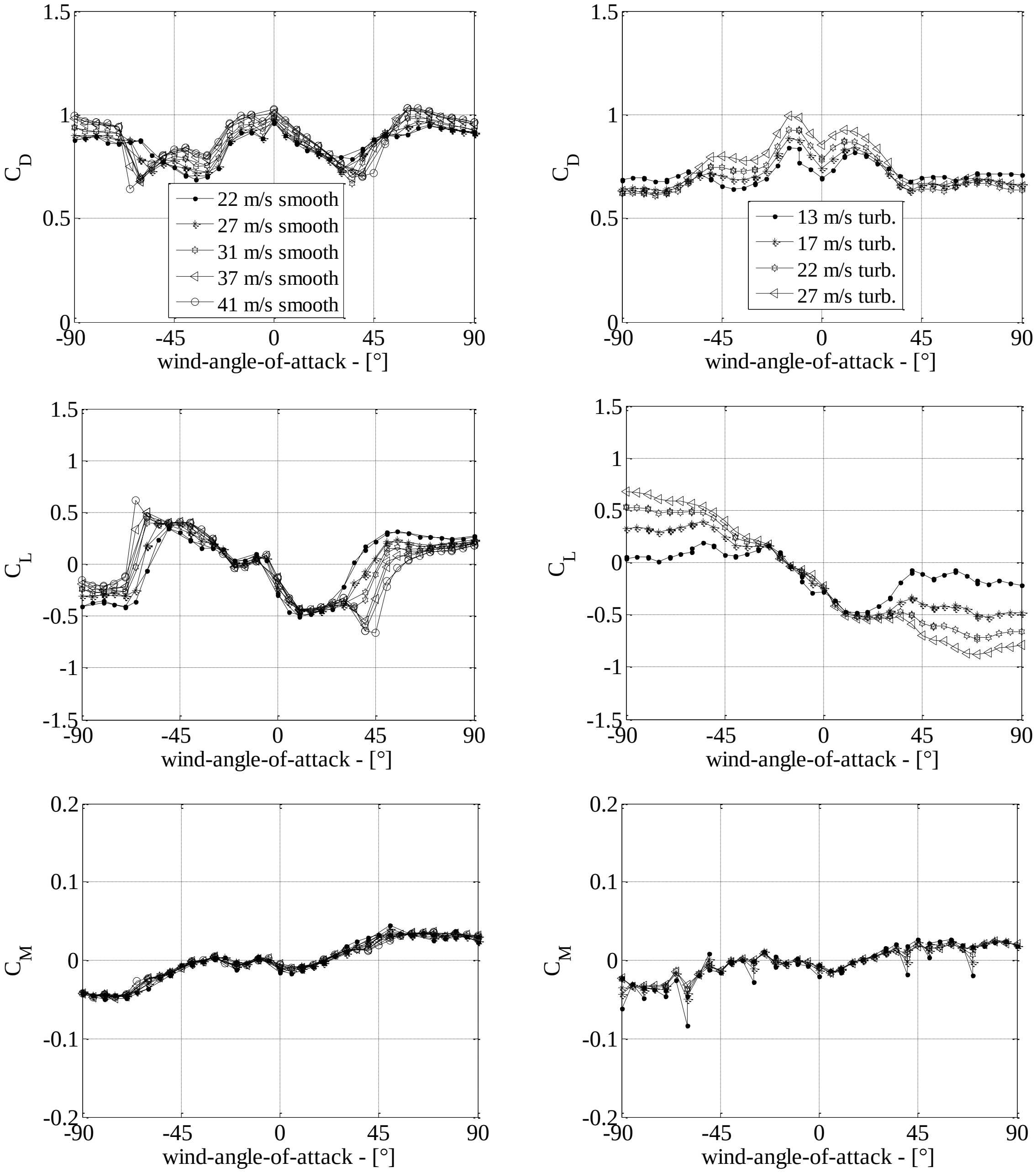

Figure 74. Hysteresis check for ice shape V: smooth flow (left) and turbulent flow (right)

5.2.3. Dynamic Rig

The following section presents the results obtained in the experiments performed in the CCWT using a dynamic rig. The models tested in the dynamic rig were chosen based on the fact that they should have an ice accretion similar to the one observed in the vibration event on the Great Belt East bridge described in section 1.2.2. The ice shapes observed at this vibration event were very thin and had some small ice protrusions. The models which were chosen to simulate ice at this vibration event are ice shape IV and V. Furthermore, tests of the generic ice shape (ice shape VI), were also performed to ensure that it is possible reproduce the experiments. Finally, the reference cylinder in ice shape VII were also tested.

The results obtained from the experiments are listed in Table 11 and presented in Figures 75 - 77. The results are presented as non-dimensional standard deviation of the vertical displacements, and the standard deviation for angular rotation and roll, in order to show regions of instability. The results are presented for both smooth and turbulent flow.

Table 11. Key Parameters for Models Used in Dynamic Experiments.

Ice shape	Vibration [direction]	Freq [Hz]	Damping [% of crit.]	Rig+Model Mass [kg]	MMI [$\mathrm{kg \cdot m^3/m}$]
IV	Vertical	1.63	0.08	10.25	0.35
	Torsional	4.99	0.43		
V	Vertical	1.64	0.08	10.14	0.36
	Torsional	4.97	0.41		
VI	Vertical	1.64	0.07	10.14	0.38
	Torsional	5.03	0.37		
VII	Vertical	1.65	0.06	10.01	0.37
	Torsional	4.99	0.51		

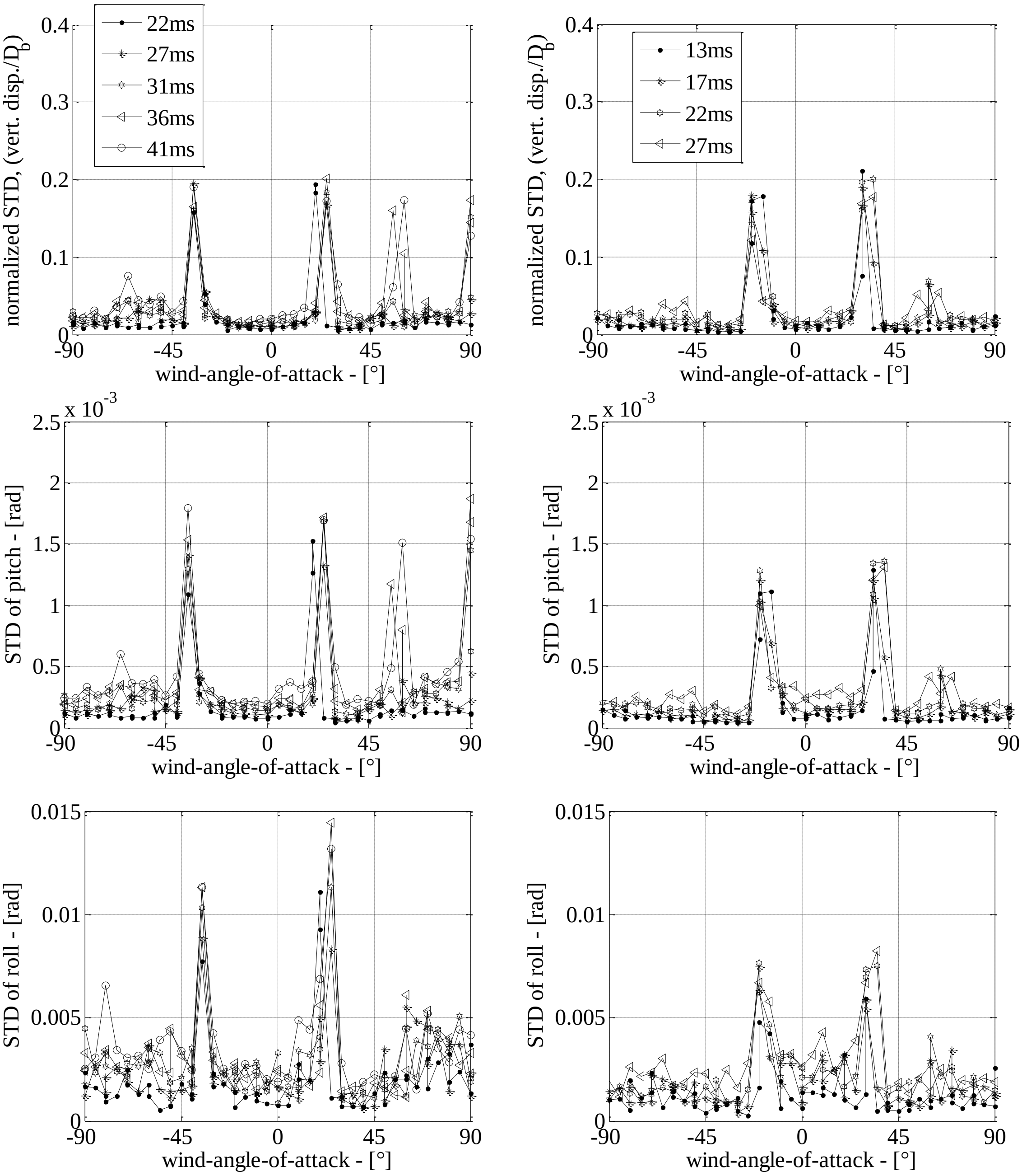

Figure 75. Dynamic response for model with ice shape IV. Non-dimensionalised STD of vertical displacement (top), STD of pitch in radians (middle) and STD of roll in radians (bottom). Smooth flow (left) and turbulent flow (right).

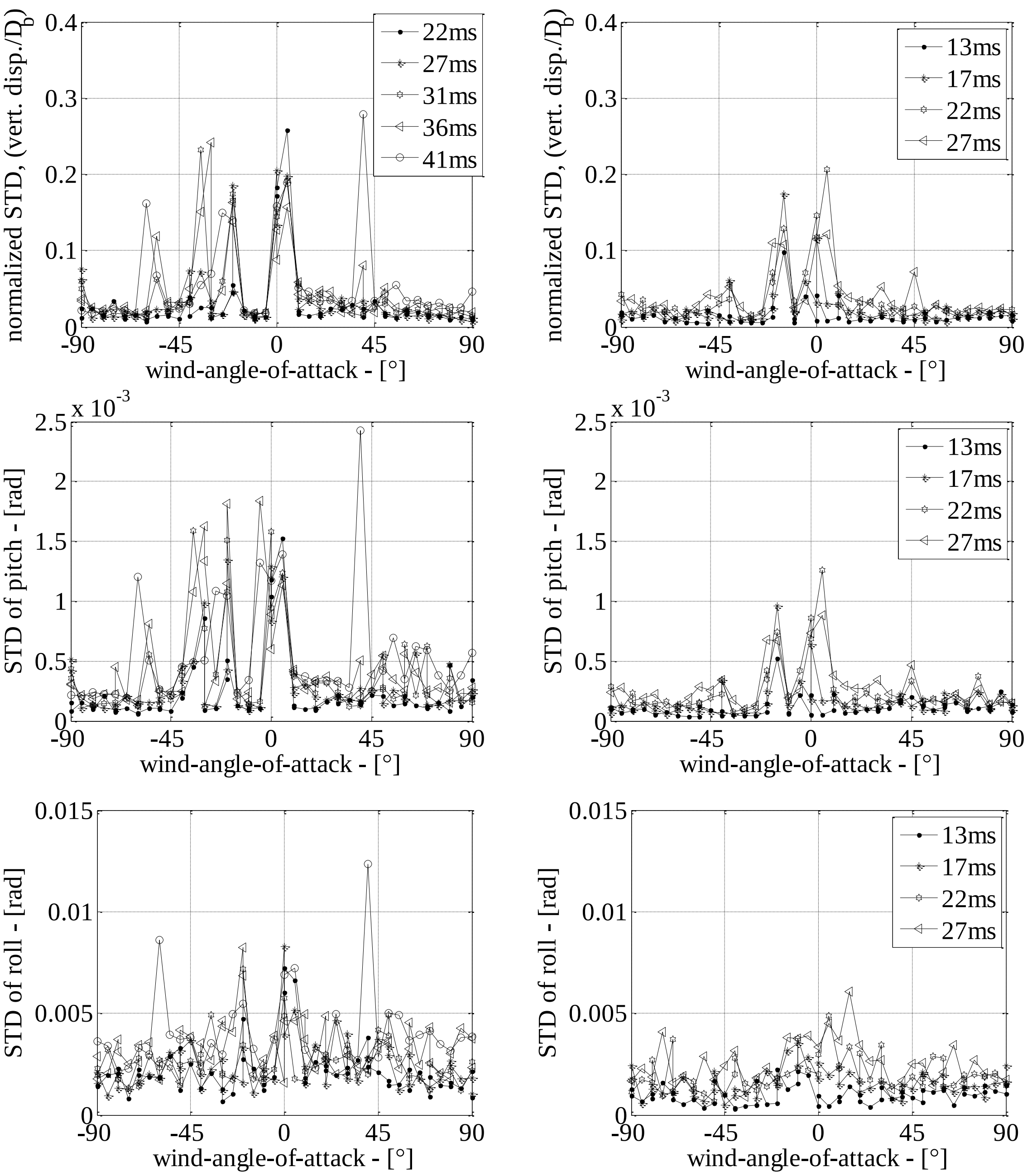

Figure 76. Dynamic response for model with ice shape V. Non-dimensionalised STD of vertical displacement (top), STD of pitch in radians (middle) and STD of roll in radians (bottom). Smooth flow (left) and turbulent flow (right).

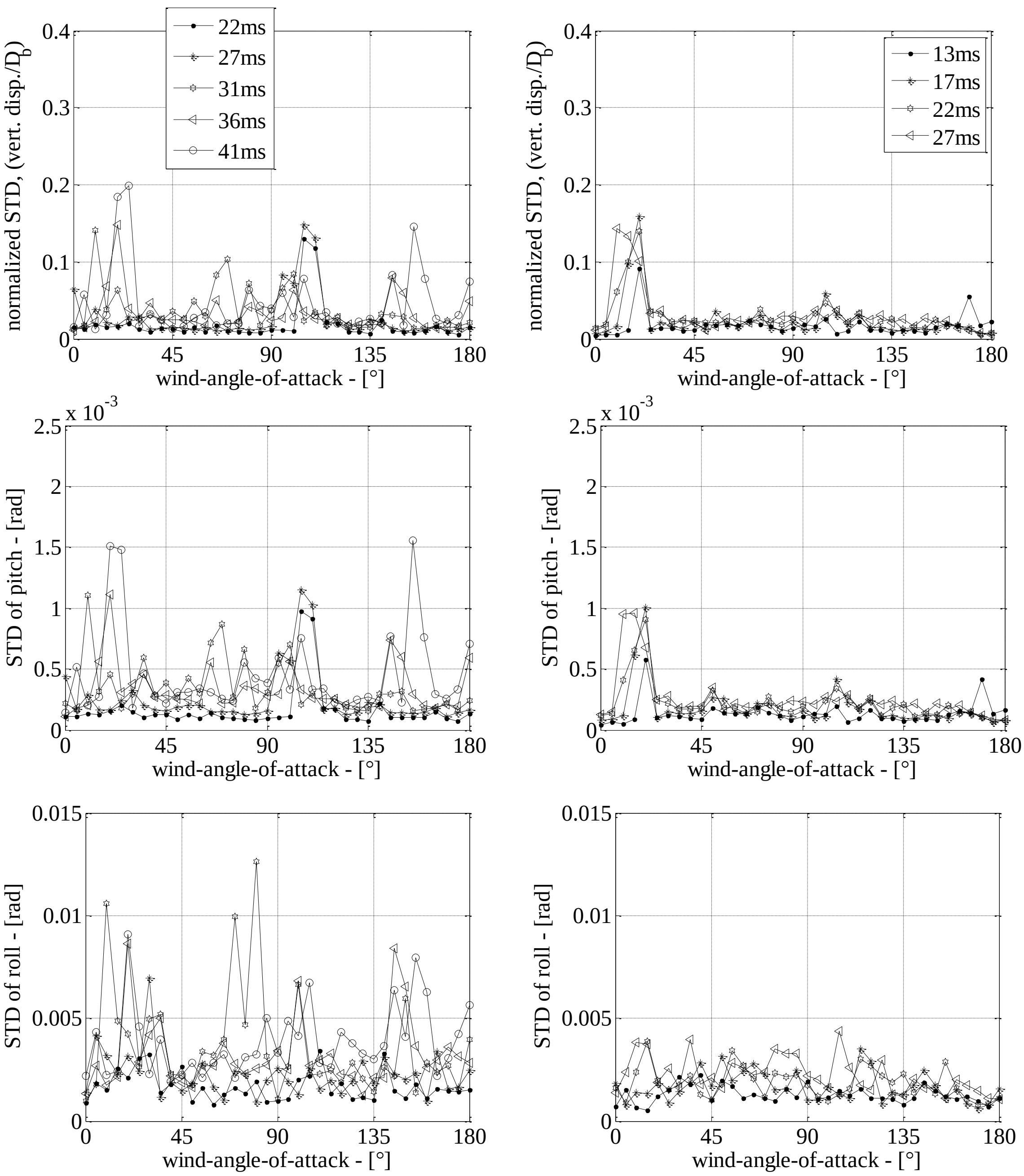

Figure 77. Dynamic response for model with ice shape VI. Non-dimensionalised STD of vertical displacement (top), STD of pitch in radians (middle) and STD of roll in radians (bottom). Smooth flow (left) and turbulent flow (right).

In general, it can be seen that the instability range in the vertical direction is close to the 0° point for the turbulent flow data. For the smooth flow data, the picture of instability is more unclear. Here, it is found that the ranges seen in turbulent flow also exist in smooth flow, but more ranges also appears in the smooth flow. For instability in the torsional direction it is seen that it is locked with the vibration in the vertical direction. The same trend is to a lesser degree seen for the instability of roll. Here, the logged vibration also follows the vibration in the vertical direction.

5.2.4. Comments on Main Findings.

The experiments on the surfaces roughness reveal that there is a difference between the smooth and rough model parts, produced by rapid prototyping. The difference in roughness has a significant effect on the result and more tests in this area have to be carried out in order make conclusive statements on the effect of the results presented here.

In general, it is seen that for relatively thin ice accretion the instability range is concentrated around the 0° point for the models showed here. This is in itself an important finding, because it shows that the wind direction do not have to be altered in order for instability to occur. Furthermore, instability of cables can occur within relatively short period of time if the ice accretion is being build up relatively fast under the right conditions, as was shown in the icing experiment performed by Gjelstrup et al., [47].

It was also found that instability in the torsional direction for thin ice accretion is very small and probably due to skewness in the model. However, it should be noted that it cannot be ruled out that the torsional instability has a negative or initiating effect on the instability.

The instability found in the roll direction was most probably due to buffeting or small skewness in the models, which might also be present in real life structures.

Chapter 6

6. Application of Theory and Experiments.

6.1. Comparisons of Results

In the following section the results from the dynamic experiments are compared to the instabilities predicted from the static force coefficients. The prediction of instability from the static coefficients is found by using the 3-DOF instability model presented by Gjelstrup and Georgakis, [42], which is summarized in section 3.3.

The predicted instability is shown as dark shading and represents the level of damping needed to suppress the instability, which means that the darker the shading the more damping is needed. For the dynamically found instability plots, the shaded areas are the non-dimensional standard deviation.

For ice shape II and ice shape III no dynamic experiments were performed so for these only the predicted instability is presented. These results are shown in Figure 78. For ice shapes IV, V and VI a full comparison is carried out The corresponding results are shown in Figure 79 - 81.

Generally, there is very good agreement between the predicted and measured motional instabilities, although some discrepancies can be observed. There are several potential reasons for this, including the small non-linearities in the dynamic test rig, the asymmetric flow conditions and the determination of the ice-accreted cylinder's cross-sectional radial length [43]. The most probable reason for the observed discrepancies lies with the likely inability of the quasi-steady theory to account for variations in the flow field around the cylinder, due to high velocity/frequency vibrations of the cylinder in the flow.

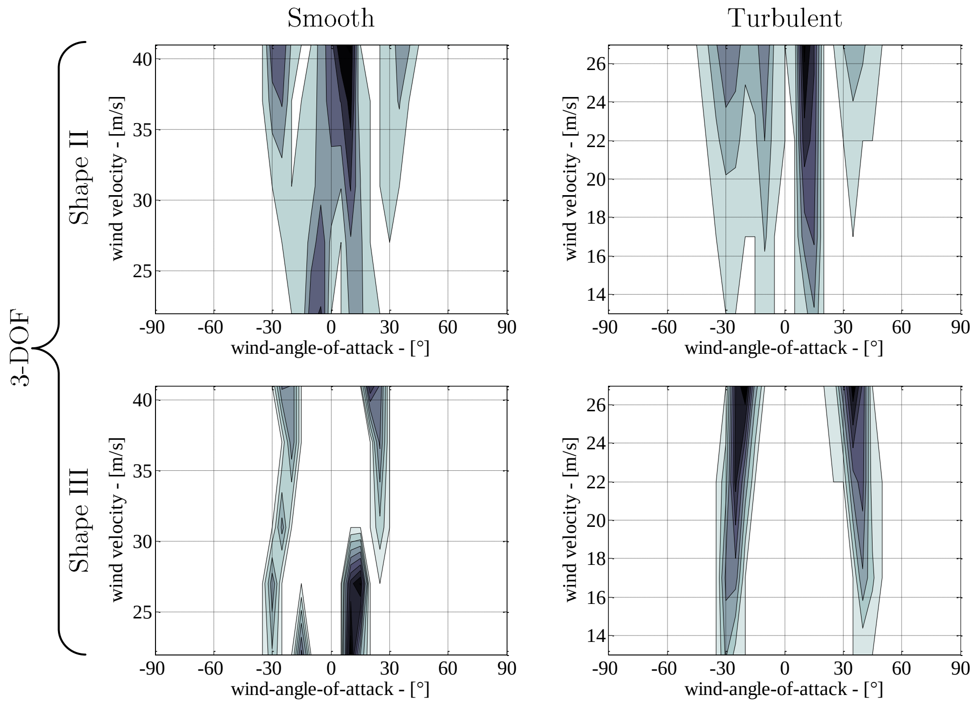

Figure 78. Instability for Ice shape II(top) and III(bottom) Calculated from Static Force Coefficients, Left: Smooth Flow, Right: Turbulent Flow.

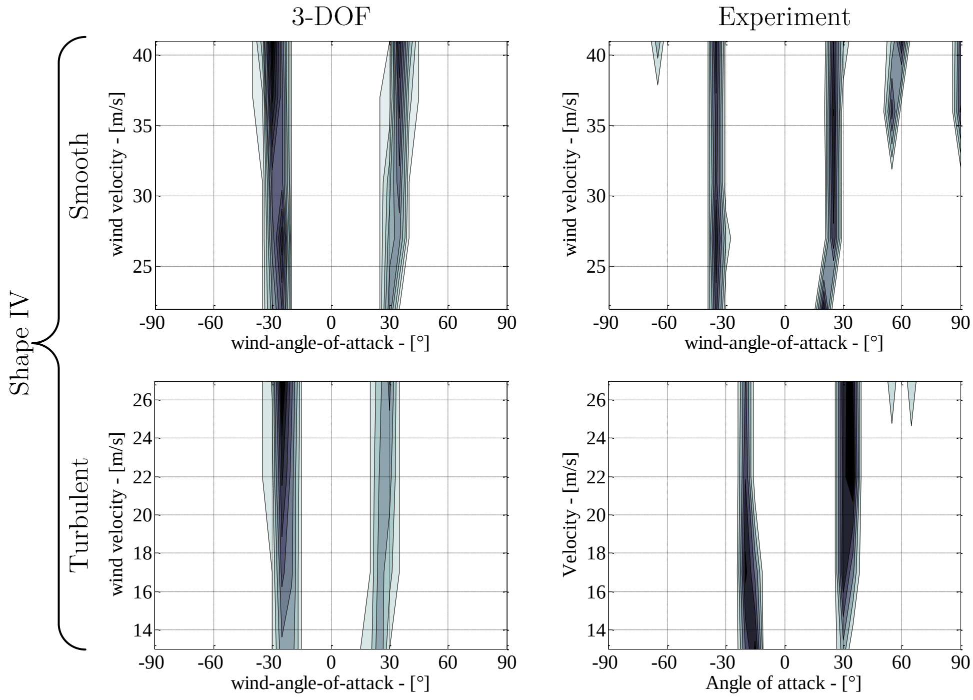

Figure 79. Vertical motional instability for ice shape IV as predicted from quasi-steady theory (left) and as determined from the dynamic tests (right). Smooth flow (top) and turbulent flow (bottom). Unstable regions are shaded. Darker regions indicate increased level of damping needed to avoid instability.

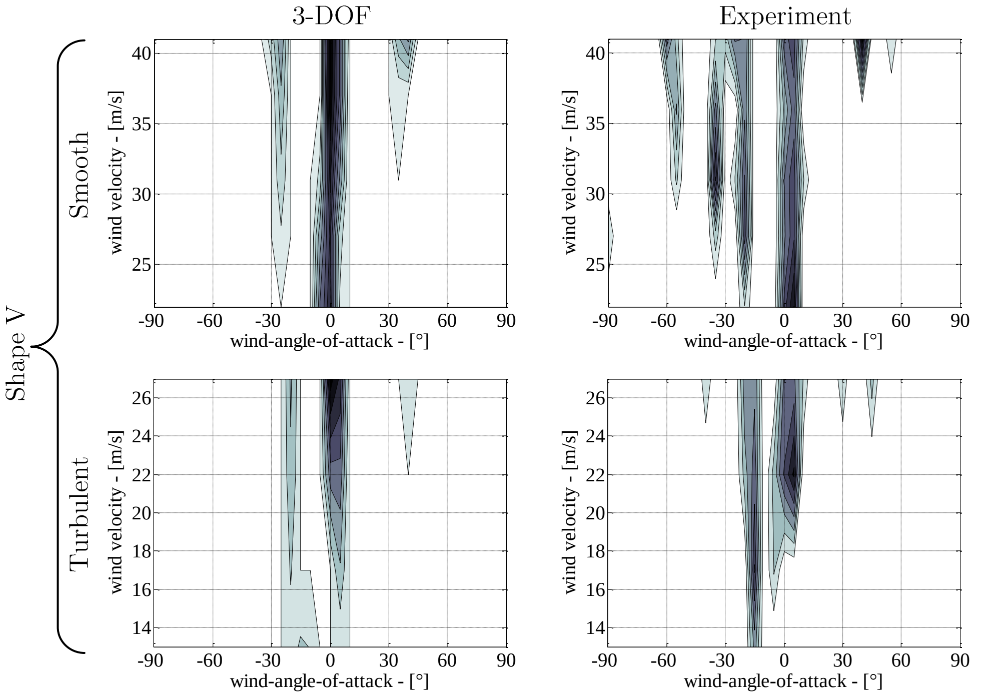

Figure 80. Vertical motional instability for ice shape V as predicted from quasi-steady theory (left) and as determined from the dynamic tests (right). Smooth flow (top) and turbulent flow (bottom). Unstable regions are shaded. Darker regions indicate increased level of damping needed to avoid instability.

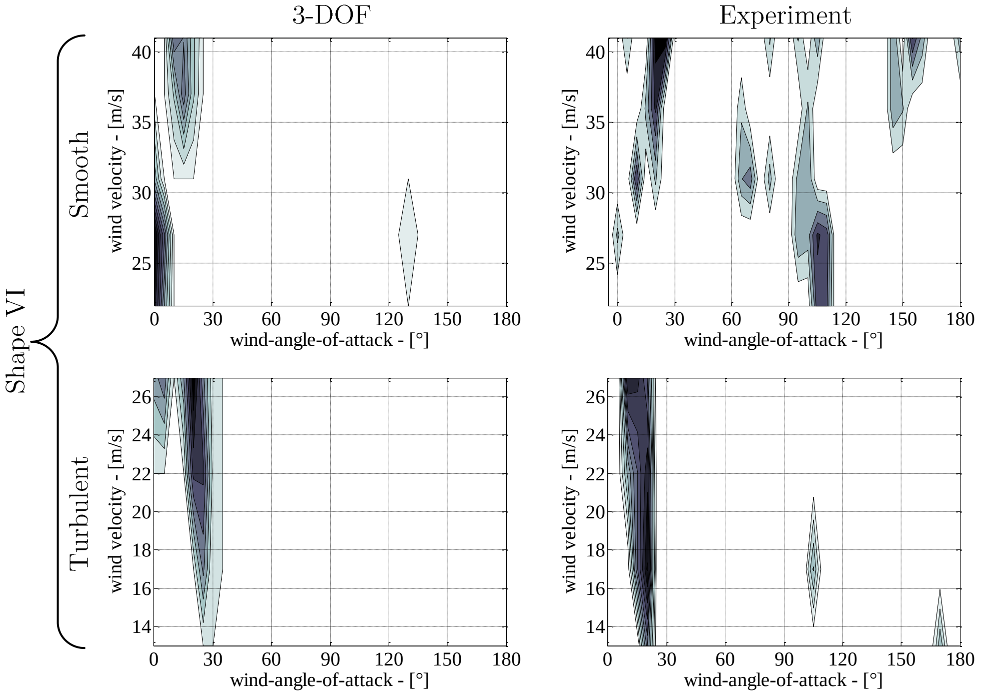

Figure 81. Vertical motional instability for ice shape VI as predicted from quasi-steady theory (left) and as determined from the dynamic tests (right). Smooth flow (top) and turbulent flow (bottom). Unstable regions are shaded. Darker regions indicate increased level of damping needed to avoid instability.

6.2. Comments on Main Findings.

The 3-DOF instability model, [43], described in this work was used with staticly obtained force coefficients and good agreement between the predicted instabilities and the experimentally found instability from dynamic experiments was obtained.

Generally, there is very good agreement between the predicted and measured motional instabilities, although some discrepancies can be observed. For some shapes it seems that the agreement are very good (shape V) and for other not that good (shape VI, smooth flow)

There are several potential reasons for these observed discrepancies, including the small non-linearities in the dynamic test rig, the asymmetric flow conditions and the determination of the ice-accreted cylinder's cross-sectional radial length [43]. The most probable reason for the observed discrepancies lies with the likely inability of the quasi-steady theory to account for variations in the flow field around the cylinder, due to high velocity/frequency vibrations of the cylinder in the flow.

Chapter 7

7. Summary and Conclusion

7.1. Summary

7.1.1. Theory

A 3-DOF sectional response model has been developed and from that an aerodynamic instability criterion has been proposed. This sectional response has also been extended into modal coordinates.

7.1.2. Experiments

The instability model has been validated through wind tunnel experiments which consist of two parts. First part of the wind tunnel experiments focuses on the formation and shape of thin ice accretions. The second part is focused on finding static aerodynamic force coefficients and dynamic response for carefully selected ice shapes, obtained in experiments carried out in Canada at NRC.

7.1.3. Comparison of Theory and Experiments

The Prediction obtained by using the 3-DOF instability model is in good agreement with the experimentally found instability from dynamic experiments. However some discrepancies were observed, which is most likely due to the inability of the quasi-steady theory to account for variations in the flow field around the cylinder due to high velocity/frequency vibrations of the cylinder in the flow. Generally, there is very good agreement between the predicted and measured motional instabilities, although some discrepancies can be observed. For some shapes it seems that the agreement is very good.

7.1.4. Knowledge Sharing

An online database with references to all collected research papers has been design and programmed and finally publish on the internet, where industry and academia can have access to a concentrated source of knowledge on cable vibration.

7.2. Conclusion

The overall aim of the presented research was to explain cable instabilities due to ice accretions. This might not have been explain to all its depths but by the use of the 3-DOF instability model researcher and bridge owners is a step close to explain different vibration events.

In relation to the vibration event which was the initiating factor and the foundation for the work presented in this thesis, it has been shown that a thin ice accretion can cause large amplitude cable vibration. The experiments with simulated ice showed that instability can occur around the stagnation point, which means that the wind does not need to change direction in order to start a cable vibration.

In using the experimental results it should be noted that the simulated ice experiments were conducted with a wind tunnel blockage of about 10 % and that the surface roughness of the ice were simulated with the inherent roughness of the rapid prototyping print.

Chapter 8

8. Future Work

8.1. Experiments and Theory

In future work it would be preferable to have static force coefficients originating from thinly ice cable experiments. These experiments will soon be possible to conduct in a new climatic wind tunnel being built at FORCE Technology situated in Kgs. Lyngby, Denmark. Furthermore it would be necessary to perform more experiments aimed at verifying the torsional instability predicted by the 3-DOF instability model.

Chapter 9

9. Bibliography

[1.] Blevins, R.D. (1994), *Flow-Induced Vibration.* 2. ed: Krieger.

[2.] Nigol, O. and Buchan, P.G. (1981), *Conductor galloping .1. Den Hartog mechanism.* Ieee Transactions on Power Apparatus and Systems, **100**(2): p. 699-707.

[3.] Nigol, O.B., P. G. (1981), *Conductor galloping .2. torsional mechanism.* Ieee Transactions on Power Apparatus and Systems, **100**(2): p. 708-720.

[4.] Chabart, O. and Lilien, J.L. (1998), *Galloping of electrical lines in wind tunnel facilities.* Journal of Wind Engineering and Industrial Aerodynamics, **74-6**: p. 967-976.

[5.] Phuc, P.V. (2005). *A wind tunnel study on unstady forces of ice accreted transmission lines. Proccedings for BBAA V 5th international Colloquium on Bluff Body Aerodynamics and Applications*, p373-376.

[6.] Shimizu, M. (2005). *A wind tunnel study on aerodynamic characteristics of ice accreted transmission lines. Proccedings for BBAA V 5th international Colloquium on Bluff Body Aerodynamics and Applications*, p369-372

[7.] Ni, Y.Q., Wang, X.Y., Chen, Z.Q., and Ko, J.M. (2007), *Field observations of rain-wind-induced cable vibration in cable-stayed Dongting Lake Bridge.* Journal of Wind Engineering and Industrial Aerodynamics, **95**(5): p. 303-328.

[8.] Gjelstrup, H., Georgakis, C., and Larsen, A. (2007). *A preliminary Investigation of the hanger vibrations on the Great Belt East Bridge. Proccedings for Seventh International Symposium on Cable Dynamics*, Vienna (Austria).

[9.] Virlogeux, M. (1998), *Cable vibrations in cable-stayed bridges,.* A. Larsen, S. Esdahl (Eds.), Bridge Aerodynamics, Balkema, Rotterdam: p. 213–233.

[10.] Oliveira, A.R.E. and Freire, D.G. (1994), *Dynamical modelling and analysis of aeolian vibrations of single conductors.* IEEE Transactions on Power Delivery, **9**(3): p. 1685-1693.

[11.] Hikami, Y. and Shiraishi, N. (1988), *Rain-Wind induced vibrations of cables in cable stayed bridges.* Journal of Wind Engineering and Industrial Aerodynamics, **29**(1-3): p. 409-418.

[12.] Caetano, E.d.S. (2007), *Cable Vibrations in Cable-Stayed Bridges* Structural Engineering Documents Vol. 9.

[13.] Matsumoto, M., Shiraishi, N., and Shirato, H. (1992), *Rain-wind induced vibration of cables of cable-stayed bridges.* Journal of Wind Engineering and Industrial Aerodynamics, **43**(1-3): p. 2011-2022.

[14.] Matsumoto, M., Saitoh, T., Kitazawa, M., Shirato, H., and Nishizaki, T. (1995), *Response characteristics of rain-wind induced vibration of stay-cables of cable-stayed bridges.* Journal of Wind Engineering and Industrial Aerodynamics, **57**(2-3): p. 323-333.

[15.] Verwiebe, C. and Ruscheweyh, H. (1998), *Recent research results concerning the exciting mechanisms of rain-wind-induced vibrations.* Journal of Wind Engineering and Industrial Aerodynamics, **74-76**: p. 1005-1013.

[16.] Hartog, J.P.D. (1932), *Transmission-Line Vibration Due to Sleet.* Institute of Electrical Engineers, **51**: p. 1074-1086.

[17.] Nigol, O. and Clarke, G.J. (1974), *Conductor galloping and control based on torsional mechanism.* Ieee Transactions on Power Apparatus and Systems, **PA93**(6): p. 1729-1729.

[18.] McComber, P. and Paradis, A. (1995), *Simulation of the galloping vibration of a 2-dimensional iced cable shape.* Transactions of the Canadian Society for Mechanical Engineering, **19**(2): p. 75-92.

[19.] ESDU, *Mean forces, pressures and flow field velocities for circular cylindrical structures: Single cylinder with two-dimensional flow; ESDU Item 80025*, in *ESDU Item 80025.* 1986.

[20.] Martin, W.W., Currie, I.G., and Naudascher, E. (1981), *Streamwise oscillations of cylinders.* Journal of the Engineering Mechanics Division-Asce, **107**(3): p. 589-607.

[21.] Bearman, P.W. and Harvey, J.K. (1993), *Control of circular cylinder flow by the use of dimples.* AIAA Journal, **31**(10): p. 1753-1756.

[22.] Tanaka, H. (2003). *Aerodynamics of cables. Proccedings for Fifth International Symposium on Cable Dynamics*, 11–25, S. Margherita Ligure, Italy.

[23.] Larose, G.L. and Zan, S.J. (2001). *The aerodynamic forces on stay cables of cable-stayed bridges in the critical Reynolds number range. Proccedings for 4th Int. Symp. Cable Dynamics*, 77-84, Montreal, Canada.

[24.] Langsoe, H.E. and Larsen, O.D. (1987). *Generating mechanisms for cable stay oscillations at the Faro Bridges. . Proccedings for Proceedings of the International Conference Cable-stayed Bridges*, 1023–1033, Bangkok.

[25.] Melby, S., Hovland, K., and Østlid, H. (1994). *Construction and maintenance of two-cable-stayed bridges in adverse environment. Proccedings for 3rd International Symposium on Strait Crossings* Ålesund, Balkema, Rotterdam.

[26.] Svensson, B., Emanuelsson, L., and Svensson, E. (2004). *Øresund Bridge – Cable system – Vibration incidents, mechanisms and alleviating measures. Proccedings for 4th Int. Cable Supported Bridge Operators' Conf.*, 99-108, Copenhagen.

[27.] Larose, G., L. , Zasso, A., and Giappino, S. (2005), *Experiments on Yawed Stay Cable in Turbulent Flow in the Critical Reynolds number Range.*

[28.] Griffiths, P., Curry, B., and Macdonald, J.H.G. (2006), *Galloping analysis of the Severn Crossing Conductor in skew winds.*

[29.] Macdonald, J.H.G. (2004-2005), *Quasi-Steady Analysis of 2DOF inclined cable galloping in the critical Reynolds number range.* p. 435-442.

[30.] Macdonald, J.H.G., Griffiths, P.J., and Curry, B.P. (2008), *Galloping analysis of stranded electricity conductors in skew winds.* Wind and Structures, **11**(4): p. 303-321.

[31.] Macdonald, J.H.G. and Larose, G.L. (2005). *Dry inclined cable galloping – Theoretical analysis and structural damping required for its prevention. Proccedings for EACWE4 — The Fourth European & African Conference on Wind Engineering*, 190, Prague.

[32.] Macdonald, J.H.G. and Larose, G.L. (2006), *A unified approach to aerodynamic damping and drag/lift instabilities, and its application to dry inclined cable galloping.* Journal of Fluids and Structures, **22**(2): p. 229-252.

[33.] Macdonald, J.H.G. and Larose, G.L. (2008), *Two-degree-of-freedom inclined cable galloping--Part 1: General formulation and solution for perfectly tuned system.* Journal of Wind Engineering and Industrial Aerodynamics, **96**(3): p. 291-307.

[34.] Macdonald, J.H.G. and Larose, G.L. (2008), *Two-degree-of-freedom inclined cable galloping--Part 2: Analysis and prevention for arbitrary frequency ratio.* Journal of Wind Engineering and Industrial Aerodynamics, **96**(3): p. 308-326.

[35.] Macdonald, J.H.G., Nikitas, N., Symes, J.A., Andersen, T.L., Jakobsen, J.B., Savage, M.G., and Larose, G.L., *Large-scale wind tunnel tests of inclined cable vibrations - Preliminary findings*, in *8th UK Conf. Wind Engineering, Guildford.* 2008.

[36.] Symes, J.A. and Macdonald, J.H.G. (2006). *Comparison of Quasi-Steady "Dry-Galloping" Analysis of Inclined Cables Using Two Sets of Wind Tunnel*

Data. Proccedings for Symp. Mechanics of Slender Structures, Northampton, 17.

[37.] McComber, P. and Paradis, A. (1998), *A cable galloping model for thin ice accretions.* Atmospheric Research, **46**(1-2): p. 13-25.

[38.] Desai, Y.M., Yu, P., Popplewell, N., and Shah, A.H. (1995), *Finite-Element Modeling of Transmission-Line Galloping.* Computers & Structures, **57**(3): p. 407-420.

[39.] Nakamura, Y. (1979), *On the aerodynamic mechanism of torsional flutter of bluff structures.* Journal of Sound and Vibration, **67**(2): p. 163-177.

[40.] Nakamura, Y. and Yoshimura, T. (1982), *Flutter and vortex excitation of rectangular prisms in pure torsion in smooth and turbulent flows.* Journal of Sound and Vibration, **84**(3): p. 305-317.

[41.] Washizu, K., Ohya, A., Otsuki, Y., and Fujii, K. (1980), *Aeroelastic instability of rectangular cylinders in a torsional mode due to a transverse wind.* Journal of Sound and Vibration, **72**(4): p. 507-521.

[42.] Gjelstrup, H., Larsen, A., Georgakis, C., and Koss, H. (2008). *A new general 3DOF quasi-steady aerodynamic instability model. Proccedings for BBAA VI International Colloquium on: Bluff Bodies Aerodynamics & Applications*, Milano, Italy, .

[43.] Gjelstrup, H. and Georgakis, C. (2010), *A quasi-steady 3-DOF model for the determination of onset for bluff body of galloping instability (submitted).* submitted to Journal of Fluids and Structures.

[44.] Nakamura, Y. and Mizota, T. (1975), *TORSIONAL FLUTTER OF RECTANGULAR PRISMS.* Journal of the Engineering Mechanics Division-Asce, **101**(NEM2): p. 125-142.

[45.] Thomsen, J.J. (2003), *Vibrations and Stability.* Second Edition ed: Springer.

[46.] Wang, J., *Large vibration of overhead electrical lines: A full 3-DOF model for galloping studies*, in *Collection des Publications de la Faculté des Sciences appliqués des de l'Université de Liège.* 1996, Universite de Liege: Liege. p. 1-227.

[47.] Gjelstrup, H., Georgakis, C., and Koss, H. (2010), *Experimental study of icing at high temperature and low wind velocities on circular cylinders of different diameter and orientation.* Unsubmitted manuscript

[48.] Lozowski, E.P., Stallabrass, J.R., and Hearty, P.F. (1983), *The icing of an unheated, nonrotating cylinder. II. Icing wind tunnel experiments.* Journal of Climate and Applied Meteorology **22**(12): p. 2063-74.

[49.] Mazin, I.P., Korolev, A.V., Heymsfield, A., Isaac, G.A., and Cober, S.G. (2001), *Thermodynamics of icing cylinder for measurements of liquid water content in supercooled clouds.* Journal of Atmospheric and Oceanic Technology, **18**(4): p. 543-558.

[50.] Hess, M., Koepke, P., and Schult, I. (1998), *Optical Properties of Aerosols and Clouds: The Software Package OPAC.* Bulletin of the American Meteorological Society, **79,**(5): p. 831–844.

[51.] Greenan, B.J.W. and List, R. (1995), *Experimental closure of the heat and mass transfer theory of spheroidal hailstones.* Journal of the Atmospheric Sciences, **52**(21): p. 3797.

[52.] Shin, J.W. (1996), *Characteristics of surface roughness associated with leading-edge ice accretion.* Journal of Aircraft, **33**(2): p. 316-321.

[53.] Hansman, R.J., Breuer, e.S., Hazan, D., Reehorst, A., and Vargas, M. (1993), *Close-up analysis of aircraft ice accretion.* AIAA Journal.

[54.] Bragg, M.B.K., M. F.; Cummings, M. J. (1994), *The effect of the initial ice roughness on airfoil aerodynamics.* AIAA Journal.

[55.] Olsen, W.W., E. , *Experimental evidence for modifying the current physical model for ice accretion on aircraft surfaces* 1986 Glenn Research Center

[56.] Hack, R.K., *A wind tunnel investigation of four conductor models with simulated ice deposits.* 1981, National aerospace laboratory NLR, The Netherlands.

[57.] Rawlins, C.B., *Galloping stability of single conductor with central electricity research laboratories, Wet snow shape 2.* 1991, Alcoa conductor products company.

[58.] Huebsch, W.W. and Rothmayer, A.P. (2002), *Effects of surface ice roughness on dynamic stall.* Journal of Aircraft, **39**(6): p. 945-953.

[59.] Mark G. Potapczuk, K.M.A.-K., and Matthew T. Velazquez, *Ice Accretion and Performance Degradation Calculations with LEWICE.* 1993, National Aeronautics and Space Administration; Lewis Research Center; Cleveland, Ohio 44135-3191.

[60.] Lozowski, E.P., Stallabrass, J.R., and Hearty, P.F. (1983), *The icing of an unheated, nonrotating cylinder .I. A simulation-model.* Journal of Climate and Applied Meteorology, **22**(12): p. 2053-2062.

[61.] Oleskiw, M.M., Hyde, F.H., and Penna, P.J. (2001). *In-flight Icing Simulation Capabilities of NRC's Altitude Icing Wind Tunnel Proccedings for 39th AIAA Aerospace Science Meeting & Exhibit*, Reno, NV.

[62.] Novak, M. and Tanaka, H. (1974), *Effect of turbulence on galloping instability.* Journal of the Engineering Mechanics Division-Asce, **100**(NEM1): p. 27-47.

[63.] Lilien, J.L., Dubois, H., and Maso, F.D., *General mathematical formulation for overhead line galloping.* 1989. p. 5.1-5.42.

[64.] Cheers, F., *A Note on Galloping Conductors.* 1950, National Research Council of Canada.

[65.] Harris, C.o., *Galloping Conductors.* 1948-49, Department of Engineering Mechanics, University of Notre Dame.

[66.] Gjelstrup, H. and Georgakis, C. (2009). *Aerodynamic Instability of a cylinder with thin ice accretion. Proccedings for ISCD 2009*, Paris.

[67.] Anderson, D.N. (1994), *Rime-, mixed- and glaze-ice evaluations of three scaling laws* AIAA, (PAPER 94-0718).

[68.] Kind, R.J., Potapczuk, M.G., Feo, A., Golia, C., and Shah, A.D. (1998), *Experimental and computational simulation of in-flight icing phenomena.* Progress in Aerospace Sciences, **34**(5-6): p. 257-345.

[69.] Szilder, K. and Lozowski, P., Edward (2004), *Novel two-dimensional modeling approach for aircraft icing.* Journal of Aircraft, **41**(4).

[70.] Gjelstrup, H., Larsen, A., and Geogakis, C. (2010), *An evaluation of iced bridge hanger vibrations through wind tunnel testing and quasi-steady theory* submitted to Wind and structures.

[71.] Dalton, C. (1971), *Allen and Vincenti blockage corrections in a wind tunnel.* AIAA Journal, **9**(9): p. 1864-&.

[72.] Allen, H.J. and Vincenti, W.G., *Wall interference in a two-dimensional-flow wind tunnel, with consideration of the effect of compressibility*, NACA, Editor. 1944.

Part II

Appended Papers

Paper I ([43])

“A quasi-steady 3-DOF model for the determination of onset for bluff body of galloping instability”

H. Gjelstrup & C.T. Georgakis

submitted to Journal of Fluids and Structures

A quasi-steady 3-DOF model for the determination of onset for bluff body of galloping instability

H. Gjelstrup[1*⁎], C.T. Georgakis[⁎]

[*]*COWI A/S, Parallelvej 2, 2800 Kgs. Lyngby, Denmark*

[⁎] *DTU Byg, Building 118, Brovej, 2800 Kgs. Lyngby, Denmark*

Abstract

In this paper, a quasi-steady three degrees-of-freedom (3-DOF) flow-induced galloping instability model for bluff-bodies is proposed. The proposed model can be applied generally for the prediction of onset of galloping instability due to negative aerodynamic damping of any prismatic compact bluff body in a fluidic medium. The three degrees-of-freedom refer to the bluff body's two orthogonal displacements perpendicular to its length axis and the rotation about its length axis. The model incorporates inertial coupling between the three degrees-of-freedom and is capable of estimating the onset of galloping instability due changes in drag, lift and moment, assuming that the bluff-body is subject to uniform flow and motion. The changes may be a function of wind angle of attack (α) perpendicular to bluff body's length axis, Reynolds number and a skew wind angle (ϕ) in relation to the length axis of the bluff

---

[1] Corresponding author. Tel.: +45 45972805/ +45 45251940; Fax: +45 45972212/ +45 45883282

E-mail address: hegj@cowi.dk/heg@byg.dtu.dk; (COWI/DTU Byg)

body. An analytical solution of the instability criterion is obtained by applying the Routh-Hurwitz criterion.

Keywords: aerodynamic damping, motional instability, quasi-steady drag, lift and moment, Routh-Hurwitz.

1. Introduction

Due to the complexity of testing and measuring fluctuating forces on a moving object in fluid, researchers and engineers have often reverted to predicting dynamic motional instabilities by applying statically derived drag, lift and moment coefficients to theoretical models. This is often referred to as the “quasi-steady” approach or assumption. During the last century a number of mathematical models have been proposed using this approach and over the last decade, aerodynamic damping, as a driving force for vibration, has received renewed attention.

In the 1930s, a stability criterion for a 1-DOF bluff-body model was proposed by den Hartog (Hartog, 1932). This model made provision for an aerodynamic lift coefficient formulated as a function of wind angle-of-attack perpendicular to the longitudinal axis of the bluff body. In the 1960s, an expression for aerodynamic damping in both the along wind and transverse wind direction of a cylinder was proposed by Davenport (Davenport, 1962). Two decades later, the instability criterion, which today is widely referred to as “drag crisis” or “drag instability”, was proposed by Martin et al., (Martin et al., 1981), in which aerodynamic instability is initiated due to changes in the drag force in the critical Reynolds number range. Up to that point, all expressions for the aerodynamic damping were considered “special cases”, which should be applied individually. In 2006, Macdonald and Larose proposed a unified approach for the determination of aerodynamically-induced motional instability of a 1-DOF bluff-body , (Macdonald and Larose, 2006). The particular model assumes changes in the drag and/or lift coefficients when the body is in motion, which could lead to either positive or negative values of aerodynamic damping. Macdonald and Larose later extended this model to two degrees-of-freedom, (Macdonald and Larose, 2008a; Macdonald and Larose, 2008b). This general quasi-steady 2-DOF instability model is capable of estimating the required structural damping for the avoidance of aerodynamic instability of a bluff body moving in the cross-sectional plane, perpendicular to the longitudinal axis of the body. The 2-DOF model is capable of predicting the aforementioned special cases, which were earlier applied individually. Nevertheless, the model does not include the effect of rotational inertial coupling, i.e. when the cross-sectional centre of mass of the body does not coincide with the centre of rotation. The effect of this coupling may be significant, as research on iced cables has identified that torsion about the longitudinal axis of a body affects the motional stability of a cable under certain conditions, (Chabart and Lilien, 1998). For this reason, a new 3-DOF aerodynamic instability model, which incorporates this torsional effect and which can be generalized for any compact bluff body under uniform flow and motion, is proposed herewith.

The addition of the third degree-of-freedom, describing a body’s cross-sectional rotation, renders the quasi-static description of the rotational speed of the cable necessary. Some research has been performed on torsional instability for models with different geometries and an approximation of the quasi-static rotational speed has been found for several geometries, (Blevins, 1994). It is worth mentioning that development of a quasi-static description of the rotational speed is non-trivial and, to the authors' knowledge, no unified expression, which would provide an unambiguous definition of the quasi-static rotational speed, has been presented thus far.

In a similar manner to Macdonald et al. (Macdonald and Larose, 2008a), a method is presented herewith in which the generalized 3-DOF quasi-static galloping instability model is used to estimate the damping needed to suppress the aerodynamic instabilities it predicts, in all three degrees-of-freedom. Additionally, the 3-DOF instability model is capable of predicting the torsional damping needed to suppress rotational instability and the combined damping needed to suppress motional instability, which is a function of simultaneous motion in all three degrees-of-freedom. It should be noted that the instability criterion is based on the assumption of a quasi-steady state, which assumes that the wind velocity acting on the cable is undisturbed by the movement of the cable (i.e. small and slow cable amplitudes in relation to the wind speed). According to Washizu et al. (Washizu et al., 1978), the quasi-steady state should be fulfilled for prismatic cylinders in heaving modes, when the reduced velocity is above 20, where the vibration of the model is found to have no significant effect on the free stream velocity felt be the model. Keeping that in mind it is recomented to use the inhere presented model with a reduced speed higher the 20 and the higher the better in oder to reduce the effect on the flow field around the model origination from the vibration of the model. Furthermore it also assumed that any variations in the force coefficients acting on the cable are relatively smooth. It should be noted that a restriction for the inclusion of the rotational degree of freedom is that the criterion is limited to a fixed centre of rotation and furthermore to compact sections, compact section is defined by a depth /height ratio ≤ 2, (Nakamura and Mizota, 1975; Blevins, 1994) .

2. Description of the model

As previously mentioned, the generalized 3-DOF model developed herewith can be used to describe the galloping instability of any compact bluff body in any fluid medium. Nonetheless, to help in the understanding of the development of the mathematical model, a section of a bridge cable in air is modeled and assumed to have a thin ice accretion. Figures 1 - 4 show the cable coordinate systems for the external wind load and the cable section response. Similar definitions would apply to a generalized compact bluff body system.

For the development of the model, it is assumed that the bluff body is a straight and rigid 2-D section model, and that the stiffness of the spring supports of the model is constant for all degrees-of-freedom, i.e. stiffness does not changes with respect to movement in x and y or rotation about the structural axis (θ). Thus, The application of this model for the determination of the galloping instability of long flexible structures, such as electrical transmission lines, can only provide indications for the onset of instability and the amplitudes of vibration, as elements such as the spanwise correlation of the wind and the geometry of the and its supports is not considered. Also it is assumed that the structural damping force is proportional to velocity and that the wind velocity U is constant. Furthermore it is assumed that the rotational speed can be represented by a cross-sectionally dependant radial length times the radial rotation speed $\left(R_\delta\dot{\theta}\right)$, that quasi-steady assumptions apply, and that gravitational forces do not influence the model. Finally, it is assumed that the cable is at rest at the initiation of any motional instability.

In the following, the notation for time-dependant variables, $x(t), y(t)$ and $\theta(t)$, shall be x, y and θ, respectively. Derivatives with respect to time are written as $(\mathrm{d}/\mathrm{dt})\mathrm{x} = \dot{\mathrm{x}}$ and $(\mathrm{d}^2/\mathrm{dt}^2)\mathrm{x} = \ddot{\mathrm{x}}$.

Both vertical and rotational motions of the cable section cause a variation in the wind angle of attack over the section, i.e. a positive rotational velocity induces a down-draft upwind of the centre of rotation and an up-draft downwind of the centre of rotation seen with Figure 1 as reference for up and down. A negative rotational velocity will create the opposite effect. The rotational velocity is approximated by the motion of a reference point defined in polar coordinates by the radial distance R_δ and angle δ, as shown in Figure 4. The length R_δ is not directly related to characteristic points of the bluff body's geometry or of the flow field, (Blevins, 1994). It is rather a variable used to adjust the aerodynamic model output to the observed instabilities. However, it has been found that the length and the angle is the same for structures with similar geometry. For example, for the torsional instability of rectangles about their centroid, R_δ has been approximated to half the distance between the centroid and the body's leading edge under the respective angle of attack (Nakamura and Mizota, 1975) another example is torsion about flutter of airfoils where R_δ is chosen to give the angle of attack at a point three-quarters of the way back from the leading edge, (Blevins, 1994).

The wind velocities acting on the iced cable section are as follows.

1. Axial component of free stream wind velocity

$$U_A = U\,cos(\phi) \tag{1}$$

Relative velocity

$$U_R = \sqrt{(U_A^2 + U_{NR}^2)} \tag{2}$$

Which can be obtain by using the following relationship

$$U_P = U \sin(\phi) - \dot{x}\,cos(\psi) - \left(\dot{y}\,sin(\psi) + R_\delta\dot{\theta}\,sin(\delta)\right) \tag{3}$$

$$U_{PR} = -\left(\dot{y}\,cos(\psi) + R_\delta\dot{\theta}\,cos(\delta)\right) + \dot{x}\,sin(\psi) \tag{4}$$

$$U_{NR} = \sqrt{(U_P^2 + U_{PR}^2)} \tag{5}$$

3. Equations of motion

For the derivation of the equations of motion, an energy balance approach using Euler-Lagrange formulation has been applied. The Euler-Lagrange formulation requires an accurate determination of the centre of mass of the cable section and, for this purpose, the coordinate systems shown in Figures 1 and 5 are used.

Coordinate system

Figure 1 shows the coordinate system of the ice-accreted cable, whilst Figure 5 illustrates the location of the centre of mass, as represented by Eq. (6) and Eq. (7), below.

$$X_G = x - L_e cos(\gamma_0 + \theta) \tag{6}$$

$$Y_G = y + L_e sin(\gamma_0 + \theta) \tag{7}$$

Euler-Lagrange

The Euler-Lagrange formulation requires the determination of the kinetic and potential energy of the cable section about its centre of mass. This formulation leads to Eq. (8), in which $\boldsymbol{F_D}$ and $\boldsymbol{F_Z}$ are the damping and aerodynamic force, respectively.

$$\begin{gathered} \frac{\partial}{\partial t}\left(\frac{\partial L}{\partial \dot{\boldsymbol{Z}}}\right) - \frac{\partial L}{\partial \boldsymbol{Z}} + \boldsymbol{F_D} = \boldsymbol{F_Z} \\ L = T - V, \qquad \boldsymbol{Z} = \{x, y, \theta\} \\ \boldsymbol{F_D} = \{C_{sxx}\dot{x}, C_{syy}\dot{y}, C_{s\theta\theta}\dot{\theta}\} \end{gathered} \tag{8}$$

where, *T* is the kinetic energy and *V* is the potential energy. These can be written as:

$$T = \frac{1}{2}m\left(\dot{X}_G^2 + \dot{Y}_G^2\right) + \frac{1}{2}J\dot{\theta}^2 \tag{9}$$

$$V = \frac{1}{2}\left(k_x x^2 + k_y y^2 + k_\theta \theta^2\right) \tag{10}$$

where, m is the mass of the system and J is the rotational inertia in relation to the mass centre.

Substitution of Equations (9) and (10) into Eq. (8) leads to Eq. (11) - (13), below:

$$m\ddot{x} + C_{sxx}\dot{x} + k_x x + mL_e\left(cos(\varphi)\,\dot{\theta}^2 + sin(\varphi)\,\ddot{\theta}\right) \; = F_x \tag{11}$$

$$m\ddot{y} + C_{syy}\dot{y} + k_y y + mL_e\left(-sin(\varphi)\,\dot{\theta}^2 + cos(\varphi)\,\ddot{\theta}\right) = F_y \tag{12}$$

$$J\ddot{\theta} + C_{s\theta\theta}\dot{\theta} + k_\theta \theta + mL_e\left(sin(\varphi)\,\ddot{x} + cos(\varphi)\,\ddot{y} + L_e\ddot{\theta}\right) = F_\theta \tag{13}$$

where, C_{sxx} is the structural damping in the x direction C_{syy} is the structural damping in the y direction $C_{s\theta\theta}$ is the structural damping in the θ direction, L_e is the length to the mass centre from the point of rotation, $\varphi = \gamma_0 + \theta$(see Figure 1). F_x, F_y and F_θ are the aerodynamic force in the x direction, y direction and for torsion respectively, which are given by:

$$F_x = \frac{1}{2}\rho U_R^2 D(C_D(\alpha_R, Re_R, \phi_R)\,cos(\alpha_R) + C_L(\alpha_R, Re_R, \phi_R)\,sin(\alpha_R)) \tag{14}$$

$$F_y = \frac{1}{2}\rho U_R^2 D(C_L(\alpha_R, Re_R, \phi_R)\,cos(\alpha_R) - C_D(\alpha_R, Re_R, \phi_R)\,sin(\alpha_R)) \tag{15}$$

$$F_\theta = \frac{1}{2}\rho U_R^2 D^2 C_M(\alpha_R, Re_R, \phi_R) \tag{16}$$

Where $\alpha_R = (\psi + \beta)$, Re_R =Relative Reynolds number, ϕ_R = Relative wind angle of attack, cable length axis, ρ = fluid density, U_R = Relative fluid velocity, D = Characteristic length of section(diameter for circular models), C_D = Drag coefficient, C_L = Lift coefficient and C_M = Moment coefficient. The inertial coupling in the x-direction, $\left(mL_e \cos(\varphi)\,\dot{\theta}^2 + mL_e \sin(\varphi)\,\ddot{\theta}\right)$, consists of two terms, namely the centripetal force, $\left(mL_e \cos(\varphi)\,\dot{\theta}^2\right)$ and the force originating from the angular acceleration $\left(mL_e \sin(\varphi)\,\ddot{\theta}\right)$. The same applies in the y-direction, but with a change in the *cosine* and *sine* functions. The inertial coupling in the θ-direction is a result of the projection of the inertial forces originated from the x- and y-direction.

Aerodynamic damping

Following Macdonald et al (Macdonald and Larose, 2008a), the motional instability of the cable section is determined based on a linearization of the cable section’s equations of motion (11)-(13). The linearization is achieved through a first order Taylor expansion of the aerodynamic forces expanded in Eq. (14)-(16) around the velocity $\dot{x} = \dot{y} = \dot{\theta} = 0$. This leads to:

$$F_{\dot{Z}}(\dot{x},\dot{y},\dot{\theta})_{\dot{x}=\dot{y}=\dot{\theta}=0} = F_{\dot{Z}} + \frac{\partial F_{\dot{Z}}}{\partial \dot{x}}\dot{x} + \frac{\partial F_{\dot{Z}}}{\partial \dot{y}}\dot{y} + \frac{\partial F_{\dot{Z}}}{\partial \dot{\theta}}\dot{\theta} + \frac{\partial F_{\dot{Z}}}{\partial \dot{x}\partial \dot{y}}\dot{x}\dot{y} + \dot{\theta}\left(\frac{\partial F_{\dot{Z}}}{\partial \dot{x}\partial \dot{\theta}}\dot{x} + \frac{\partial F_{\dot{Z}}}{\partial \dot{y}\partial \dot{\theta}}\dot{y} + \frac{\partial F_{\dot{Z}}}{\partial \dot{x}\partial \dot{y}\partial \dot{\theta}}\dot{x}\dot{y}\right), where \ \left(F_{\dot{Z}} = F_{\dot{Z}}(0,0,0)\right) \tag{17}$$

The expansion results in equivalent static wind forces for all three degrees-of-freedom, which are assumed zero, and a dynamic force, which can be represented by the Jacobian damping matrix (C_a) multiplied with the sectional velocity in the three directions, $C_a\dot{Z}$ where $\dot{Z} = [\dot{x},\dot{y},\dot{\theta}]'$.

$$C_a = -\begin{bmatrix} \frac{\partial F_x}{\partial \dot{x}} & \frac{\partial F_x}{\partial \dot{y}} & \frac{\partial F_x}{\partial \dot{\theta}} \\ \frac{\partial F_y}{\partial \dot{x}} & \frac{\partial F_y}{\partial \dot{y}} & \frac{\partial F_y}{\partial \dot{\theta}} \\ \frac{\partial F_\theta}{\partial \dot{x}} & \frac{\partial F_\theta}{\partial \dot{y}} & \frac{\partial F_\theta}{\partial \dot{\theta}} \end{bmatrix}_{\dot{x}=\dot{y}=\dot{\theta}=0} \tag{18}$$

The values of the aerodynamic damping matrix C_a are calculated for small initial displacements and rotations ($\theta \ll 1°$) and determined following Macdonald and Larose (Macdonald and Larose, 2006). The derivation of the torsional terms in the aerodynamic damping matrix is presented in Appendix A, whereas the terms relating to movement in x and y can be found in (Macdonald and Larose, 2006).

Furthermore, by applying the assumption of zero initial motion on the cable section, all higher order terms in the equations of motions can be neglected. The total damping matrix with both structural and aerodynamic damping is now:

$$C_T = C_s + C_a = \begin{bmatrix} C_{sxx} & 0 & 0 \\ 0 & C_{syy} & 0 \\ 0 & 0 & C_{s\theta\theta} \end{bmatrix} + \begin{bmatrix} C_{axx} & C_{axy} & C_{ax\theta} \\ C_{ayx} & C_{ayy} & C_{ay\theta} \\ C_{a\theta x} & C_{a\theta y} & C_{a\theta\theta} \end{bmatrix}$$
$$= \begin{bmatrix} C_{xx} & C_{xy} & C_{x\theta} \\ C_{yx} & C_{yy} & C_{y\theta} \\ C_{\theta x} & C_{\theta y} & C_{\theta\theta} \end{bmatrix} \tag{19}$$

With the above mention assumptions the aerodynamic stability of the 3-DOF cable section can now be evaluated by rewriting the equations of motions (11)-(13) into state space and solving the resulting eigenvalue problem.

Assuming the static aerodynamic force equal to zero, $F_Z = 0$ where $Z = [x, y, \theta]'$, the linearization of the equations of motions (11)-(13) leads to Eqs. (20)-(22). Assuming the static wind force to be zero lead to the assumption the equilibrium position does not change, which result in an instability analysis is around a local equilibrium point.

$$\begin{aligned}\ddot{x} = -\frac{1}{Jm}\Bigg(& J\big(m\omega_x^2 x + C_{xx}\dot{x} + C_{xy}\dot{y} + C_{x\theta}\dot{\theta}\big) \\ & + sin(\varphi)L_e^2 m\Bigg(-\frac{1}{L_e}\big(J\omega_\theta^2\theta + C_{\theta x}\dot{x} + C_{\theta y}\dot{y} + C_{\theta\theta}\dot{\theta}\big) \\ & + sin(\varphi)\big(\omega_x^2 m x + C_{xx}\dot{x} + C_{xy}\dot{y} + C_{x\theta}\dot{\theta}\big) \\ & + cos(\varphi)\big(\omega_y^2 m y + C_{yx}\dot{x} + C_{yy}\dot{y} + C_{y\theta}\dot{\theta}\big)\Bigg)\Bigg)\end{aligned} \tag{20}$$

$$\begin{aligned}\ddot{y} = -\frac{1}{Jm}\Bigg(& J\big(m\omega_y^2 y + C_{yx}\dot{x} + C_{yy}\dot{y} + C_{y\theta}\dot{\theta}\big) \\ & + cos(\varphi)L_e^2 m\Bigg(-\frac{1}{L_e}\big(J\omega_\theta^2\theta + C_{\theta x}\dot{x} + C_{\theta y}\dot{y} + C_{\theta\theta}\dot{\theta}\big) \\ & + sin(\varphi)\big(\omega_x^2 m x + C_{xx}\dot{x} + C_{xy}\dot{y} + C_{x\theta}\dot{\theta}\big) \\ & + cos(\varphi)\big(\omega_y^2 m y + C_{yx}\dot{x} + C_{yy}\dot{y} + C_{y\theta}\dot{\theta}\big)\Bigg)\Bigg)\end{aligned} \tag{21}$$

$$\begin{aligned}\ddot{\theta} = -\frac{1}{J}\Big(& \big(J\omega_\theta^2\theta + C_{\theta x}\dot{x} + C_{\theta y}\dot{y} + C_{\theta\theta}\dot{\theta}\big) \\ & - L_e\Big(sin(\varphi)\big(\omega_x^2 m x + C_{xx}\dot{x} + C_{xy}\dot{y} + C_{x\theta}\dot{\theta}\big) \\ & + cos(\varphi)\big(\omega_y^2 m y + C_{yx}\dot{x} + C_{yy}\dot{y} + C_{y\theta}\dot{\theta}\big)\Big)\Big)\end{aligned} \tag{22}$$

The state-space matrix, obtained from Eqs. (20) - (22), is thus:

$$\boldsymbol{S_{ij}} z_i = \dot{z}_\iota \Rightarrow \begin{bmatrix} 0 & 0 & 0 & 1 & 0 & 0 \\ 0 & 0 & 0 & 0 & 1 & 0 \\ 0 & 0 & 0 & 0 & 0 & 1 \\ & \vdots & & \vdots & \vdots & \vdots \\ \cdots & \boldsymbol{A} & \cdots & \boldsymbol{B} & \boldsymbol{C} & \boldsymbol{D} \\ & \vdots & & \vdots & \vdots & \vdots \end{bmatrix} \begin{bmatrix} x_1 \\ y_1 \\ \theta_1 \\ x_2 \\ y_2 \\ \theta_2 \end{bmatrix} = \begin{bmatrix} \dot{x}_1 \\ \dot{y}_1 \\ \dot{\theta}_1 \\ \dot{x}_2 \\ \dot{y}_2 \\ \dot{\theta}_2 \end{bmatrix} \tag{23}$$

where, $\boldsymbol{A}$ is a 3x3 sub-matrix and $\boldsymbol{B}, \boldsymbol{C}$ and $\boldsymbol{D}$ are 3x1 sub-vectors. Also,

$(x_1, y_1, \theta_1) = (x, y, \theta)$ represents the position of the bluff body in relation to the rotational axis.

$(x_2, y_2, \theta_2) = (\dot{x}_1, \dot{y}_1, \dot{\theta}_1)$ represents the velocity of the bluff body in relation to the rotational axis.

$(\dot{x}_2, \dot{y}_2, \dot{\theta}_2) = (\ddot{x}_1, \ddot{y}_1, \ddot{\theta}_1)$ represents the acceleration of the bluff body in relation to the rotational axis.

$$\boldsymbol{A} = \begin{bmatrix} -\omega_x^2 - \dfrac{sin(\varphi)^2 L_e^2 m \omega_x^2}{J} & -\dfrac{cos(\varphi) sin(\varphi) L_e^2 m \omega_y^2}{J} & sin(\varphi) L_e \omega_\theta^2 \\ -\dfrac{cos(\varphi) sin(\varphi) L_e^2 m \omega_x^2}{J} & -\omega_y^2 - \dfrac{cos(\varphi)^2 L_e^2 m \omega_y^2}{J} & cos(\varphi) L_e \omega_\theta^2 \\ \dfrac{sin(\varphi) L_e m \omega_x^2}{J} & \dfrac{cos(\varphi) L_e m \omega_y^2}{J} & -\omega_\theta^2 \end{bmatrix} \tag{24}$$

$$\boldsymbol{B} = \begin{bmatrix} \dfrac{sin(\varphi) C_{\theta x} L_e}{J} - \dfrac{sin(\varphi)^2 C_{xx} L_e^2}{J} - \dfrac{cos(\varphi) sin(\varphi) C_{yx} L_e^2}{J} - \dfrac{C_{xx}}{m} \\ \dfrac{cos(\varphi) C_{\theta x} L_e}{J} - \dfrac{cos(\varphi) sin(\varphi) C_{xx} L_e^2}{J} - \dfrac{cos(\varphi)^2 C_{yx} L_e^2}{J} - \dfrac{C_{yx}}{m} \\ -\dfrac{C_{\theta x}}{J} + \dfrac{sin(\varphi) C_{xx} L_e}{J} + \dfrac{cos(\varphi) C_{yx} L_e}{J} \end{bmatrix} \tag{25}$$

$$\boldsymbol{C}=\begin{bmatrix}\frac{sin(\varphi)C_{\theta y}L_e}{J}-\frac{sin(\varphi)^2C_{xy}L_e^2}{J}-\frac{cos(\varphi)sin(\varphi)C_{yy}L_e^2}{J}-\frac{C_{xy}}{m}\\ \frac{cos(\varphi)C_{\theta y}L_e}{J}-\frac{cos(\varphi)sin(\varphi)C_{xy}L_e^2}{J}-\frac{cos(\varphi)^2C_{yy}L_e^2}{J}-\frac{C_{yy}}{m}\\ -\frac{C_{\theta y}}{J}+\frac{sin(\varphi)C_{xy}L_e}{J}+\frac{cos(\varphi)C_{yy}L_e}{J}\end{bmatrix} \tag{26}$$

$$\boldsymbol{D}=\begin{bmatrix}\frac{sin(\varphi)C_{\theta\theta}L_e}{J}-\frac{sin(\varphi)^2C_{x\theta}L_e^2}{J}-\frac{cos(\varphi)sin(\varphi)C_{y\theta}L_e^2}{J}-\frac{C_{x\theta}}{m}\\ \frac{cos(\varphi)C_{\theta\theta}L_e}{J}-\frac{cos(\varphi)sin(\varphi)C_{x\theta}L_e^2}{J}-\frac{cos(\varphi)^2C_{y\theta}L_e^2}{J}-\frac{C_{y\theta}}{m}\\ -\frac{C_{\theta\theta}}{J}+\frac{sin(\varphi)C_{x\theta}L_e}{J}+\frac{cos(\varphi)C_{y\theta}L_e}{J}\end{bmatrix} \tag{27}$$

From the state-space matrix of Eq. (23), the eigenvalue problem, $\left(\boldsymbol{S}_{ij}\text{-}\lambda\boldsymbol{I}_{ij}=\mathbf{0}\right)$, is formulated. Mathematical manipulation of this leads to a 6th order polynomial, which can be solved either numerically or analytically. Here the eigenvalue problem is solved analytically through application of the Routh-Hurwitz stability criterion, (Thomsen, 2003).

The Routh-Hurwitz stability criterion dictates that a system of equations is stable if the "real" parts of the criterion's resulting coefficients are greater than zero. Application of the Routh-Hurwitz stability criterion results in 13 coefficients (7 from the polynomial, $(H_0 - H_6)$, and 6 from the Hurwitz determinant$(D_0 - D_5)$. The full expression of coefficients $(H_0 - H_6)$ and $(D_0 - D_5)$ is provided in Appendix B. The 6th order polynomial, representing the solution to the aforementioned eigenvalue problem is:

$$H_0\lambda^6 + H_1\lambda^5 + H_2\lambda^4 + H_3\lambda^3 + H_4\lambda^2 + H_5\lambda + H_6 \tag{28}$$

where, (H_0)– (H_6) are defined in Eqs. (B.2) - (B.9). Here, $\varphi = \gamma_0 + \theta$ is equal to $\varphi = \gamma_0$, due to the assumption of the initial condition of the cable at rest, i.e. all displacements, velocities and accelerations are zero.

4. Reducing the 3-DOF model to the proven 2-DOF model

In cases where the motion of the rotational degree of freedom of the bluff-body is considered insignificant, the 3-DOF model can be simplified, so as to only cover the cases of motion of the two translational degrees-of-freedom. The 2-DOF model is obtained by omitting the rotational degree of freedom ($\theta = 0$) and the coupling to the XY-plan ($L_e = 0$). The resulting state-space matrix is shown in Eq. (29)

$$\begin{bmatrix} 0 & 0 & 1 & 0 \\ 0 & 0 & 0 & 1 \\ -\omega_x^2 & 0 & -\dfrac{C_{xx}}{m} & -\dfrac{C_{xy}}{m} \\ 0 & -\omega_y^2 & -\dfrac{C_{yx}}{m} & -\dfrac{C_{yy}}{m} \end{bmatrix} \begin{bmatrix} x_1 \\ y_1 \\ x_2 \\ y_2 \end{bmatrix} = \begin{bmatrix} \dot{x}_1 \\ \dot{y}_1 \\ \dot{x}_2 \\ \dot{y}_2 \end{bmatrix} \tag{29}$$

Similar to the 3-DOF model formulation, the eigenvalue problem here reduces to

$$\lambda^4 + \left(\frac{C_{\mathrm{xx}} + C_{\mathrm{yy}}}{m}\right)\lambda^3 + \left(\frac{C_{\mathrm{xx}}C_{\mathrm{yy}} - C_{\mathrm{xy}}C_{\mathrm{yx}}}{m^2} + \omega_x^2 + \omega_y^2\right)\lambda^2 + \left(\frac{C_{\mathrm{xx}}\omega_y^2 + C_{\mathrm{yy}}\omega_x^2}{m}\right)\lambda + \omega_x^2\omega_y^2 = 0 \tag{30}$$

It can be seen that the eigenvalue problem of the resulting 2-DOF model is identical to that of the proven model of Macdonald and Larose (Macdonald and Larose, 2008a). Finally, the expressions governing the known special cases, such as “dry inclined galloping”, “den Hartog galloping ($C_D + \partial C_L/\partial\alpha < 0$)” and “inline drag crisis ($2C_D + (\partial C_D/\partial Re)Re < 0$)” can be determined from the proven 2-DOF models, following the procedures outlined by (Griffiths et al., 2006; Macdonald and Larose, 2008a)

5. Example application of the 3-DOF model

In 1998, Chabart and Lilien (Chabart and Lilien, 1998) reported the results from a series of wind-tunnel tests that were undertaken on a heavily iced cable. The aerodynamic drag, lift and moment coefficients obtained from these tests are presented in Figure 6. A cross-sectional view of the iced cable, as tested, is shown in Figure 7. Furthermore the body’s radial length R_δ, for a specific wind angle of attack, is also provided in Figure 7. As R_δ is a length which variants from geometry to geometry if was found that setting R_δ as the length between the centre of rotation and the leading edge of the model for the given wind angle of attack, at all times resulted in a good match with the experiments which are used for comparison.

Regions of galloping instability for the iced cable are determined employing the proposed 3-DOF model, through use of the experimentally derived force coefficients (Figure 6), in conjunction with the structural and aerodynamic parameters of the body

(Table 1). The predicted regions of galloping instability are shown in Figure 8a in the shaded areas. Regions of instability are from ~25° - 45°, ~70° - 135° and ~170° - 180°. Figure 8a also shows the result of the application of the traditionally used (in these cases) den Hartog criterion for galloping. The den Hartog criterion predicts instability in two regions, 30° - 45° and 170° - 180°. As the in-plane and out-of-plane frequencies are de-tuned, similar results are found through the application of the existing 2-DOF model except the lower region runs from 30° - 40°. The wind-tunnel tests performed by Chabart and Lilien (Chabart and Lilien, 1998) show that the iced cable experiences galloping for wind angles of attack in the region of 20° to 180°. Looking at Figure 9a, which shows a plot of the torsional component from the 3-DOF model, reveals in comparison to the full 3-DOF(Figure 9b) and the 2-DOF(Figure 8b) that the additional instability seen in the experiments is probably due to the torsional component. It can be seen that, unlike the den Hartog criteria and the 2-DOF model, the 3-DOF model proposed herewith is capable of predicting instability over a wider range of wind angles-of-attack. Nevertheless, the 3-DOF model is not able to predict the full range of instability. This could be attributable to the specialized test-rig used in the wind-tunnel tests, the lack of exact values for the force coefficients, the small variations between the theoretical model and the experimental model, (the experimental models springs will pull at the model under an angle, inducing false force component in comparison to the proposed model) or most likely the limited description of the quasi-static rotational speed. In any case, the 3-DOF model is capable of providing a better prediction of the onset of instability in comparison to the 1-DOF and 2-DOF models. Furthermore as stated in (Blevins, 1994) the prediction of torsional instability using the approach shown in this paper is more a illustration of potential instability rather than predicting accurate onset of the instability. The same will probably be true for the proposed 3-DOF model presented in this paper.

The shaded areas seen on Figure 8a and Figure 9a represent the level of instability. The darker the gray the more damping is need for suppressing the instability. It would be possible to show a estimate on the need damping but due to the above stamen on the accuracy and the lack of experimental verification this part was been postponed to future work.

6. Conclusions

A new quasi-steady 3-DOF flow-induced galloping instability model is proposed. The model can be used to examine the galloping instability of any bluff-body in any fluidic medium, as a result of negative fluidic damping. Furthermore, the eigenvalue solution to the equations of motion governing the model allow for the determination of the needed damping for the avoidance of motional instability, but due to above mention of accuracy and the lack of experimental verification this part was been postponed to future work.

It is shown that the currently proposed 3-DOF model is capable of estimating instabilities due negative aerodynamic damping for the special cases of “den Hartog galloping”, “drag crisis” and “dry inclined cable galloping”, as the 3-DOF case is shown to be equivalent to the 2-DOF case proposed by (Macdonald and Larose, 2008a) when eliminating the rotational degree of freedom.

Through an example, it is shown that the currently proposed model is able to reasonably predict the observed galloping instabilities from wind-tunnel tests performed by Chabart and Lilien (1998). Regions of instability compare favorably, except in the regions from ~45° - ~70° and ~135° - ~170°. The reasons for this discrepancy may be numerous, including model amplitude, force coefficient determination/reporting errors or most likely the limited description of the quasi-static rotational speed. Nevertheless, it has been shown that the 3-DOF model provides a better estimate of galloping instability in comparison to existing 1- and 2-DOF models.

7. List of symbols

$x, \dot{x}, \ddot{x}$ = displacement, velocity, acceleration.

$y, \dot{y}, \ddot{y}$ = displacement, velocity, acceleration.

$\theta, \dot{\theta}, \ddot{\theta}$ = rotation, angular velocity, angular acceleration.

γ_0 = angle offset for mass centre.

L_e = mass centre offset.

k_x = structural stiffness in x direction.

k_y = structural stiffness in y direction.

k_θ = structural damping in θ direction.

C_{sxx} = structural damping in x direction.

C_{syy} = structural damping in y direction.

$C_{s\theta\theta}$ = structural stiffness in θ direction.

C_{axx} = aerodynamic damping in x direction.

C_{ayy} = aerodynamic damping in y direction.

$C_{a\theta\theta}$ = aerodynamic stiffness in θ direction.

(X_G,Y_G) = mass centre.

m = total mass of the system per meter

J = rotational inertia in relation to the models mass centre.

$x_\theta, \dot{x}_\theta$ = displacement, velocity.

$y_\theta, \dot{y}_\theta$ = displacement, velocity.

α_0 = steady wind angle of attack

α = wind angle of attack, cable surface.

β = angle of rotation, relative wind.

ϕ = wind angle of attack, cable length axis.

F_L = lift force.

F_D = drag force.

F_θ = moment force.

C_L = lift coefficient.

C_D = drag coefficient.

C_M = moment coefficient.

R_δ = length determining rotational velocity.

U = mean wind velocity.

U_R = relative wind velocity.

U_{PR} = projected relative vertical wind velocity.

U_p = projected relative horizontal wind velocity.

U_{NR} = normal projected relative wind velocity.

U_A = along axis wind velocity.

ψ = $\alpha_0 + \theta$.

(t) = time depented

$(\quad)_R$ = relative

T = kinetic energy.

V = potential energy.

φ = $\gamma_0 + \theta$.

F_x = aerodynamic for in the x direction.

F_y = aerodynamic for in the y direction.

F_θ = aerodynamic for in the θ direction.

D = characteristic length, Diameter for a cabel.

C_T = the total damping matrix.

C_s = the structural damping matrix.

C_a = the aerodynamic damping matrix.

Re = Reynold number.

ω_x = cyclic frequency in the x direction.

ω_y = cyclic frequency in the x direction.

ω_θ = cyclic frequency in the x direction.

$H_0 - H_6$ = coefficients for the eigenvalue polynomial

$D_0 - D_5$ = Hurwitz sub-determinants

Appendix A.

The aerodynamic damping matrix.

The Aerodynamic damping matrix, C_a, consists of nine terms, see Eq. (A.1). Three terms for each of the x-, y- and θ-directions respectively.

$$C_a = -\begin{bmatrix} \frac{\partial F_x}{\partial \dot{x}} & \frac{\partial F_x}{\partial \dot{y}} & \frac{\partial F_x}{\partial \dot{\theta}} \\ \frac{\partial F_y}{\partial \dot{x}} & \frac{\partial F_y}{\partial \dot{y}} & \frac{\partial F_y}{\partial \dot{\theta}} \\ \frac{\partial F_\theta}{\partial \dot{x}} & \frac{\partial F_\theta}{\partial \dot{y}} & \frac{\partial F_\theta}{\partial \dot{\theta}} \end{bmatrix}_{\dot{x}=\dot{y}=\dot{\theta}=0} \tag{A.1}$$

Where the forces F_x, F_y and F_θ are given in Eq. (A.2)-(A.4)

$$F_x = \frac{1}{2}\rho U_R^2 D(C_D(\alpha_R, Re_R, \phi_R)\, cos(\alpha_R) + C_L(\alpha_R, Re_R, \phi_R)\, sin(\alpha_R)) \tag{A.2}$$

$$F_y = \frac{1}{2}\rho U_R^2 D(C_L(\alpha_R, Re_R, \phi_R)\, cos(\alpha_R) - C_D(\alpha_R, Re_R, \phi_R)\, sin(\alpha_R)) \tag{A.3}$$

$$F_\theta = \frac{1}{2}\rho U_R^2 D^2 C_M(\alpha_R, Re_R, \phi_R) \tag{A.4}$$

The nine terms are presented in short form in Eqs. **Error! Reference source not found.**-(A.5), where $\dot{z}$ represents the differentiated terms $(\dot{x}, \dot{y}, \dot{\theta})$. Terms relating to movement in x and y can be found in (Macdonald and Larose, 2006) whereas the torsional terms in the aerodynamic damping matrix is presented in following,

$$\left.\frac{\partial F_\theta}{\partial \dot{z}}\right|_{\dot{z}=0} = \frac{1}{2} D^2 \rho U \left(2 \left.\frac{\partial U_R}{\partial \dot{z}}\right|_{\dot{z}=0} C_M + U \left.\frac{\partial C_M}{\partial \dot{z}}\right|_{\dot{z}=0} \right) \tag{A.5}$$

$$\begin{aligned}\frac{\partial F_x}{\partial \dot{\theta}} = &-\frac{1}{2} R_\delta Re\mu \left(-\frac{cos(\gamma_0)}{sin(\phi_R)} \left(\left(C_L - \frac{dC_D}{d\alpha_R} \right) cos(\psi_R) \right.\right. \\ &\left. + \left(C_D + \frac{dC_L}{d\alpha_R} \right) sin(\psi_R) \right) \\ &+ sin(\gamma_0) \left(cos(\psi_R) \left(\frac{dC_D}{d\phi_R} cos(\phi_R) \right.\right. \\ &\left. + \left(2\, C_D + \frac{dC_D}{dRe_R} Re \right) sin(\phi_R) \right) \\ &\left.\left. - \left(\frac{dC_L}{d\phi_R} cos(\phi_R) + \left(2\, C_L + \frac{dC_L}{dRe_R} Re \right) sin(\phi_R) \right) sin(\psi_R) \right) \right)\end{aligned} \tag{A.6}$$

$$\frac{\partial F_y}{\partial \dot{\theta}} = -\frac{1}{2} R_\delta Re\mu \left(-\frac{cos(\gamma_0)}{sin(\phi_R)} \left(\left(C_L - \frac{dC_D}{d\alpha_R} \right) cos(\psi_R) \right.\right.$$
$$+ \left(C_D + \frac{dC_L}{d\alpha_R} \right) sin(\psi_R) \Bigg)$$
$$+ sin(\gamma_0) \left(cos(\psi_R) \left(\frac{dC_D}{d\phi_R} cos(\phi_R) \right.\right. \tag{A.7}$$
$$+ \left(2\ C_D + \frac{dC_D}{dRe_R} Re \right) sin(\phi_R) \Bigg)$$
$$\left.\left. - \left(\frac{dC_L}{d\phi_R} cos(\phi_R) + \left(2\ C_L + \frac{dC_L}{dRe_R} Re \right) sin(\phi_R) \right) sin(\psi_R) \right) \right)$$

$$\frac{\partial F_\theta}{\partial \dot{x}} = -\frac{1}{2} D\ Re\ \mu \left(\frac{dC_M}{d\phi_R} cos(\phi_R) cos(\psi_R) \right.$$
$$\left. + \left(2\ C_M + \frac{dC_M}{dRe_R} Re \right) cos(\psi_R) sin(\phi_R) - \frac{dC_M}{d\alpha_R} \frac{sin(\psi_R)}{sin(\phi_R)} \right) \tag{A.8}$$

$$\frac{\partial F_\theta}{\partial \dot{y}} = -\frac{1}{2} D\ Re\ \mu \left(\frac{dC_M}{d\alpha_R} \frac{cos(\psi_R)}{sin(\phi_R)} \right.$$
$$\left. + \left(\frac{dC_M}{d\phi_R} cos(\phi_R) + \left(2\ C_M + \frac{dC_M}{dRe_R} Re \right) sin(\phi_R) \right) sin(\psi_R) \right) \tag{A.9}$$

$$\frac{\partial F_\theta}{\partial \dot{\theta}} = -\frac{1}{2} D\ R_\delta Re\mu \left(\frac{dC_M}{d\alpha_R} \frac{cos(\gamma_0)}{sin(\phi_R)} + sin(\gamma_0) \left(\frac{dC_M}{d\phi_R} cos(\phi_R) + \left(2\ C_M + \frac{dC_M}{dRe_R} Re \right) sin(\phi_R) \right) \right) \tag{A.10}$$

Appendix B.

Analytical solution to 6th order eigenvalue problem.

The eigenvalue problem, presented in Eq. (23) leads to a 6th order polynomial, which can be solved analytically by the use of the Routh-Hurwitz stability criterion. The Routh-Hurwitz Criterion can be used in determining if a polynomial of order *n* have all positive or negative real part roots. Using this on an eigenvalue problem gives the solution to where the system is stable or unstable by using the coefficient of the resulting polynomial in the Routh-Hurwitz determinant, for more information on how to use the criterion and calculate the determinant, see (Thomsen, 2003).

$$H_0\lambda^6 + H_1\lambda^5 + H_2\lambda^4 + H_3\lambda^3 + H_4\lambda^2 + H_5\lambda + H_6 \tag{B.1}$$

The Routh-Hurwitz stability criterion states that a system of equations is stable if the “real” parts of all the Routh-Hurwitz coefficients are greater than zero. Applying the Routh-Hurwitz stability criterion results in 13 coefficients (7 from the polynomial, $(H_0 - H_6)$, and 6 from the Hurwitz determinant, $(D_0 - D_5)$). The 13 coefficients are shown here below:

$$H_0 = 1 \tag{B.2}$$

$$\begin{aligned} H_1 = \frac{1}{2Jm_{tot}^2}\big(&2JC_{xx}m_{tot} + 2JC_{yy}m_{tot} + 2C_{\theta\theta}m_{tot}^2 \\ &- 2sin(\gamma_0)(C_{x\theta} + C_{\theta x})L_e m_{tot}^2 - 2cos(\gamma_0)\big(C_{y\theta} + C_{\theta y}\big)L_e m_{tot}^2 \\ &+ 2sin(\gamma_0)^2 C_{xx}L_e^2 m_{tot}^2 + 2cos(\gamma_0)sin(\gamma_0)C_{xy}L_e^2 m_{tot}^2 \\ &+ sin(2\gamma_0)C_{yx}L_e^2 m_{tot}^2 + C_{yy}L_e^2 m_{tot}^2 + cos(2\gamma_0)C_{yy}L_e^2 m_{tot}^2\big) \end{aligned} \tag{B.3}$$

$$\begin{aligned}H_2 = \frac{1}{2Jm_{tot}^2}\big(&-2JC_{xy}C_{yx} - 2C_{x\theta}C_{\theta x}m_{tot} - 2C_{y\theta}C_{\theta y}m_{tot} + 2C_{xx}C_{\theta\theta}m_{tot}\\ &+ 2C_{yy}C_{\theta\theta}m_{tot} + 2cos(\gamma_0)C_{x\theta}C_{yx}L_e m_{tot}\\ &+ 2sin(\gamma_0)C_{xy}C_{y\theta}L_e m_{tot} + 2cos(\gamma_0)C_{xy}C_{\theta x}L_e m_{tot}\\ &- 2sin(\gamma_0)C_{yy}(C_{x\theta} + C_{\theta x})L_e m_{tot} + 2sin(\gamma_0)C_{yx}C_{\theta y}L_e m_{tot}\\ &- 2cos(\gamma_0)C_{xx}\big(C_{y\theta} + C_{\theta y}\big)L_e m_{tot} - 2C_{xy}C_{yx}L_e^2 m_{tot}\\ &+ 2C_{xx}C_{yy}(J + L_e^2 m_{tot}) + 2Jm_{tot}^2\omega_x^2 + L_e^2 m_{tot}^3\omega_x^2 + 2Jm_{tot}^2\omega_y^2\\ &+ L_e^2 m_{tot}^3\omega_y^2 + cos(2\gamma_0)L_e^2 m_{tot}^3\big(-\omega_x^2 + \omega_y^2\big) + 2Jm_{tot}^2\omega_\theta^2\big)\end{aligned} \tag{B.4}$$

$$\begin{aligned}H_3 = \frac{1}{2Jm_{tot}^2}\big(&-2C_{x\theta}C_{yy}C_{\theta x} + 2C_{xy}C_{y\theta}C_{\theta x} + 2C_{x\theta}C_{yx}C_{\theta y} - 2C_{xx}C_{y\theta}C_{\theta y}\\ &- 2C_{xy}C_{yx}C_{\theta\theta} + 2C_{xx}C_{yy}C_{\theta\theta} + 2JC_{yy}m_{tot}\omega_x^2 + 2C_{\theta\theta}m_{tot}^2\omega_x^2\\ &- 2cos(\gamma_0)\big(C_{y\theta} + C_{\theta y}\big)L_e m_{tot}^2\omega_x^2 + 2C_{yy}L_e^2 m_{tot}^2\omega_x^2\\ &+ 2C_{\theta\theta}m_{tot}^2\omega_y^2 - 2sin(\gamma_0)(C_{x\theta} + C_{\theta x})L_e m_{tot}^2\omega_y^2\\ &+ 2C_{xx}m_{tot}(J + L_e^2 m_{tot})\omega_y^2 + 2JC_{xx}m_{tot}\omega_\theta^2 + 2JC_{yy}m_{tot}\omega_\theta^2\big)\end{aligned} \tag{B.5}$$

$$\begin{aligned}H_4 = \frac{1}{2Jm_{tot}^2}\big(&-2C_{y\theta}C_{\theta y}m_{tot}\omega_x^2 + 2C_{yy}C_{\theta\theta}m_{tot}\omega_x^2 - 2C_{x\theta}C_{\theta x}m_{tot}\omega_y^2\\ &+ 2C_{xx}C_{\theta\theta}m_{tot}\omega_y^2 + 2Jm_{tot}^2\omega_x^2\omega_y^2 + 2L_e^2 m_{tot}^3\omega_x^2\omega_y^2\\ &- 2JC_{xy}C_{yx}\omega_\theta^2 + 2JC_{xx}C_{yy}\omega_\theta^2 + 2Jm_{tot}^2\omega_x^2\omega_\theta^2 + 2Jm_{tot}^2\omega_y^2\omega_\theta^2\big)\end{aligned} \tag{B.6}$$

$$\begin{aligned}H_4 = \frac{1}{2Jm_{tot}^2}\big(&-2C_{y\theta}C_{\theta y}m_{tot}\omega_x^2 + 2C_{yy}C_{\theta\theta}m_{tot}\omega_x^2 - 2C_{x\theta}C_{\theta x}m_{tot}\omega_y^2\\ &+ 2C_{xx}C_{\theta\theta}m_{tot}\omega_y^2 + 2Jm_{tot}^2\omega_x^2\omega_y^2 + 2L_e^2 m_{tot}^3\omega_x^2\omega_y^2\\ &- 2JC_{xy}C_{yx}\omega_\theta^2 + 2JC_{xx}C_{yy}\omega_\theta^2 + 2Jm_{tot}^2\omega_x^2\omega_\theta^2 + 2Jm_{tot}^2\omega_y^2\omega_\theta^2\big)\end{aligned} \tag{B.7}$$

$$H_5 = \frac{1}{2Jm_{tot}^2}\big(2C_{\theta\theta}m_{tot}^2\omega_x^2\omega_y^2 + 2JC_{yy}m_{tot}\omega_x^2\omega_\theta^2 + 2JC_{xx}m_{tot}\omega_y^2\omega_\theta^2\big) \tag{B.8}$$

$$H_6 = \omega_x^2\omega_y^2\omega_\theta^2 \tag{B.9}$$

Eq. (B.10) - (B.15) presents the 6 Hurwitz determinants where as Eq. (B.16) - (B.21) shows the 6 determinates written out in full length.

$$D_0 = |H_1| \tag{B.10}$$

$$D_1 = \begin{vmatrix} H_1 & H_0 \\ H_3 & H_2 \end{vmatrix} \tag{B.11}$$

$$D_2 = \begin{vmatrix} H_1 & H_0 & 0 \\ H_3 & H_2 & H_1 \\ H_5 & H_4 & H_3 \end{vmatrix} \tag{B.12}$$

$$D_3 = \begin{vmatrix} H_1 & H_0 & 0 & 0 \\ H_3 & H_2 & H_1 & H_0 \\ H_5 & H_4 & H_3 & H_2 \\ 0 & H_6 & H_5 & H_4 \end{vmatrix} \tag{B.13}$$

$$D_4 = \begin{vmatrix} H_1 & H_0 & 0 & 0 & 0 \\ H_3 & H_2 & H_1 & H_0 & 0 \\ H_5 & H_4 & H_3 & H_2 & H_1 \\ 0 & H_6 & H_5 & H_4 & H_3 \\ 0 & 0 & 0 & H_6 & H_5 \end{vmatrix} \tag{B.14}$$

$$D_5 = \begin{vmatrix} H_1 & H_0 & 0 & 0 & 0 & 0 \\ H_3 & H_2 & H_1 & H_0 & 0 & 0 \\ H_5 & H_4 & H_3 & H_2 & H_1 & H_0 \\ 0 & H_6 & H_5 & H_4 & H_3 & H_2 \\ 0 & 0 & 0 & H_6 & H_5 & H_4 \\ 0 & 0 & 0 & 0 & 0 & H_6 \end{vmatrix} \tag{B.15}$$

$$D_0 = H_1 \tag{B.16}$$

$$D_1 = H_1H_2 - H_0H_3 \tag{B.17}$$

$$D_2 = H_1H_2H_3 - H_0H_3^2 \tag{B.18}$$

$$D_3 = H_1H_2H_3H_4 - H_0H_3^2H_4 - H_1^2H_4^2 \tag{B.19}$$

$$\begin{aligned} D_4 = {} & H_1H_2H_3H_4H_5 - H_0H_3^2H_4H_5 - H_1^2H_4^2H_5 - H_1H_2^2H_5^2 + H_0H_2H_3H_5^2 \\ & + 2H_0H_1H_4H_5^2 - H_0^2H_5^3 \end{aligned} \tag{B.20}$$

$$\begin{aligned} D_5 = {} & H_1H_2H_3H_4H_5H_6 - H_0H_3^2H_4H_5H_6 - H_1^2H_4^2H_5H_6 - H_1H_2^2H_5^2H_6 \\ & + H_0H_2H_3H_5^2H_6 + 2H_0H_1H_4H_5^2H_6 - H_0^2H_5^3H_6 - H_1H_2H_3^2H_6^2 \\ & + H_0H_3^3H_6^2 + H_1^2H_3H_4H_6^2 + 2H_1^2H_2H_5H_6^2 - 3H_0H_1H_3H_5H_6^2 \\ & - H_1^3H_6^3 \end{aligned} \tag{B.21}$$

8. References

Blevins, R. D. (1994). Flow-Induced Vibration, Krieger.

Chabart, O. and J. L. Lilien (1998). "Galloping of electrical lines in wind tunnel facilities." Journal of Wind Engineering and Industrial Aerodynamics **74-6**: 967-976.

Davenport, A. G. (1962). "Buffeting of suspension bridge by storm winds." American Society of Civil Engineers -- Proceedings **88**: 233-268.

Griffiths, P., B. Curry, et al. (2006). "Galloping analysis of the Severn Crossing Conductor in skew winds.".

Hartog, J. P. D. (1932). "Transmission-Line Vibration Due to Sleet." Institute of Electrical Engineers **51**: 1074-1086.

Macdonald, J. H. G. and G. L. Larose (2006). "A unified approach to aerodynamic damping and drag/lift instabilities, and its application to dry inclined cable galloping." Journal of Fluids and Structures **22**(2): 229-252.

Macdonald, J. H. G. and G. L. Larose (2008a). "Two-degree-of-freedom inclined cable galloping--Part 1: General formulation and solution for perfectly tuned system." Journal of Wind Engineering and Industrial Aerodynamics **96**(3): 291-307.

Macdonald, J. H. G. and G. L. Larose (2008b). "Two-degree-of-freedom inclined cable galloping--Part 2: Analysis and prevention for arbitrary frequency ratio." Journal of Wind Engineering and Industrial Aerodynamics **96**(3): 308-326.

Martin, W. W., I. G. Currie, et al. (1981). "Streamwise oscillations of cylinders." Journal of the Engineering Mechanics Division-Asce **107**(3): 589-607.

Nakamura, Y. and T. Mizota (1975). "TORSIONAL FLUTTER OF RECTANGULAR PRISMS." Journal of the Engineering Mechanics Division-Asce **101**(NEM2): 125-142.

Thomsen, J. J. (2003). Vibrations and Stability, Springer.

Washizu, K., A. Ohya, et al. (1978). "Aeroelastic instability of rectangular cylinders in a heaving mode." Journal of Sound and Vibration **59**(2): 195-210.

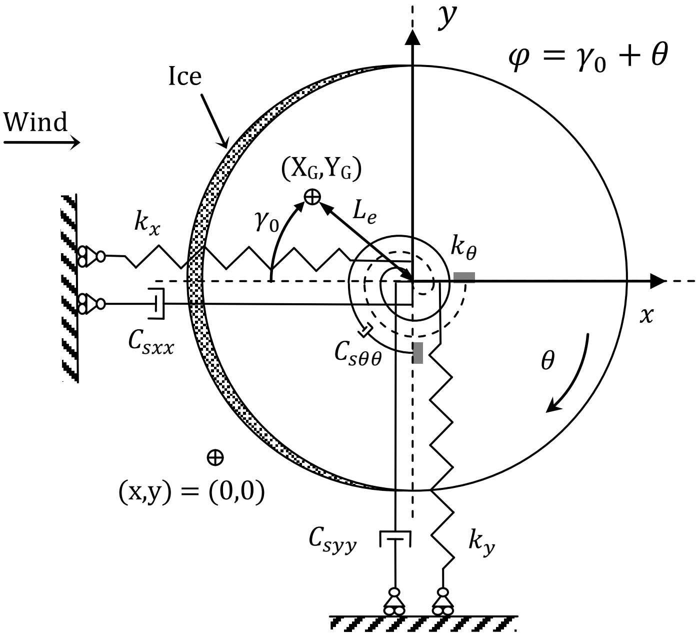
y
$\varphi = \gamma_0 + \theta$
Ice
Wind
(X_G, Y_G)
k_x
γ_0
L_e
k_θ
x
C_{sxx}
$C_{s\theta\theta}$
θ
$(x,y) = (0,0)$
C_{syy}
k_y

x = displacement direction.

y = displacement direction.

θ = rotation direction.

γ_0 = angle offset for mass centre.

L_e = mass centre offset.

k_x = structural stiffness in x direction.

k_y = structural stiffness in y direction.

k_θ = structural stiffness in θ direction.

C_{sxx} = structural damping in x direction.

C_{syy} = structural damping in y direction.

$C_{s\theta\theta}$ = structural damping in θ direction.

(X_G, Y_G) = mass centre.

Figure 1. Definition of 3-DOF section-based dynamic system.

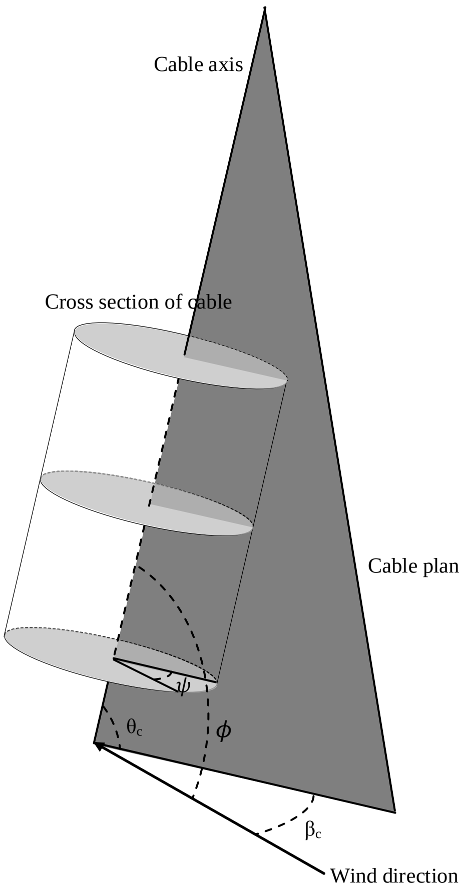
Cable axis
Cross section of cable
Cable plan
ψ
θ_c
ϕ
β_c
Wind direction

θ_c = cable inclination angle

$\psi = \alpha_0 + \theta$.

ϕ = wind angle of attack, cable length axis.

(cable/wind plan).

β_c = wind/cable yaw angle

$\cos(\phi) = \cos(\beta_c)\cos(\theta_c)$.

Figure 2. Angle definition for inclined cable.

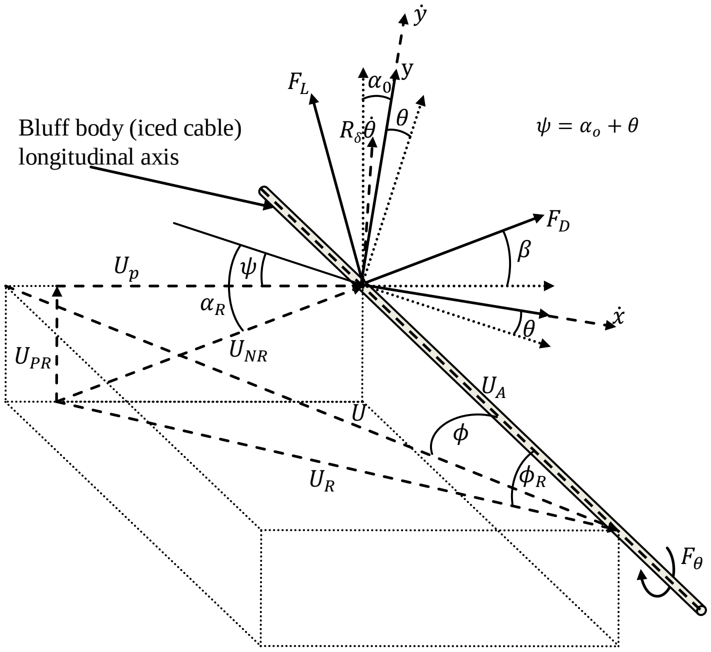
$\dot{y}$
y
F_L
α_0
θ
Bluff body (iced cable)
longitudinal axis
$R_\delta \dot{\theta}$
$\psi = \alpha_o + \theta$
F_D
β
U_p
ψ
α_R
θ
$\dot{x}$
U_{NR}
U_{PR}
U_A
U
ϕ
ϕ_R
U_R
F_θ

$x_\theta, \dot{x}_\theta$ = displacement, velocity.

$y_\theta, \dot{y}_\theta$ = displacement, velocity.

α_0 = steady wind angle of attack

$\theta, \dot{\theta}$ = structural rotation, angular velocity.

α_R = wind angle of attack, cable surface.

β = angle of rotation, relative wind.

ϕ = wind angle of attack, cable length axis.

F_L = lift force.

F_D = drag force.

F_θ = moment force.

R_δ = length determining rotational velocity.

U = mean wind velocity.

U_R = relative wind velocity.

U_{PR} = projected relative vertical wind velocity.

U_p = projected relative horizontal wind velocity.

U_{NR} = normal projected relative wind velocity.

U_A = along axis wind velocity.

$\psi = \alpha_o + \theta$

Figure 3. Schematic model of cable section with ice accretion.

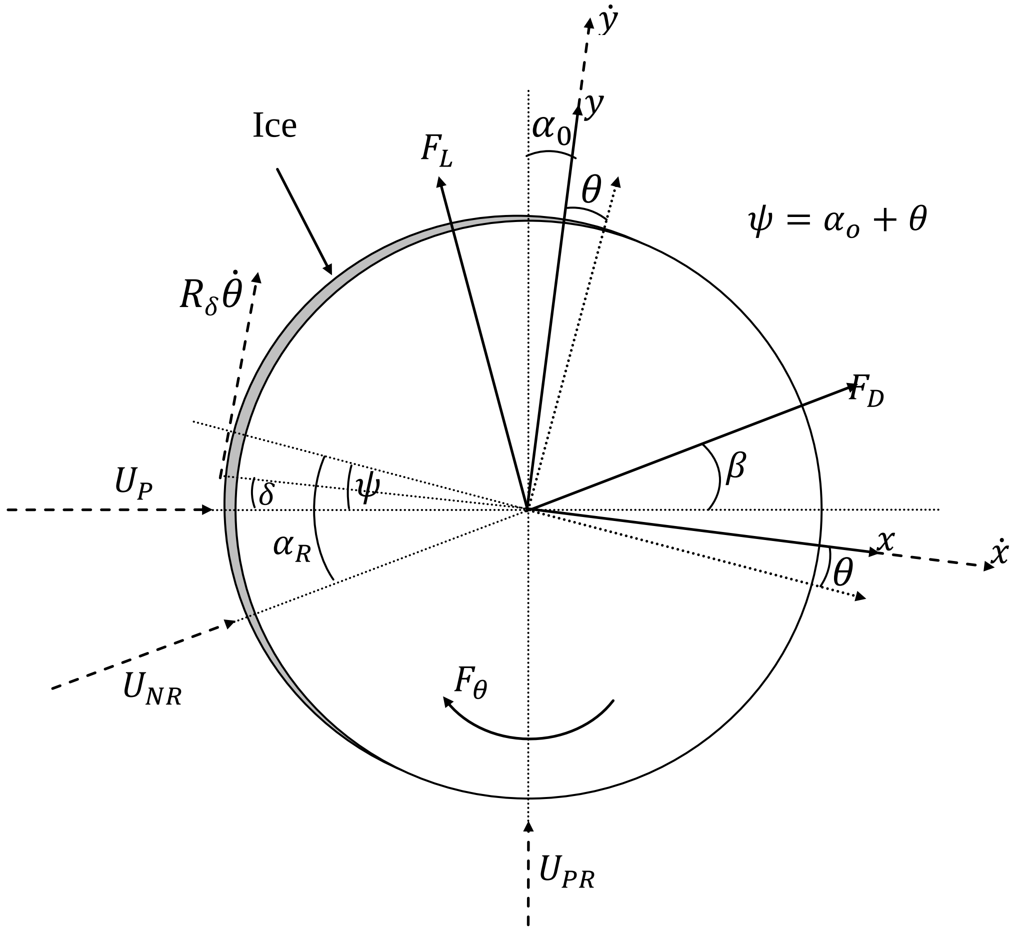
$\dot{y}$
y
α_0
θ
Ice
F_L
$\psi = \alpha_o + \theta$
$R_\delta\dot{\theta}$
F_D
β
U_P
δ
ψ
α_R
x
$\dot{x}$
θ
U_{NR}
F_θ
U_{PR}

Figure 4. Analytical model of cable section with ice accretion.$R_\delta$is only shown as the total radius as illustratively, but is in fact a variable length depending on the geometry.

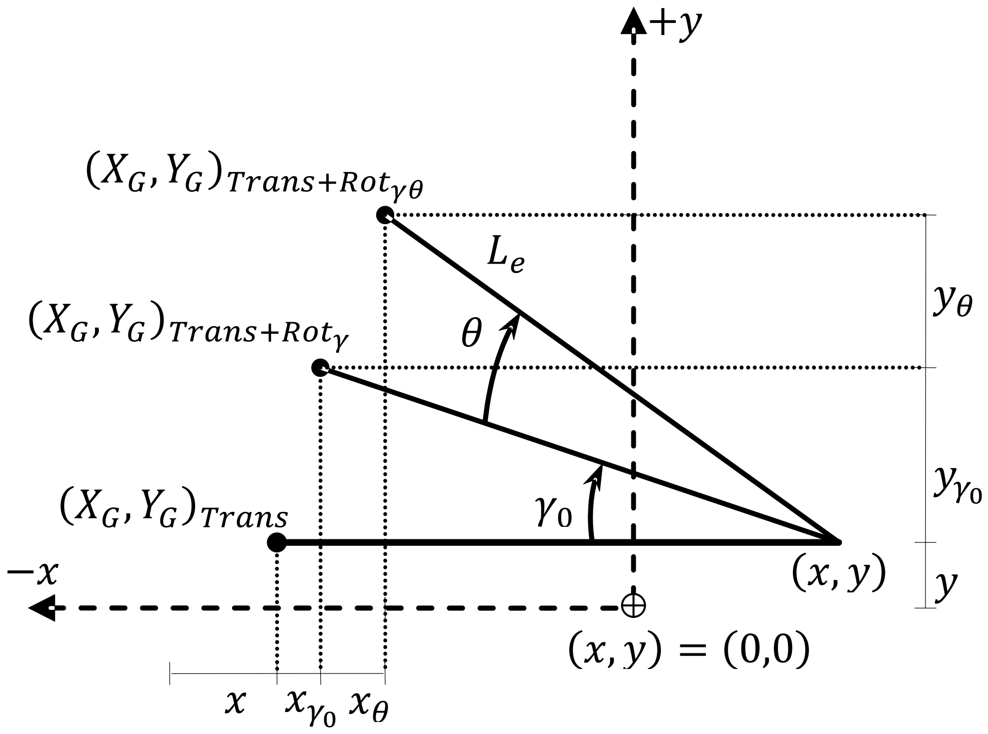
$+y$
$(X_G, Y_G)_{Trans+Rot_{\gamma\theta}}$
L_e
y_θ
$(X_G, Y_G)_{Trans+Rot_{\gamma}}$
θ
y_{γ_0}
$(X_G, Y_G)_{Trans}$
γ_0
$-x$
(x, y)
y
$(x, y) = (0,0)$
x
x_{γ_0}
x_θ

Figure 5. Definition of mass centre coordinates. $(X_G, Y_G)_{Trans}$= displacement in relation to translation in x and y. $(X_G, Y_G)_{Trans+Rot_{\gamma\theta}}$= displacement in relation to translation in x and y and rotation about the structural axis.

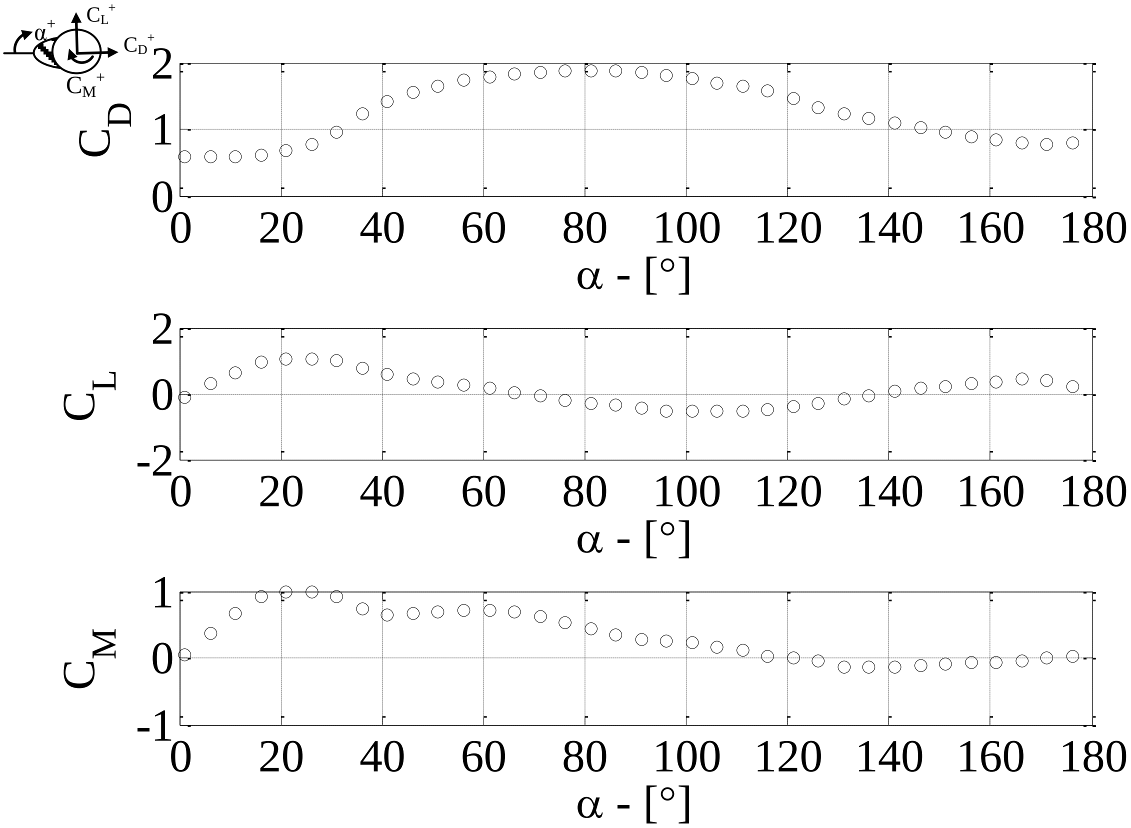

Figure 6. Aerodynamic force coefficients for a iced cable, (Chabart and Lilien, 1998)

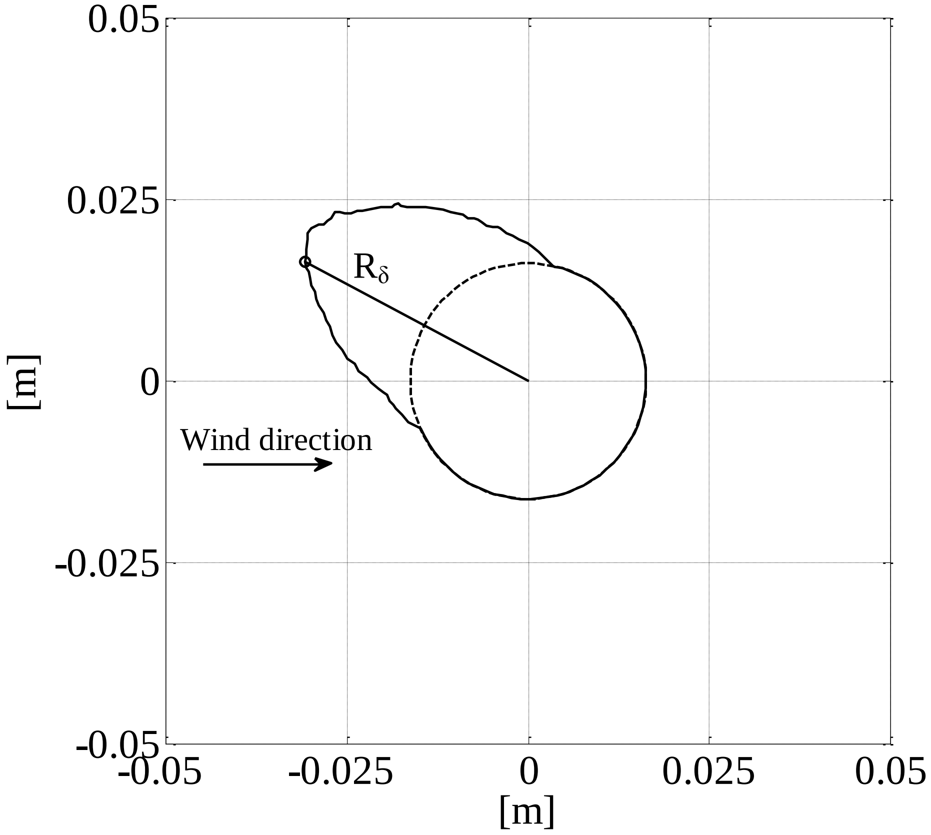

Figure 7. Iced cable with radial length R_δ to the leading edge.

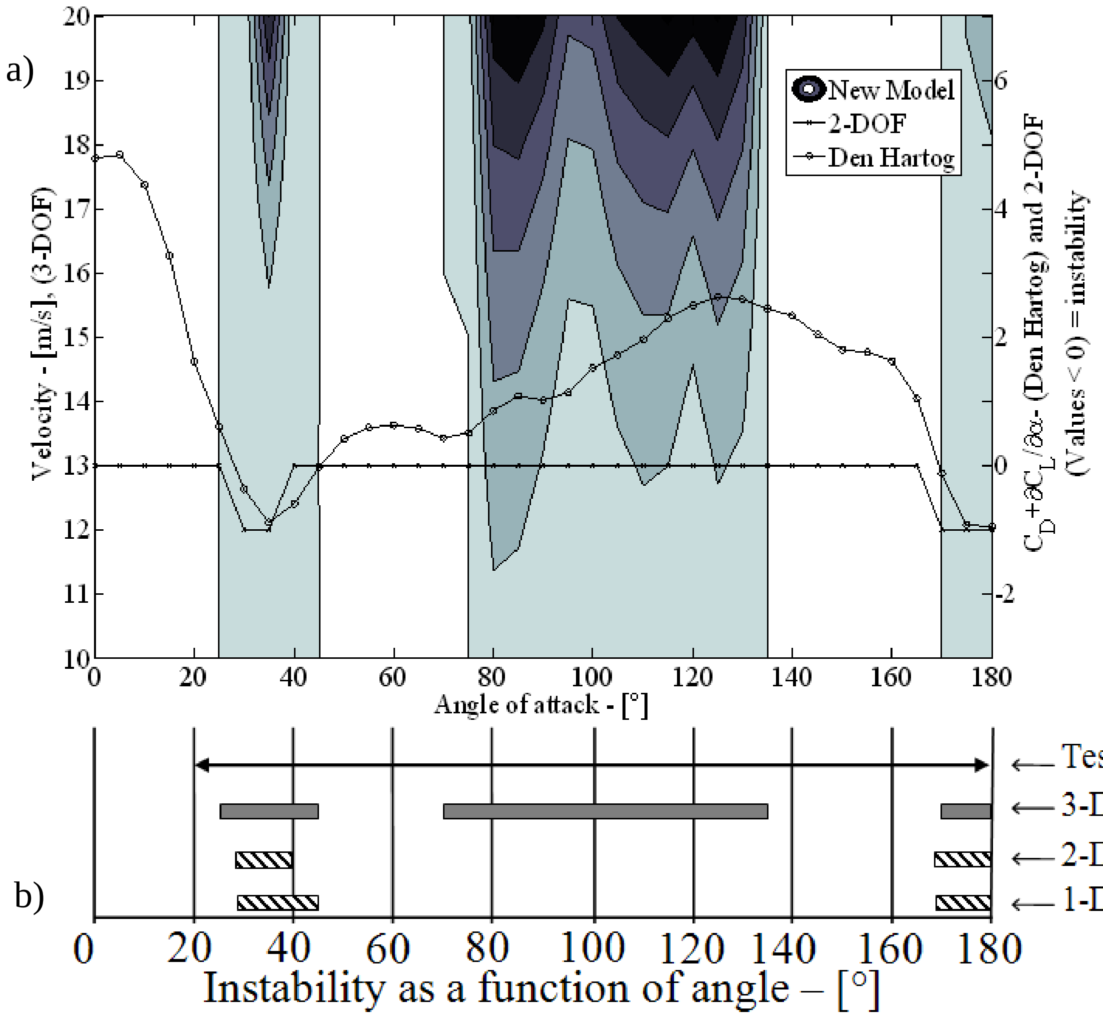

Figure 8. a) Range of predicted instability for the combined Drag, Lift and moment. b) Comparison of experimental found instability with Den Hartog(1-DOF), 2-DOF and the 3-DOF model. Results from test case is obtain from previous made experiments, (Chabart and Lilien, 1998).

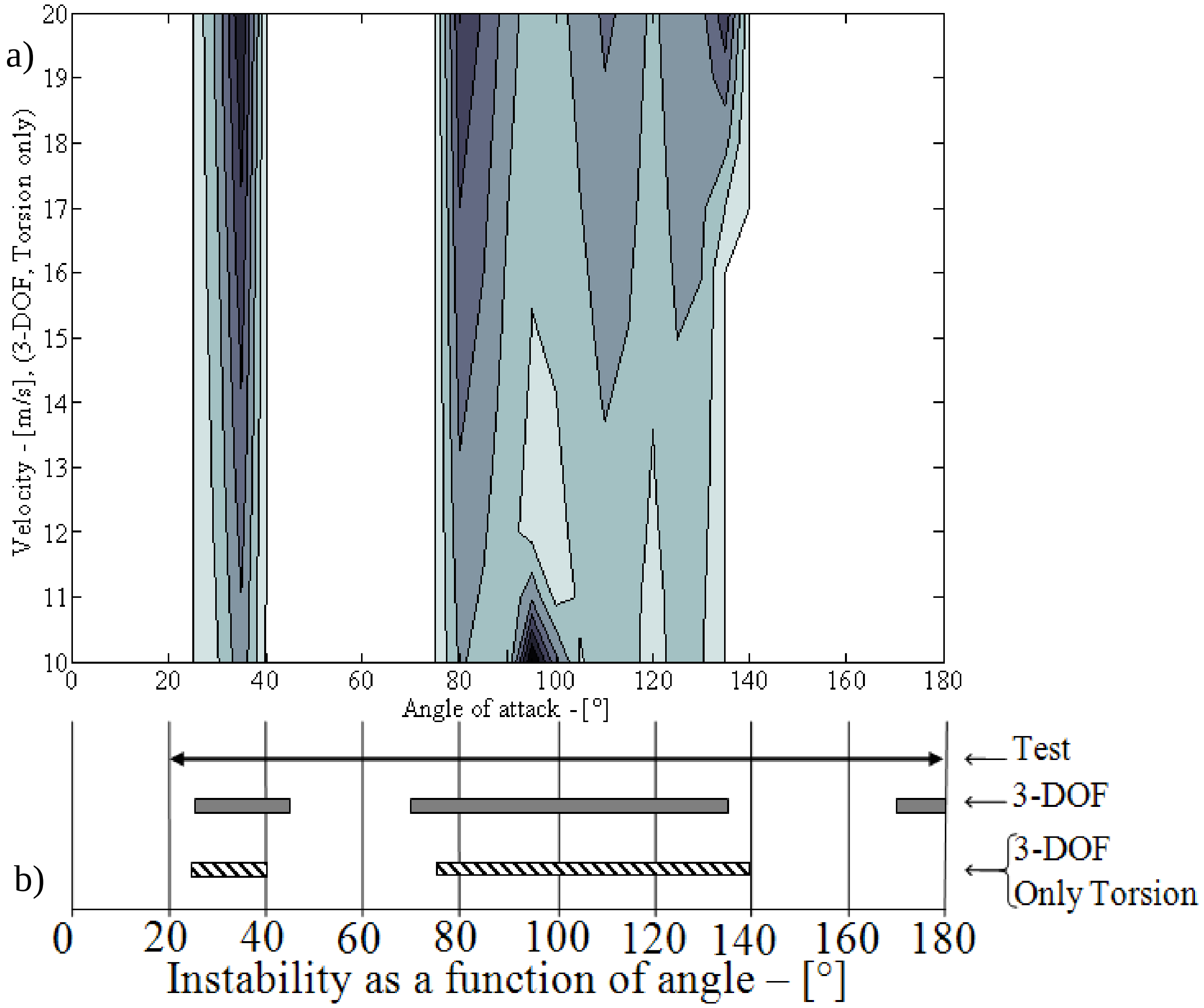

Figure 9. a) Range of predicted instability for the moment. b) Comparison of experimental found instability with the 3-DOF model and only torsion from the 3-DOF model. Results from test case is obtain from previous made experiments, (Chabart and Lilien, 1998).

Table 1 Structural and aerodynamic parameters for example iced-cable

Variables	Value	Units	Description
f_x	0.995	[Hz]	x-direction frequency.
f_y	0.845	[Hz]	y-direction frequency.
f_θ	0.865	[Hz]	θ-direction frequency.
D	0.0325	[m]	Cable diameter.
L_e	0.0025	[m]	Length to mass centre.
m	2.99	[kg/m]	Total mass of iced cable section.
J	4.9689e-4	[kg*m^2]	Rotational inertia in relation to the models mass centre.
ρ	1.292	[kg/m^3]	Air density.
$\zeta_{x,y}$	0.08	[%]	% damping of critical
ζ_θ	0.3	[%]	% damping of critical
ϕ	π/2	[rad]	Wind angle of attack, cable length axis
γ_0	0	[°]	Angle offset for the mass centre.

Paper II ([47])

“Experimental study of icing at high temperature and low wind velocities on circular cylinders of different diameter and orientation”

H. Gjelstrup, C.T. Georgakis & H. Koss

Unsubmitted manuscript

Experimental study of icing at high temperature and low wind velocities on circular cylinders of different diameter and orientation

H. Gjelstrup[1*×], C.T. Georgakis[×], H. Koss[×]

[*]*COWI A/S, Parallelvej 2, 2800 Kgs. Lyngby , Denmark*

[×]*Department of Civil Engineering, Technical University of Denmark, Building 118, Brovej, 2800 Kgs. Lyngby , Denmark*

Abstract

An experimental investigation on icing of non-rotating cylinders simulating ice bridge hangers is undertaken in this paper. This paper focus on experiments performed at temperatures between -5ºC and -1ºC and wind velocities between 10m/s to 30m/s. The additional parameters ranges from a small range of Liquid Water Content (LWC), Droplet size, and accretion time applied on two circular cylinder of different diameter, namely a small cylinder with a diameter of 3.81cm and a large cylinder with a diameter of 8.9cm. A total of 46 test was performed in this investigation and several ice accretions coefficients is defined in order to perform an analysis of the obtain results, where the analysis ranges from symmetry around the stagnation line, stagnation line ice growth, horn location and accreted ice as a function of time, LWC, temperature and droplet size. Through the analysis, it is shown that for low exposure times the ice accretion mass and stagnation line growth is not linear, that the symmetry of the ice accretion is low at higher temperatures and the horn location seems to be a linear function of temperature.

---

[1] Corresponding author. Tel.: +45 45972805/ +45 45251940; Fax: +45 45972212/ +45 45883282

E-mail address: hegj@cowi.dk/heg@byg.dtu.dk; (COWI/DTU)

Keywords: Wind tunnel tests, circular cylinder, bridge hangers, ice accretion, motional instability, low temperatures, quasi-steady aerodynamics

Introduction

While many structures and geometries have, ice problems it seems that icing of at cylinder remains a basic research geometry due to the well define problem. Papers on icing of a round cylinder have been published in the past, but mostly concentrating on icing of cylinders in high wind velocities 30m/s and up, and likewise in low temperatures of -5°C and down, (Anderson et al., 1998; Hansman et al., 1993; Lozowski et al., 1983a; Lozowski et al., 1983b). Little research has been performed on cylinders at temperatures of -5°C and up and wind velocities from 30m/s and down.

In the present literature, shapes of ice accreting on the surface of power lines or other circular structures are reported. However, the meteorological conditions for theses reported cases (Dalle and Admirat; McComber and Paradis, 1995; Nigol and Buchan, 1981; Nigol and Clarke, 1974; Nigol, 1981; Phuc, 2005; Shimizu, 2005), differ from the situations where large cable vibrations have been reported from large-span bridges. Recently bridges owners have shown interest in icing of bridge hangers/stays for a temperature range of -5°C to -1°C and wind velocities of 30m/s and down. This is due to observations of vibrating cables with a thin ice accretion where several cases has been reported and some results has been published, (Gjelstrup et al., 2007). Gjelstrup et al. talks about the possible effect of thinly iced vertical hangers on one of the world larges suspension bridges, The Great Belt Bridge. Figure 1 shows two pictures of iced bridge cables (A) shows a iced main cable, unfortunately no information about vibration or the metrological condition is available for this case of cable icing. (B) shows a thinly iced vertical hanger, which was observed during a vibration event.

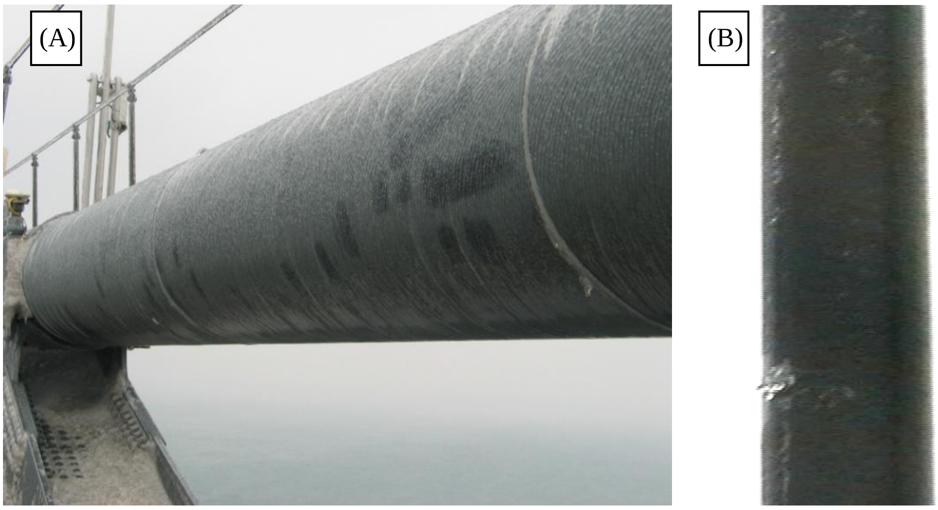

Figure 1 Iced bridge cables (A) Iced main cable, (B) Iced vertical hanger.

The amplitude of the observed bridge hanger vibrations was measured to about 2 m on a 168 meter long twin hanger with a diameter of 0.11 meter of each hanger and a spacing of 5.4 cable diameters, Figure 2. The vibration event observed with the vertical iced bridge hanger shown in (B) has initiated a series of investigations into the cause of the vibration, (Gjelstrup and Georgakis, 2009; Gjelstrup et al., 2007). This paper is a continuation of these investigations and the results will is used in submitted papers on the topic of iced cables (Gjelstrup and Georgakis, 2010; Gjelstrup et al., 2010).

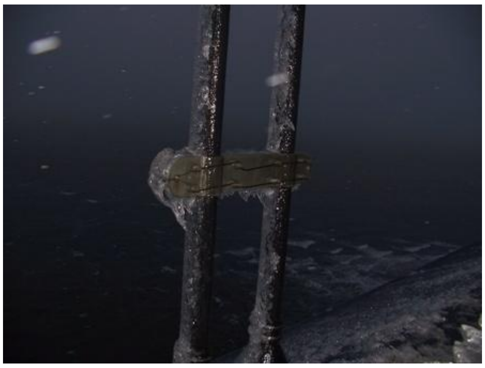

Figure 2 Iced twin hanger

The experiment describe in this paper focus on temperatures between -5ºC and -1ºC and wind velocities between 10m/s to 30m/s. The additional parameters ranges from a small range of Liquid Water content (LWC), Droplet size, and accretion time applied on two circular cylinder of different diameter, namely a small cylinder with a diameter of 3.81cm and a large cylinder with a diameter of 8.9cm. The cylinders were both tested in a horizontal and vertical position and were both made of aluminum.

Wind tunnel used for creating ice shapes

The ice accretion tests were performed at the National Research Council (NRC) Institute for Aerospace Research Altitude Icing Wind Tunnel Facility (AIWT) in Ottawa. The AIWT has a test section of 0.57mx0.57m, and the overall design and capability of the facility is described in detail in (Oleskiw et al., 2001). Figure 3 shows an illustrative sketch of the wind tunnel at NRC.

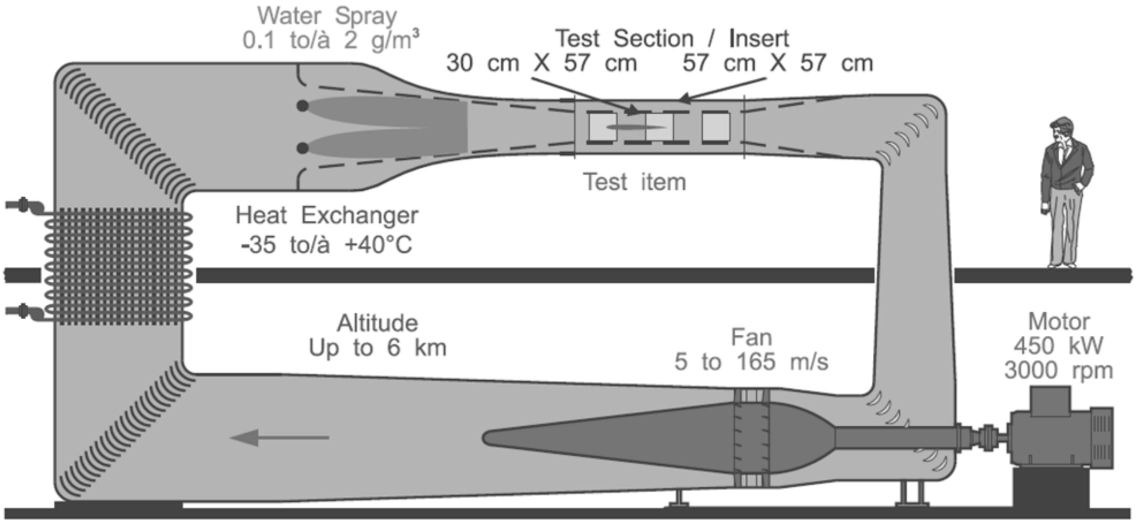
Water Spray
0.1 to/à 2 g/m³
Test Section / Insert
30 cm X 57 cm
57 cm X 57 cm
Test item
Heat Exchanger
-35 to/à +40°C
Altitude
Up to 6 km
Fan
5 to 165 m/s
Motor
450 kW
3000 rpm

Figure 3 Principle sketch of the high-altitude icing wind tunnel at NRC, (Oleskiw et al., 2001).

Setup at Test Section

The experimental setup of the tests is in essence described in Figure 4, which shows a cylinder mounted horizontally in the wind tunnel. Two cylinders with different diameter were tested under different conditions and orientation. The icing of the cylinders was recorded by two fixed mounted cameras, which were a mini-cam on the near side and a video camera on the far side of the test section. Additionally, some tests have been recorded with one movable high definition camera mounted on a tripod.

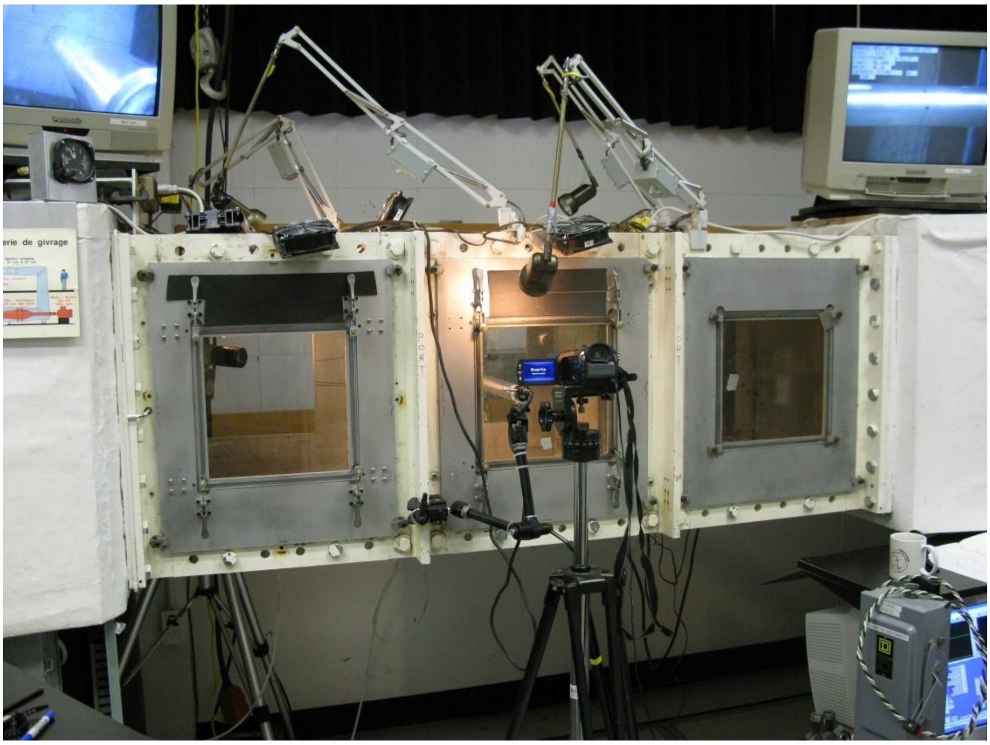

Figure 4 Outside view on the test section of the high-altitude icing wind tunnel. The flow is from the left to the right. Access to the inside was for the performed tests through the left window.

The two cylinders were mounted horizontal and vertical in the wind tunnel were Figure 5 shows the small cylinder mounted horizontal, whereas Figure 6 shows the small cylinder in the vertical position. The large cylinder was mounted likewise in the wind tunnel.

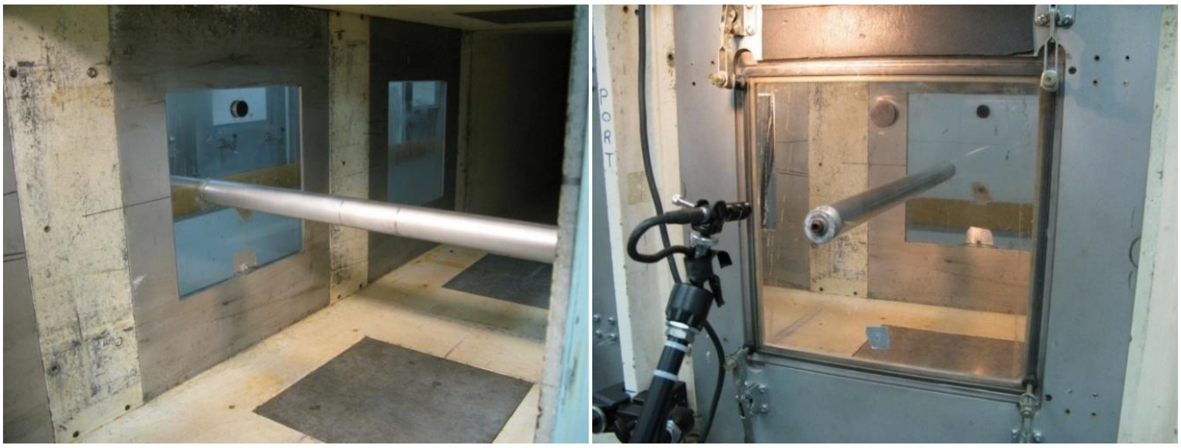

Figure 5 Arrangement of horizontally mounted small cylinder in the test section centre.

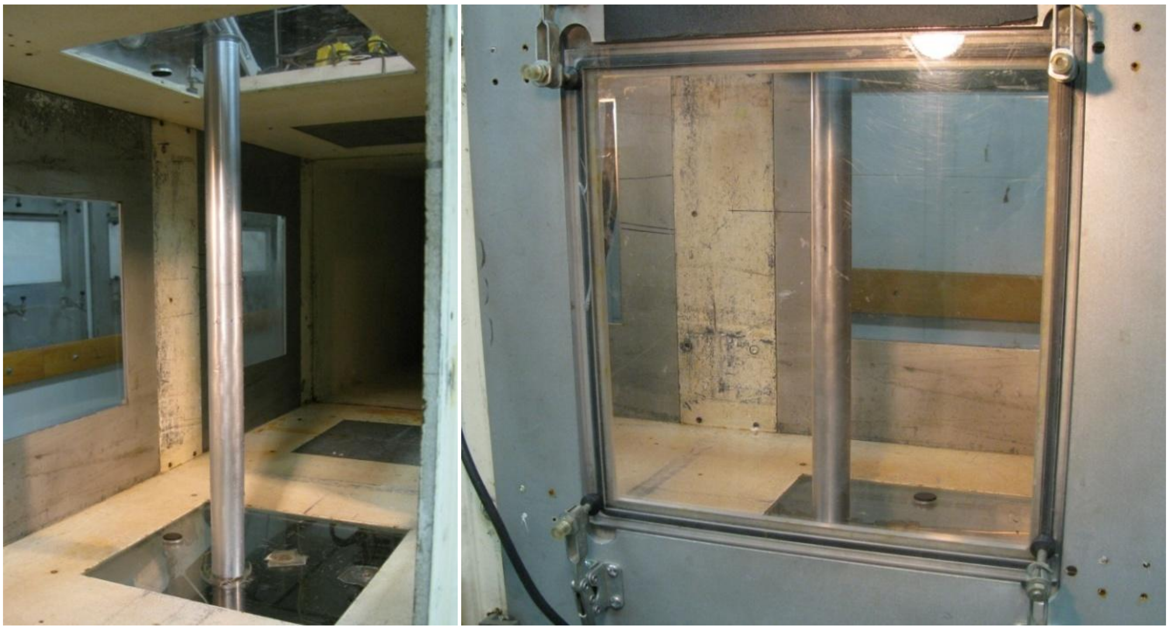

Figure 6 Arrangement of vertically mounted small cylinder in the test section centre.

The blockage and projected areas perpendicular to the flow for the two cylinder used in the experiments are listed in Table 1.

Table 1
Desrpition of mountings in the wind tunnel

Item	projected area perpendicular to flow			blockage $A_i/A_{section}$		
Test section cross-sectional area:	$A_{section}$	=	3249cm^2		-	
Small cylinder:	A_{small}	=	217.17cm^2	S_1	=	6.7%
Large cylinder:	A_{large}	=	507.3cm^2	S_2	=	15.6%

For the large cylinder, a blockage of 15.6% was obtained and should be taken into consideration when using the data.

Documenting the Ice Accretions

Identifying the shape of the icing was done by cutting the ice surface with a warm metal plate at two positions for the small cylinder but only one cut for the large cylinder. For the small cylinder one cut was made at the centre of the cylinder, length wise, and another cut near the ¼ point from the wall. This was done to document the gradient of change in the ice accretion in relation to the length axis. For the large cylinder, the one cut was made at the centre lengthwise.

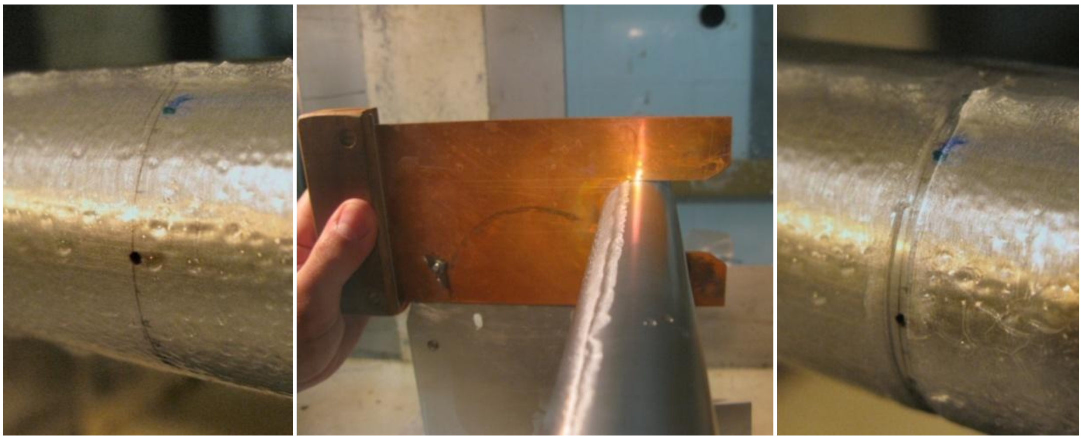

Figure 7 Series of pictures showing the cutting procedure.

To prevent water from melting and from running down the test specimen when cutting the ice accretion with the warm blade, compressed air is blown over the cut area. This fixation procedure has some side effects where one of the side effects is that the ice accretion might develop some cracks. This effect only changes the optical appearance of the ice accretion and leaves no changes to the outer shape of the ice accretion. Another side effect is that the air blast might blow away parts of the outer ice accretion layer. This is due to the temperature range in which the tests were performed. The high end of this temperature range (-1ºC or -2ºC) causes the ice accretions to develop inhomogeneous regions with respect to solid ice and liquid water phases. Another effect at theses high temperatures is that tracing the ice accretion is practical impossible because the pen-device used in tracing the surface structure of the ice accretion melts the ice, as soon there is contact with the ice surface. In order to trace the ice accretion for experiments performed at temperatures of -1ºC or -2ºC, which often leaves the outer layer wet (liquid outer layer), the surface shape is fixed by lowering the air temperature below -4ºC. This result in the freezing of the liquid phase but for some cases the liquid phase does not attach completely to the harder core of ice below. The above mention fixation procedure using compressed air might blow this outer layer away, revealing the presence of a liquid outer layer at the end of the testing time. For illustration of the above described phenomena, see Figure 8(A-B), where A is showing the cracks and B is showing the pealing of the outer layer of ice.

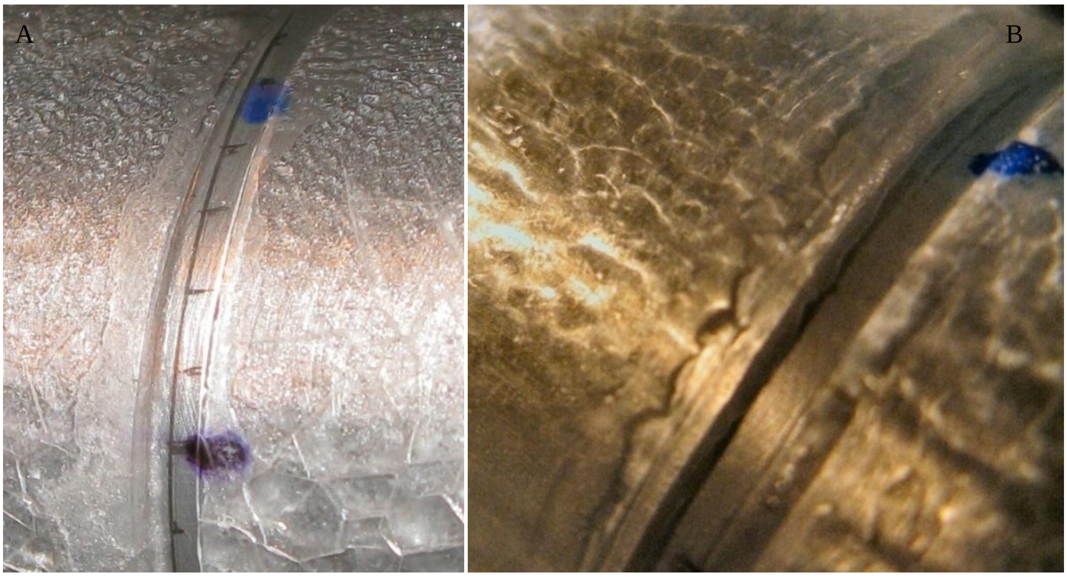

Figure 8 A) Cooling shock effect of the air blast (picture taken from Test #6). B) Effects of air blast, outer layer blowed off (picture taken from Test #14).

The shapes of the ice are copied to paper by tracing the surface of the ice pen, Figure 9. By tracing the surface of the ice accretion by this method, some of the fine surface details, especially with respect to roughness characteristics, are lost. The max resolution of the traced ice roughness is determined by the size of the used pen-devise, which in this case is 0.5mm. Furthermore, the tracing is also affected by the documenting person's drawing skills, which also introduce a variation from surface tracing to surface tracing.

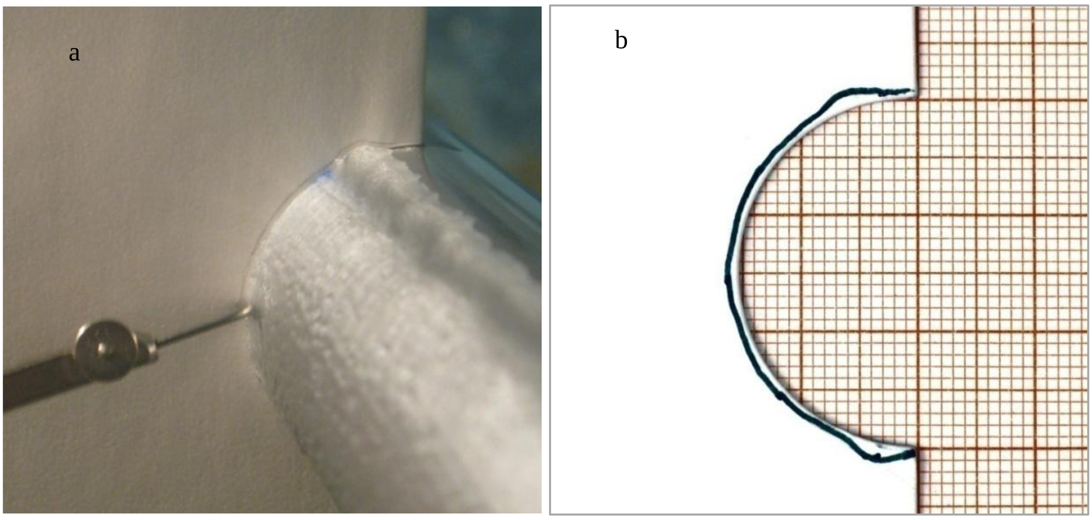

Figure 9 a) The diameter of the pen-device holder induced an offset of the tracing line from the true surface. The angle of the holder tip in relation to cylinder surface parallel to its axis induces further inaccuracies. b) Trace from the ice accretion shown in a). The line has been manually enhanced for better contrast. **Note:** the paper is scaled in inches.

Some ice accretions show a significant three-dimensional characteristic, Figure 10. For example, large ice crystal formation at the accretion area edge can be local and discontinuous. This feature will only be reflected by the above mentioned method of tracing to a limited degree, even if several cuts and tracings are performed. In future experiments it would be preferable to examine other tracing techniques, which could capture the three-dimensional characteristics of the ice accretion and improve the resolution of the trace.

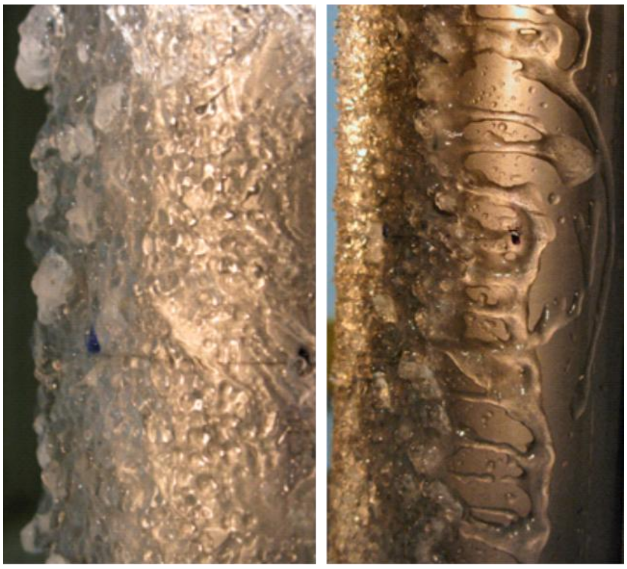

Figure 10 Example of trhree-dimensional characteristic along the length axis(Test 39).

Application of Circumferential Scale

For better evaluation and description of the evolution of water accumulation and ice accretion a circumferential scale was applied on the cylinders surface, where the steps is spaced with 10°. The Stagnation point (0º) and maximum lateral perimeter (±90º) are marked with a black dot. The 45º position was marked with a blue dot (Figure 11).

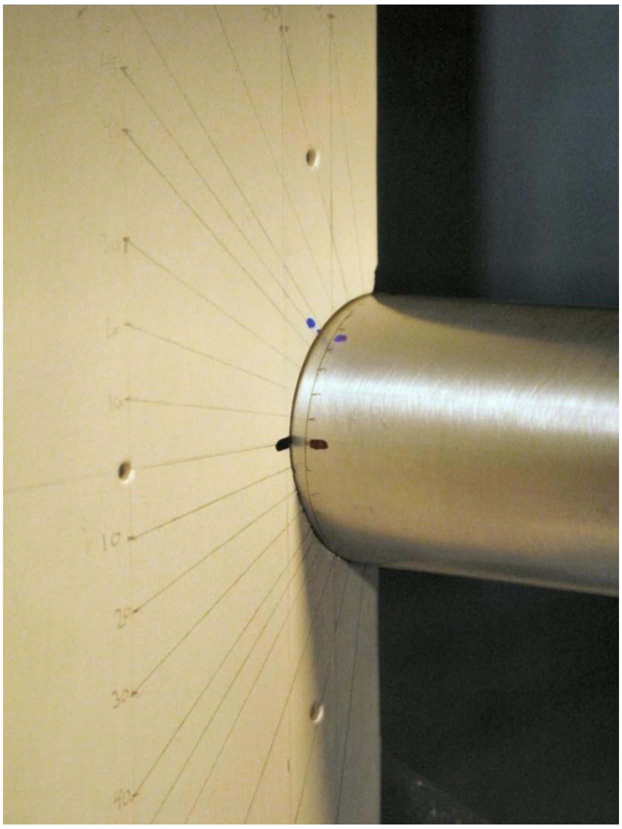

Figure 11 Cardboard with degree scale and applied scale on the small cylinder. Similar scale was applied on the large cylinder as well.

Test program

The test program was setup to look at temperatures of -1°C to -5°C, and wind velocities of 10m/s, 20m/s and 30m/s. These two parameter was then varied by length of exposure time, cylinder diameter, cylinder orientation and water droplet size. Forty-six tests were made in total and the complete test program is listed in Table 2.

Table 2
Listing of all test performed at NRC. # = test number, LWC = Liquid water content, U = wind velocity, DS = water Droplet Size, T_{air} = temperature of air, Time = exposure time for the cylinder to the water spray, Dia. = Diameter of the cylinder in the test and Orie.= The orientation of the cylinder, Horizontal(H) and Vertical(V)

#	LWC	U	DS	T_{air}	Time	Dia.	Pos.
[-]	[-]	[m/s]	[μm]	[ºC]	[min]	[mm]	[-]
1	0.4	10	50	-5	15	3.81	H
2	0.4	10	50	-5	10	3.81	H
3	0.4	10	30	-5	10	3.81	H
4	0.4	10	10	-5	10	3.81	H
5	0.4	10	50	-5	15	3.81	H
6	0.4	10	50	-4	10	3.81	H
7	0.4	10	50	-3	10	3.81	H
8	0.4	10	50	-2	10	3.81	H
9	0.4	10	50	-1	10	3.81	H
10	0.4	10	50	-5	30	3.81	H
11	0.4	20	50	-5	10	3.81	H
12	0.4	20	50	-4	10	3.81	H
13	0.4	20	50	-3	10	3.81	H
14	0.4	20	50	-2	10	3.81	H
15	0.4	20	50	-1	10	3.81	H
16	0.4	30	50	-5	10	3.81	H
17	0.4	30	50	-4	10	3.81	H
18	0.4	30	50	-3	10	3.81	H
19	0.4	30	50	-2	10	3.81	H
20	0.4	30	50	-1	10	3.81	H
21	0.4	10	50	-5	60	3.81	H
22	0.4	30	20	-5	5	3.81	H
23	0.4	30	20	-5	10	3.81	H
24	0.4	30	20	-5	30	3.81	H
25	0.4	20	50	-3	30	3.81	H
26	0.4	20	50	-2	30	3.81	H
27	0.4	20	50	-1	30	3.81	H
28	0.4	20	50	-1	60	3.81	H
29	0.4	20	50	-3	10	8.9	H
30	0.4	20	50	-3	30	8.9	H
31	0.4	20	50	-2	10	8.9	H
32	0.4	20	50	-2	30	8.9	H
33	0.4	20	50	-1	30	8.9	H
34	0.4	20	50	-3	10	8.9	V
35	0.4	20	50	-3	30	8.9	V
36	0.4	20	50	-2	10	8.9	V
37	0.4	20	50	-2	30	8.9	V
38	0.4	20	50	-1	30	8.9	V
39	0.4	10	50	-1	30	8.9	V
40	0.4	10	50	-2	30	8.9	V
41	0.4	20	50	-3	10	3.81	V
42	0.4	10	50	-3	10	3.81	V
43	0.4	20	50	-2	10	3.81	V
44	0.4	20	50	-1	10	3.81	V
45	0.4	10	50	-1	10	3.81	V
46	0.4	10	50	-2	10	3.81	V

The total test program has been separate in to six sub-tests programs, which makes a comparison in relation to the test parameters. These sub-test programs is shown in Table 3 to Table 11 and list a comparison sorted by Time, Temperature, Droplet size, Velocity, Diameter and Position. Some of the sub-test programs reveals limited information about the ice formation, but is listed to give a better overview of the total test program.

Parameter used in classifying ice accretion attributes

In order to perform this study, a series of parameters has been defined. Earlier research,(Anderson, 1994), has defined an accumulation parameter A_c, Eq. (1).

$$A_c = \frac{LWC * U * t}{c * \rho_{ice}} \tag{1}$$

Where LWC is the liquid water content, U is the wind velocity, t is the exposure time, c is a characteristic length of the structure, and ρ_{ice} is the density of ice. This parameter (A_c) only revels information about the potential ice accretion on a given structure and predicts a linear relation between ice mass and time. The experiments presented in this paper shows that this is not the case for short exposure times. It is suggested that a general ice accretion coefficient is used for comparison between test parameter instead, which is introduced below.

To study the overall ice accretion on the cylinder under different boundary conditions, a general accretion coefficient, C_{accr}, is introduced.

$$C_{accr} = \frac{m_{accr}}{m_{appr}} \tag{2}$$

This coefficient gives the ratio of the accreted ice mass, m_{accr}, at a particular time to the water mass in the approaching airflow that passed the projected cross-flow area of the cylinder since the beginning of the test, m_{appr}, (since spray-on).

$$m_{accr} = A_{ice} \cdot \rho_{ice} \tag{3}$$

Here, A_{ice} is the integrated cross-sectional area of the accreted ice. The perimeter of the ice shape was determined with the shape tracing method mentioned above and later digitalized with a line-tracing program. The obtained data are used to integrate the area of the accreted ice and allow for further numerical analysis of the ice surface features. The density of the ice, ρ_{ice}, is set to 996g/cm^3.

$$m_{appr} = LWC \cdot D \cdot U_{mean} \cdot t \tag{4}$$

Again, LWC is the Liquid Water Content in [g/m^3], D is here the cylinder diameter but in general the cross flow length of the structure being tested, U_{mean} the time averaged airflow speed in the test and t the time since spray-on, equivalent to exposure time.

The values of the general accretion coefficient, C_{accr} are for lower time values between zero and one since the accreted ice mass cannot exceed the provided water mass. This is mainly valid for the first 10 to 30 minutes, where the cross-wind extension of the body, i.e. cylinder + accreted ice, is zero or negligible. At sixty minutes, significant accretion can change the crosswind dimension, which might lead to an increased adhesion of water droplets, leading to a $C_{accr} > 1$.

Over time, the surface roughness also increases significant due to different shapes of ice accretion. The texture of the accretion multiplies the initial dry cylinder surface and creates additionally local turbulent wake flow behind large accreted ice structures leading to attachment of droplets due to sedimentation effects, which again can lead to $C_{accr} > 1$.

Variation of Time

The sub-test program listed in Table 3, which show ice accretions depended on time, provides substantial information about the development of the ice accretions. Through this sub-program, it is here possible to study the total ice accretion, stagnation point thickness, and symmetry around the stagnation point, all as a function of time.

Table 3
Listing of test sorted by Variation of Time

No.	Umean [m/s]	Tair [°C]	D [cm]	DS [µm]	LWC [g/m^3]	Pos. [-]	Variation Run#(t[min])
A1	10	-5	3.81	50	0.4	H	2(10) ; 5(15) ; 10(30) ; 21(60)
A2	30	-5	3.81	20	0.4	H	22(5) ; 23(10) ; 24(30)
A3	20	-1	3.81	50	0.4	H	15(10) ; 27(30) ; 28(60)
A4	20	-2	3.81	50	0.4	H	14(10) ; 26(30)
A5	20	-3	3.81	50	0.4	H	13(10) ; 25(30)
A6	20	-2	8.9	50	0.4	H	31(10) ; 32(30)
A7	20	-3	8.9	50	0.4	V	34(10) ; 35(30)
A8	20	-2	8.9	50	0.4	V	36(10) ; 37(30)
A9	20	-3	8.9	50	0.4	H	29(10) ; 30(30)

Ice accretion coefficient

Figure 12 shows a plot of this ice accretion coefficient as a function of time. It is seen that the ice accretion coefficient has a tendency to approach a constant value for experiments with higher time values and especially test A2 seems to have settled on a constant value for a relative short exposure time. A2 is a test series with a droplet size of 20µm. This fact could suggest that as soon as the cylinders plus ice accretion has form a better aerodynamic shape, the inertia of the water drops are so small that that the water drops at the outer edge of the cylinder is carried past the cylinder without hitting surface of the cylinder or ice.

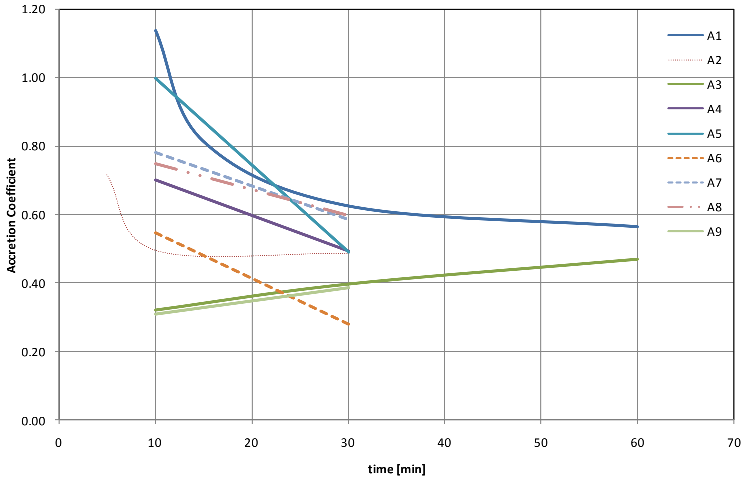

Figure 12 Plot of Accretion coefficient as a function of time for different variation in test parameters.

Figure 12 might suggest that for longer exposure time to icy condition a constant of about 0.5 might be a good estimate on a constant ice accretion coefficient for the entire test program presented in this paper. A constant value of the ice accretion coefficient C_{accr} also implies a linear relationship between the ice accretion and higher values of time, which was suggested in previously mentioned research. Test series A6 falls outside this prediction for no apparent reason and a comparison between test series A6 and A8 revels that these tests are identical except for the position of the cylinder, where A6 is place horizontal and A8 is placed vertical. Likewise, if A6 and A9 are compared, it is seen that the different is only the temperature, which is -2°C for A6 and -3°C for A9. If the position has a significant effect then it would be expected to see a similar offset for A9 in comparison to A7, but this is not the case. If it is the temperature, which are a governing factor and it is assumed that cylinder size is not a ruling parameter, one would expect to see the similar offset for A4 and A5, but again this is not the case. The conclusion must be that either that the size of the cylinder in conjunction with temperature is a vital combination in ice accretion or test series A6 is not valid.

Stagnation line

Looking at the stagnation lines growth speed, Figure 13, it is seen that the different sub-test series show a tendency to reach a constant growth rate at higher exposure times. Returning to sub-test A6 and comparing the result from Figure 12 and Figure 13, it is suggested that the stagnation line thickness has been traced correctly meaning that the results for A6 are valid. This in turn might suggest that the rest of the total area may have been traced in such a location that the found area could be treated as extreme point of either run 31 or run 32. In either case, more tests should be made in order to verify the A6 ice coefficients and A6 should be disregarded until comparative test has been made.

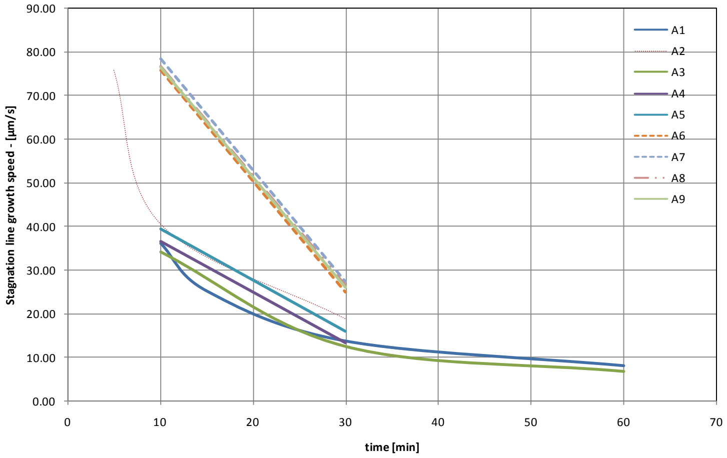

Figure 13 Plot of Stagnation line growth as a function of time for different variation in test parameters.

Using the information derived from Figure 13 in conjunction with the information from Figure 12 suggest that an overall ice accretion growth speed is reach at higher exposure times, which supports the above findings of a constant ice accretion coefficient, C_{accr} for higher accretions times.

Symmetry

A small study in the symmetry of the ice accretion around the stagnation point was also conducted. Figure 14 shows the results of that study and it is seen that for low temperatures the symmetry is high whereas for high temperatures the symmetry is relatively low.

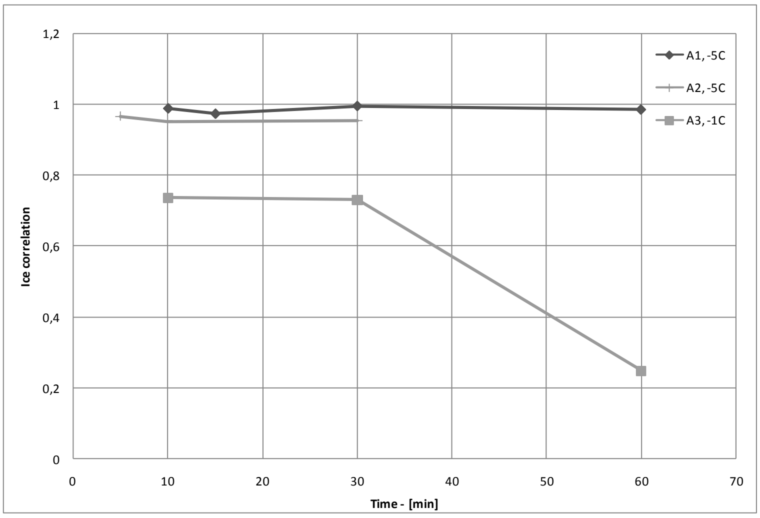

Figure 14 Plot of correlation coefficient between the two sides split by the stagnation line. The plot is shown as a function of time for the tests which have more then two time steps.

Below is shown a series of three figures (Figure 15, Figure 16 and Figure 17), which displays the ice accretions used in calculating the correlation coefficients shown in Figure 14. For each of these the figures, the ● indicates the end of the correlation series starting from the stagnation point. The stagnation point is situated at [Arc_L/D_{cyl}] = zero and is marked by a solid vertical line. The horizontal das-dot line "-·-·-" represent the mean ice accretion thickness. Here Arc_L is the Arc length on the cylinder from the stagnation point and round the cylinder perimeter and D_{cyl} is the Cylinder diameter.

Table 4, Table 5 and Table 6 show pictures of the different ice accretion shapes, which was used in tracing the ice accretion shown in figures Figure 15, Figure 16 and Figure 17. Comparing these pictures shows a clear difference between the low and high temperatures. The high temperature from A3 has an ice formation, which has a much rougher surface then the relative low temperatures from A1 and A2.

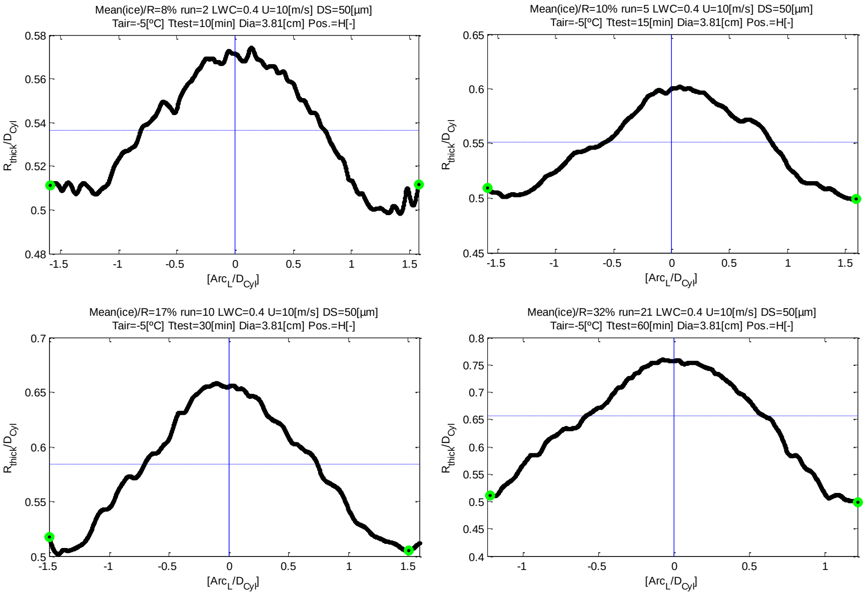

Figure 15 Ice accretion for A1 showed with radial length from cylinder center as a function of the arclenght from the stagation line. ● end point of the correlation series starting from the stagnation point. “-·-·-” = mean ice accretion thickness.

Table 4
Pictures of the found ice accretion on run 2, run 5, run 10 and run 21

Run 2	Run 5	Run 10	Run 21
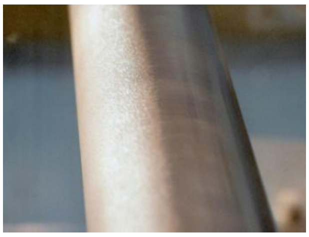 Upper half of	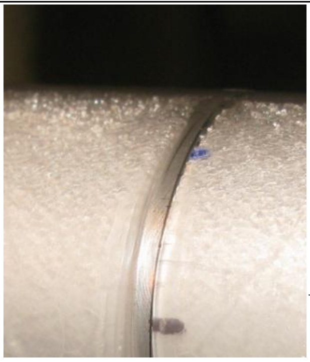 Upper accretion edge.	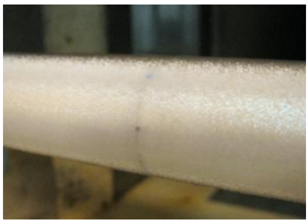 Upstream side.	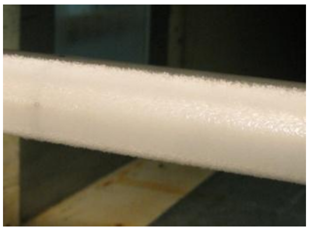 Upstream part of the cylinder.
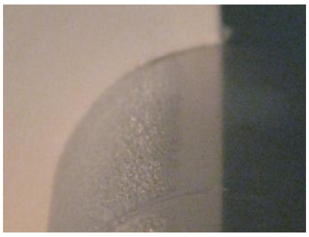 Close-up on the upper half.	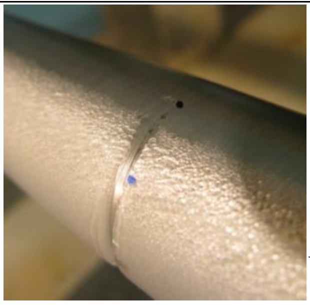 Upper accretion edge.	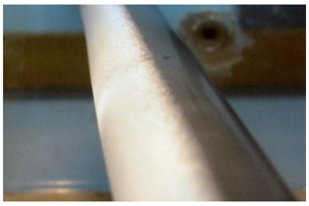 Upper edge of accretion area.	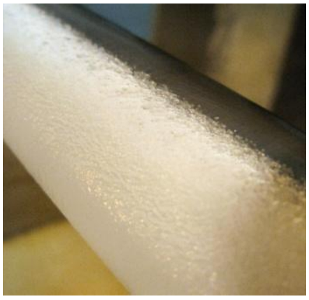 Upper part of the cylinder.
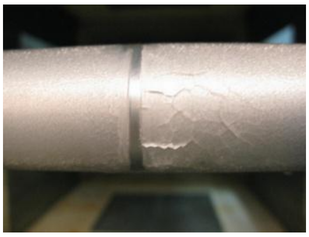 Front side	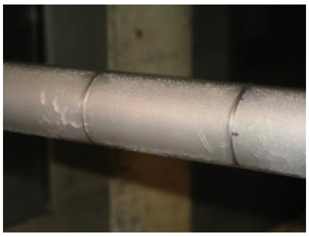 Front side	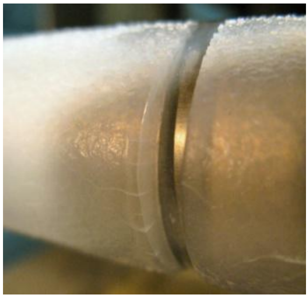 Cut through	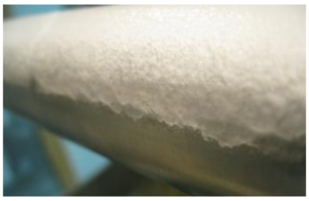 Underside of the cylinder

Another way to describe the difference between A3 and A1, A2 is that A1 and A2 has at more uniform 3D structure, which leads to less dependency of the point for the surface tracing when it comes to a comparison of symmetry. In order to make a satisfactory analyzing of the symmetry of A3, several cut should have been made, from which a combined symmetry analysis could be made. The two cuts, which were made during this experiment, are far from producing a satisfactory symmetry analysis. In further experiments, it would be preferable to do a small study, which look at how many cuts would give a satisfactory symmetry analysis, or use a different way of tracing the 3D structure of the ice accretion.

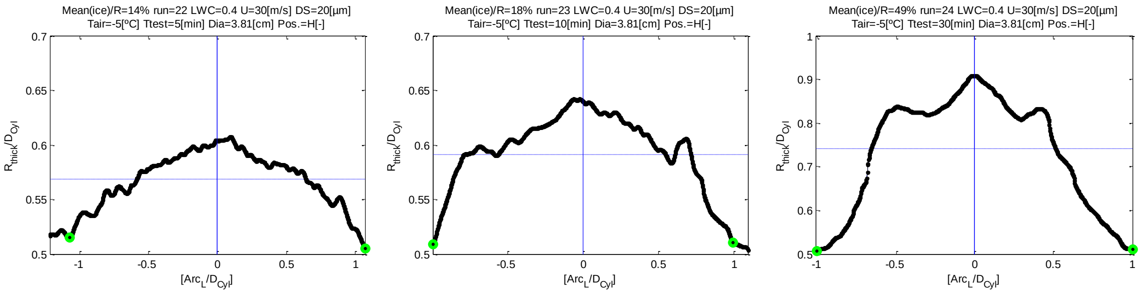

Figure 16 Ice accretion for A2 showed with radial length from cylinder center as a function of the arclenght from the stagation line. ● end point of the correlation series starting from the stagnation point. "-·-·-" = mean ice accretion thickness.

Table 5
Pictures of the found ice accretion on run 22, run 22 and run 24

Run 22	Run 23	Run 24
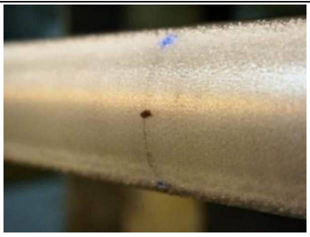 Upstream side.	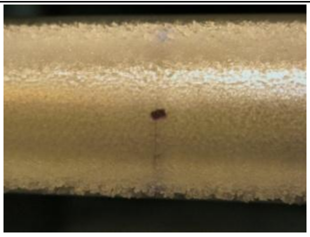 Upstream side of the cylinder.	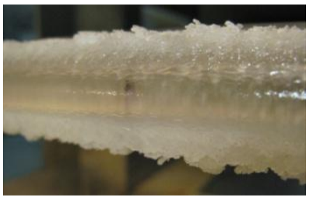 Upstream side.
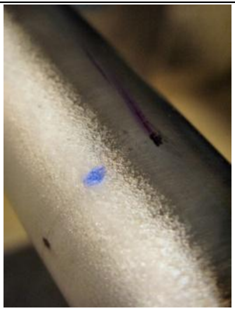 Upper side.Upper side	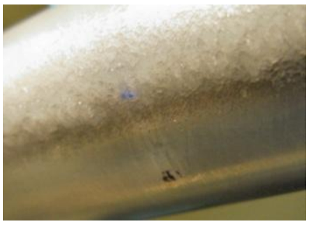 Underside of the cylinder.	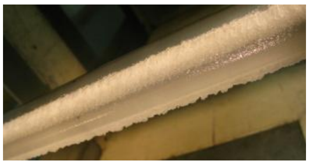 Front side + upper half
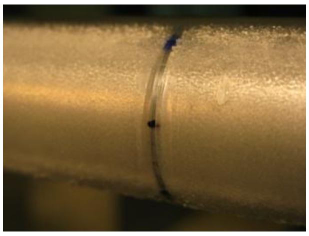 Front side	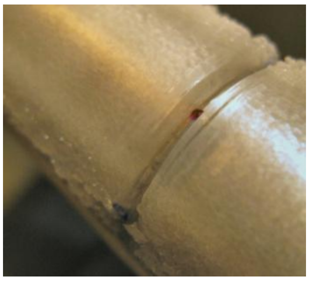 Cut through	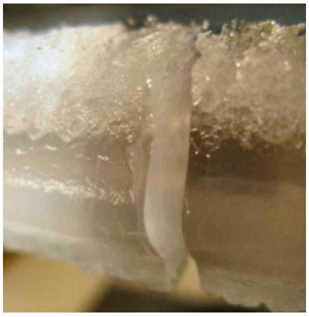 Cut through

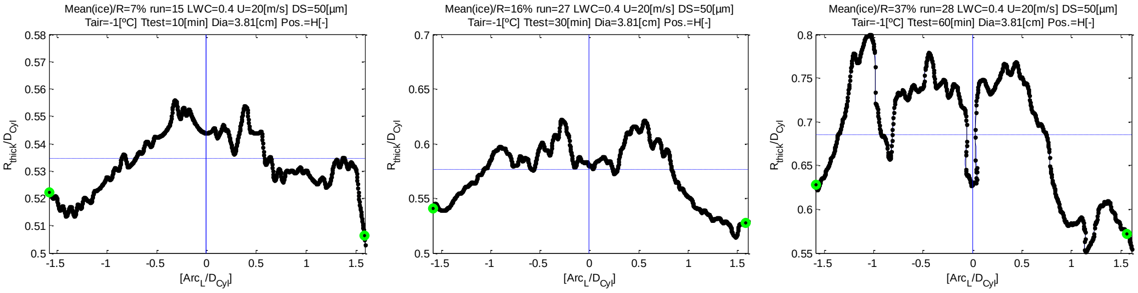

Figure 17 Ice accretion for A3 showed with radial length from cylinder center as a function of the arclenght from the stagation line. ● end point of the correlation series starting from the stagnation point. "-.-.-" = mean ice accretion thickness.

Table 6
Pictures of the found ice accretion on run 15, run 27 and run 28

Run 15	Run 27	Run 28
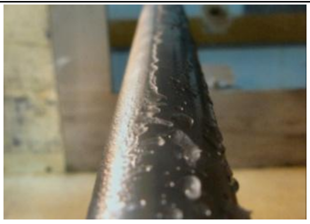 Upper part.	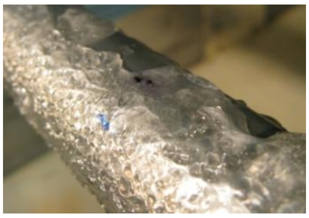 Upper ice accretion edge.	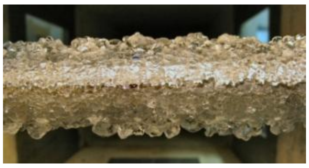 Front side at mid-section.
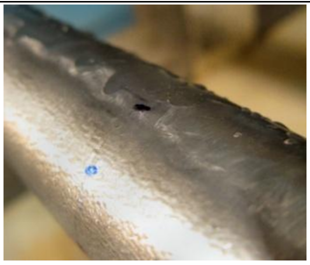 Forward upper part.	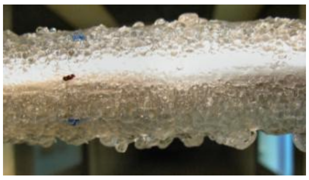 Forward Ice accretion	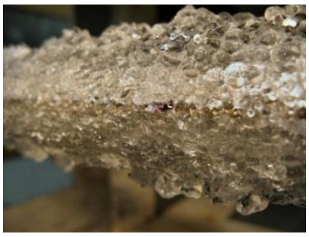 Stagnation point.
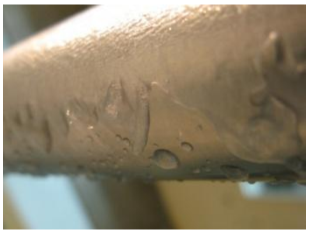 Underside.	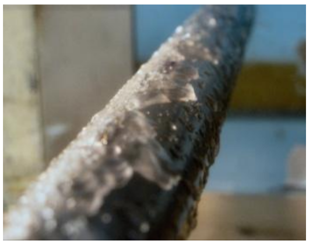 Backside of the cylinder	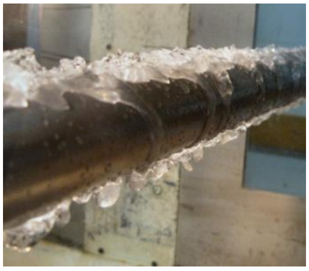 Rear side

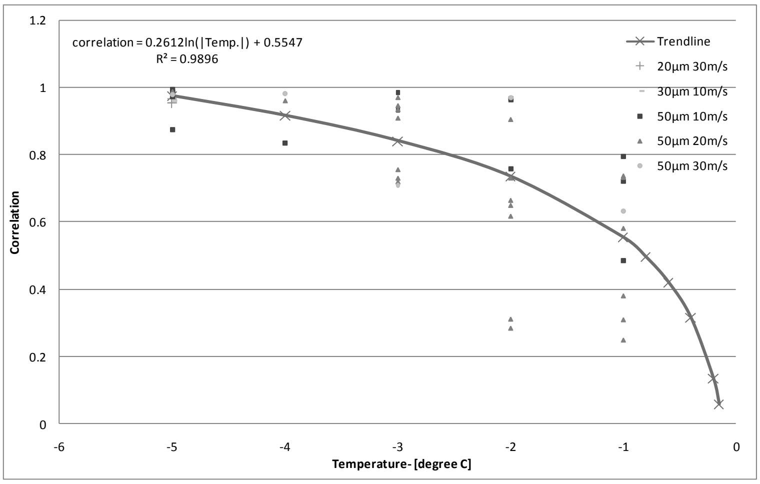

Figure 18 Symmetry correlation for all experiments as a function of temperature and plotted in gruped velocities

Looking at the total test program and plotting the symmetry correlation as a function of time shows that symmetry is high at low temperature and relatively lower at high temperatures, Figure 18. It is furthermore seen that the range of which the correlation spans shift from a broad range to a relatively narrow is between -2°C to -3°C. This indication of a shift in span range is support by visual observations during the experiments, where a significant change in the ice formation behavior was observed around this temperature range.

Influence of Temperature

Examining the sub-test program "B" which looks at the significance of temperature also reveals information about the formation of ice accretion.

Table 7
Listing of test sorted by Influence of Temperature

No.	Umean	Time	D	DS	LWC	Pos.	Variation
	[m/s]	[min]	[cm]	[µm]	[g/m^3]	[-]	Run#(T[°C])
B1	10	10	3.81	50	0.4	H	2(-5) ; 6(-4) ; 7(-3) ; 8(-2) ; 9(-1)
B2	20	10	3.81	50	0.4	H	11(-5) ; 12(-4) ; 13(-3) ; 14(-2) ; 15(-1)
B3	30	10	3.81	50	0.4	H	16(-5) ; 17(-4) ; 18(-3) ; 19(-2) ; 20(-1)
B4	20	30	3.81	50	0.4	H	25(-3) ; 26(-2) ; 27(-1)
B5	20	30	8.9	50	0.4	H	30(-3) ; 32(-2) ; 33(-1)
B6	20	10	8.9	50	0.4	H	29(-3) ; 31(-2)
B7	20	30	8.9	50	0.4	V	35(-3) ; 37(-2) ; 38(-1)
B8	20	10	8.9	50	0.4	V	34(-3) ; 36(-2)
B9	10	30	8.9	50	0.4	V	40(-2); 39(-1)
B10	20	10	3.81	50	0.4	V	41(-3) ; 43(-2) ; 44(-1)
B11	10	10	3.81	50	0.4	V	42(-3) ; 46(-2) ; 45(-1)

Stagnation line

If the analysis focuses on the stagnation thickness, it is seen that there is a tendency for the stagnation growth speed to be higher at lower temperature. Plotting the stagnation growth speed as non-dimensional shows that the overall growth rate has a tendency to be a linear function of the temperature, but has a relatively wide spread in relation to the different experiments, Figure 19. This suggests that the growth rate is highly dependent on the all the condition present under each experiment.

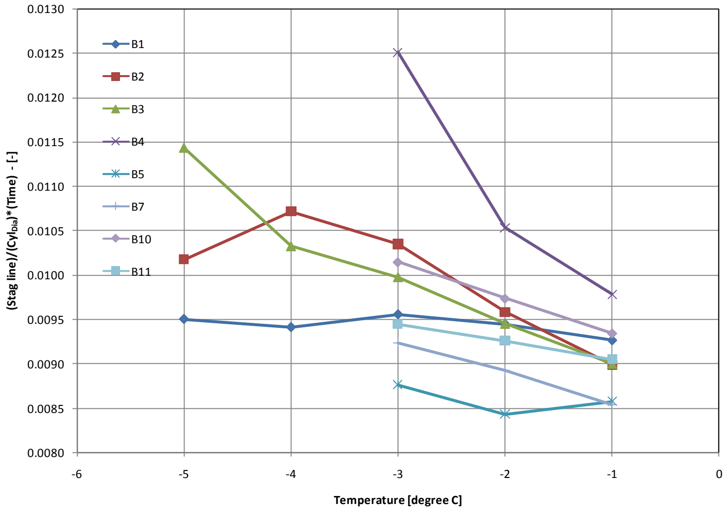

Figure 19 Plot of Stagnation line growth coefficient as a function of the temperatures test in the wind tunnel experiments. The plots are shown as a function of time for the test, which have more than two temperature steps.

Horn location

Similarly, to the symmetry analysis on all the experiments, which is shown above, it is also possible to look at the influence of temperature on the ice accretion on the cylinders. Figure 20 shows such an analysis of the horn location. The horns of the ice accretion are defined by protrusion on the ice accretion. These protrusions are usually located in a range from the stagnation line to 90° from the stagnation line. Furthermore, the horn location for some ice accretion is a subjective matter, which will introduce some spread in the horn location depending on the person looking at the data. The horn location coefficients is defined as

$$H_c = \frac{Arc\ length\ from\ stagnation\ line\ to\ horn\ location}{\text{Cylinder diameter}} \tag{5}$$

Looking at the overall trend of the data shows that the horn location has a tendency to move closer to the stagnation point as temperatures gets lower, which is supported by finding in (Szilder and Lozowski, 2004). This is most likely because the lower temperature fix the water at a faster rate, which in turn shorten the distance of which the water runs back on the cylinder.

The time of exposure has of cause also a significant impact on the horn locations, which will be looked at in the droplet size case below.

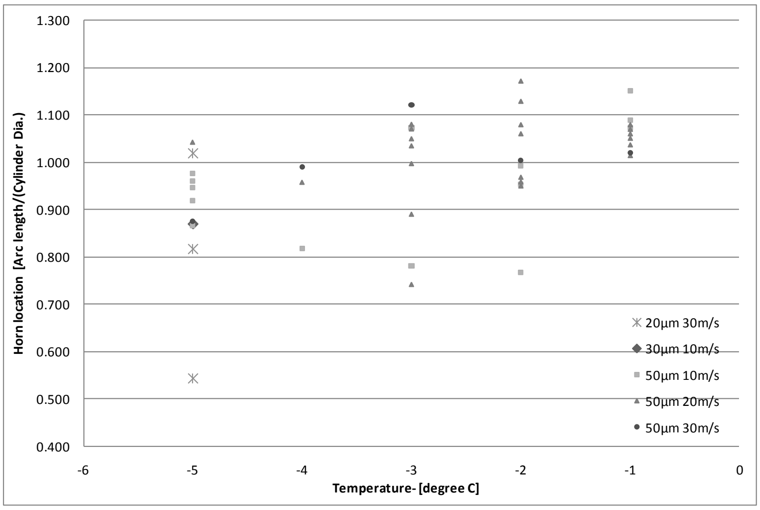

Figure 20 Horn location for all experiments as a function of temperature and plotted in gruped velocities and droplet size

Variation of Droplet size

The sub-test program base on droplet size is listed in Table 8. These test series contain limited information, which make any analysis difficult. Figure 21 shows the plots of the Subseries, where a comparison between accreted ices based on droplet size is shown. Some information can be derived from looking at the total number of test and sorting them according to droplet size, which reveals a tendency in the horn location as a function of the droplet size. This tendency is shown in Figure 22, where it is seen that the smaller the droplet size the close to the stagnation point the horns are located in relation to time and temperature. For the experiments with a droplet size of 50µm, the tendency is less apparent then for the experiments with a droplet size of 20µm where there is a significant drop in the horn location coefficient,

It should be note that the number of test with 20µm is limited to three, which should be taken in to consideration when using the data.

Table 8
Listing of test sorted by Variation of Droplet size

No.	Umean	Tair	Time	D	LWC	Pos.	Variation
	[m/s]	[°C]	[min]	[cm]	[g/m^3]	[-]	Run#(DS[μm])
C1	10	-5	10	3.81	0.4	H	2(50) ; 3(30)
C2	10	-5	10	3.81	0.4	H	16(50) ; 23(20)

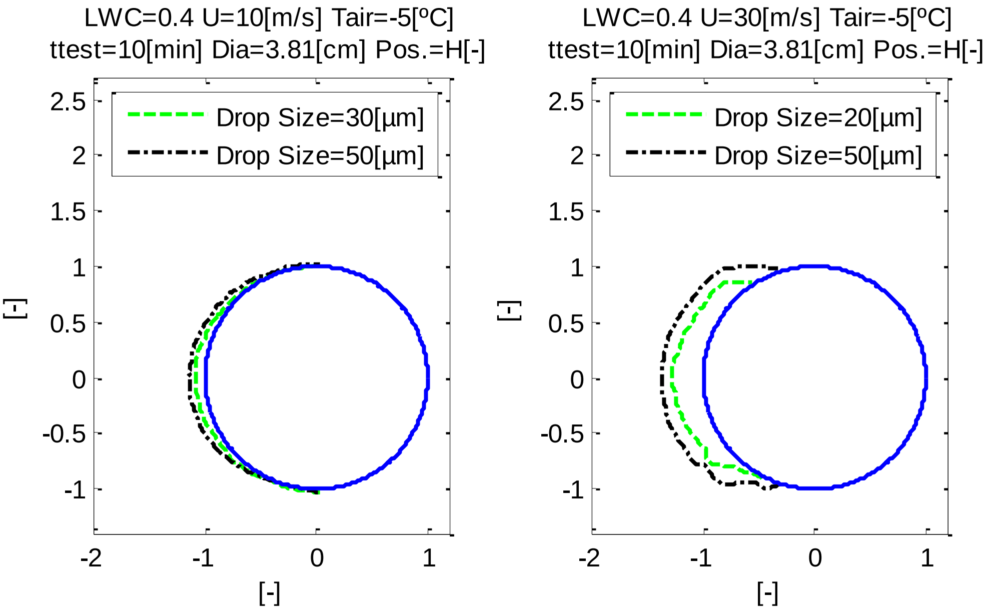
LWC=0.4 U=10[m/s] Tair=-5[ºC] ttest=10[min] Dia=3.81[cm] Pos.=H[-]

LWC=0.4 U=30[m/s] Tair=-5[ºC] ttest=10[min] Dia=3.81[cm] Pos.=H[-]

Figure 21 Ice accretion from Subseries C plotted on a normalized cylider for comparison. To the left C1 is showed and to the rigth C2 is showed.

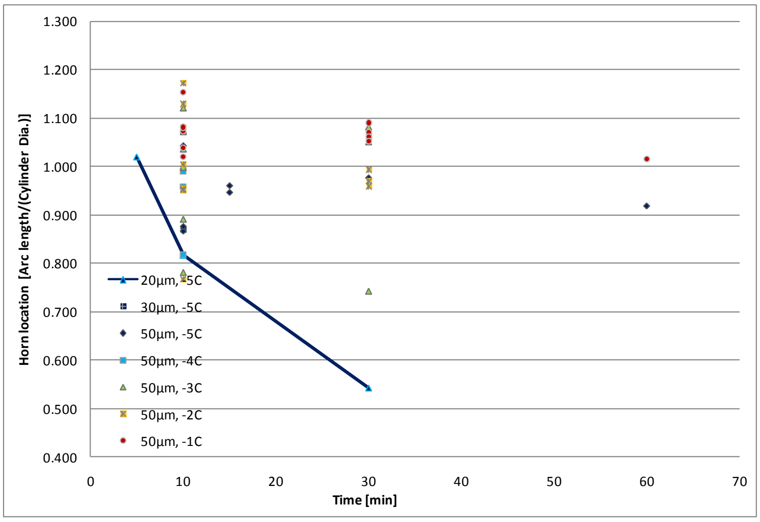

Figure 22 Horn location for all experiments as a function of time and plotted in gruped droplet sizes and temeperatures

Variation of Velocity

Variation due to wind velocity plays a significant role in predicting the ice shapes, which might occur, and the sub-test series is listed in Table 9.

Stagnation line

From the experiments presented in this paper, it is difficult to say anything about the horn locations dependency of wind velocity. It seems that the higher the wind velocity the smaller the spread of the horn location is, Figure 23.

Table 9
Listing of test sorted by Variation of Velocity

No.	Tair	Time	D	DS	LWC	Pos.	Variation
	[°C]	[min]	[cm]	[μm]	[g/m^3]	[-]	Run#(U[m/s])
D1	-1	10	3.81	50	0.4	V	44(20) ; 45(10)
D2	-2	10	3.81	50	0.4	V	43(20) ; 46(10)
D3	-3	10	3.81	50	0.4	V	41(20) ; 42(10)
D4	-2	30	8.9	50	0.4	V	37(20) ; 40(10)
D5	-1	30	8.9	50	0.4	V	38(20) ; 39(10)
D6	-1	10	3.81	50	0.4	H	9(10) ; 15(20) ; 20(30)
D7	-2	10	3.81	50	0.4	H	8(10) ; 14(20) ; 19(30)
D8	-3	10	3.81	50	0.4	H	7(10) ; 13(20) ; 18(30)
D9	-4	10	3.81	50	0.4	H	6(10) ; 12(20) ; 17(30)
D10	-5	10	3.81	50	0.4	H	2(10) ; 11(20) ; 16(30)

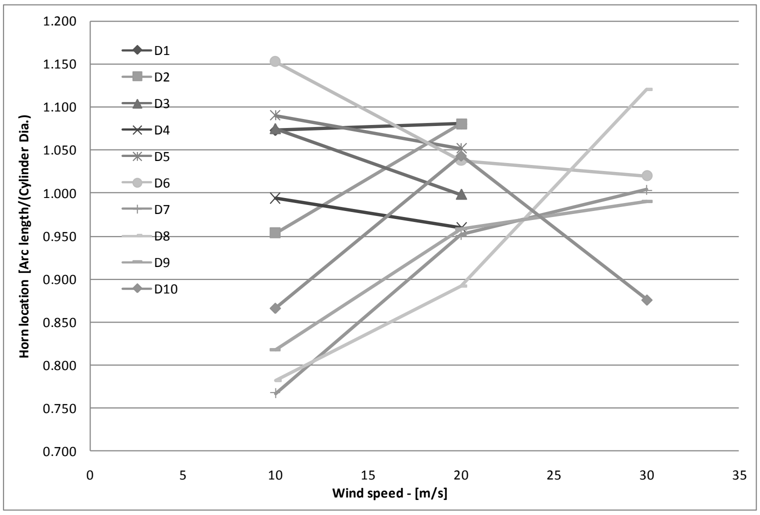

Figure 23 Horn location for sub-series test D

Figure 24 present the stagnation line growth coefficient as a function of wind velocity for the total test series presented in Table 2. Here it is see that for all the experiments perform there is little dependency of wind velocity on the stagnation growth speed, except for one sub-test series D10, which is the only series with a temperature of -5°C. Here it seems that the stagnation line growth speed increase significant with the wind velocity.

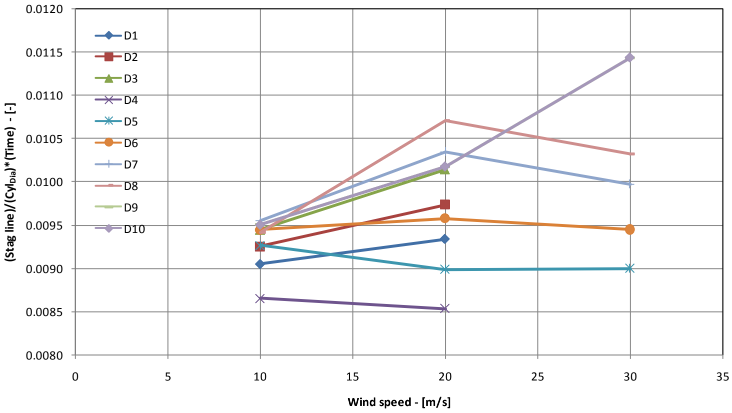

Figure 24 Stagnation line growth speed for sub-series test D

Figure 25 show an overall picture of the horn location dependency of wind velocity. It is seen that the overall dependency is small, but as mention before the horn location is partly subjective and this might have a significant influence on the large span range for each wind velocity.

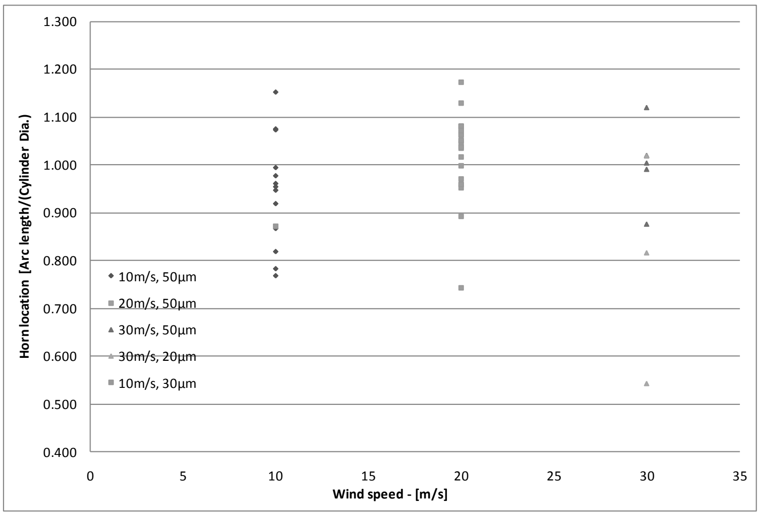

Figure 25 Horn location for all experiemts grouped in droplet size and wind velocity.

Variation of Diameter

The variation in the test setup for ice accretion dependency on cylinder diameter is small and the test setup is listed in Table 10.

Stagnation line

It does reveal some information about the stagnation line growth speed, and Figure 26 shows the comparison of the stagnation line growth coefficient. Here it is seen that the stagnation line growth speed falls significantly for the large cylinder. More tests with different cylinder diameter would be preferable in future test programs.

Table 10
Listing of test sorted by Variation of Diameter

No.	Umean	Tair	Time	DS	LWC	Pos.	Variation
	[m/s]	[°C]	[min]	[µm]	[g/m^3]	[-]	Run#(D[cm])
E1	20	-3	10	50	0.4	V	41(3.81) ; 34(8.9)
E2	20	-2	10	50	0.4	V	43(3.81) ; 36(8.9)
E3	20	-3	10	50	0.4	H	13(3.81) ; 29(8.9)
E4	20	-2	10	50	0.4	H	14(3.81) ; 31(8.9)
E5	20	-3	30	50	0.4	H	25(3.81) ; 30(8.9)
E6	20	-2	30	50	0.4	H	26(3.81) ; 32(8.9)
E7	20	-1	30	50	0.4	H	27(3.81) ; 33(8.9)

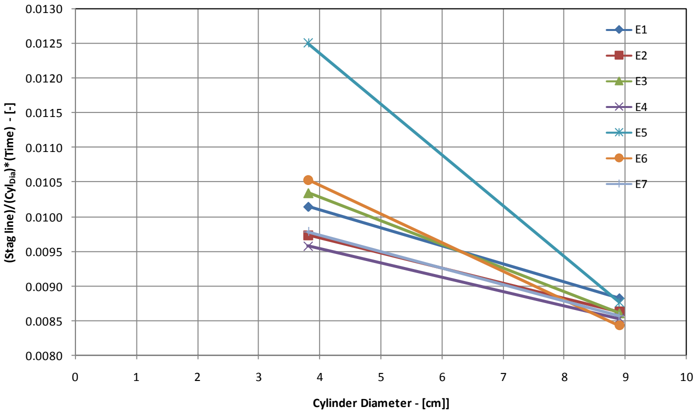

Figure 26 Stanation line growth coefficient sub-series test E

Influence of Position

The experiment reported in this paper did not show any dependency of the position of the cylinder in the wind tunnel, but the number of different sizes tested is not large enough to draw any satisfactory conclusion. Figure 27 show the stagnation point growth coefficient as a function of the cylinder size and it is seen that there is limited dependency of cylinder diameter size. Plot for other parameter show a similarly picture.

Table 11
Listing of test sorted by Influence of Position

No.	Umean	Tair	Time	D	DS	LWC	Variation
	[m/s]	[°C]	[min]	[cm]	[µm]	[g/m^3]	Run#(Pos.)
F1	20	-3	10	8.9	50	0.4	29(H) ; 34(V)
F2	20	-3	30	8.9	50	0.4	30(H) ; 35(V)
F3	20	-2	10	8.9	50	0.4	31(H) ; 36(V)
F4	20	-2	30	8.9	50	0.4	32(H) ; 37(V)
F5	20	-1	30	8.9	50	0.4	33(H) ; 38(V)
F6	20	-3	10	3.81	50	0.4	13(H) ; 41(V)
F7	10	-3	10	3.81	50	0.4	7(H) ; 42(V)
F8	20	-2	10	3.81	50	0.4	14(H) ; 43(V)
F9	20	-1	10	3.81	50	0.4	15(H) ; 44(V)
F10	10	-1	10	3.81	50	0.4	9(H) ; 45(V)
F11	10	-2	10	3.81	50	0.4	8(H) ; 46(V)

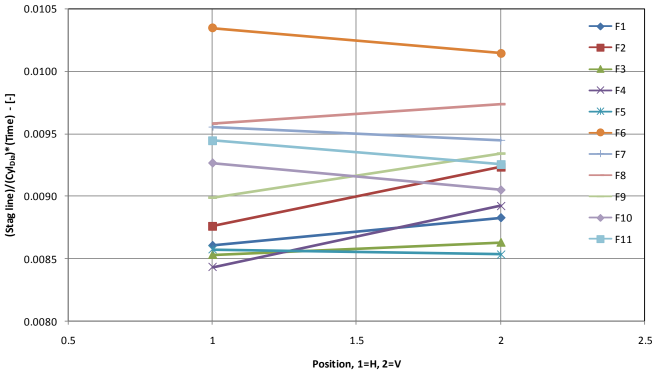

Figure 27 Plot of Stagnation point growth coefficient as a function of position of the cylinders in the wind tunnel.

Conclusion

A large test series of ice accretions on two circular cylinders of different diameters has been presented in this paper. The ice accretions has been produced at temperatures in the range of -5°C to -1°C and at wind velocities between 10m/s to 30m/s.

Several ice accretion coefficients have been presented in order to analysis the different ice accretions found from the experiments. A general ice accretion coefficients, which looks at the ration of water attaching to the cylinders, a horn location coefficient and a landscape plot of the accretion used for comparing symmetry around the stagnation line.

It have been shown that the general ice accretion coefficient have a tendency, for higher values of time exposure, to be a constant value. A good estimate on this value might be 0.5.

Likewise it has been shown that the stagnation line growth speed also have a tendency to approach a constant value. More experiments needs to be performed in order to give an estimate on this value.

It has also been shown that the symmetry around the stagnation line is high for low temperature and low for high temperature. The symmetry analysis also reveals a jump in how the ice accretion is formed. This jump happens between -2°C and -3°C and was observed visually during the experiments.

It has also been shown that the wind velocity has a possible effect on the horn location. The higher the wind velocity the less spread of the horn location is seen over the total test series.

References

Anderson, D.N., 1994. Rime-, mixed- and glaze-ice evaluations of three scaling laws AIAA(PAPER 94-0718).

Anderson, D.N., Hentschel, D.B. and Ruff, G.A., 1998. Measurement and correlation of ice accretion roughness. AIAA-98-0486.

Dalle, B. and Admirat, P., Wet snow accretion on overhead lines with French report of experience. Cold Regions Science and Technology, In Press, Corrected Proof.

Gjelstrup, H. and Georgakis, C., 2009. Aerodynamic Instability of a cylinder with thin ice accretion, ISCD 2009, Paris.

Gjelstrup, H. and Georgakis, C., 2010. A quasi-steady 3-DOF model for the determination of onset for bluff body of galloping instability (submitted). Journal of Fluids and Structures.

Gjelstrup, H., Georgakis, C. and Larsen, A., 2007. A preliminary Investigation of the hanger vibrations on the Great Belt East Bridge, Seventh International Symposium on Cable Dynamics, Vienna (Austria).

Gjelstrup, H., Larsen, A. and Geogakis, C., 2010. Wind tunnel test on simulated ice accretions. Wind and structures.

Hansman, R.J., Breuer, e.S., Hazan, D., Reehorst, A. and Vargas, M., 1993. Close-up analysis of aircraft ice accretion. AIAA Journal.

Lozowski, E.P., Stallabrass, J.R. and Hearty, P.F., 1983a. The icing of an unheated, nonrotating cylinder .I. A simulation-model. Journal of Climate and Applied Meteorology, 22(12): 2053-2062.

Lozowski, E.P., Stallabrass, J.R. and Hearty, P.F., 1983b. The icing of an unheated, nonrotating cylinder. II. Icing wind tunnel experiments. Journal of Climate and Applied Meteorology 22(12): 2063-74.

McComber, P. and Paradis, A., 1995. Simulation of the galloping vibration of a 2-dimensional iced cable shape. Transactions of the Canadian Society for Mechanical Engineering, 19(2): 75-92.

Nigol, O. and Buchan, P.G., 1981. Conductor galloping .1. Den Hartog mechanism. Ieee Transactions on Power Apparatus and Systems, 100(2): 699-707.

Nigol, O. and Clarke, G.J., 1974. Conductor galloping and control based on torsional mechanism. Ieee Transactions on Power Apparatus and Systems, PA93(6): 1729-1729.

Nigol, O.B., P. G., 1981. Conductor galloping .2. torsional mechanism. Ieee Transactions on Power Apparatus and Systems, 100(2): 708-720.

Oleskiw, M.M., Hyde, F.H. and Penna, P.J., 2001. In-flight Icing Simulation Capabilities of NRC’s Altitude Icing Wind Tunnel 39th AIAA Aerospace Science Meeting & Exhibit, Reno, NV.

Phuc, P.V., 2005. A wind tunnel study on unstady forces of ice accreted transmission lines, BBAA V 5th international Colloquium on Bluff Body Aerodynamics and Applications, pp. p373-376.

Shimizu, M., 2005. A wind tunnel study on aerodynamic characteristics of ice accreted transmission lines, BBAA V 5th international Colloquium on Bluff Body Aerodynamics and Applications, pp. p369-372

Szilder, K. and Lozowski, P., Edward 2004. Novel two-dimensional modeling approach for aircraft icing. Journal of Aircraft, 41(4).

Paper III ([70])

"An evaluation of iced bridge hanger vibrations through wind tunnel testing and quasi-steady theory"

H. Gjelstrup, C.T. Georgakis & A. Larsen

submitted to Wind and Structures

An evaluation of iced bridge hanger vibrations through wind tunnel testing and quasi-steady theory

H. Gjelstrup[1*×], C.T. Georgakis[×], A. Larsen[*]

[*] *COWI A/S, Parallelvej 2, 2800 Kgs. Lyngby , Denmark*

[×] *Department of Civil Engineering, Technical University of Denmark, Building 118, Brovej, 2800 Kgs. Lyngby , Denmark*

Abstract

Bridge hanger vibrations have been reported under icy conditions. In this paper, the results from a series of static and dynamic wind tunnel tests on a circular cylinder representing a bridge hanger with simulated thin ice accretions are presented. The experiments focus on ice accretions produced for wind perpendicular to the cylinder at velocities below 30m/s and for temperatures between -5°C and -1°C. Aerodynamic drag, lift and moment coefficients are obtained from the static tests, whilst mean and fluctuating responses are obtained from the dynamic tests. The influence of varying surface roughness is also examined. The static force coefficients are used to predict parameter regions where motional instability of the iced bridge hanger might be expected to occur, through use of an adapted theoretical 3-DOF quasi-steady galloping instability model, which accounts for sectional axial rotation. A comparison between the 3-DOF model and the instabilities found through two degree-of-freedom (2-DOF) dynamic tests is presented. It is shown that, although there is good agreement between the instabilities found through use of the quasi-steady theory and the dynamic tests, discrepancies exist – indicating the inability of quasi-steady theory to fully predict vibrational instabilities.

Keywords: Wind tunnel tests, circular cylinder, bridge hangers, ice accretion, motional instability, low temperatures, quasi-steady aerodynamics

---

[1] Corresponding author. Tel.: +45 45972805/ +45 45251940; Fax: +45 45972212/ +45 45883282

E-mail address: hegj@cowi.dk/heg@byg.dtu.dk; (COWI/DTU)

1. Introduction

Several recently observed vibrations of bridge hangers have been attributed to the formation of thin ice on the outer surface of the hanger (Gjelstrup, Georgakis *et al.* 2007). Although, this is not necessarily a new phenomenon, little research has been undertaken on the effects of ice on the vibrational stability of cables or other circular sections, for wind velocities below 30m/s and temperatures above -5°C (Lozowski, Stallabrass *et al.* 1983; Lozowski, Stallabrass *et al.* 1983; Hansman, Breuer *et al.* 1993; Anderson, Hentschel *et al.* 1998) .

There are two traditional industries for which ice accretion of cylinders is of importance; the telecommunication and power line industry, and the aerospace industry. For the aerospace industry, temperatures of -5°C to -1°C and wind velocities lower than 30m/s are of little or no interest. For the telecommunication and power line industry, cables are usually of very small diameter. Furthermore, even though several studies involving real and simulated ice accretions on circular power lines have been reported (Dalle and Admirat ; Nigol and Clarke 1974; Hack 1981; Nigol and Buchan 1981; Nigol 1981; Jamaleddine, McClure *et al.* 1993; McComber and Paradis 1995; Chabart and Lilien 1998; Gurung, Yamaguchi *et al.* 2002; Phuc 2005; Shimizu 2005; Kudzys 2006; Fo-chi, Yue-fan *et al.* 2009; Wang, Li *et al.* 2010), the meteorological conditions associated with these cases differ from the situations in which large bridge cable vibrations have been reported. Apart from experiments different

To compensate for the lack of experimental data on the ice accretion of circular cylinders, under the aforementioned meteorological conditions of interest, Gjelstrup *et al.* (2009) performed a series of cylinder icing tests at the NRC Institute for Aerospace Research, Altitude Icing Wind Tunnel Facility (AIWT), in Ottawa, Canada. Several of the accreted ice shapes found from this research, together with several reported by Lozowski *et al.* (1983) and Szilder and Lozowski (2004), were reproduced employing a rapid prototyping technique and used for both the static and the dynamic wind tunnel tests on an example cylinder. The static tests provided force coefficients that were used for the prediction of regions of vertical motional instability, by applying an adapted theoretical 3-DOF quasi-steady galloping instability model proposed by Gjelstrup and Georgakis (2010), in which the along flow degree-of-freedom was constrained. The dynamic tests were used to experimentally determine regions of motional instability, noting that the dynamic wind-tunnel rig was only capable of movement in two degrees-of-freedom, namely allowing for cross flow displacements and axial torsion. For all of the tests, the wind flow was perpendicular to the cylinder.

The results from both the static and the dynamic tests, together with a comparison between the theoretically determined regions of motional instability and those determined experimentally, are presented herewith.

2. Ice shapes considered for testing

Several shapes of ice accretion were initially considered for testing. Six ice shapes, either as reported in literature (Lozowski, Stallabrass *et al.* 1983; Szilder and Lozowski 2004) or as determined by Gjelstrup *et al.* (2009) were finally chosen. These were based on either their resemblance to previously witnessed bridge hanger ice shapes that might have led to associated cable vibrations or those that are most likely to form under the most prevalent meteorological conditions. Shapes I-VI are shown in Fig. 2 and a picture of ice shape IV obtained in wind tunnel test is shown in Fig. 1

Table 1. LWC, U, temperature and ice accretion time for ice shapes I-VI

Ice shape	LWC	U	Temp	Time
	[g/m^3]	[m/s]	[°C]	[min]
I	0.4	30	-15	5
II	0.4	30	-2	5
III	0.4	30	-5	5
IV	0.4	20	-2	30
V	0.4	10	-1	30
VI	Cylinder with generic ice: 2mm thick at the stagnation point			

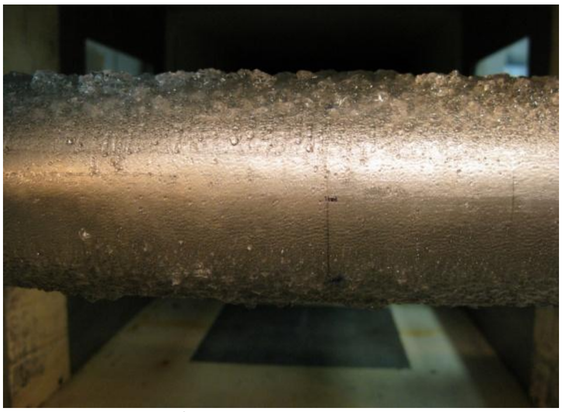

Figure 1. Picture of Ice shape IV obtain in wind tunnel test

The variation in ice shape is predominantly due to five parameters, the liquid water content (LWC) of the air, the wind velocity (U), the external temperature (Temp), the accretion time (Time) and the diameter (D) of the cylinder. The variation on these parameters for each shape is provided in Table 1. Note that for all the tests, the base cylindrical cross section was D_b = 70mm in diameter.

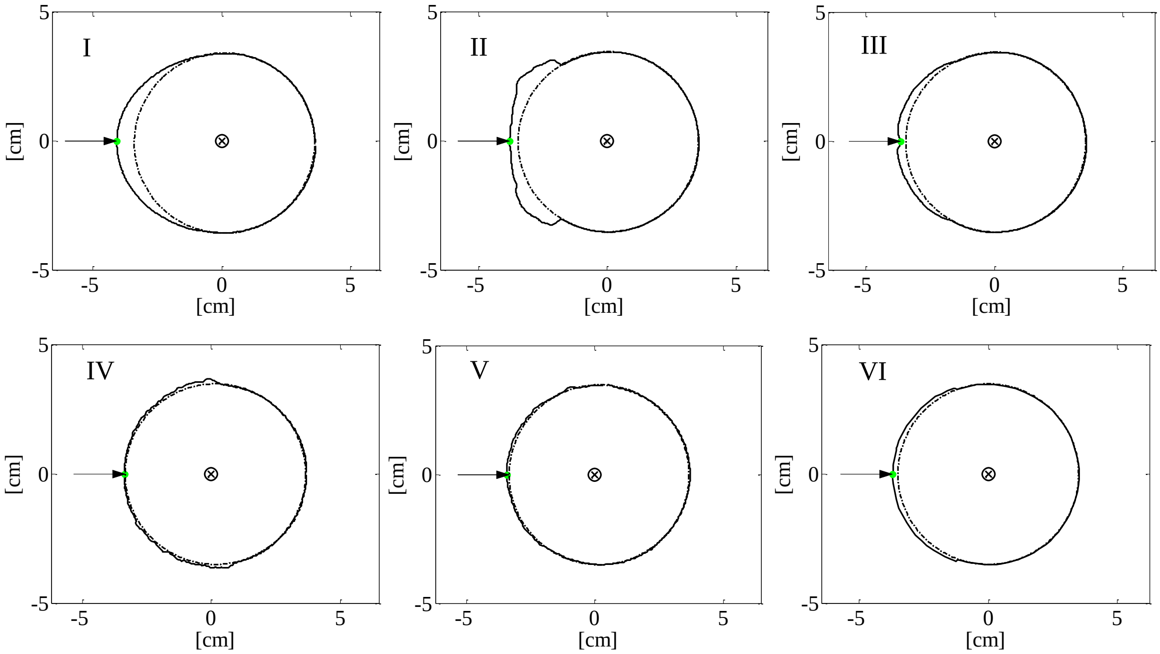

Figure 2. Ice accretion shapes according to icing conditions presented in Table 1. ⊗ indicates the center of the cylinder and "→" indicates the stagnation point of the section from which the 0° angle is defined. The positive change in wind angle-of-attack is counterclockwise. The dotted line illustrates the cylinder boundary behind the ice accretion. In all cases, the cylindrical section has a diameter of 70mm.

The coordinate system and sign convention used for all the experiments performed in the wind tunnel is presented in Fig. 3.

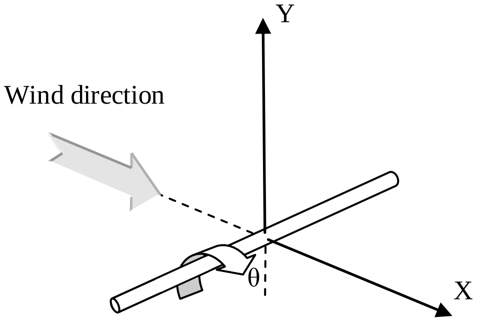

Figure 3. Sign convention and model coordinate system

3. Simulation of ice accretion

For lack of availability of a specially designed climatic wind tunnel, simulated, and not real ice, was used for the static and dynamic wind-tunnel tests described herewith. Consequently, ice accretion shapes I-VI were reproduced using a non-melting material and a rapid-prototyping (3-D printing) technique. The accretion was printed as an additional piece that could be glued on to the base cylinder longitudinally. This led to the printing of accretion strips, along the length of the model axis, which retained a constant ice shape from one end to the other. This also meant that the inevitable print lines (striations) produced by rapid-prototyping were perpendicular to the axis of the model, i.e. parallel to the direction of the flow (see Fig. 4).

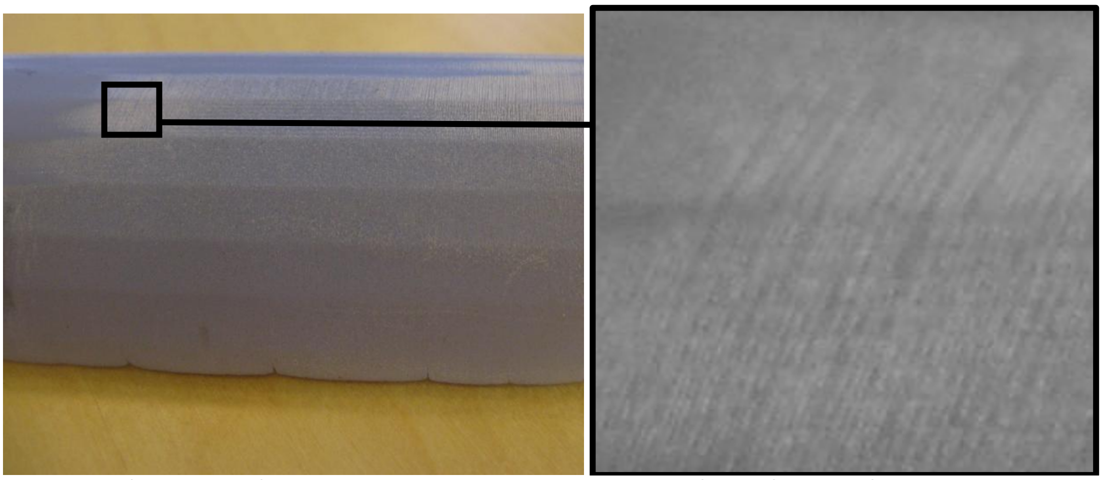

Figure 4. Surface texture of rapid prototyping on a test print: original surface (left) and surface treated with sand paper to visualize the printing lines (right)

The striations leave a relatively rough surface that was not explicitly measured using roughness measurement equipment, but that is visually and texturally equivalent to an ISO/FEPA grit designation of P150 or slightly higher. The surface roughness was considered beneficial, as it is known to shift the critical Reynolds number region to lower wind velocities (ESDU 1986). Furthermore, at least two distinct levels of roughness could be tested by treating the surface with different layers of varnish in order to obtain a smoother surface. For the experiments presented in the present paper, “rough” model surface will refer to the originally manufactured surface, whilst “smooth” will refer to the model surface that has been treated with four layers of varnish.

A photograph of the simulated ice accretion using rapid-prototyping is shown in Fig.5 (right). The specific accretion is based on generic ice shape VI and has a mid-point (stagnation point) thickness of 2mm. For the specific shape, the thickness of the prototyped ice accretion zeroes at ±80° from the stagnation point. The ice thickness, *t*, as a function of angle from stagnation point can be expressed as:

$$t = -r + t_{max} * \cos(\alpha) + \sqrt{(-t_{max}^2 + r^2 + t_{max}^2 * \cos(a))} \tag{1}$$

where, r is the base cylinder radius, t_{max} is the ice stagnation thickness and α is the angle. The definition of the variables in Eq. (1) can also be found in Fig. 5(left).

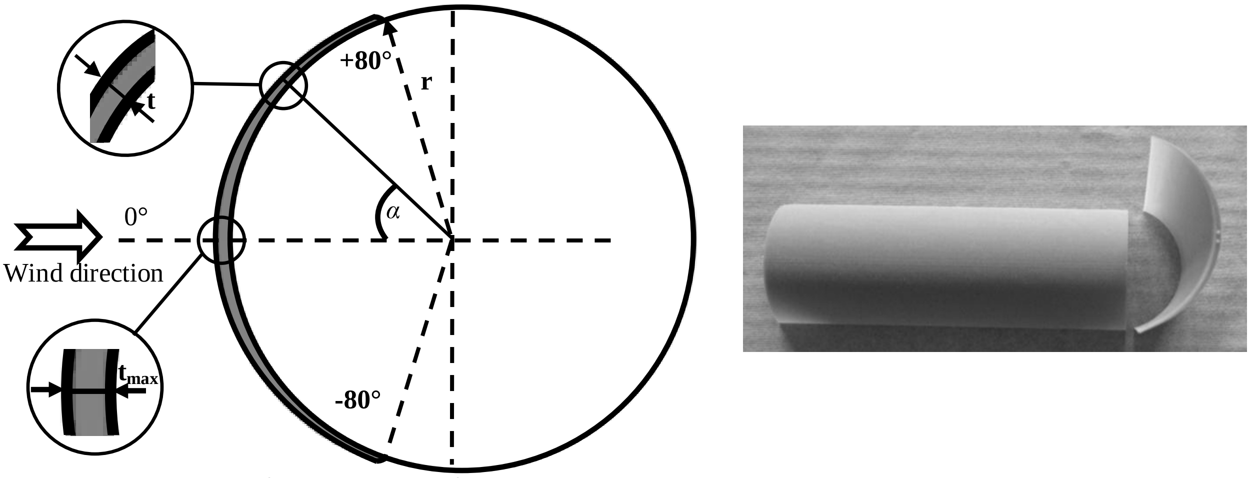
t
+80°
r
0°
α
Wind direction
t_max
-80°

Figure 5. Cross-section of model with ice (left) and simulated ice strip produced by rapid prototyping (right)

4. Testing facility and instrumentation

The experiments on the cylinders with simulated ice accretion were performed at the Closed Circuit Wind Tunnel (CCWT) facility at FORCE Technology, Lyngby, Denmark. The CCWT has a test section with a height of 0.70m and a depth of 1.00m. An overall sketch of the wind tunnel is provided in Fig. 6 In the configuration used, the wind tunnel has a maximum wind velocity of approximately 60m/s for smooth flow, i.e. with a turbulence intensity of $I_x \leq 1\%$. The maximum wind velocity drops to approximately 35m/s for turbulent flow, i.e. an along-wind turbulence intensity approximately of $I_x = 6\%-7\%$.

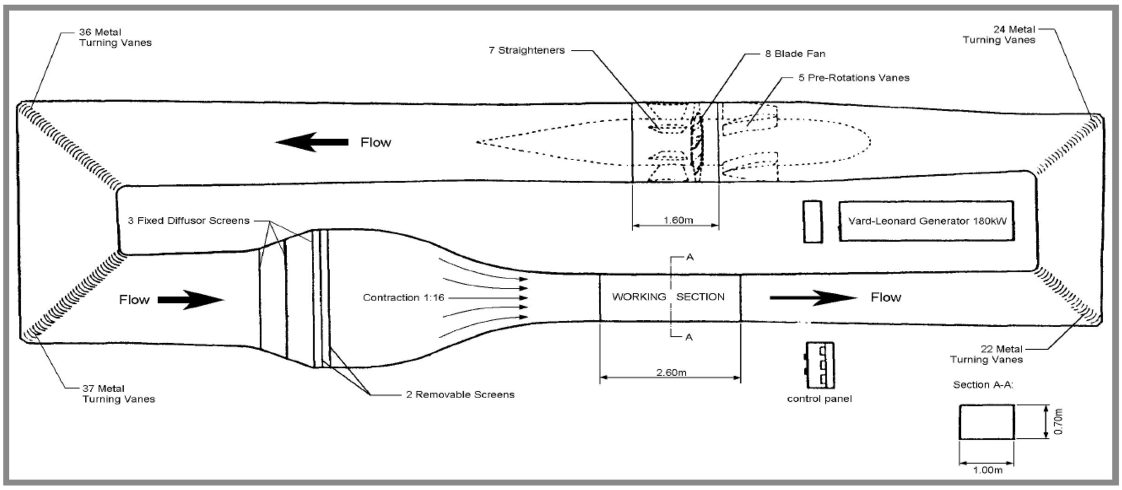
36 Metal Turning Vanes
7 Straighteners
8 Blade Fan
5 Pre-Rotations Vanes
24 Metal Turning Vanes
Flow
1.60m
Vard-Leonard Generator 180kW
3 Fixed Diffusor Screens
A
Flow
Contraction 1:16
WORKING SECTION
Flow
A
2.60m
22 Metal Turning Vanes
37 Metal Turning Vanes
2 Removable Screens
control panel
Section A-A:
0.70m
1.00m

Figure 6. Plan view of the Close Circuit Wind Tunnel (CCWT) facility at FORCE Technology, Lyngby, Denmark.

In order to produce turbulent flow, a grid (Fig. 7) was placed in the wind tunnel at a distance of 0.84m upstream of the models, as indicated in Fig. 10. The dimensions of the turbulence grid can be seen in Fig. 7, where A and B is the height and width of the square hole in the grid and C is the width of the wooden elements comprising the grid.

The instrumentation used for the experiments can be split in to two groups centred around the type of test rig used. The static rig can be seen in Fig. 8, whiles the dynamic rig is illustrated in Fig. 9. The wind velocity was measurement with a pitot tube, which was located in the middle of the test chamber’s cross-section and placed 0.5m upstream of the tested models.

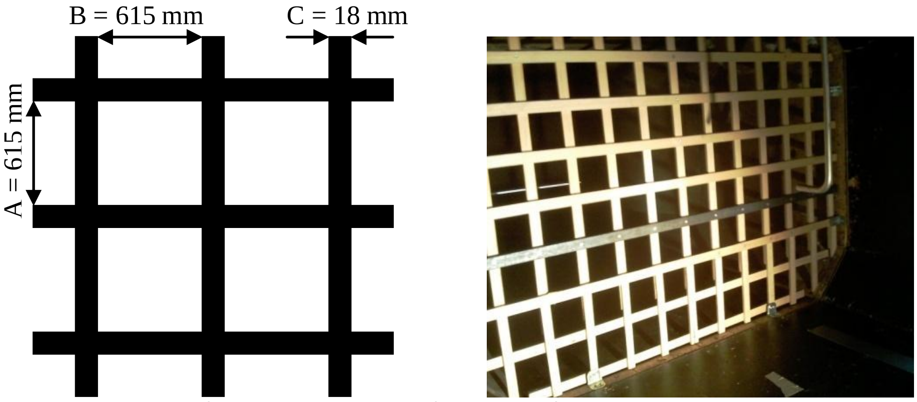

Figure 7. Dimensions of the turbulence grid (left), Picture of the turbulence grid and pitot tube location (right)

The static test rig (Fig. 8) has a load range of ±300N and an A/D resolution 12bit The section model is suspended between two 3-DOF force gauges (Fig. 8 (1)), which for the specific experiments measure the about-axis moment and the forces acting on the model in the two directions, X and Y. The 3-DOF gauges are mounted on the outside of the tunnel walls on aluminium bars that are fitted across the door opening. Play-less disk joints (Fig. 8 (5)) at both ends of the section model ensure that no other force components exist than those measured. A worm-drive (Fig. 8 (2)) is used to rotate the section model, which is thereafter fixed in both ends by the tightening screws (Fig. 8 (4)). An electronic inclinometer is used to measure the angle of wind incidence (Fig. 8 (3)). After the model is set to the required angle-of-attack and the screws on the balance are tightened, all six gauges are then plugged into DC strain-gauge amplifiers from which the signal is run through an analogue low pass filer of 80hz .

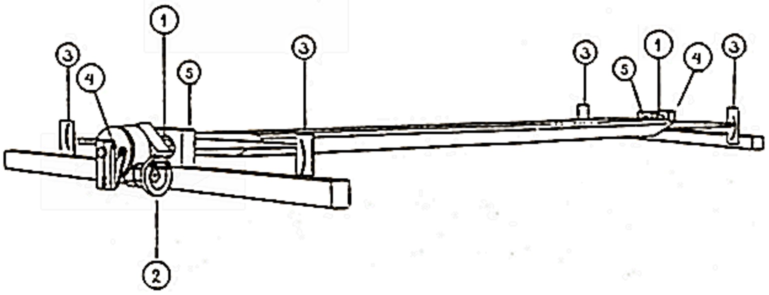

Figure 8. Static test rig

The dynamic rig (Fig. 9) consists primarily of 4 springs, which allow the simulation of the vertical and torsional oscillations of a section model. The section model (Fig. 9 (1)) forms an integral part of the dynamic test rig which is double symmetric with regards to the model span and chord, except for the drag wires (Fig. 9 (5,6)), which have slightly different lengths on either side. The vertical and torsional stiffness of the dynamic test rig is provided by a set of helical springs (Fig. 9 (4)) onto which the section model is suspended. Secondary stiffness is provided by the dynamic test rig arms and the section model itself, and needs to be considered when determining the modal stiffness of the overall dynamic test rig. Model vibration frequencies are adjusted by varying the spring length, and the spring spacing. Adjustment of model mass and mass moment of inertia is achieved through addition or subtraction of mass to the dynamic test rig arms (Fig. 9 (8,9)).

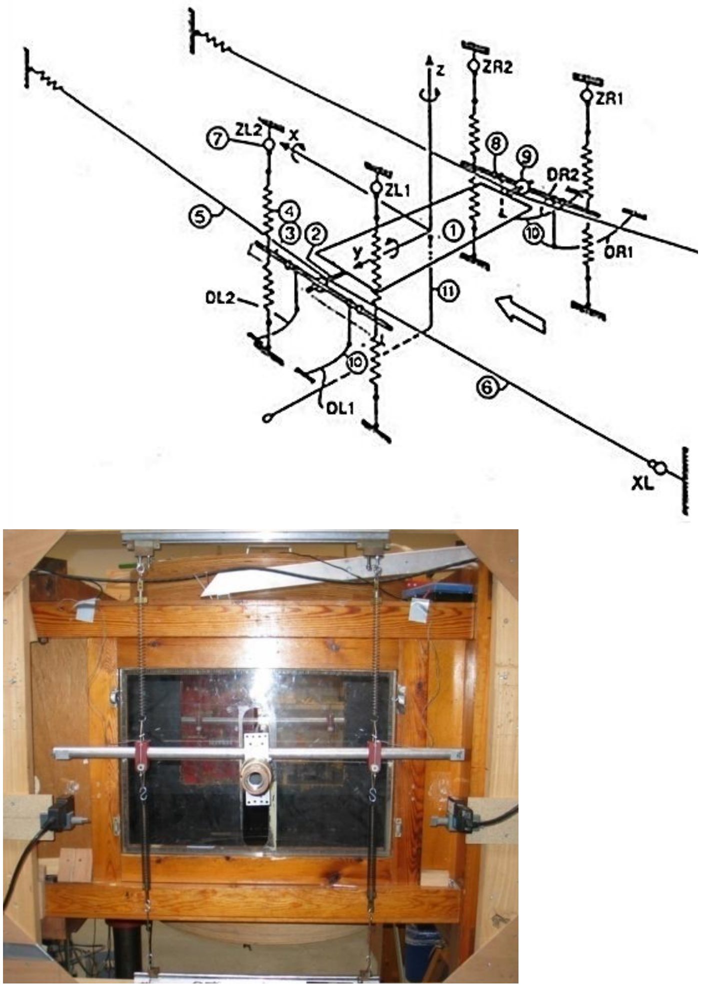

Figure 9. Dynamic test rig: general sketch (left) and picture of model and test rig (right).

The displacements and rotations of the section model were measured using four optical displacement sensors (ODSs), the locations of which are indicated by (A) in Fig. 9 (right). Four accelerometers were used for backup measurements, with their locations indicated by (B) in Fig. 9 (right). The ODSs were produced by DME A/S (Denmark) and have a measuring range of max ±20mm about a centered position or max 40mm in one direction. The resolution of the ODS 70 is 0.02mm and each has a voltage output of 0-10 Volt (DC). The accelerometers are produced by Entran and behave linearly. They are model number EGAX-10 and measure accelerations within a $\pm 10g$ ($g = 9.81 m/sec^2$) range.

5. Wind profile measurements

Due to potential flow asymmetry and variable wall friction that wind tunnels often exhibit, it was deemed necessary to map the wind profile of the wind tunnel in the velocity range of the planned experiments. The map of the wind profile was generated at 5 different heights in order to have a detailed picture of the wind velocity profile that both a static and dynamic model would be subjected too. The measured wind velocity profiles are used when calculating the aerodynamic drag, lift and moment coefficients, so that:

$$C_D = \sum_{i=1}^{n} \frac{F_x}{1/2\,\rho U^2 D}\left(\frac{S_i}{L}\right)$$

$$C_L = \sum_{i=1}^{n} \frac{F_y}{1/2\,\rho U^2 D}\left(\frac{S_i}{L}\right)$$

$$C_M = \sum_{i=1}^{n} \frac{F_\theta}{1/2\,\rho U^2 D^2}\left(\frac{S_i}{L}\right)$$

where F_x, F_y and F_θ are the aerodynamic forces measured in the X, Y and θ directions respectively. ρ and D are the density of air and the diameter of the cylinder without ice, respectively. *n* represents a sequential position along the width of the test section and the axis of the model. The numbering is from 1-28 for smooth flow and 1-26 for turbulent flow. S_i is a section length of the model, which is defined by the length between the midpoint of the position of the wind profile point $P_{i-1}$and P_i and wind profile point P_i and P_{i+1}, which can be calculated by $S_i = \frac{1}{2}(\mathrm{P}_{\mathrm{i+1}} + 2\mathrm{P}_{\mathrm{i}} - 3\mathrm{P}_{\mathrm{i-1}})$, where the boundaries at *i* = 1 and *i* = *n(28) or n(26)* are given by $S_1 = \mathrm{P}_1 + \frac{\mathrm{P}_2}{2}$ and $S_n = \frac{1}{2}(L - 3\mathrm{P}_{\mathrm{n-1}} + 2\mathrm{P}_{\mathrm{n}})$. L is the total length of the section model being tested. $U = U_E\left(\frac{U_i}{U_p}\right)$ is the corrected wind velocity for section length S_i for the tested model, where U_i is the wind velocity for point *i* in the wind velocity profile and U_p is the wind velocity obtain from the pitot tube in the wind velocity profile test and finally U_E is the wind velocity obtain from the pitot tube when undertaking the section model experiments.

5.1. Position of wind profiles

As previously mentioned, five horizontal profiles for each wind velocity were measured along the height of wind tunnel test section. The five different heights for the velocity profiles are named H1 to H5 (Fig. 10). For each wind profile, the wind velocity was measured at 28 points across along the width of the test section for smooth flow and 26 points along the width for turbulent flow.

Measurements were taken for all points at 7 distinct wind velocities for smooth flow and 4 distinct wind velocities for turbulent flow. This was done to document any potential Reynolds number effects on the wind profile. Table 2 lists the wind velocities used for the profile measurements. The position of each measurement point along the width of the test section is listed in Table A1 of Appendix A for both smooth and turbulent flow profiles. Note that zero position starts at “Side 2” of the wind tunnel (see Fig. 10). All of the resulting velocity profiles can found in Appendix A.

Table 2.Wind velocities at which the profile was measured for smooth flow

Flow condition	Wind velocities – [m/s]						
Smooth ($I_x \leq 1\%$)	20	25	30	35	40	50	60
Turbulent ($I_x = 6\%-7\%$)	20	25	30	35	-	-	-

By examining the plots, it can be seen that the velocity profiles for smooth flow are more or less symmetric across the width of the wind tunnel for lower wind velocities. For wind velocities higher than 50m/s some skewness seems to develop. For turbulent flow the maximum possible wind velocity was 35 m/s and up to this velocity no noticeable skewness is discernable, although significant “speed-up” near the wind tunnel walls is observed. Contrary to the horizontal velocity profiles, it can be seen that the vertical profiles for turbulent flow vary significantly over the height.

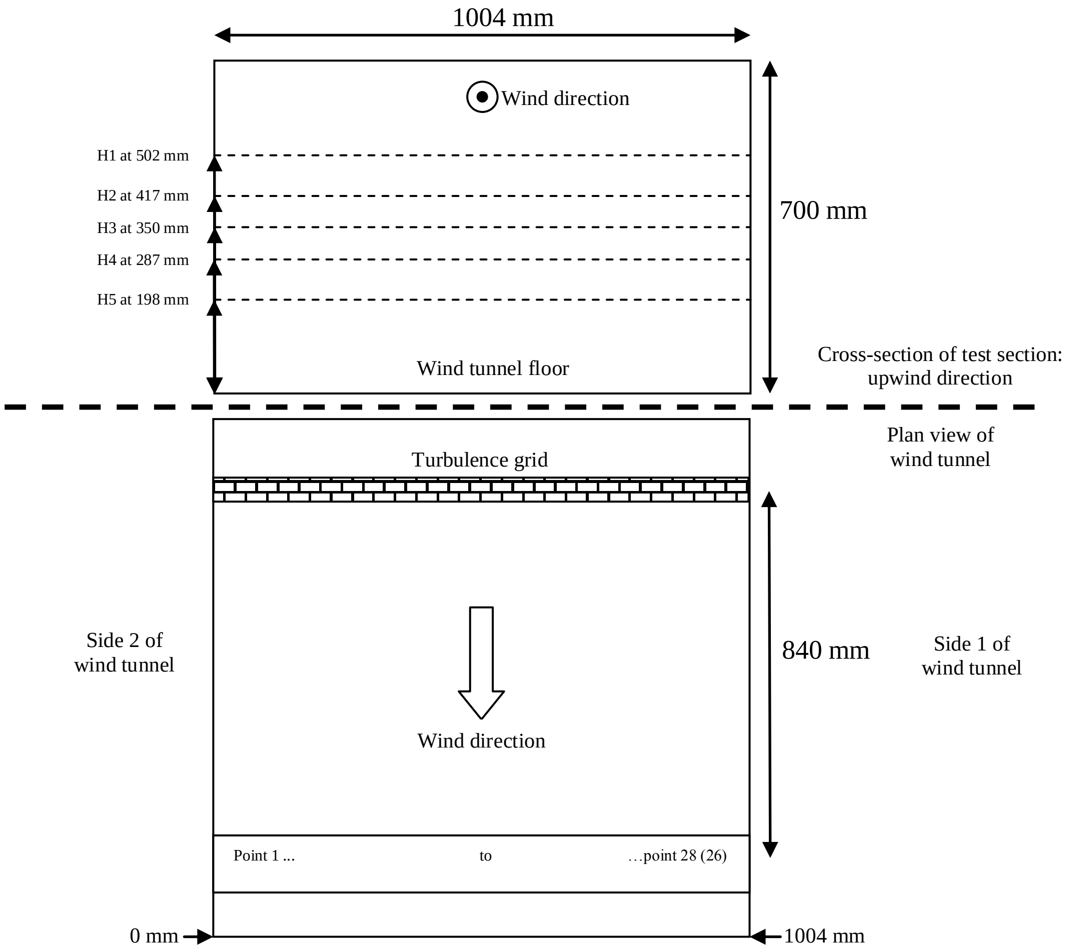
1004 mm
Wind direction
H1 at 502 mm
H2 at 417 mm
H3 at 350 mm
H4 at 287 mm
H5 at 198 mm
700 mm
Wind tunnel floor
Cross-section of test section: upwind direction
Plan view of wind tunnel
Turbulence grid
Side 2 of wind tunnel
840 mm
Side 1 of wind tunnel
Wind direction
Point 1 ...
to
…point 28 (26)
0 mm
1004 mm

Figure 10. Cross-section (top) and plan view (bottom) of the wind tunnel test section showing the vertical and horizontal positions for the wind-profile measurements

6. Section model blockage correction

A list of the tested ice shapes and their resulting blockage during testing is presented in Table 3. The mean blockage is found by taking the mean diameter of the model, except for ice shape I, where the model was not tested for a large range of angles. Here the mean blockage is found by calculating the mean diameter perpendicular to the flow for the range of angles-of-attack tested.

Table 3. Ice shape and blockage for the prescribed wind tunnel tests

Ice shape	D_{mean} = mean(D_i)	D_{max} = max(D_i)	Mean blockage $D_{mean}/D_{section}$	Max blockage $D_{max}/D_{section}$
I	7.56cm	7.67cm	10.78%	10.96%
II	7.20cm	7.74cm	10.29%	11.06%
III	7.14cm	7.39cm	10.20%	10.56%

IV	9.01cm	9.29cm	12.88%	13.27%
V	8.96cm	9.13cm	12.79%	13.04%
VI	7.07cm	7.22cm	10.10%	10.31%
VII	70cm	70cm	10%	10%

The maximum blockage of each model is determined as the ratio between the maximum cable/ice diameter $\boldsymbol{D_{max} = 2r + t_{max}}$ and the cross-sectional height of the tunnel.

Corrections on the measured drag coefficients are made to account for the effect of tunnel blockage. Dalton (1971) presented an improved correction based on an originally proposed correction by Allan & Vincenti (1944), so that:

$$C_D = C_D^{'}\left(1 - \frac{1}{4}\left(\frac{D}{h}\right)^2 - \frac{1}{2}C_D^{'}\left(\frac{D}{h}\right)\right) \tag{2}$$

where $C_D^{'}$ is the measured drag coefficients, D is the cylinders diameter, h is the height of the test section in the wind tunnel and C_D is the corrected drag coefficient.

According to Dalton, the application of Eq. (2) is valid for drag coefficients obtained in wind tunnel tests on circular cylinders in free stream, as long as the blockage generated by the cylinder is less than ~30%. It is assumed that this can be applied herewith, even though the cylinders are not perfectly circular.

7. Test series and results

A series of 30 static wind tunnel tests and 17 dynamic wind tunnel tests were undertaken on cylinders with and without simulated ice accretions. The tests are described below.

7.1. Static tests

The complete static test series is outlined in Table 4. Is should be noted that the test velocity ranges were chosen so as to lie in the anticipated regions of galloping instability. The critical vortex-shedding velocity for the tested cylinders is below 1m/sec.

The resulting drag, lift and moment coefficients obtained from the static tests are presented in Figs. 12-23. All of the figures, except Fig. 12, show the resulting coefficients for smooth and turbulent flow in the top and bottom rows, respectively. Fig. 12 shows the effect of the change in surface roughness and will be discussed later. All aerodynamic force coefficients have been corrected according to the measured velocity profiles and for blockage.

Table 4. Test series employing static rig

Ice shape	Flow	Surface of simulated ice accretion	Wind velocity [m/s]	Wind angles of attack [°]	Hysteresis check at angles
I	Smooth	Rough	[22, 27, 31, 36, 41]	[0, 10, 20, 30, 40]	-
	Smooth	Smooth	[22, 27, 31, 36, 41]	[0, 10, 20, 30, 40]	-
II	Smooth	Rough	[22, 27, 31, 36, 41]	[-90, -85,…, 85, 90]	-
	Turbulent	Rough	[13, 17, 22, 27]	[-90, -85,…, 85, 90]	-
III	Smooth	Rough	[22, 27, 31, 36, 41]	[-90, -85,…, 85, 90]	-
	Turbulent	Rough	[13, 17, 21, 27]	[-90, -85,…, 85, 90]	-
IV	Smooth	Rough	[22, 27, 31, 36, 41]	[-90, -85,…, 85, 90]	[-90, -80,…, 80, 90]
	Turbulent	Rough	[13, 17, 22, 27]	[-90, -85,…, 85, 90]	[-90, -80,…, 80, 90]
V	Smooth	Rough	[22, 27, 31, 36, 41]	[-90, -85,…, 85, 90]	[-90, -80,…, 80, 90]
	Turbulent	Rough	[13, 17, 22, 27]	[-90, -85,…, 85, 90]	[-90, -80,…, 80, 90]
VI	Smooth	Rough	[22, 27, 31, 36, 41]	[0, 5,…, 175, 180]	-
	Turbulent	Rough	[13, 17, 22, 27]	[0, 5,…, 175, 180]	-
VII	Smooth	No ice	[22, 27, 31, 36, 41]	-	-
	Turbulent	No ice	[13, 17, 22, 27]	-	-

7.1.1. Reynolds number test

A Reynolds number test was performed on a smooth reference circular cylinder, labeled shape VII in Table 4. The smooth cylinder was tested under both smooth and turbulent flow. The results of these two Reynolds number tests are presented in Fig. 11. It is seen that the critical Reynolds number range for the turbulent flow is obtained for much lower Reynolds numbers. From this, it can be inferred that for turbulent flow the critical Reynolds number range was included in the test program for all cylinders. For smooth flow, it can be seen that the aerodynamic drag coefficient of the smooth cylinder is more or less constant for the whole range of Reynolds numbers.

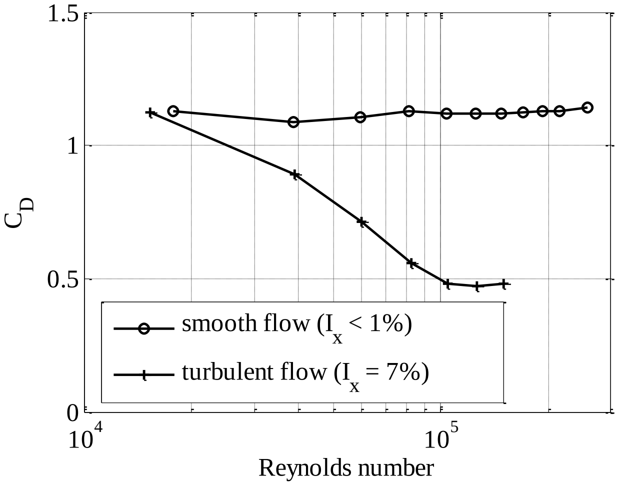

Figure 11. Reynolds number tests in smooth and turbulent flow on a smooth reference circular cylinder (ice shape VII)

7.1.2. Surface roughness effect

As the small series of Reynolds number tests indicated, Reynolds number effects can be observed when comparing the drag coefficients of smooth cylinders with and without turbulence. A series of tests were performed on ice shape I, in order to understand the effect of the surface roughness and the results are presented in Fig. 12. Here, the rapidly prototyped model was first tested with inherent surface roughness of the model after production. Then this was followed by a test where the model surface had been coated with four layers of varnish to create a smooth surface. The tests show that the difference in drag and moment coefficients is small for most wind angles-of-attack – the exclusion being wind angle-of-attack of 10° for 22m/sec wind velocity. No explanation can currently be provided for this. On the other hand, the lift force is prone to large variations with changes in surface roughness.

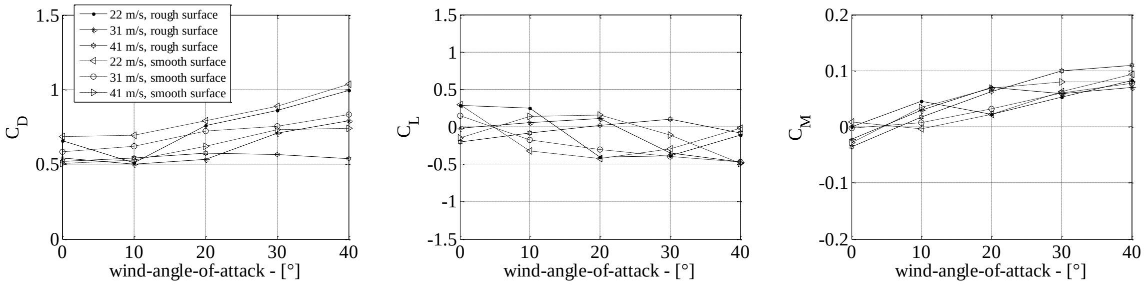

Figure 12. Static force coefficients for ice shape I, with varying model surface roughness

The tests clearly demonstrate the effect of surface roughness on the force coefficients and show that, although dominant for the resulting flow field, cross-sectional shape is not the only parameter that affects the generated forces on an iced cylinder. In any case, as the roughness on an iced cylinder is not only difficult to measure, but it also varies greatly from one condition to another, it was deemed adequate to use the aforementioned manufactured roughness from the rapid prototyping process. Furthermore, the roughness obtained from this manufacturing process was found to be qualitatively similar to that observed during the icing wind-tunnel tests.

7.1.3. Force coefficients

Figs. 13 and 14 show the resulting force coefficients for ice shapes II and III. It is seen that the Reynolds number effects are most pronounced for turbulent flow and are particularly evident when examining the lift coefficient, C_L, for ice shape III. Furthermore, there are Reynolds number effects present for the drag coefficient, C_D, for a range of wind angles-of-attack, namely around -50° and +50°. For the moment coefficient, C_M, it is seen that the Reynolds number effect is only present for ice shape III in turbulent flow, for wind angles-of-attack about -25° and +25°.

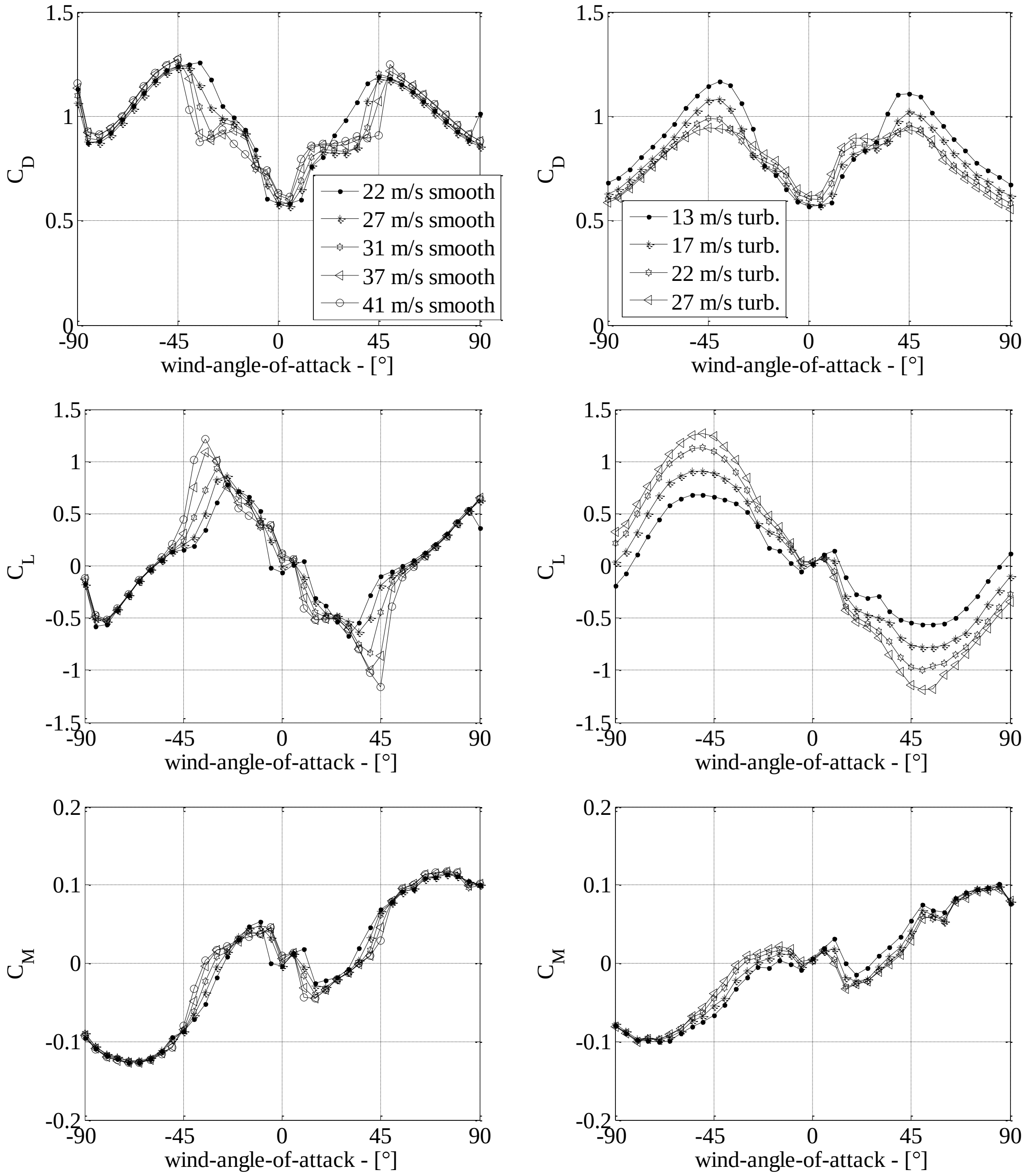

Figure 13. Static force coefficients for ice shape II: smooth flow (left) and turbulent flow (right)

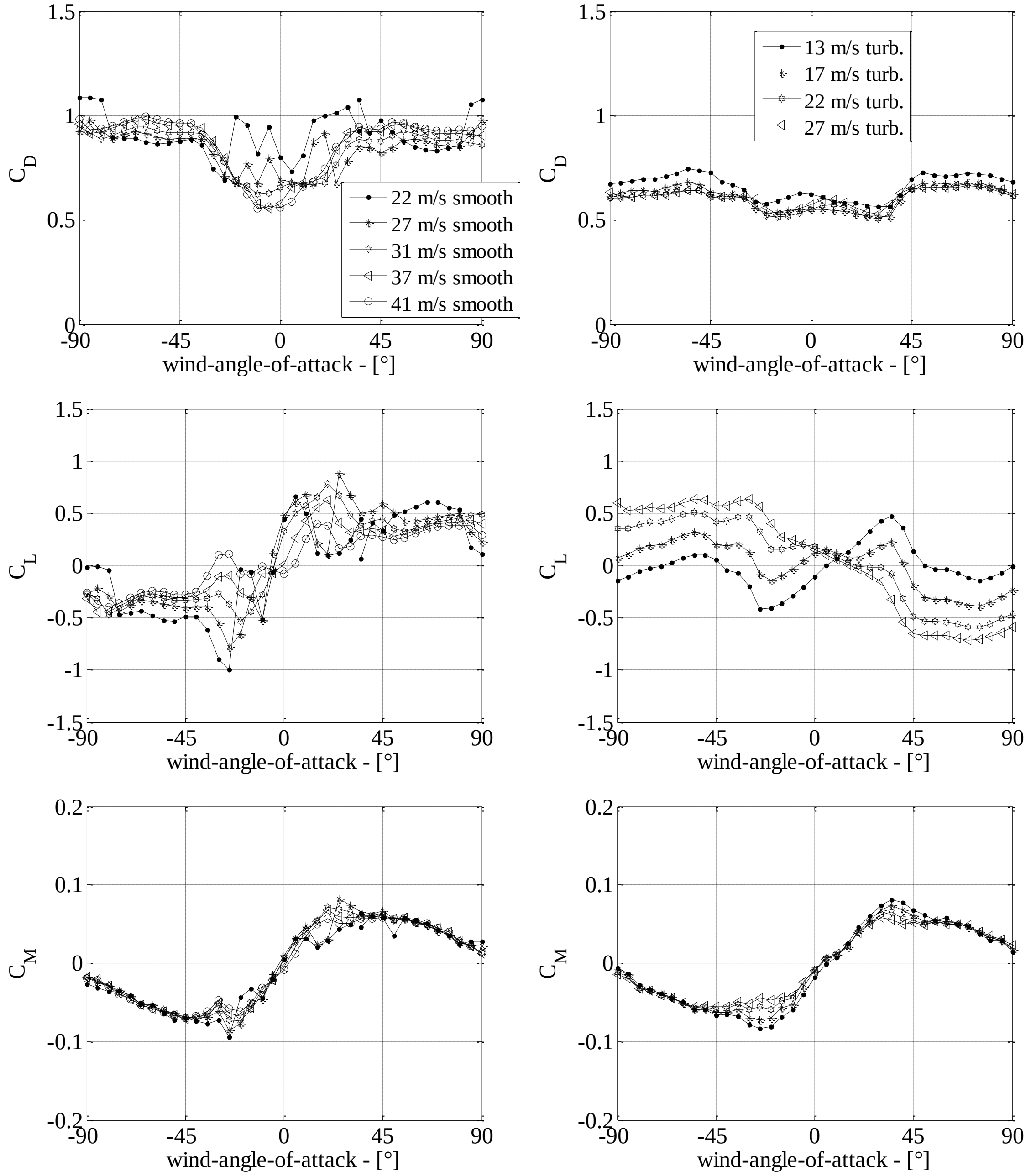

Figure 14. Static force coefficients for ice shape III: smooth flow (left) and turbulent flow (right)

The force coefficients for ice shapes IV and V are presented in Figs.15 and 16. Once again, the same trend of greater Reynolds number dependency for turbulent flow is observed. For the drag coefficients, the Reynolds number dependency seems to follow critical Reynolds number range identified in Fig. 10. For the lift force coefficients, the Reynolds number dependency is concentrated for angles less than -30° and greater than +30°, except for at narrow range close to the stagnation point (0°). No significant Reynolds number dependency is found for the moment coefficients.

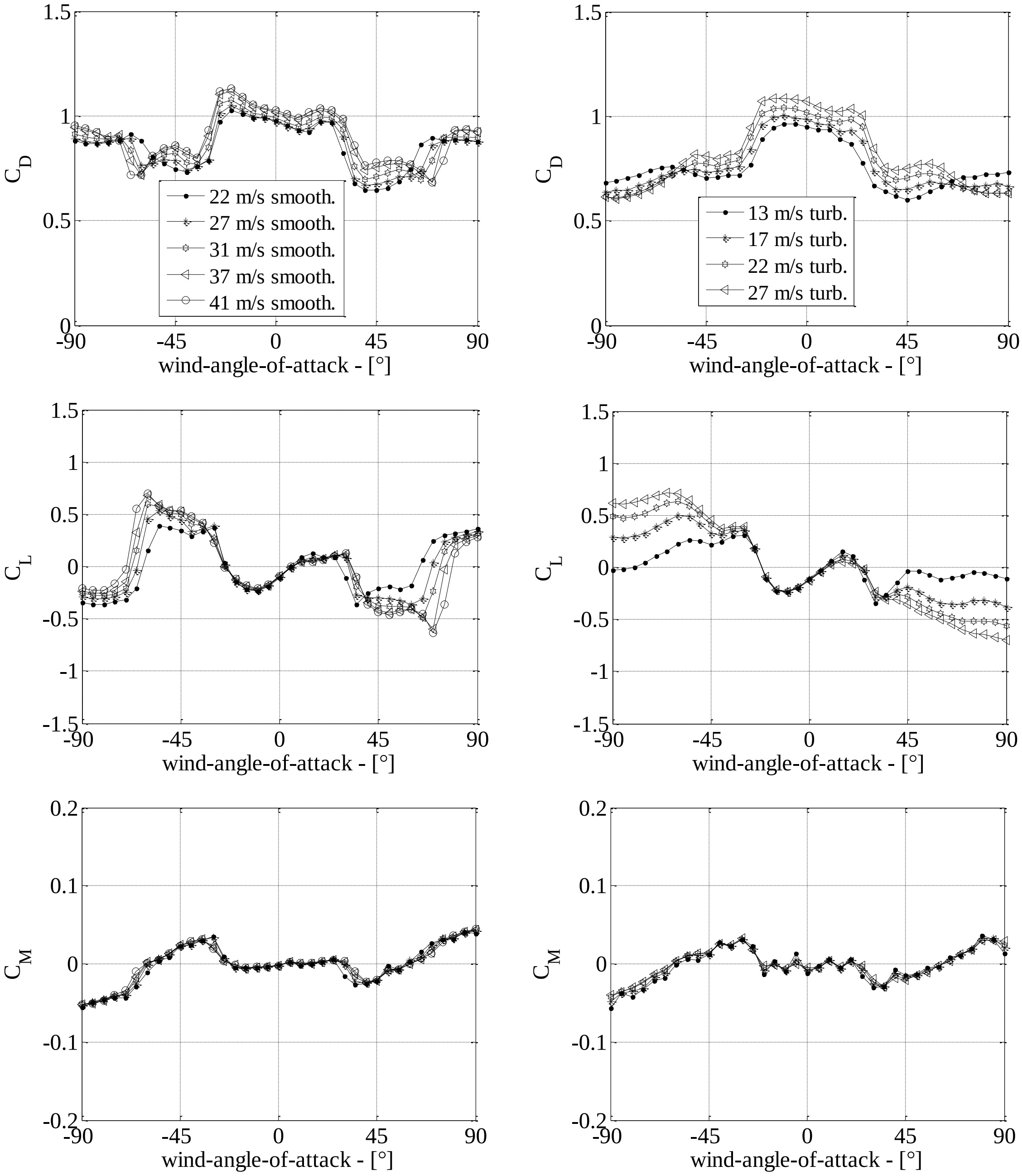

Figure 15. Static force coefficients for configuration IV: smooth flow (left) and turbulent flow (right)

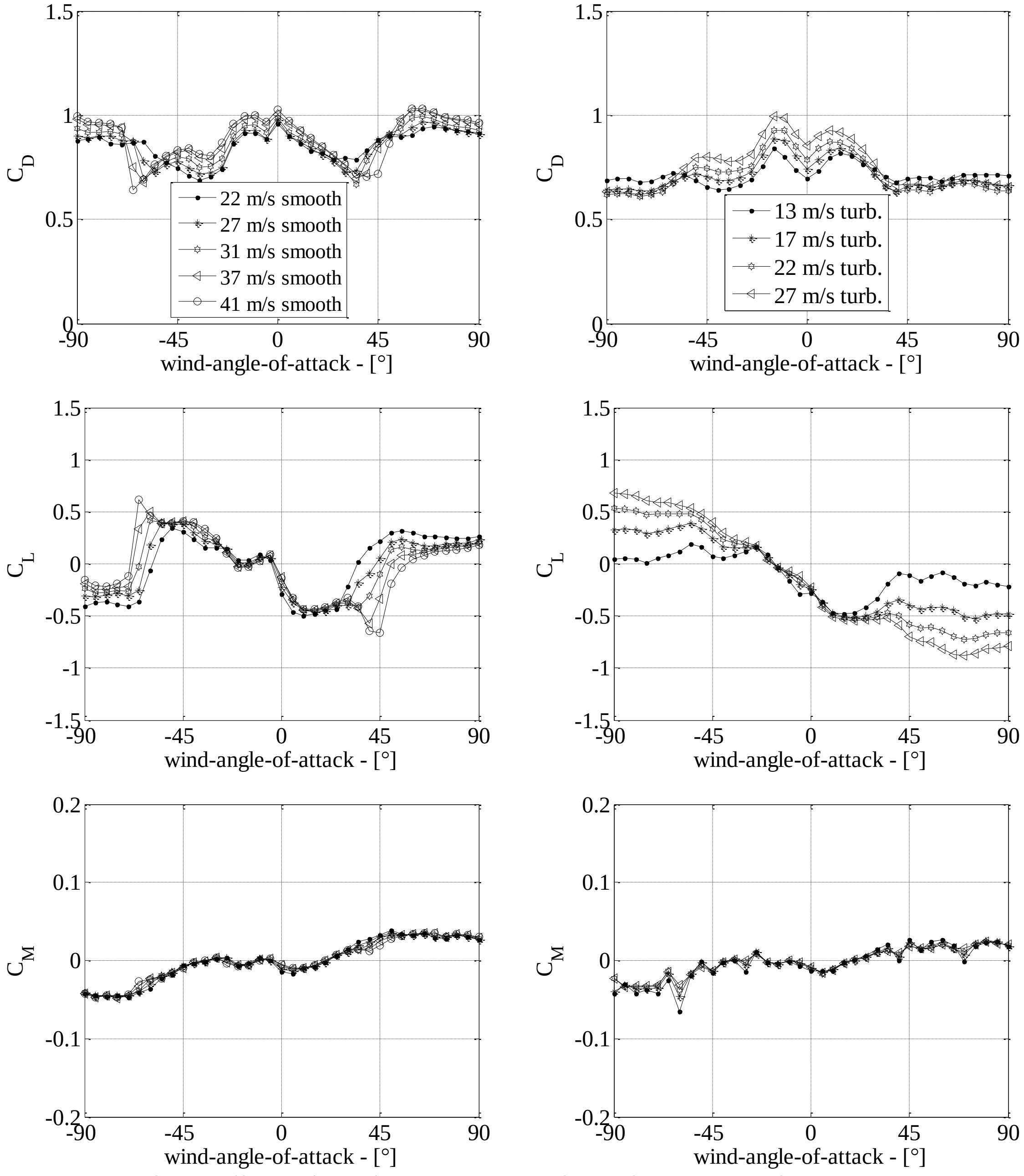

Figure 16. Static force coefficients for configuration V: smooth flow (left) and turbulent flow (right)

For ice shape VI, the drag and lift coefficients (Fig. 17) generally exhibit Reynolds number dependency for both smooth and turbulent flow. The moment coefficients exhibit Reynolds number dependency for turbulent flow between wind angles-of-attack 10° and 75°.

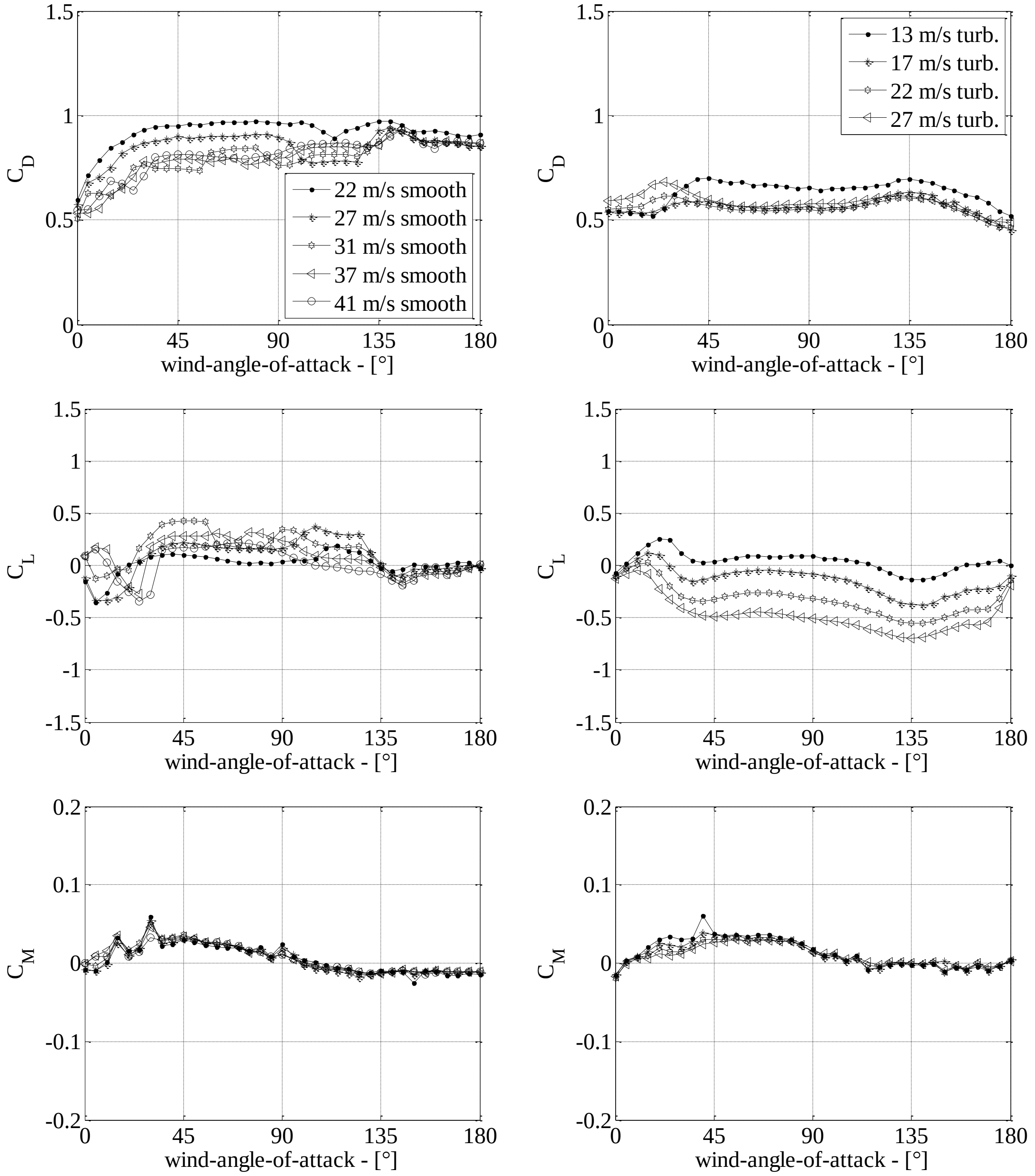

Figure 17. Static force coefficients for configuration VI: smooth flow (left) and turbulent flow (right)

A closer examination of the drag and lift coefficients for ice shape VI reveals a dependency of the drag on the lift and vice-versa. A sudden drop or rise in the lift force is often accompanied by a sudden rise or drop in the drag. This may indicate a shift in the location of a flow separation bubble. Further work would be needed to verify this.

Finally, checks for hysteresis in respect to wind velocity where performed. Hysteresis is defined here as a noticeable change to the force coefficients for a particular wind angle-of-attack and velocity when testing the model in the wind tunnel by rotating it in one direction and then rotating it back in the opposite direction for varying wind velocities. This was done for ice shapes IV and V, for both smooth and turbulent flow by rotating the model forward by 5° increments and back by 10° increments. The results for these tests are presented in Fig. 18 and Fig. 19. No significant hysteresis was observed.

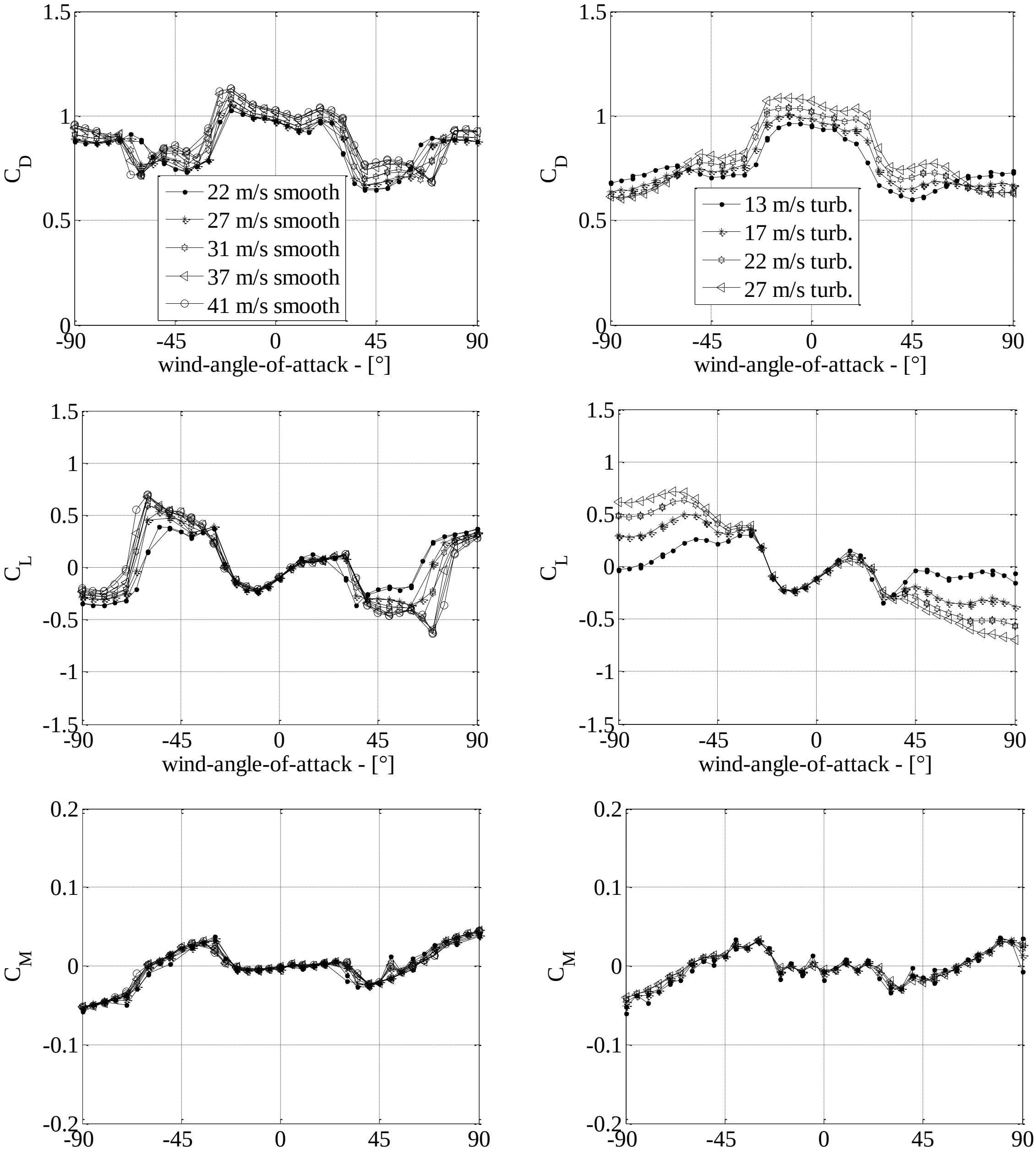

Figure 18. Hysteresis check for ice shape IV: smooth flow (left) and turbulent flow (right)

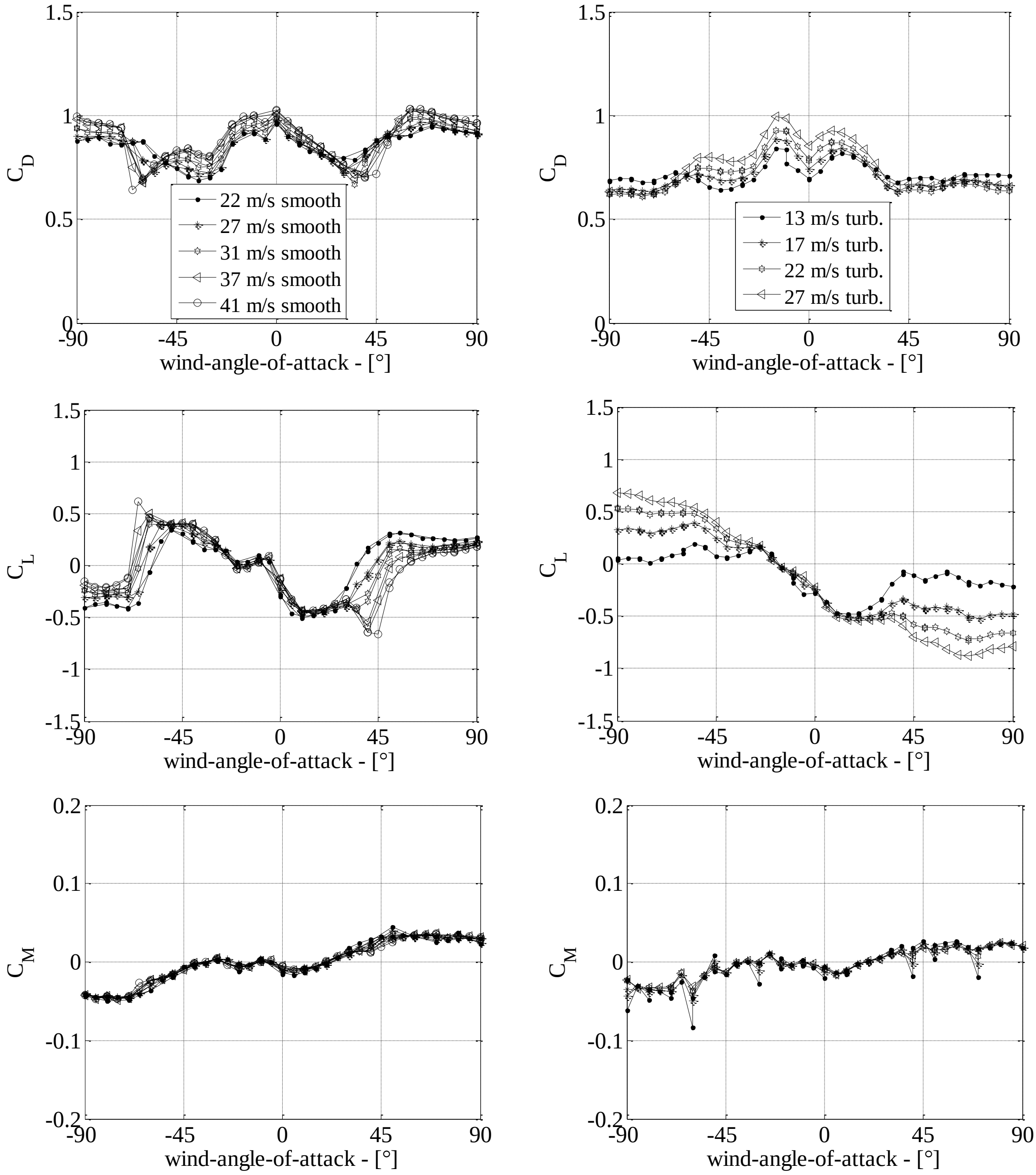

Figure 19. Hysteresis check for ice shape V: smooth flow (left) and turbulent flow (right)

7.2. Dynamic tests

Not all of the ice shapes were tested dynamically. The models with ice shapes that were tested dynamically were given dynamic properties of an example cable, equivalent to a typical scaled suspension bridge hanger. Furthermore, the ice shapes used for the dynamic testing were chosen so as to be similar to those observed when large amplitude hanger vibrations were recorded on the Great Belt Suspension Bridge in Denmark (Gjelstrup, Georgakis *et al.* 2007). The ice shapes visually observed during this vibration event were very thin, with small protrusions of ice. Qualitatively, these are very similar to ice shapes IV and V. Furthermore, generic ice shape VI was also chosen for ease of repeatability of future experiments. Finally, the reference cylinder with ice shape VII was also tested.

Table 5 outlines the test series, whilst Table 6 presents the model parameters for the dynamic tests, namely vertical and torsional frequencies and damping, and the mass and mass moments of inertia.

Table 5. Dynamic test series

Ice shape	Flow	Surface of ice	Wind velocity [m/s]	Angles [°]	Hysteresis check for wind velocitys
IV	Smooth	Rough	[22, 27, 31, 36, 41]	[90, 85,…, -85, -90]	[90, 80,…, -80, -90]
	Turbulent	Rough	[13, 17, 22, 27]	[-90, -85,…, 85, 90]	[-90, -80,…, 80, 90]
V	Smooth	Rough	[22, 27, 31, 36, 41]	[90, 85,…, -85, -90]	[90, 80,…, -80, -90]
	Turbulent	Rough	[13, 17, 22, 27]	[-90, -85,…, 85, 90]	[-90, -80,…, 80, 90]
VI	Smooth	Rough	[22, 27, 31, 36, 41]	[0, 5,…, 175, 180]	-
	Turbulent	Rough	[13, 17, 22, 27]	[0, 5,…, 175, 180]	-
VII	Smooth	No ice	[22, 27, 31, 36, 41]	-	-

Table 6. Model dynamic properties used for dynamic testing

Ice shape	Vibration [direction]	Freq [Hz]	Damping [% of crit.]	Rig+Model Mass [kg]	MMI [kg·m³/m]
IV	Vertical	1.63	0.08	10.25	0.35
	Torsional	4.99	0.43		
V	Vertical	1.64	0.08	10.14	0.36
	Torsional	4.97	0.41		
VI	Vertical	1.64	0.07	10.14	0.38
	Torsional	4.99	0.56		
VII	Vertical	1.65	0.06	10.01	0.37
	Torsional	4.99	0.51		

The measured dynamic response for each ice shape is presented in Figs. 20-22. The results are presented as the non-dimensionalized standard deviation (STD) of the vertical displacement (top) and the STD of the angular rotation for pitch (axial rotation) (middle) and roll (bottom). The results are presented for both smooth and turbulent flow. Plots for smooth flow are on the left, whilst plots for turbulent flow are placed to the right.

No instabilities were found in the experiments preformed on the reference cylinder (shape VII).

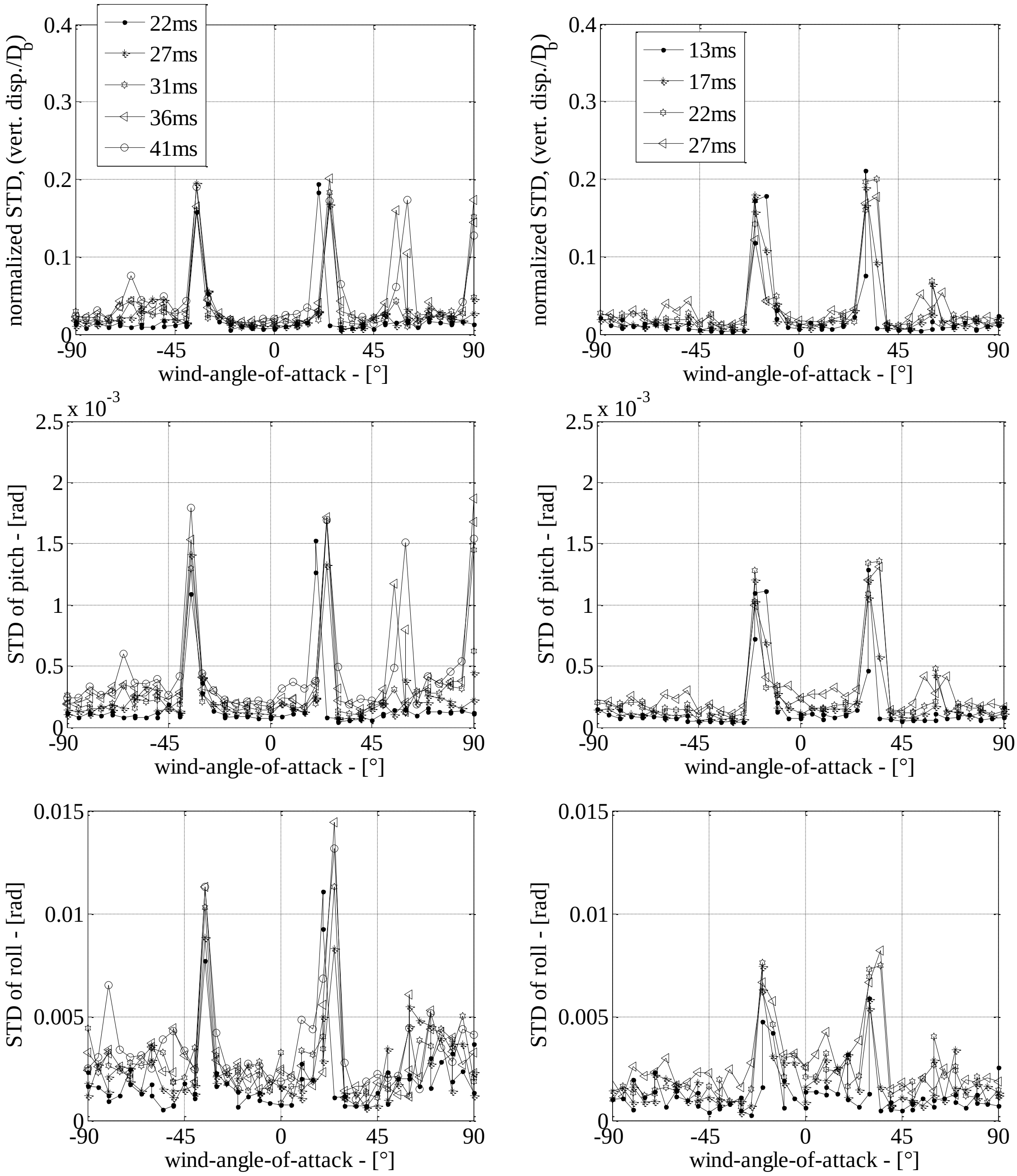

Figure 20. Dynamic response for model with ice shape IV. Non-dimensionalised STD of vertical displacement (top), STD of pitch in radians (middle) and STD of roll in radians (bottom). Smooth flow (left) and turbulent flow (right).

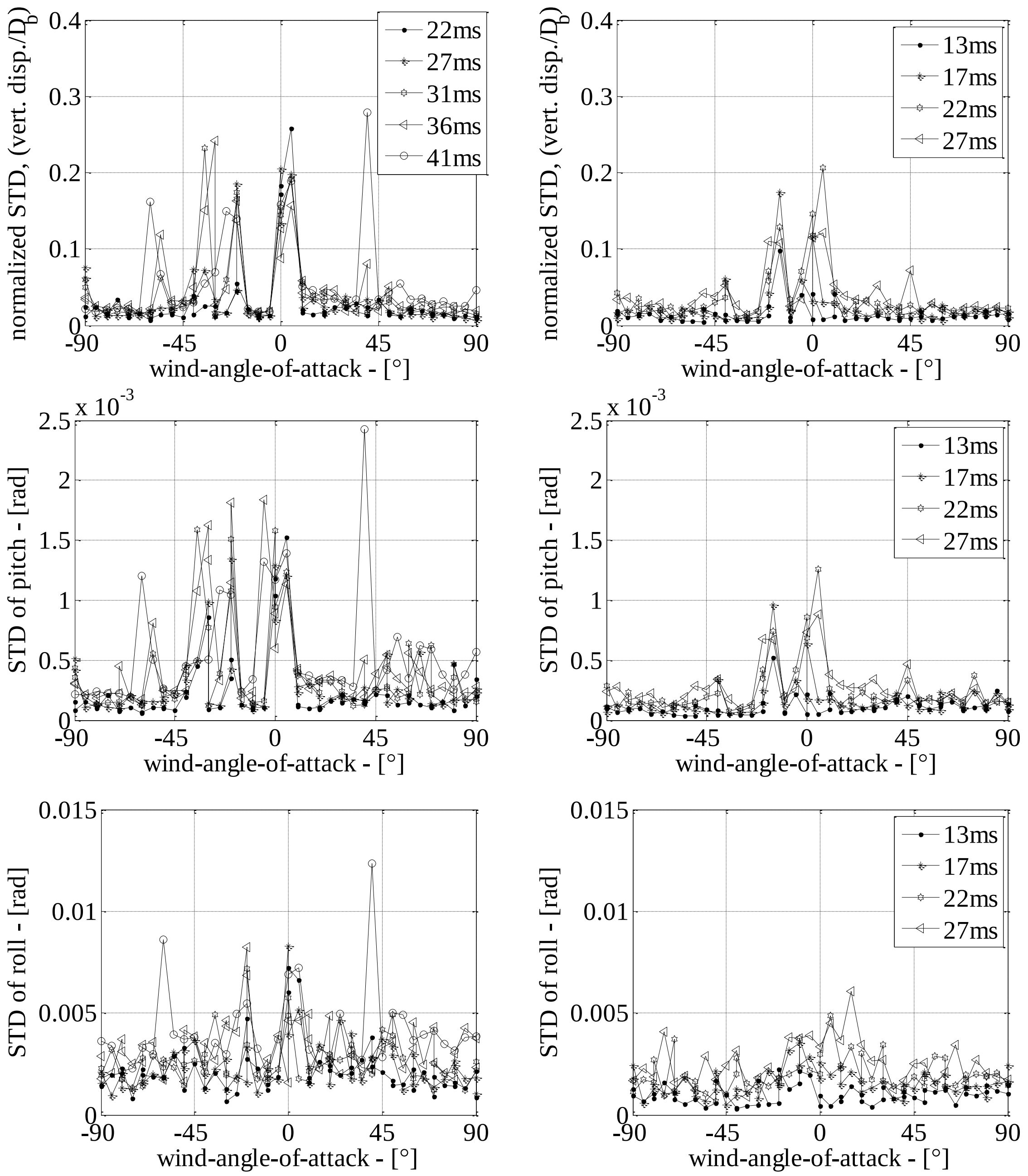

Figure 21. Dynamic response for model with ice shape V. Non-dimensionalised STD of vertical displacement (top), STD of pitch in radians (middle) and STD of roll in radians (bottom). Smooth flow (left) and turbulent flow (right).

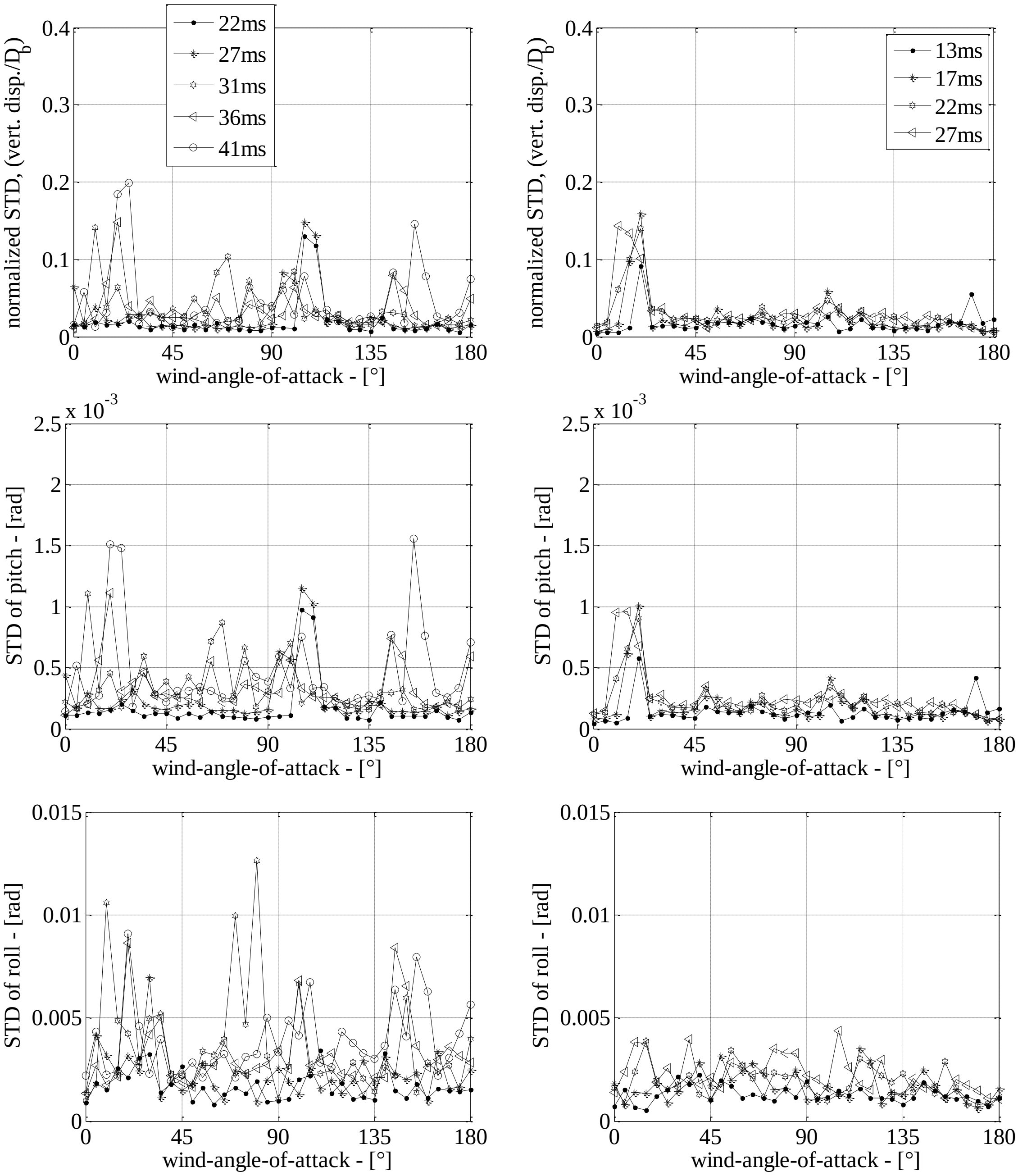

Figure 22. Dynamic response for model with ice shape VI. Non-dimensionalised STD of vertical displacement (top), STD of pitch in radians (middle) and STD of roll in radians (bottom). Smooth flow (left) and turbulent flow (right).

For the purposes of analyzing the figures and, later, for the development of instability plots, motional "instability" is defined as any normalized STD vertical displacement greater than 0.05, i.e. 5% of the base cylinder diameter.

For the turbulent flow tests, it can be seen that motional instability in the vertical direction occurs near 0° wind angle-of-attack. This is particularly true for ice shapes V and VI, where instability is observed exclusively in the range ±20°. Instability for configuration IV in turbulent flow occurs within two intervals on each side of the stagnation point (0°), namely between -25° and -10°, and between 25° and 40°.

For the smooth flow tests, motional instability is generally more scattered. Instability occurs not only in the regions found for turbulent flow, but also for other wind angles-of-attack. Thus, the turbulent flow is shown to exhibit a stabilizing effect for certain angles.

Axial rotational instability, defined as a rotation greater than 0.5×10^{-3} rad, seems to be coincident with vertical instability in most cases. However, it should also be noted that this rotation is relatively small and is most probably due to the offset between the cross-sectional center of mass and center of rotation.

The same picture is more or less observed for roll instability, where the measured response follows the trends observed in the vertical direction.

8. 3-DOF quasi-steady model

The static force coefficients obtained from the static tests were used for a galloping instability analysis employing quasi-steady theory. A adapted version of the 3-DOF quasi-steady model (accounting for the lack of horizontal translation) initially proposed by Gjelstrup and Georgakis (2010) and Gjelstrup *et al.* (2008) was used and is summarized herewith.

Fig. 23 shows a schematic model of a cylinder section with ice accretion. It is assumed that this is representative of an iced hanger section. Also, it is assumed that the model is two-dimensional, with a section that is straight and rigid. The stiffness of the spring supports of the model is constant for all degrees-of-freedom, i.e. stiffness does not change with respect to movement in x and y or rotation about the structural axis (θ). Also it is assumed that the structural damping force is proportional to velocity and that the wind velocity U is constant. Furthermore it is assumed that the rotational velocity can be represented by a cross-sectionally dependant radial length times the radial rotational velocity, $\dot{\theta}$. Finally it is assumed that quasi-steady assumptions apply, that gravitational forces do not influence the model and that the cable is at rest at the initiation of any motional instability.

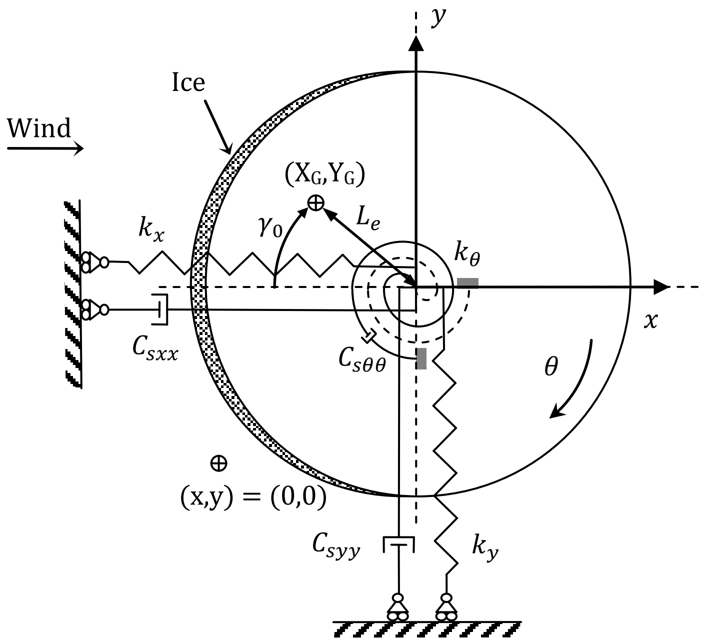

Figure 23. Schematic model of cable section with ice accretion, (X_G,Y_G) = mass centre.

The equations of motion of the model presented in Fig. 23 can be written as:

$$m\ddot{x} + C_{sxx}\dot{x} + k_x x + mL_e\big(cos(\varphi)\,\dot{\theta}^2 + sin(\varphi)\,\ddot{\theta}\big) = F_x \tag{3}$$

$$m\ddot{y} + C_{syy}\dot{y} + k_y y + mL_e\big(-sin(\varphi)\,\dot{\theta}^2 + cos(\varphi)\,\ddot{\theta}\big) = F_y \tag{4}$$

$$J\ddot{\theta} + C_{s\theta\theta}\dot{\theta} + k_\theta\theta + mL_e\big(sin(\varphi)\,\ddot{x} + cos(\varphi)\,\ddot{y} + L_e\ddot{\theta}\big) = F_\theta \tag{5}$$

where the notation for time-dependant variables, $x(t), y(t)$ and $\theta(t)$, is represented as x, y and θ, respectively. Derivatives with respect to time are written as $(d/dt)x = \dot{x}$ and $(d^2/dt^2)x = \ddot{x}$. m is the mass of the system and J is the rotational inertia in relation to the mass centre, C_{sxx} , is the structural damping in the x direction C_{syy} , is the structural damping in the y direction, $C_{s\theta\theta}$, is the structural damping in the θ direction, k_x, k_y and k_θ are the structural stiffnesses in the x, y and θ directions, respectively, L_e is the length to the centre of mass from the point of rotation, $\varphi = \gamma_0 + \theta, \gamma_0$ is the angle offset for mass centre, θ is the structural rotation. F_x, F_y and F_θ are the aerodynamic forces in the x direction, y direction and for torsion respectively, which are given by:

$$F_x = \frac{1}{2}\rho U_R^2 D(C_D(\alpha_R, Re_R)\,cos(\alpha_R) + C_L(\alpha_R, Re_R)\,sin(\alpha_R)) \tag{6}$$

$$F_y = \frac{1}{2}\rho U_R^2 D(C_L(\alpha_R, Re_R)\,cos(\alpha_R) - C_D(\alpha_R, Re_R)\,sin(\alpha_R)) \tag{7}$$

$$F_\theta = \frac{1}{2}\rho U_R^2 D^2 C_M(\alpha_R, Re_R) \tag{8}$$

where $\alpha_R = (\alpha_0 + \theta + \beta)$, α_0 is the static wind-angle-of-attack, β is the angle between static and relative wind directions, Re_R is the relative Reynolds number, ρ is the fluid density, D is the characteristic length of a section model (the diameter for circular models), C_D is the static drag coefficient, C_L is the static lift coefficient and C_M is the static moment coefficient. U_R is the relative wind direction due to structural motion and rotation.

Again, following Gjelstrup and Georgakis (2010), the motional instability of the cable section is determined based on a linearization of the cable section's equations of motion (3)-(5) around the velocity $\dot{x} = \dot{y} = \dot{\theta} = 0$. This linearization results in a dynamic force, which can be represented by the Jacobian damping matrix $(\boldsymbol{C_a})$ multiplied with the sectional velocity in the three directions, $(\boldsymbol{C_a}\dot{Z})$, where $\dot{Z} = [\dot{x}, \dot{y}, \dot{\theta}]'$ and

$$\boldsymbol{C_a} = -\begin{bmatrix} \frac{\partial F_x}{\partial \dot{x}} & \frac{\partial F_x}{\partial \dot{y}} & \frac{\partial F_x}{\partial \dot{\theta}} \\ \frac{\partial F_y}{\partial \dot{x}} & \frac{\partial F_y}{\partial \dot{y}} & \frac{\partial F_y}{\partial \dot{\theta}} \\ \frac{\partial F_\theta}{\partial \dot{x}} & \frac{\partial F_\theta}{\partial \dot{y}} & \frac{\partial F_\theta}{\partial \dot{\theta}} \end{bmatrix}_{\dot{x}=\dot{y}=\dot{\theta}=0} \tag{9}$$

With the aforementioned assumptions, the aerodynamic stability of the 3-DOF cable section can now be evaluated by rewriting Eqs. (3)-(5) into state space and solving the resulting eigenvalue problem.

The proposed 3-DOF quasi-steady galloping instability model can be used to generate 2-dimensional plots of vertical motional instability in the parameter plane of wind angle-of-attack against wind velocity. An example of the application can be viewed in Figs. 24 and 25, where the vertical instability for ice shapes II and III is presented. The greyed areas represent regions of instability, with darker areas denoting a greater need for structural damping to avoid instability. Note that ice shapes II and III were not tested dynamically.

Here again, the effect of turbulence on the predicted instability can be seen. Turbulence has a stabilizing effect and it is hypothesized that might be due to the 3-dimensional velocity fluctuations in the flow which do not allow for well defined flow structures, such as moving separation bubbles, to fully develop.

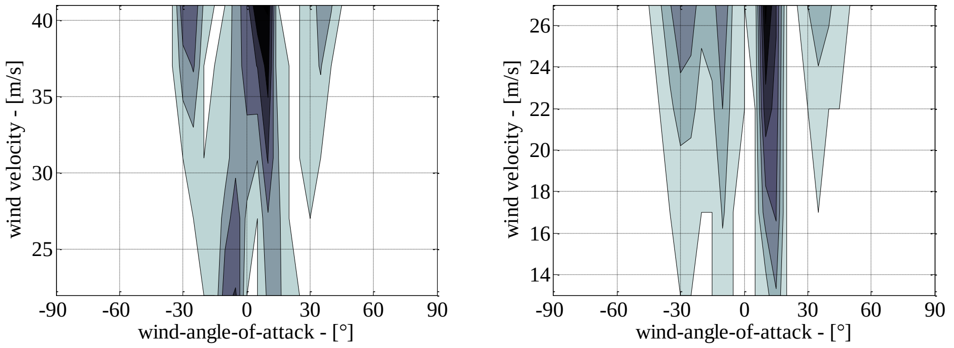

Figure 24. Predicted motional instability for ice shape II using quasi-steady theory. Smooth flow (left) and turbulent flow (right)

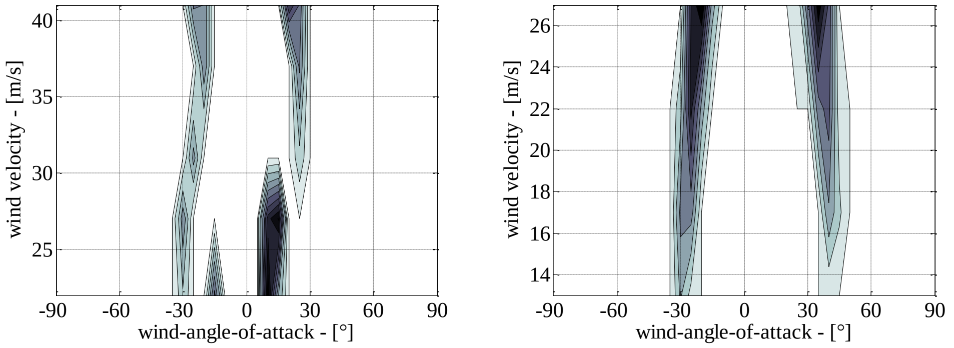

Figure 25. Predicted motional instability for ice shape III using quasi-steady theory. Smooth flow (left) and turbulent flow (right)

9. Comparison of predicted and measured instability

As ice shapes IV-VI were tested dynamically, a comparison between the predicted and determined vertical motional instabilities is made. This comparison can be viewed in Figs. 26-28.

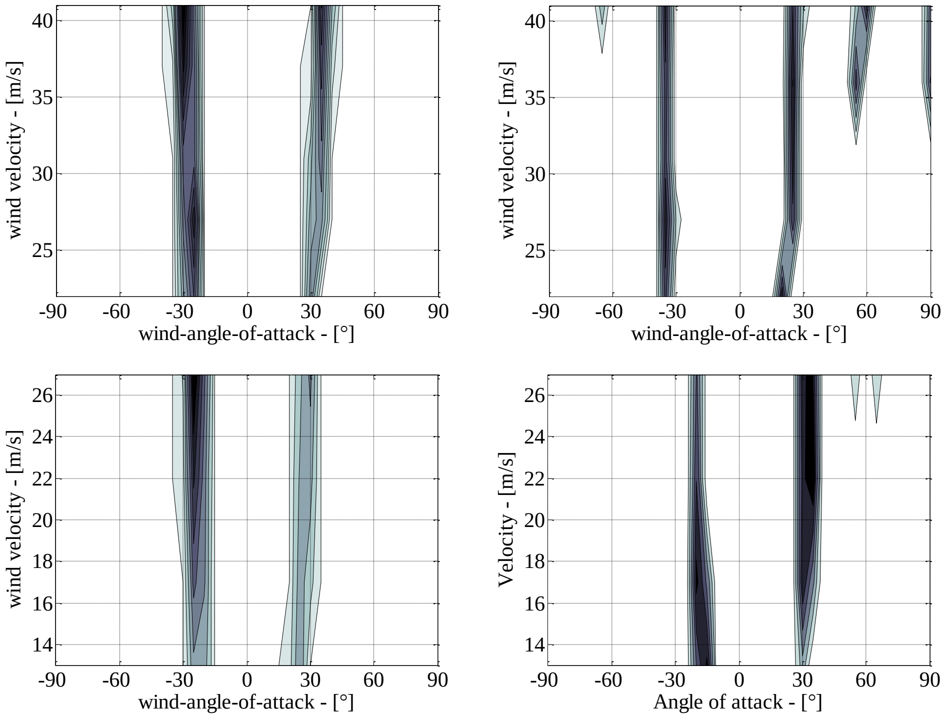

Figure 26. Vertical motional instability for ice shape IV as predicted from quasi-steady theory (left) and as determined from the dynamic tests (right). Smooth flow (top) and turbulent flow (bottom). Unstable regions are shaded. Darker regions indicate increased level of damping needed to avoid instability.

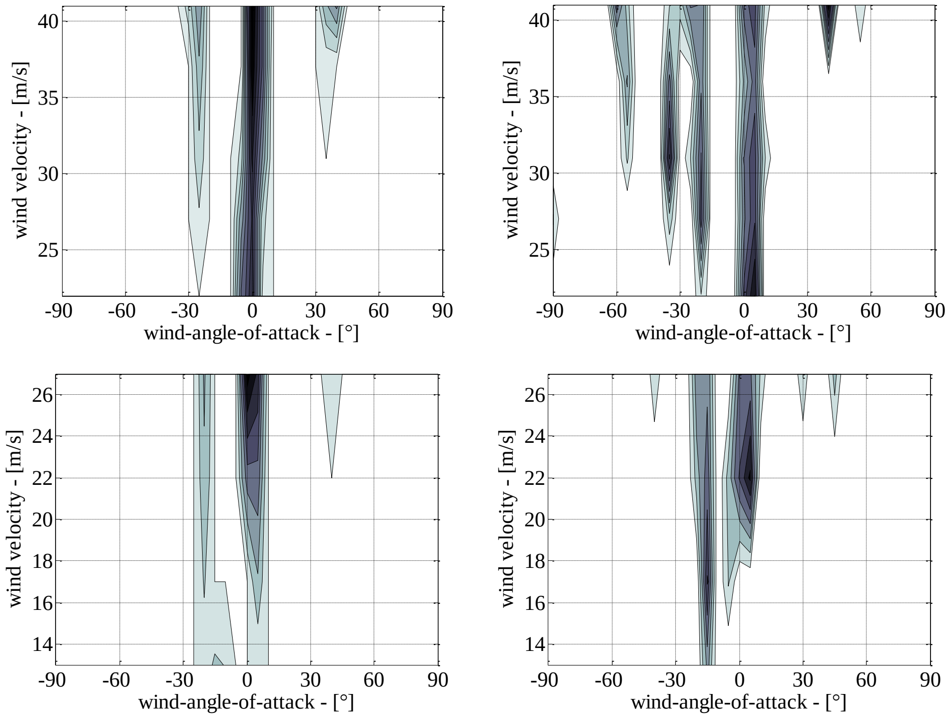

Figure 27. Vertical motional instability for ice shape V as predicted from quasi-steady theory (left) and as determined from the dynamic tests (right). Smooth flow (top) and turbulent flow (bottom). Unstable regions are shaded. Darker regions indicate increased level of damping needed to avoid instability.

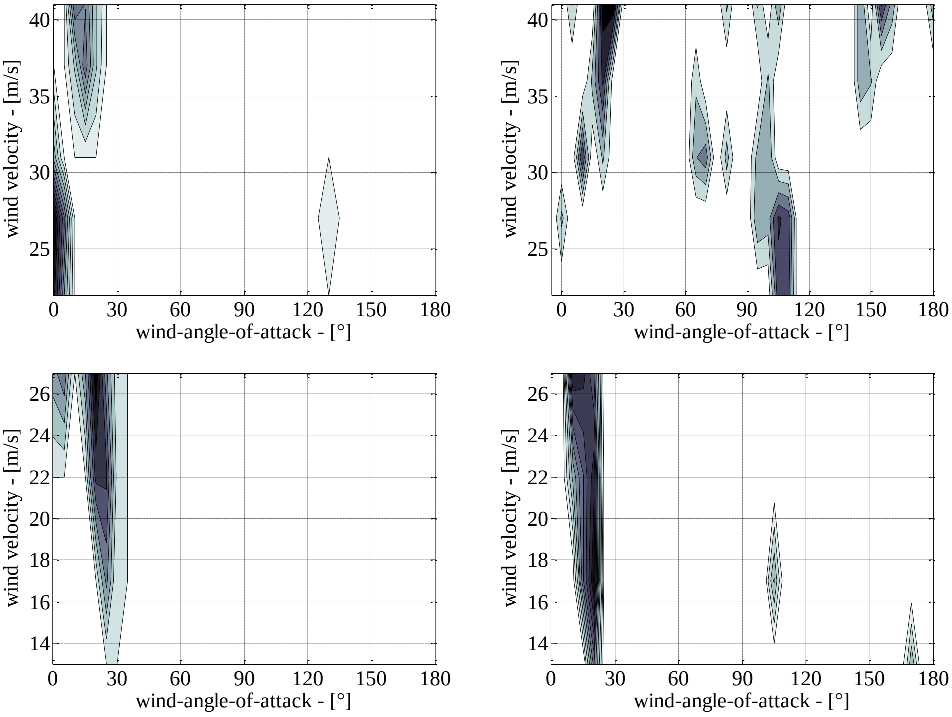

Figure 28. Vertical motional instability for ice shape VI as predicted from quasi-steady theory (left) and as determined from the dynamic tests (right). Smooth flow (top) and turbulent flow (bottom). Unstable regions are shaded. Darker regions indicate increased level of damping needed to avoid instability.

Generally, there is very good agreement between the predicted and measured motional instabilities, although some discrepancies can be evidenced. There are several potential reasons for this, including the small non-linearities in the dynamic test rig, the asymmetric flow conditions and the determination of the ice-accreted cylinder’s cross-sectional radial length (Gjelstrup and Georgakis 2010). The most probable reason for the observed discrepancies though lies with the likely inability of the quasi-steady theory to account for variations in the flow field around the cylinder, due to high velocity/frequency vibrations of the cylinder in the flow.

10. Conclusions

Static wind tunnel tests on a series of (simulated) iced cylinders reveal the effect of ice on the static force coefficients of the cylinder. Utilizing example dynamic properties for the cylinder, application of the force coefficients to an adapted 3-DOF quasi-steady instability model produces regions of predicted vertical motional instability. These regions are predicted for both smooth and turbulent flow. Wind tunnel tests of several of these cylinders using a dynamic rig reveal actual regions of motional instability. When compared, it is shown that the

3-DOF quasi-steady model is good at predicting the vertical motional instability observed from the dynamic wind tunnel tests.

Furthermore, by examining the regions of instability, is can be observed that motional instability of a thinly iced cylinder occurs for wind angles-of-attack that are not far from the ice stagnation point (about 0°). This is an important observation, as it implies that only small changes in wind angle-of-attack are necessary to facilitate cylinder vibrations. This effect has already been hypothesised by Gjelstrup *et al. (2007)* for suspension bridge hangers.

Wind tunnel tests with ice accretions of varying roughness, reveal that roughness plays an important role for the force coefficients of the ice accreted cylinder, particularly for the lift coefficients.

11. References

Allen, H.J. and Vincenti, W.G. (1944), *Wall interference in a two-dimensional-flow wind tunnel, with consideration of the effect of compressibility*,

Anderson, D.N., Hentschel, D.B. and Ruff, G.A. (1998), "Measurement and correlation of ice accretion roughness", *AIAA-98-0486*.

Chabart, O. and Lilien, J.L. (1998), "Galloping of electrical lines in wind tunnel facilities", *J WIND ENG IND AEROD*. **74-6** 967-976.

Dalle, B. and Admirat, P. "Wet snow accretion on overhead lines with French report of experience", *Cold Regions Science and Technology*. **In Press, Corrected Proof**.

Dalton, C. (1971), "Allen and Vincenti blockage corrections in a wind tunnel", *Aiaa J.*, **9**(9), 1864-&.

ESDU (1986), *Mean forces, pressures and flow field velocities for circular cylindrical structures: Single cylinder with two-dimensional flow; ESDU Item 80025*,

Fo-chi, W., Yue-fan, D., Cheng-rong, L., Yu-zhen, L. and Yu-qian, Z. (2009), "Icing Simulation System for Transmission Line", *High Voltage Engineering*. **35**(9), 2313-2316.

Gjelstrup, H. and Georgakis, C. (2010), "A quasi-steady 3-DOF model for the determination of onset for bluff body of galloping instability (submitted)", *J FLUID STRUCT*.

Gjelstrup, H., Georgakis, C. and Koss, H. (2009), "Experimental study of icing at high temperature and low wind speeds on stationary cylinders of different diameter and orientation".

Gjelstrup, H., Georgakis, C. and Larsen, A. (2007), *A preliminary Investigation of the hanger vibrations on the Great Belt East Bridge*, Vienna (Austria).

Gjelstrup, H., Larsen, A., Georgakis, C. and Koss, H. (2008), *A new general 3DOF quasi-steady aerodynamic instability model*, Milano, Italy, .

Gurung, C.B., Yamaguchi, H. and Yukino, T. (2002), "Identification of large amplitude wind-induced vibration of ice-accreted transmission lines based on field observed data", *Engineering Structures*. **24**(2), 179-188.

Hack, R.K. (1981), *A wind tunnel investigation of four conductor models with simulated ice deposits*, National aerospace laboratory NLR, The Netherlands

Hansman, R.J., Breuer, e.S., Hazan, D., Reehorst, A. and Vargas, M. (1993), "Close-up analysis of aircraft ice accretion", *Aiaa J.*

Jamaleddine, A., McClure, G., Rousselet, J. and Beauchemin, R. (1993), "Simulation of ice-shedding on electrical transmission lines using adina", *Computers & Structures*. **47**(4-5), 523-536.

Kudzys, A. (2006), "Safety of power transmission line structures under wind and ice storms", *Engineering Structures*. **28**(5), 682-689.

Lozowski, E.P., Stallabrass, J.R. and Hearty, P.F. (1983), "The icing of an unheated, nonrotating cylinder .I. A simulation-model", *Journal of Climate and Applied Meteorology*. **22**(12), 2053-2062.

Lozowski, E.P., Stallabrass, J.R. and Hearty, P.F. (1983), "The icing of an unheated, nonrotating cylinder. II. Icing wind tunnel experiments", *Journal of Climate and Applied Meteorology* **22**(12), 2063-2074.

McComber, P. and Paradis, A. (1995), "Simulation of the galloping vibration of a 2-dimensional iced cable shape", *Transactions of the Canadian Society for Mechanical Engineering*. **19**(2), 75-92.

Nigol, O. and Buchan, P.G. (1981), "Conductor galloping .1. Den Hartog mechanism", *Ieee Transactions on Power Apparatus and Systems*. **100**(2), 699-707.

Nigol, O. and Clarke, G.J. (1974), "Conductor galloping and control based on torsional mechanism", *Ieee Transactions on Power Apparatus and Systems*. **PA93**(6), 1729-1729.

Nigol, O.B., P. G. (1981), "Conductor galloping .2. torsional mechanism", *Ieee Transactions on Power Apparatus and Systems*. **100**(2), 708-720.

Phuc, P.V. (2005), *A wind tunnel study on unstady forces of ice accreted transmission lines*,

Shimizu, M. (2005), *A wind tunnel study on aerodynamic characteristics of ice accreted transmission lines*, Szilder, K. and Lozowski, P., Edward (2004), "Novel two-dimensional modeling approach for aircraft icing", *J. Aircr.*, **41**(4).

Wang, F., Li, C., Lv, Y., Lv, F. and Du, Y. (2010), "Ice accretion on superhydrophobic aluminum surfaces under low-temperature conditions", *Cold Regions Science and Technology*. **62**(1), 29-33.

Appendix A: Velocity profiles

Table A. Positions measured, starting from "Side 2" of the wind tunnel

smooth flow

Point	*1*	*2*	*3*	*4*	*5*	*6*	*7*	*8*	*9*	*10*	*11*	*12*	*13*	*14*
Position [mm]	12	19	26	33	40	47	54	61	68	75	122	232	342	452
Point	*15*	*16*	*17*	*18*	*19*	*20*	*21*	*22*	*23*	*24*	*25*	*26*	*27*	*28*
Position [mm]	562	672	782	892	925	932	939	946	953	960	967	974	981	988

turbulent flow

Point	*1*	*2*	*3*	*4*	*5*	*6*	*7*	*8*	*9*	*10*	*11*	*12*	*13*	*14*
Position [mm]	9	16	23	30	37	44	51	58	63	72	116	226	336	667
Point	*15*	*16*	*17*	*18*	*19*	*20*	*21*	*22*	*23*	*24*	*25*	*26*	-	-
Position [mm]	777	887	931	938	945	952	959	966	973	980	987	994	-	-

11.1. Plots of the velocity profiles

The following section shows the five different velocity profiles found at different wind velocities and turbulent intensities.

Smooth flow

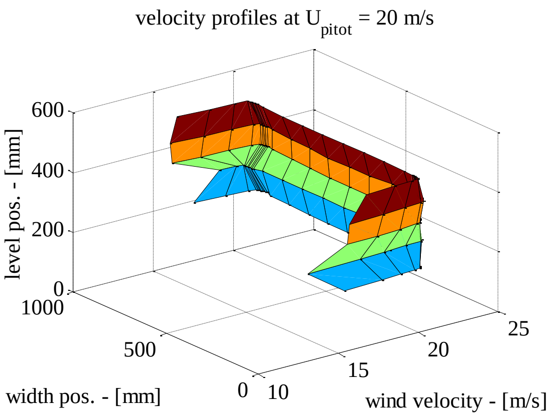
velocity profiles at U_{pitot} = 20 m/s
level pos. - [mm]
600
400
200
0
1000
500
0
width pos. - [mm]
10
15
20
25
wind velocity - [m/s]

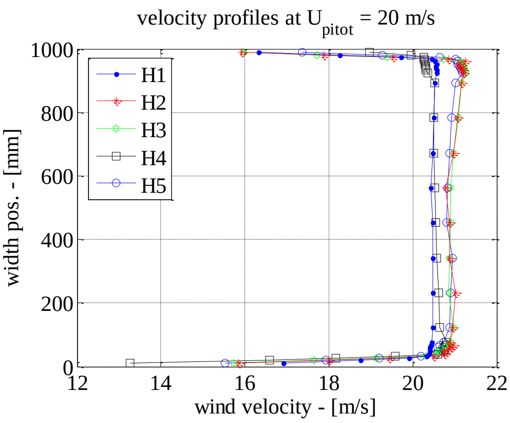
velocity profiles at U_{pitot} = 20 m/s
width pos. - [mm]
1000
800
600
400
200
0
12
14
16
18
20
22
wind velocity - [m/s]
H1
H2
H3
H4
H5

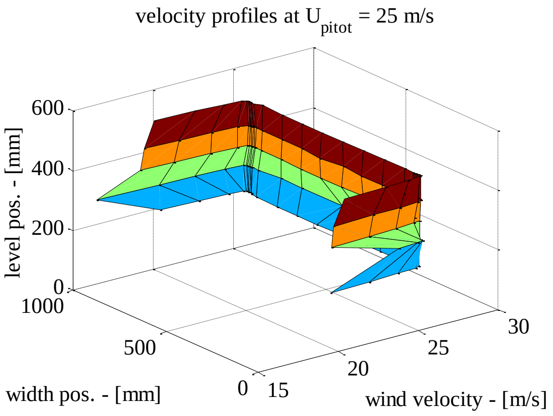
velocity profiles at U_{pitot} = 25 m/s
level pos. - [mm]
600
400
200
0
1000
500
0
width pos. - [mm]
15
20
25
30
wind velocity - [m/s]

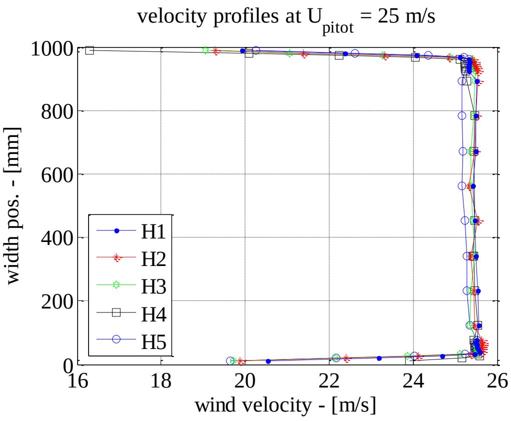
velocity profiles at U_{pitot} = 25 m/s
width pos. - [mm]
1000
800
600
400
200
0
16
18
20
22
24
26
wind velocity - [m/s]
H1
H2
H3
H4
H5

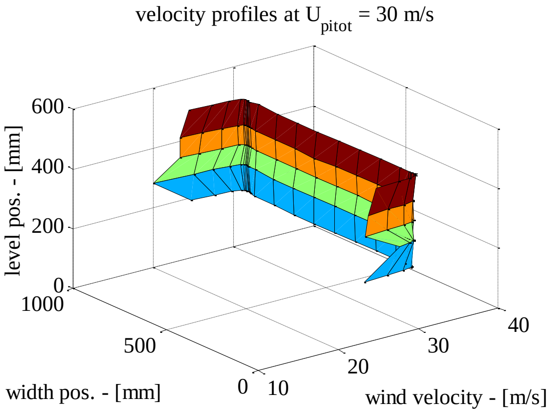
velocity profiles at U_{pitot} = 30 m/s
level pos. - [mm]
600
400
200
0
1000
500
0
width pos. - [mm]
10
20
30
40
wind velocity - [m/s]

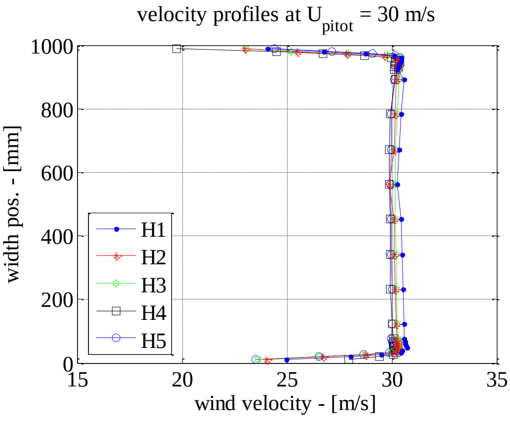
velocity profiles at U_{pitot} = 30 m/s
width pos. - [mm]
1000
800
600
400
200
0
15
20
25
30
35
wind velocity - [m/s]
H1
H2
H3
H4
H5

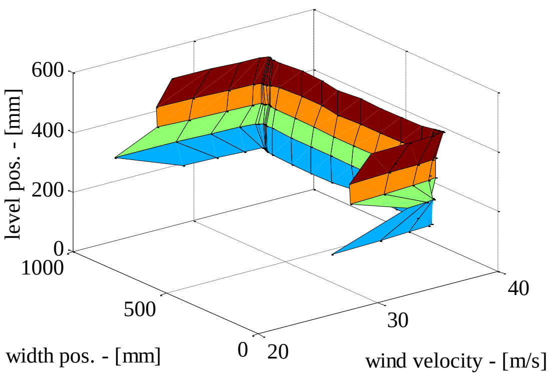
velocity profiles at U_{pitot} = 35 m/s

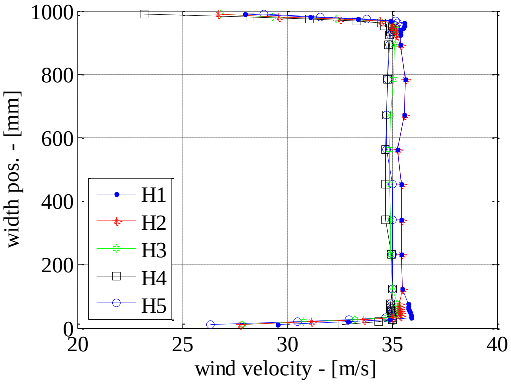
velocity profiles at U_{pitot} = 35 m/s

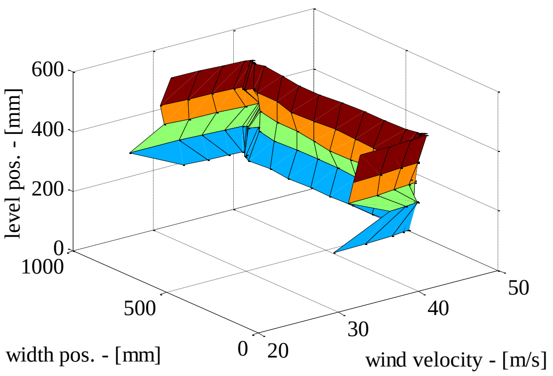
velocity profiles at U_{pitot} = 40 m/s

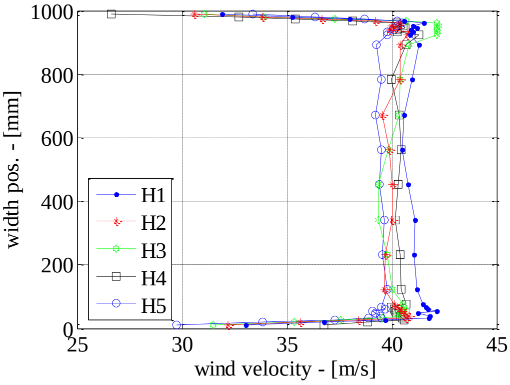
velocity profiles at U_{pitot} = 40 m/s

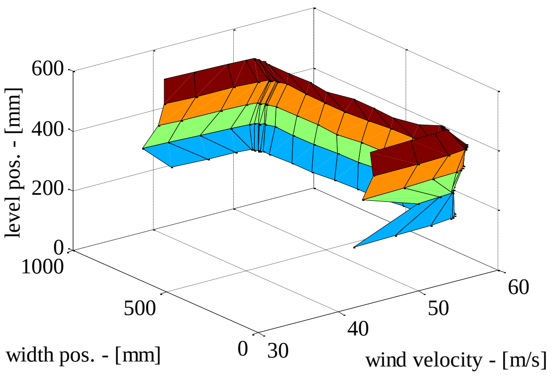
velocity profiles at U_{pitot} = 50 m/s

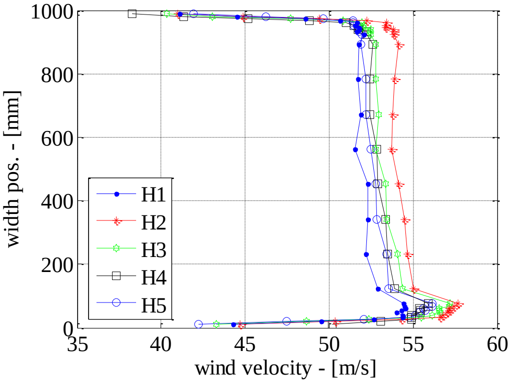
velocity profiles at U_{pitot} = 50 m/s

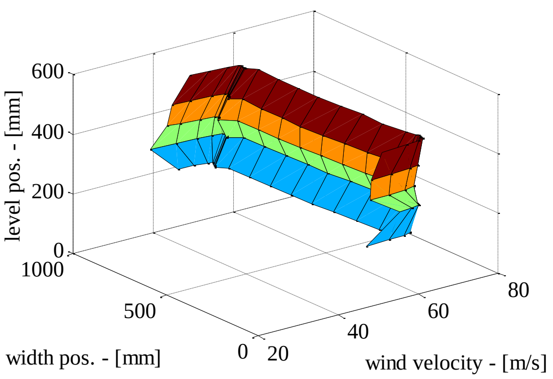
velocity profiles at U_{pitot} = 60 m/s

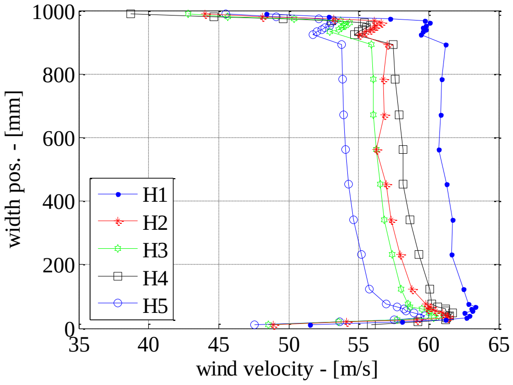
velocity profiles at U_{pitot} = 60 m/s

Turbulent flow

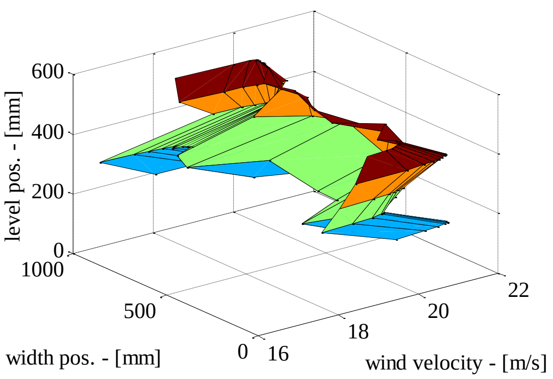
velocity profiles at U_{pitot} = 20 m/s

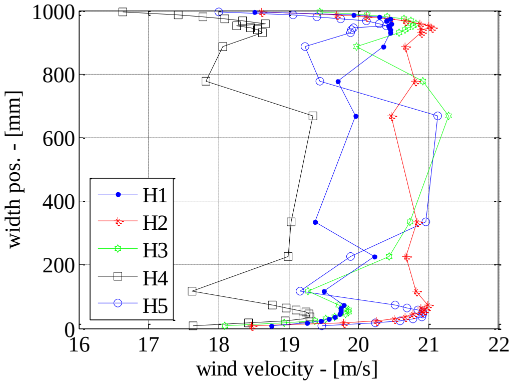
velocity profiles at U_{pitot} = 20 m/s

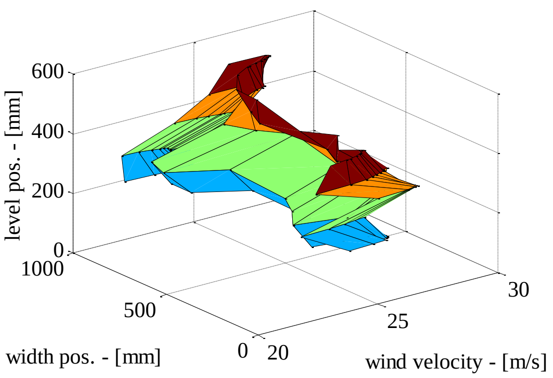
velocity profiles at U_{pitot} = 25 m/s

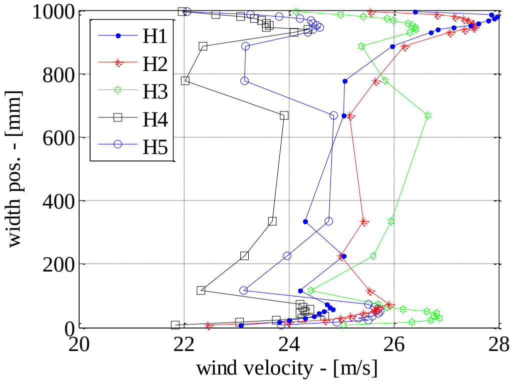
velocity profiles at U_{pitot} = 25 m/s

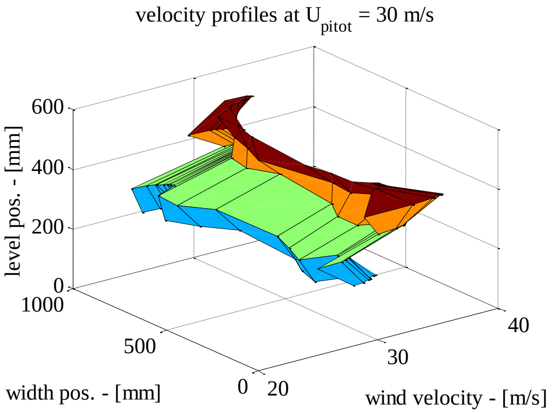
velocity profiles at U_{pitot} = 30 m/s
level pos. - [mm]
600
400
200
0
1000
500
0
width pos. - [mm]
20
30
40
wind velocity - [m/s]

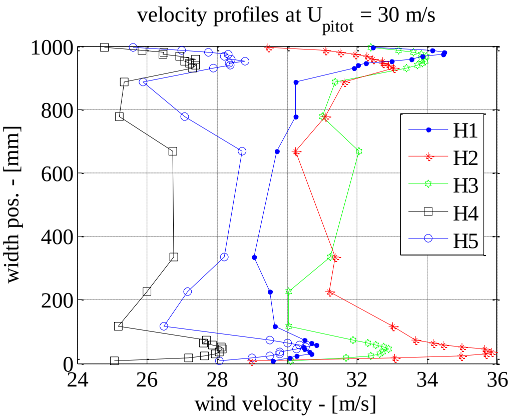
velocity profiles at U_{pitot} = 30 m/s
width pos. - [mm]
1000
800
600
400
200
0
24
26
28
30
32
34
36
wind velocity - [m/s]
H1
H2
H3
H4
H5

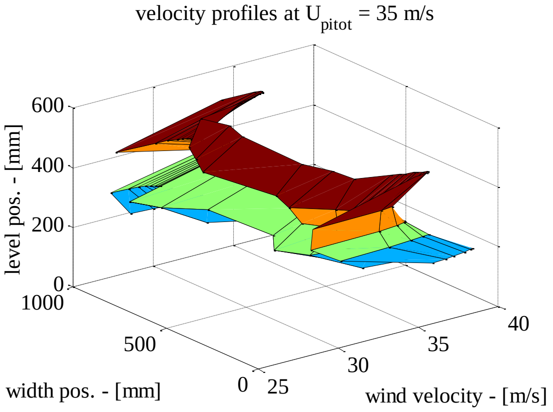
velocity profiles at U_{pitot} = 35 m/s
level pos. - [mm]
600
400
200
0
1000
500
0
width pos. - [mm]
25
30
35
40
wind velocity - [m/s]

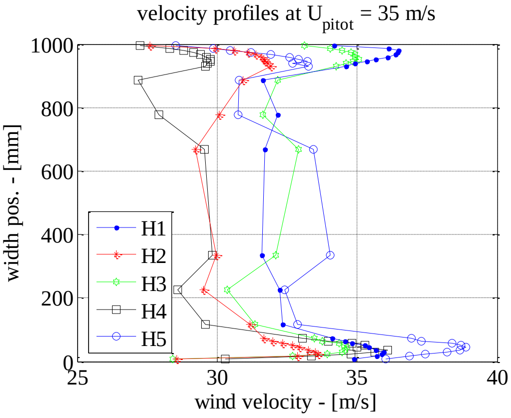
velocity profiles at U_{pitot} = 35 m/s
width pos. - [mm]
1000
800
600
400
200
0
25
30
35
40
wind velocity - [m/s]
H1
H2
H3
H4
H5

Paper IV ([8])

"A preliminary Investigation of the hanger vibrations on the Great Belt East Bridge"

H. Gjelstrup, C.T. Georgakis & A. Larsen

In proceedings: *7th International Symposium on Cable Dynamics, 2007*

A PRELIMINARY INVESTIGATION OF THE HANGER VIBRATIONS ON THE GREAT BELT EAST BRIDGE

Henrik GJELSTRUP[1,2] , Christos T. GEORGAKIS[2], Allan. LARSEN[1]

1. COWI A/S, Parallelvej 2, 2800 Kgs. Lyngby , Denmark
2. BYG•DTU, Building 118, Brovej, 2800 Kgs. Lyngby , Denmark

hegj@cowi.dk /heg@byg.dtu.dk; cg@byg.dtu.dk; aln@cowi.dk

Introduction

On March 29, 2001, the Great Belt East Bridge exhibited large-amplitude hanger vibrations having elliptical orbits for wind speeds of between 16 – 18m/s. Vibrational amplitudes were in the order of 2m in the across-wind direction and 0.6m in the along-wind. In this paper, a preliminary investigation behind the causes of this relatively isolated hanger vibration event on the Great Belt East Bridge is undertaken. One of the main assumptions of the investigation is that icy conditions may have contributed in some way to large hanger response by changing the cylindrical cross-sectional shape or partially changing the surface texture of the hangers. The change in shape or the surface texture has the effect of a change in the aerodynamic lift and drag coefficients in a certain Reynolds number range which in turn may lead to a form of "drag instability". From the visual observations of the vibrations it is assumed that the aerodynamic moment coefficient is zero.

HANGERS AND INSTRUMENTATION

On March 29, 2001, large amplitude hanger vibrations in the order of 2m where recorded on the Great Belt Bridge. Eight accelerometers, placed 2 meters above the anchorage points of the second longest pairs of hangers on the bridge's eastern backspan, recorded the oscillations (Fig 2). The instrumented hangers are of the "locked coil" type sheathed by a polyethylene tube with identical cross-sections (Fig 1). Their dimensions and mass per unit length are listed in Table 1.

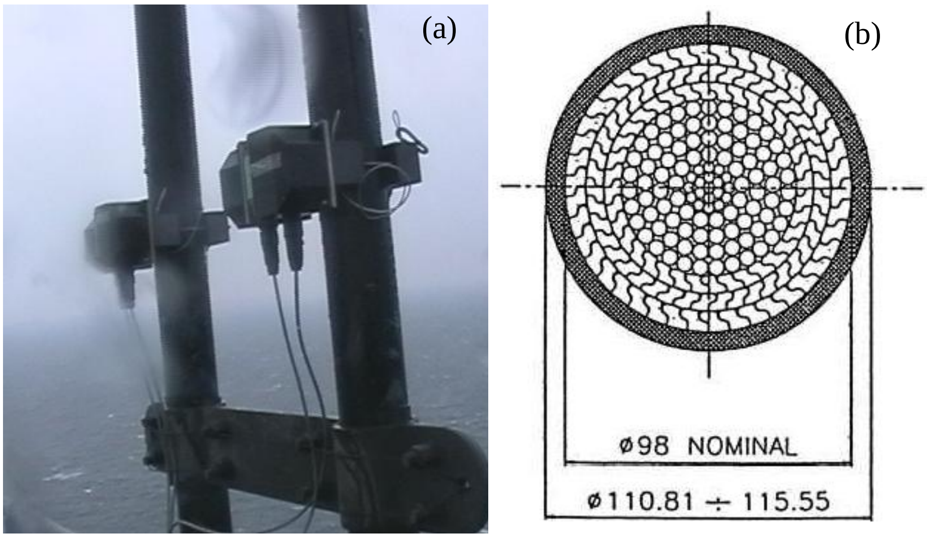

Figure 1. (a) Placement of accelerometers on hangers. (b) Hanger cross-section

The placement of the accelerometers on hanger 147 south is shown in Fig 1a, whilst Fig 2 shows the sign convention of the accelerometers with respect to the bridge layout.

TABLE 1. Data for hanger with instrumentation

Length : L_0	~ 168 meters
Diameter : D	~ 0.11 meters
Mass : m	~ 54 kg/meter

The accelerometers depicted in Fig 2 are designated such that 147SWT is the accelerometer situated on the west hanger of the 147 south hanger pair, measuring accelerations in the transverse direction with respect to the bridge deck, whilst 147SWL is measuring accelerations in the longitudinal direction with respect to the bridge deck. Furthermore, the accelerometers are of the "K-Beam" type, produced by Kistler (8324A20) and calibrated to measure ±20g.

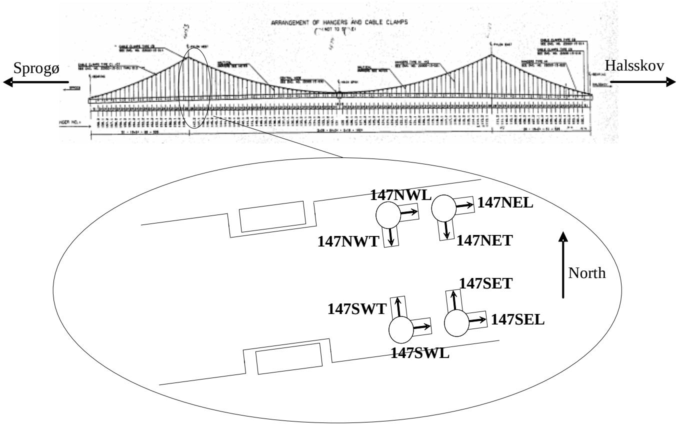

Figure 2. Sign convention and placement of the accelerometers on the Great Belt Bridge

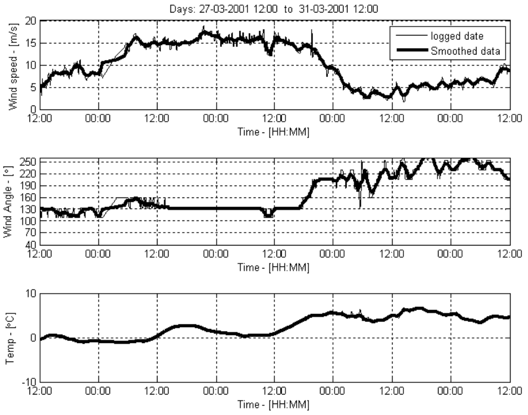

Figure 3. Collected weather data during vibration event. Wind angle is zero perpendicular to the bridge deck.

MEASUREMENTS

The vibration event discussed herewith began just before midnight on March 28, 2001 and ended at around approximately 10:00AM the following day. Fig 3 shows the collected weather data preceding, during and following the vibration event. The initiation of the hanger oscillations were recorded for a wind velocity of 16m/s and continued until the wind velocity reached about 18m/s. Fig 4a shows the fully developed acceleration signal of hanger 147NEL at the beginning of the event. Peak hanger accelerations occurred for a wind velocity of approximately 18m/s^2. The wind direction in the time interval of the event was constant and measured to be about 130° relative to the bridge deck (Fig 3). The wind angle was measured in intervals of 20°.

Double integration of the acceleration time-history leads to the hanger displacement, 2 meters from its anchor point, as depicted in Fig 4b. Fig 4b represents the last hour of measured data for the vibration event depicted in Fig 4a.

TABLE 2. Modal properties for hanger 147NEL.

Mode shape: i	1	2	3	4	5	6
Frequency [Hz]: $\omega_i/(2*\pi)$	0.64	1.27	1.91	2.55	3.19	3.84
Phase angle [rad]: Φ_i	2.57	1.44	1.76	0.24	3.56	4.31
Amplitude [m]: A_i	-1.744	0.202	-0.075	0.019	-0.008	-0.002

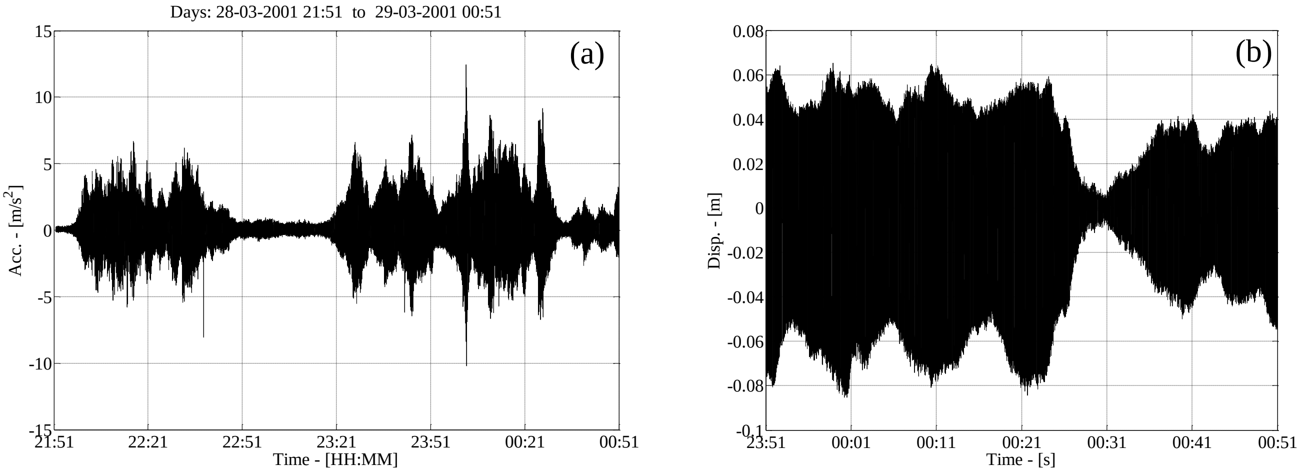

Figure 4. (a) Acceleration at 2m from the hanger anchor point of hanger 147NEL during the vibration event. (b) Displacement at 2m from the hanger anchor point about midnight.

Visual observations of the vibrations indicated that the displacements were dominated by the first mode shape. To verify this, a modal decomposition of the measured displacements of hanger 147NEL is performed so that the displacements can be described by a Fourier series containing only sinusoidal functions, $[z] = \sum_{i=1}^{n} A_i \sin(\omega_i t + \Phi_i), \quad n = 6$. The use of measured modal frequencies allows for the determination of the remaining unknowns, which are A_i, ω_i and Φ_i, where A_i is the modal amplitude, ω_i is the cyclic frequency of the mode and Φ_i is the phase angle of the mode. Values for the unknown modal properties are presented in Table 2. For the calculation of the modal amplitudes of Table 2, it is assumed that the generic hanger mode shape is: $\varphi(s) = \sin(i\pi s/L_0)$. The maximum displacement amplitude for mode 1 is 1.7m.

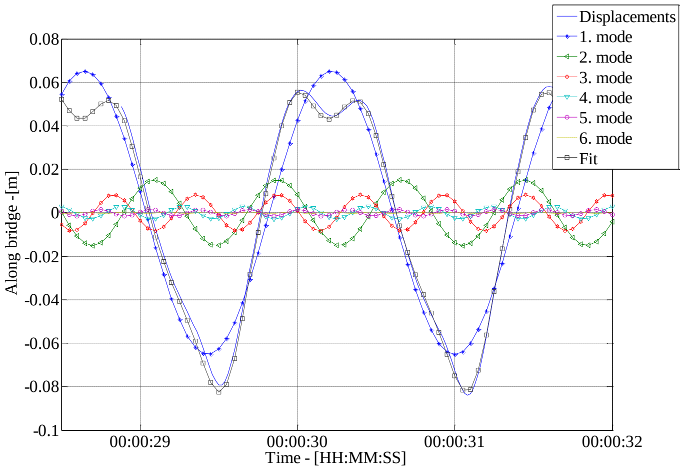

Figure 5. Max displacement and modal contribution for hanger 147NEL at 2m from the hanger anchor point which occur around midnight (Fig 4b).

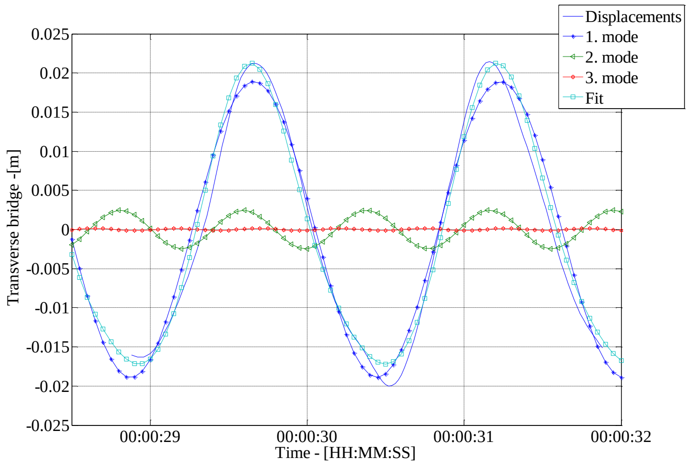

Figure 6. Max displacement and modal contribution for hanger 147NET at 2m from the hanger anchor point which occur around midnight (Fig 4b).

Similarly the transverse direction (perpendicular to the bridge deck, 147NET) was examined and a maximum displacement of approximately 0.6m was found. Fig 6 shows the modal fits to the displacement of hanger 147NET 2 meters above the anchor point of the hanger. From this it can be seen that the first three modes can adequately model the displacement, so as to be in good agreement with the measured displacements. Table 3 presents the modal properties for hanger 147NET.

TABLE 3. Modal properties for hanger 147NET.

Mode shape: i	1	2	3
Frequency [Hz]: $\omega_i/(2*\pi)$	0.63	1.27	1.89
Phase angle [rad]: Φ_i	1.65	3.68	2.34
Amplitude [m]: A_i	0.505	0.033	-0.002

GENERAL ANALYTICAL MODEL

A general analytical three degree-of-freedom (3DOF) model of a bluff body is developed to further analyse possible causes of the large amplitude cable vibrations. The bluff body is assumed herewith to be an iced vertical bridge hanger (Fig. 7). Using the 3DOF model it is possible to simulate a general response of a hanger which is subject to changes in drag, lift and moment, thus obtaining an estimate of the aerodynamic properties necessary to reproduce the observed vibration event. Furthermore a quasi-steady stability criterion for the general 3DOF model is developed following a similar approach by Macdonald *et al.* [1]. The derived equations of motion are obtained assuming a uniformly iced vertical hanger section of fixed length. Adjustments are made to account for changes in hanger stiffness due to elongation of the hanger. The time-varying hanger stiffness will be, $k_s(t) = k_s/L_0 \int_0^{L_0} \sqrt{1+(d(A_i(t)\sin(i\pi s/L_0))/ds)^2}\,ds$ where $A_i(t)$ is the amplitude of the displacement, i is the mode number and k_s is the static structural stiffness without vibration.

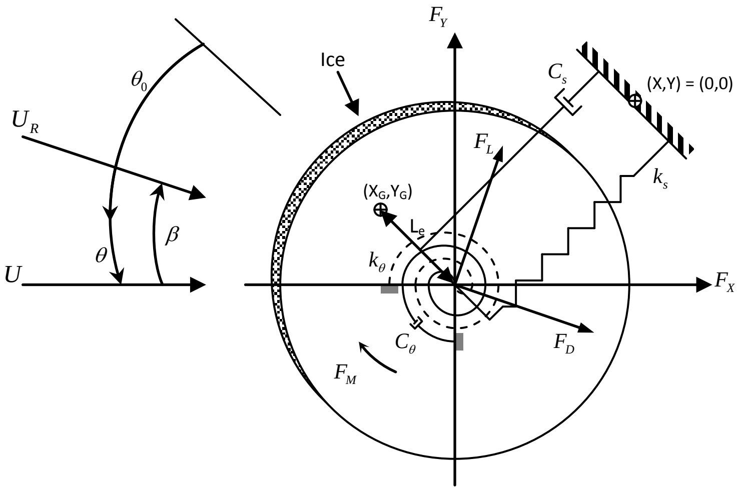

Figure 7. Analytical model of hanger section with ice accretion.

The equations of motion are derived through use of an Euler-Lagrange formulation and they are presented in Equations (1)-(3). X_G and Y_G is the location of the mass centre, L_e is the length from the hanger centre to the mass centre. k_s and k_θ is the hanger stiffness for movement in the xy- and torsional planes, respectively. θ_0 is the initial rotation of the hanger with respect to the wind direction. θ is the rotation of the hanger with time. C_s and C_θ is the structural damping of the hanger in the xy- and torsional planes respectively. U is the static wind speed and U_R is the relative wind speed, which depends on the movement of the hanger in the xy- and the torsional planes.

$$m\ddot{x} + C_s\dot{x} + k_s x + mL_e\left(\cos(\theta_0+\theta)\,\dot{\theta}^2 + \sin(\theta_0+\theta)\,\ddot{\theta}\right) = F_x \tag{1}$$

$$m\ddot{y} + C_s\dot{y} + k_s y + mL_e\big(-\sin(\theta_0 + \theta)\,\dot{\theta}^2 + \cos(\theta_0 + \theta)\,\ddot{\theta}\big) = F_y \tag{2}$$

$$J\ddot{\theta} + C_\theta\dot{\theta} + k_\theta\theta + mL_e\big(\sin(\theta_0 + \theta)\,\ddot{x} + \cos(\theta_0 + \theta)\,\ddot{y} + L_e\ddot{\theta}\big) = F_\theta \tag{3}$$

F_x, F_y and F_θ is the external aerodynamic forces so that:

$$F_X = \frac{1}{2}\rho U_r D(C_D(\alpha, \mathrm{Re}, \phi)\cos(\beta) + C_L(\alpha, \mathrm{Re}, \phi)\sin(\beta)) \tag{4}$$

$$F_Y = \frac{1}{2}\rho U_r D(C_L(\alpha, \mathrm{Re}, \phi)\cos(\beta) - C_D(\alpha, \mathrm{Re}, \phi)\sin(\beta)) \tag{5}$$

$$F_M = \frac{1}{2}\rho U_r D C_M(\alpha, \mathrm{Re}, \phi) \tag{6}$$

where α is the relative wind angle in respect to the hanger and is given by, $\alpha = \theta_0 + \theta - \beta$. The definitions of θ_0, θ and β are provided in Fig 7. Re is the Reynolds number. ϕ is the wind angle in relation the hanger length axis, which in this case is assumed to be zero. In order to estimate the displacements of the hanger it is useful to rewrite the above equations in the form of modal coordinates. This is done through the use of $z(t,s) = Z(t)\sin(i\pi s/L_0)\,, z = x, y, \theta$ and $Z = X, Y, \Theta$ in Equations (1)-(6). Furthermore the equations are multiplied by $\sin(i\pi s/L_0)$. Sinusoidal orthogonality is used when integrating over s from zero to L_0.

The corresponding equations of motion are:

$$m\ddot{X} + C_s\dot{X} + k_s X = \frac{2}{L_0}\int_0^{L_0} F_{XX}\,\sin\left(\frac{i\pi s}{L_0}\right) ds \tag{7}$$

$$m\ddot{Y} + C_s\dot{Y} + k_s Y = \frac{2}{L_0}\int_0^{L_0} F_{YY}\,\sin\left(\frac{i\pi s}{L_0}\right) ds \tag{8}$$

$$J\ddot{\Theta} + C_\theta\dot{\Theta} + k_\theta\Theta = \frac{2}{L_0}\int_0^{L_0} F_{\Theta\Theta}\,\sin\left(\frac{i\pi s}{L_0}\right) ds \tag{9}$$

Where $\frac{2}{L_0}\int_0^{L_0} F_{XX}\,\sin\left(\frac{i\pi s}{L_0}\right) ds$, $\frac{2}{L_0}\int_0^{L_0} F_{YY}\,\sin\left(\frac{i\pi s}{L_0}\right) ds$ and $\frac{2}{L_0}\int_0^{L_0} F_{\Theta\Theta}\,\sin\left(\frac{i\pi s}{L_0}\right) ds$ is the dynamic components of the aerodynamic forces for the i^{th} mode in the respective directions.

The stability criterion for the 3DOF are based on a Taylor expansion of the aerodynamic forces about $\dot{x} = \dot{y} = \dot{\theta} = 0$ which results in a static wind force and a velocity proportional aerodynamic force, i.e. damping force (Equation (10)). Furthermore it is assumed that all higher order terms in the equations of motion are negligible. These assumptions correspond to the instant where a vibration event is initiated. With these assumptions it is possible to estimate the stability of the 3DOF system by rewriting the equations of motion (1)-(3) into state-space and thereafter solving the eigenvalue problem.

The eigenvalue problem produces a 6th order polynomial, which cannot be solved analytically. Nevertheless, by applying the Routh-Hurwitz stability criterion to the 6th order polynomial it is possible to obtain the stability criterion of the 3DOF system [2]. The Routh-Hurwitz stability criterion states that a system is stable if the Real parts of all the Routh-Hurwitz coefficients are greater then zero. The resulting 13 coefficients (7 from the polynomial and 6 from the Hurwitz determinant) can be solved analytically, which makes it possible, within a relative short time, to obtain an estimate on the needed structural damping for varying wind angles of attack and wind velocities.

$$C_a = -\begin{bmatrix} \frac{dF_x}{d\dot{x}} & \frac{dF_x}{d\dot{y}} & \frac{dF_x}{d\dot{\theta}} \\ \frac{dF_y}{d\dot{x}} & \frac{dF_y}{d\dot{y}} & \frac{dF_y}{d\dot{\theta}} \\ \frac{dF_\theta}{d\dot{x}} & \frac{dF_\theta}{d\dot{y}} & \frac{dF_\theta}{d\dot{\theta}} \end{bmatrix}_{\dot{x}=\dot{y}=\dot{\theta}=0} \tag{10}$$

COMPUTATIONAL RESULTS

From visual observations just after the event, it is assumed that the hanger had an asymmetrical profile due to the ice accretion, which should lead to a lift force for certain angles of attack. Values for the drag, lift and moment coefficients of the ice-accreted hangers are currently being determined through wind-tunnel testing. In the absence of these values an estimate of the aerodynamic coefficients has been made, assuming that the roughness and shape of the ice accretions lie between those of a smooth circular cylinder and a multi-stranded cable. Furthermore, it is assumed that the observed aerodynamic instability is dependant on both a fluctuating drag and lift coefficient. For the purposes of the preliminary analyses presented herewith, it is assumed that the moment coefficients are zero.

Due to its roughness, the multi-stranded cable exhibits a drop in its Reynolds-dependent lift and drag coefficients at about $Re = 4.5 \times 10^4$ [3]. For the drag coefficient, this is a factor of 10 lower then that of a smooth circular cylinder subject to laminar flow. Thus, it is assumed that an iced hanger with low levels of along-wind roughness should have similar drag coefficients to that of a circular cylinder, whilst the across-wind lift coefficients will be similar to that of the multi-stranded cable, adjusted for a large reduction in roughness. The adjusted smooth surface – zero turbulence drag and lift coefficients are presented in Fig 8. Through the use of ESDU [4], corrections to aerodynamic coefficients for roughness and turbulence are made. A turbulence intensity of 8% in the along wind direction and a turbulence intensity of 5% in the across wind direction is used. Furthermore a surface roughness of $8\text{x}10^{-6}$ from ESDU [4], is used. The corrected and adjusted values are used within the numerical simulations.

The maximum displacements found from the numerical analyses are presented in Fig 9. The presented displacements are about the static equilibrium originating from the wind load and are displayed in the bridge coordinate system. It is seen that for wind-speeds ranging between 17-19 m/s, displacements are found to be approximately 1.6 meters and 0.6 meters for the across-wind and along-wind directions, respectively. These calculated displacements in the bridge coordinate system are in good agreement with the observed displacements of the Great Belt East Bridge hangers. Due to the low levels of damping that is generally measured in long suspension bridge hangers, a value of 0.03% of critical is assumed for the structural damping.

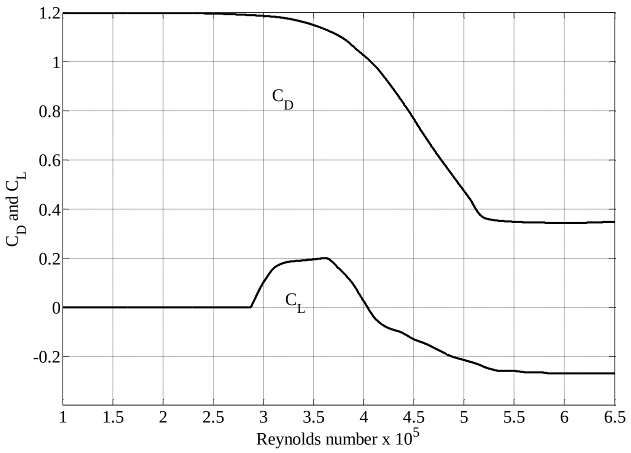

Figure 8. Applied aerodynamic coefficient for ice-accreted hanger

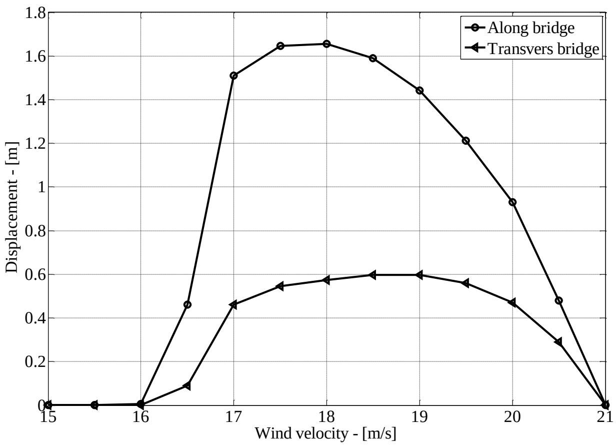

Figure 9. Maximum calculated hanger displacements 0% damping.

Using the stability criterion in conjunction with the aerodynamic coefficients to estimate the wind velocity range where instability is to be expected (Fig 10), results in a wind velocity range of about 15-21 m/s which are in good agreement with the results found from the modal equations (Fig 9) and the measured full scale data.

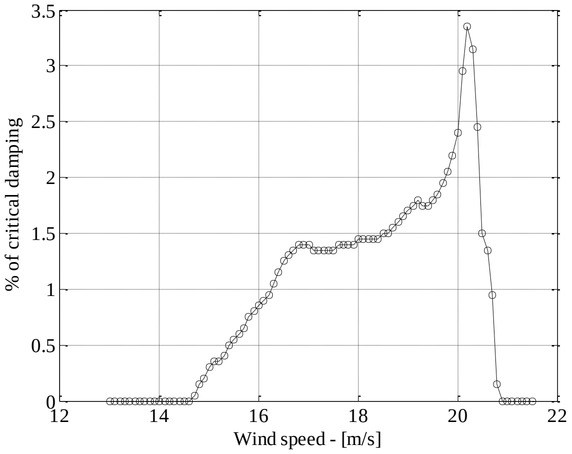

Figure 10. Estimated instability range (x-axis) and estimated needed structural damping (y-axis)

SUMMARY

This paper presents an iced-hanger vibration event on the Great Belt Bridge in the period around March 29, 2001, where large amplitude vibrations in the order of 2m in the along bridge direction and 0.6m in the transverse bridge direction where recorded. It is shown that mode 1 is the dominating vibration mode for this event. In order to investigate the possible cause of the vibration, a general 3DOF model is developed. The model needs input in terms of aerodynamic drag, lift and moment. Values for the drag, lift and moment coefficients of the ice-accreted hangers are currently being determined through wind-tunnel testing. In the absence of these values an estimate of the aerodynamic coefficients has been made, assuming that the roughness and shape of the ice accretions lie between those of a smooth circular cylinder and a multi-stranded cable. Results obtained from the model, by using previously determined aerodynamic coefficients that have been corrected to be within the estimated turbulence intensities and surface roughness, are in good agreement with the measured data. A stability criterion for the 3DOF system is also developed in order to find the wind velocity range where instability is to be expected and in order to evaluate the structural damping needed for the avoidance of aerodynamic instability. The velocity range where instability is expected is in good agreement with the numerically calculated result and the measured data.

FURTURE WORK

The numerical results from the analytical model presented herewith are in good agreement with the observed and measured displacements of the Great Belt Bridge hangers for the aforementioned vibration event. Nevertheless, due to the large number of assumptions made mainly with regard to the aerodynamic coefficients, a series of wind tunnel tests are planned, in which different configurations of hanger surface roughness and ice accretion thickness will be tested. Furthermore, simulations shall be performed using the Discrete Vortex Method (DVM) and the commercial CFD program Fluent. Preliminary simulations indicate that it is possible to obtain lift coefficients depending on the angle of attack which is similar to the one shown in Fig 8.

ACKNOWLEDGEMENTS

The authors would like to acknowledge the kind permission given by A/S Storebaeltforbindelsen for making the measured hanger data available for this paper. We would also like to thank Jacob Egede Andersen for sorting the data, maintaining and supervising of the data acquisition system.

REFERENCES

[1] Macdonald, J.H.G. and Larose, G.L., 2006, "A unified approach to aerodynamic damping and drag/lift instabilities, and its application to dry inclined cable galloping", *J FLUID STRUCT*, vol.22, 229-252.

[2] Thomsen, J.J., 2003, *Vibrations and Stability,* Springer, 404.

[3] Counihan, J., 1963, "Lift and Drag Measurements on Stranded Cables".

[4] ESDU, 1986, "Mean forces, pressures and flow field velocities for circular cylindrical structures: Single cylinder with two-dimensional flow; ESDU Item 80025". *ESDU Item 80025*.

Paper V ([42])

“A new general 3DOF quasi-steady aerodynamic instability model”

H. Gjelstrup, A. Larsen, C. Georgakis & H. Koss

In proceedings: *International Colloquium on: Bluff Bodies Aerodynamics & Applications, 2008*

BBAA VI International Colloquium on:
Bluff Bodies Aerodynamics & Applications
Milano, Italy, July, 20-24 2008

A NEW GENERAL 3DOF QUASI-STEADY AERODYNAMIC INSTABILITY MODEL.

Henrik Gjelstrup[*×], Allan Larsen[*], Christos Georgakis[×] and Holger Koss[×]

[*]COWI A/S, Parallelvej 2, 2800 Kgs. Lyngby , Denmark
e-mails: `hegj@cowi.dk`, `aln@cowi.dk`

[×]BYG•DTU, Building 118, Brovej, 2800 Kgs. Lyngby , Denmark
e-mails: `heg@byg.dtu.dk`, `cg@byg.dtu.dk`, `hko@byg.dtu.dk`

Keywords: Aerodynamic instability criterion, Aerodynamic damping, Bluff body

Abstract

This paper proposes a three degrees of freedom (3DOF) quasi-steady aerodynamic model and an instability criterion for a bluff body, which is uniform along the length axis. The model and criterion has been developed in the frame of investigating aerodynamic instability of cables due to ice accretions but can generally be applied for aerodynamic instability prediction for prismatic bluff bodies. The 3DOF, which make up the movement of the model, are the displacements in the XY-plane and the rotation around the bluff body's rotational axis. The proposed model incorporates inertia coupling between the three degrees of freedom and is capable of estimating the onset of aerodynamic instability for changes in drag, lift and moment, which is a function of wind angle of attack (α) in relation to the x-axis of the bluff body, Reynolds number and wind angle (ϕ) in relation to the length axis of the bluff body. Further more the model is capable of predicting an estimate for the structural damping needed for avoiding instability of the bluff body.

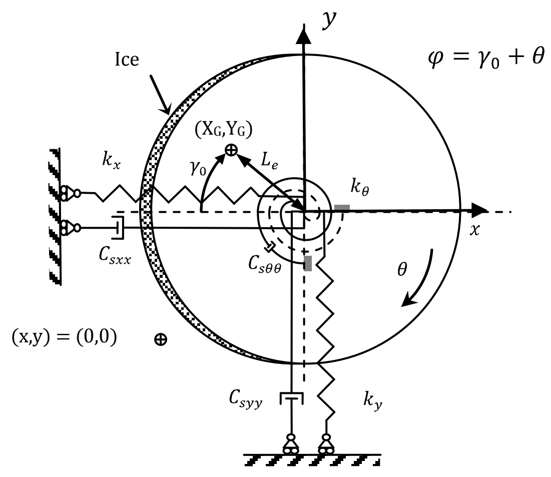

x = displacement direction.
y = displacement direction.
θ = rotation direction.
γ_0 = angle offset for mass centre.
L_e = mass centre offset.
k_x = structural stiffness in x direction.
k_y = structural stiffness in y direction.
k_θ = structural damping in θ direction.
C_{sxx} = structural damping in x direction.
C_{syy} = structural damping in y direction.
$C_{s\theta\theta}$ = structural stiffness in θ direction.
(X_G,Y_G) = mass centre.

Figure 1. Definition of system.

1 INTRODUCTION

The main purpose for models, which investigates aero-elastic behaviour, is to predict when aerodynamic instability occurs. During the last 80 years a number of models have been proposed and over the last couple of years aerodynamic damping, as a driving force for vibration, has received some renewed attention. Den Hartog proposed his stability criterion in 1932, Ref. [5], for a 1DOF system, which was defined for a bluff body with an aerodynamic lift coefficient formulated as a function of wind angle of attack in relation to the surface of the bluff body. Later, 1962, Davenport proposed an expression for the aerodynamic damping in the along wind and the transverse wind direction of a cylinder Ref. [3]. In 1981 Martin *et al.* proposed the instability criteria, which now is known under the name of “Drag instability” Ref. [7]. Up to that point all expressions for the aerodynamic damping were special cases, which should be applied individually. In 2006 a unified approach to damping and drag/lift instabilities was proposed by Macdonald and Larose Ref. [6] for a 1DOF system, which was later extended to a 2DOF system. This general quasi-steady 2DOF instability model is able to estimate the structural damping needed for avoiding instability of a bluff body moving in the XY-plane. The 2DOF model is capable of predicting the special cases, which earlier were applied individually, but lack the possibility of predicting inertial coupling for a bluff body with a mass centre offset from its rotational axis.

Through an ongoing research project on iced cables, which focuses on the different effects that ice accretions might have on the aerodynamic stability, it was found that torsion also played a vital role in the stability of a cable, Ref. [2], under certain conditions. This sparked the foundation for the idea to add the rotational dimension to the model developed by Macdonald and Larose in order to obtain a more comprehensive tool for analysing the stability of cables based on the quasi-static aerodynamic forces. In order to expand the model presented in Ref. [6] with an extra dimension it was necessary to find a quasi-static description of the rotational speed of the cable. Some research has been performed on torsional instability for models with different geometries and an approximation of the quasi-static rotational speed has been found for several geometries. A summary of this research can be found in Ref. [1] section 4.2.2. It is worth noticing that making a quasi-static description of the rotational speed seems to be difficult and according to the author’s knowledge no unified expression, which clearly defines how to calculate the speed, has been devolved so far.

Using the research on an approximation to a quasi-static rotational speed, Ref. [1] section 4.2.2, it was possible to develop a new 3DOF quasi-steady model, which is proposed in this paper. This new 3DOF general quasi-static aerodynamic instability model incorporates the rotational movement of the cable and the coupling of all three degrees of freedom. In addition to prediction the instability of the cable in the XY-plane the new model is also capable of prediction instability due to the rotation of the cable and to predict instability due to a combination of movement in all the three degrees of freedom.

Furthermore, this new 3DOF general quasi-static aerodynamic instability model is also capable of estimating the damping need to suppress this instability. The model is able to predict the same levels of damping as the 2DOF model proposes by Macdonald et al. Additionally, it is capable of predicting the torsional damping needed to suppress instability and the combined damping need to suppress damping for an instability, which is a function of simultaneous motion in all three degrees of freedom.

2 THE MODEL

The bluff body model is based on a section model approach and developed for a cable with a thin ice accretion. The application of this model can be expanded to any geometry of a prismatic bluff body subjected to aerodynamic instability. Figure 1, Figure 2 and Figure 3 shows the bluff body coordinate systems for load and structural respone, defined for a cable with a thin ice accretion.

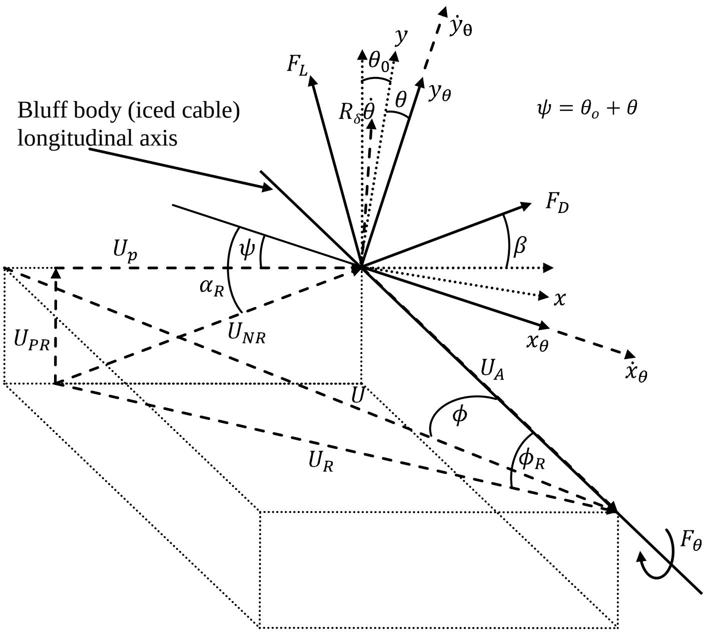

$x_\theta, \dot{x}_\theta$ = displacement, velocity.
$y_\theta, \dot{y}_\theta$ = displacement, velocity.
θ_0 = steady wind angle of attack
$\theta, \dot{\theta}$ = structural rotation, angular velocity.
α_R = wind angle of attack, cable surface.
β = angle of rotation, relative wind.
ϕ = wind angle of attack, cable length axis.
F_L = lift.
F_D = drag.
F_M = moment.
R_δ = Radial length for rotational speed.
δ = leading edge angle.
U = mean wind velocity.
U_R = relative wind velocity.
U_{PR} = projected relative vertical wind velocity.
U_p = projected relative horizontal wind velocity.
U_{NR} = normal projected relative wind velocity.
U_A = along axis wind velocity.

Figure 2. Schematic model of cable section with ice accretion.

The position of the ice accretion is described in the x-y coordinate system of the cross-sectional plane of the still body (Figure 3). If rotation is induced the angle θ describes the magnitude of rotation around the length axis of the bluff body.

Projected overall velocities

$$U_A = U\cos(\phi) \tag{1}$$

Relative velocities

$$\begin{aligned} U_P &= U\sin(\phi) - \dot{x}\cos(\psi) - \big(\dot{y}\sin(\psi) + R_\delta\dot{\theta}\sin(\delta)\big) \\ U_{PR} &= -\big(\dot{y}\cos(\psi) + R_\delta\dot{\theta}\cos(\delta)\big) + \dot{x}\sin(\psi) \\ U_{NR} &= \sqrt{(U_P^2 + U_{PR}^2)} \\ U_R &= \sqrt{(U_A^2 + U_{NR}^2)} \end{aligned} \tag{2}$$

Assumptions used in deriving the model:

- The model is based on a section model approach for a prismatic cable, which makes the assumption implying that the cable is straight and rigid at the midpoint of the cable.
- The ice shape is assumed to be prismatic.
- The structural damping is proportional to the velocity.
- The stiffness of the cable is constant.
- The overall wind speed, U, is constant.
- The rotational speed can be represented by motion of the leading edge point.
- Quasi-steady theory can be applied.

- Gravitational forces are not included.

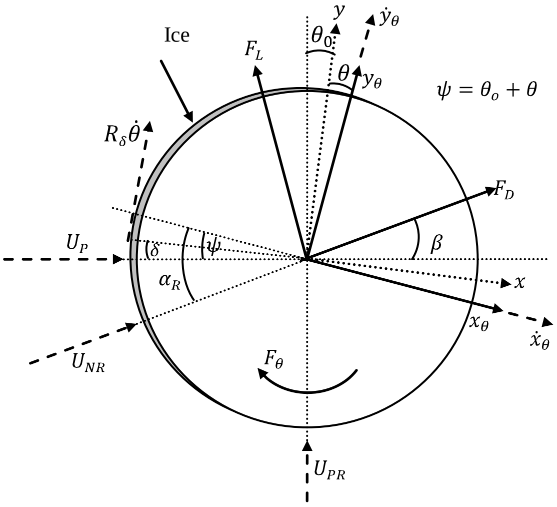

Figure 3. Analytical model of cable section with ice accretion.

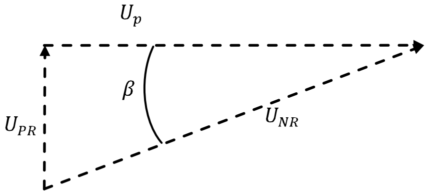

Figure 4. Definition of β.

Assumptions used in deriving the instability criterion:

- The cable is at rest at the initiation of the instability.
- Quasi-steady theory can be applied.

The instability criterion should only be used for a reduced velocity greater then $U/fD = 20$ due to the assumption of quasi-steady state and if the rotational degree of freedom is included then the criterion is limited to compact sections, see Ref. [1] section 4.2.2.

In the following the notation for time depended variables as $x(t), y(t)$ and $\theta(t)$ is written x, y and θ. Derivatives in respect to time are written as $(d/dt)x = \dot{x}$ and $(d^2/dt^2)x = \ddot{x}$

Both, the vertical and rotational motion of the cable section cause the angle of attack to vary over the section. For example, a positive rotational velocity induces a down draft forward of the centre of rotation and an updraft behind the centre of rotation and vice versa. The rotational velocity is approximated by the motion of a reference point defined in polar coordinates by the radial distance R_δ and angle δ as shown in Figure 3. As discussed in Ref. [1] section 4.2.2, the length R_δ is not directly related to characteristic points of the section geometry or of the flow field. It is rather a variable used to adjust the aerodynamic model output to the observed instabilities. For example for torsional instability of rectangles about the centroid R_δ has been approximated to half the distance between the centroid and the body's leading edge under the respective angle of attack. In the case discussed in this paper the length R_δ is chosen to be the length between the centre of rotation and to the leading edge of the model.

3 FORMULATION OF EQUATIONS

In deriving the equation of motion the energy approach has been applied using the Euler-Lagrange equation, see Eq. (3).

$$\begin{gathered}\frac{\partial}{\partial t}\left(\frac{\partial L}{\partial \dot{q}}\right)-\frac{\partial L}{\partial q}+DampForce=Force\\ L=T-V \qquad q=\{x,y,\theta\}\\ DampForce=\left\{C_{sxx}\dot{x},C_{syy}\dot{y},C_{s\theta\theta}\dot{\theta}\right\}\end{gathered} \tag{3}$$

where *T* is the kinetic energy of the system and *V* is the potential energy of the system.

3.1 Equations of motion

Figure 5 shows the coordinate system of the cable with ice accretion and illustrates the mass centre location of the model.

The dotted line shows the sign convention and the origin of the coordinate system $(0,0)$, which is the centre of the cable model shown in Figure 1. The point (x,y) is the displaced centre of the cable due to motion of the cable section in the *x*-*y*-plane. X_G and Y_G define the location of the mass centre of the cable section, where γ_0 and L_e are the polar coordinates of the mass centre in the *x*-*y*-plane and θ the additional angle due to rotation of the cable. The indices *Trans* and *Rot* refer to the movement of the mass centre due to translation and rotation respectively.

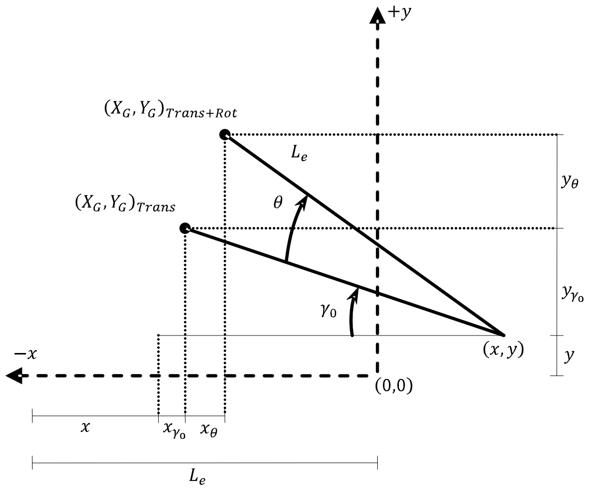

Figure 5. Definition of mass centre coordinates.

Eq. (4) and Eq. (5) gives the position for the mass centre of the cable.

$$X_G=x-L_e cos(\gamma_0+\theta) \tag{4}$$

$$Y_G=y+L_e sin(\gamma_0+\theta) \tag{5}$$

Using the Euler-Lagrange equation requires that one calculates the kinetic energy and potential energy according to the coordinate system shown in Figure 5. The obtained expressions for the energies are shown in Eq. (6) to Eq. (7).

$$T=\frac{1}{2}m_{tot}\left(\dot{X}_G^2+\dot{Y}_G^2\right)+\frac{1}{2}J\dot{\theta}^2 \tag{6}$$

$$V=\frac{1}{2}\left(k_x x^2+k_y y^2+k_\theta \theta^2\right) \tag{7}$$

where m_{tot} is the mass of the system and J is the rotational inertia about the mass centre.

Using the Euler-Lagrange approach results in obtaining the equation of motions (EOMs), which are given in Eq. (8) to Eq. (10).

$$m_{tot}\ddot{x} + C_{sxx}\dot{x} + k_x x + m_{tot}L_e\big(cos(\varphi)\,\dot{\theta}^2 + sin(\varphi)\,\ddot{\theta}\big) = F_x \tag{8}$$

$$m_{tot}\ddot{y} + C_{syy}\dot{y} + k_y y + m_{tot}L_e\big(-sin(\varphi)\,\dot{\theta}^2 + cos(\varphi)\,\ddot{\theta}\big) = F_y \tag{9}$$

$$(L_e^2 m_{tot} + J)\ddot{\theta} + C_{s\theta\theta}\dot{\theta} + k_\theta\theta + m_{tot}L_e(sin(\varphi)\,\ddot{x} + cos(\varphi)\,\ddot{y}) = F_\theta \tag{10}$$

F_x, F_y and F_θ are the external aerodynamic forces, which are presented in Eq. (11) to Eq. (13) for small initial displacements, where $\alpha_R = (\psi + \beta)$ and φ are given in Figure 3 and Figure 1, respectively.

The inertial coupling term for the x-direction, $\big(mL_e\cos(\varphi)\,\dot{\theta}^2 + mL_e\sin(\varphi)\,\ddot{\theta}\big)$, consists of two terms. The first coupling term is the centripetal force, $\big(mL_e\cos(\varphi)\,\dot{\theta}^2\big)$, and the second coupling term is the force originating from the angular acceleration, $\big(mL_e\sin(\varphi)\,\ddot{\theta}\big)$. Similar applies for the inertia coupling formulation in the y-direction. The inertial coupling in the θ-direction is based on tangential projections of the acceleration forces originating from the acceleration in the x- and y-direction.

$$F_x = \frac{1}{2}\rho U_R^2 D(C_D(\alpha_R, Re_R, \phi_R)\,cos(\alpha_R) + C_L(\alpha_R, Re_R, \phi_R)\,sin(\alpha_R)) \tag{11}$$

$$F_y = \frac{1}{2}\rho U_R^2 D(C_L(\alpha_R, Re_R, \phi_R)\,cos(\alpha_R) - C_D(\alpha_R, Re_R, \phi_R)\,sin(\alpha_R)) \tag{12}$$

$$F_\theta = \frac{1}{2}\rho U_R^2 D^2 C_M(\alpha_R, Re_R, \phi_R) \tag{13}$$

3.2 Aerodynamic damping

The instability criterion is based on a linearized version of the EOMs. This linearization is obtained by performing a Taylor expansion of the aerodynamic forces given in Eq. (11) to Eq. (13) to first order around the velocity of $\dot{x} = \dot{y} = \dot{\theta} = 0$.

$$\begin{aligned} &F_Z\big(\dot{x}, \dot{y}, \dot{\theta}\big)_{\dot{x}=\dot{y}=\dot{\theta}=0} \\ &\quad = F_Z + \frac{\partial F_Z}{\partial \dot{x}}\dot{x} + \frac{\partial F_Z}{\partial \dot{y}}\dot{y} + \frac{\partial F_Z}{\partial \dot{\theta}}\dot{\theta} + \frac{\partial F_Z}{\partial \dot{x}\partial \dot{y}}\dot{x}\dot{y} \\ &\quad + \dot{\theta}\left(\frac{\partial F_Z}{\partial \dot{x}\partial \dot{\theta}}\dot{x} + \frac{\partial F_Z}{\partial \dot{y}\partial \dot{\theta}}\dot{y} + \frac{\partial F_Z}{\partial \dot{x}\partial \dot{y}\partial \dot{\theta}}\dot{x}\dot{y}\right), where\ \big(F_Z = F_Z(0,0,0)\big) \end{aligned} \tag{14}$$

The Taylor expansion (Eq. (14)) of the aerodynamic forces results in a static wind force for all three directions and a dynamic force, which is equal to a Jacobian matrix (C_a) multiplied with the velocity in the three directions, $C_a\dot{Z}$ where $\dot{Z} = \big[\dot{x}, \dot{y}, \dot{\theta}\big]'$.

C_a is the aerodynamic damping matrix as given in eq. (15). The values of the aerodynamic damping matrix C_a are calculated for small initial displacements $(\cos(\theta) = 1,\ \sin(\theta) = 0)$ and found by applying an approach presented and discussed in Ref. [6].

$$C_a = -\begin{bmatrix} \frac{\partial F_x}{\partial \dot{x}} & \frac{\partial F_x}{\partial \dot{y}} & \frac{\partial F_x}{\partial \dot{\theta}} \\ \frac{\partial F_y}{\partial \dot{x}} & \frac{\partial F_y}{\partial \dot{y}} & \frac{\partial F_y}{\partial \dot{\theta}} \\ \frac{\partial F_\theta}{\partial \dot{x}} & \frac{\partial F_\theta}{\partial \dot{y}} & \frac{\partial F_\theta}{\partial \dot{\theta}} \end{bmatrix}_{\dot{x}=\dot{y}=\dot{\theta}=0} \tag{15}$$

Furthermore, it is assumed that all higher order terms in the EOMs are negligible. These assumptions derive from the instant where a vibration event is initiated on the body. Eq. (16) gives the total damping matrix containing both structural and aerodynamic damping.

$$C_D = C_s + C_a = \begin{bmatrix} C_{sxx} & 0 & 0 \\ 0 & C_{syy} & 0 \\ 0 & 0 & C_{s\theta\theta} \end{bmatrix} + \begin{bmatrix} C_{axx} & C_{axy} & C_{ax\theta} \\ C_{ayx} & C_{ayy} & C_{ay\theta} \\ C_{a\theta x} & C_{a\theta y} & C_{a\theta\theta} \end{bmatrix} = \begin{bmatrix} C_{xx} & C_{xy} & C_{x\theta} \\ C_{yx} & C_{yy} & C_{y\theta} \\ C_{\theta x} & C_{\theta y} & C_{\theta\theta} \end{bmatrix} \tag{16}$$

With these assumptions it is possible estimate the stability of the 3DOF system by rewriting the equations of motions (Eq. (8) to Eq. (10)) into state space and solving the eigenvalue problem which can be obtained here from.

Eq. (17) to Eq. (19) give the linearized version for the equations of motions Eq. (8) to Eq. (10), with the static aerodynamic force equal to zero, $\mathrm{F_Z} = 0$ where $\mathrm{Z} = [\mathrm{x}, \mathrm{y}, \theta]'$.

$$\ddot{x} = -\frac{1}{Jm_{tot}}\left(J\left(m_{tot}\omega_x^2 x + C_{xx}\dot{x} + C_{xy}\dot{y} + C_{x\theta}\dot{\theta}\right) + sin(\varphi)L_e^2 m_{tot}\left(-\frac{1}{L_e}\left(J\omega_\theta^2\theta + C_{\theta x}\dot{x} + C_{\theta y}\dot{y} + C_{\theta\theta}\dot{\theta}\right) + sin(\varphi)\left(\omega_x^2 m_{tot}x + C_{xx}\dot{x} + C_{xy}\dot{y} + C_{x\theta}\dot{\theta}\right) + cos(\varphi)\left(\omega_y^2 m_{tot}y + C_{yx}\dot{x} + C_{yy}\dot{y} + C_{y\theta}\dot{\theta}\right)\right)\right) \tag{17}$$

$$\ddot{y} = -\frac{1}{Jm_{tot}}\left(J\left(m_{tot}\omega_y^2 y + C_{yx}\dot{x} + C_{yy}\dot{y} + C_{y\theta}\dot{\theta}\right) + cos(\varphi)L_e^2 m_{tot}\left(-\frac{1}{L_e}\left(J\omega_\theta^2\theta + C_{\theta x}\dot{x} + C_{\theta y}\dot{y} + C_{\theta\theta}\dot{\theta}\right) + sin(\varphi)\left(\omega_x^2 m_{tot}x + C_{xx}\dot{x} + C_{xy}\dot{y} + C_{x\theta}\dot{\theta}\right) + cos(\varphi)\left(\omega_y^2 m_{tot}y + C_{yx}\dot{x} + C_{yy}\dot{y} + C_{y\theta}\dot{\theta}\right)\right)\right) \tag{18}$$

$$\ddot{\theta} = -\frac{1}{J}\left(\left(J\omega_\theta^2\theta + C_{\theta x}\dot{x} + C_{\theta y}\dot{y} + C_{\theta\theta}\dot{\theta}\right) - L_e\left(sin(\varphi)\left(\omega_x^2 m_{tot}x + C_{xx}\dot{x} + C_{xy}\dot{y} + C_{x\theta}\dot{\theta}\right) + cos(\varphi)\left(\omega_y^2 m_{tot}y + C_{yx}\dot{x} + C_{yy}\dot{y} + C_{y\theta}\dot{\theta}\right)\right)\right) \tag{19}$$

Below Eq. (20) shows the state-space matrix, which is obtained from Eq. (17) to Eq. (19)

$$\begin{bmatrix} 0 & 0 & 0 & 1 & 0 & 0 \\ 0 & 0 & 0 & 0 & 1 & 0 \\ 0 & 0 & 0 & 0 & 0 & 1 \\ & \vdots & & \vdots & \vdots & \vdots \\ \cdots & A & \cdots & B & C & D \\ & \vdots & & \vdots & \vdots & \vdots \end{bmatrix} \begin{bmatrix} x_1 \\ y_1 \\ \theta_1 \\ x_2 \\ y_2 \\ \theta_2 \end{bmatrix} = \begin{bmatrix} \dot{x}_1 \\ \dot{y}_1 \\ \dot{\theta}_1 \\ \dot{x}_2 \\ \dot{y}_2 \\ \dot{\theta}_2 \end{bmatrix} \tag{20}$$

Where A is a 3x3 sub-matrix, see Eq. (21), and B, C and D is a 3x1 sub-vector, see Eq. (22) to Eq. (24) and

(x_1, y_1, θ_1) represents the position of the cable section.
$(x_2, y_2, \theta_2) = (\dot{x}_1, \dot{y}_1, \dot{\theta}_1)$ represents velocity of the cable section.

$(\dot{x}_2, \dot{y}_2, \dot{\theta}_2) = (\ddot{x}_1, \ddot{y}_1, \ddot{\theta}_1)$ represents acceleration of the cable section.

$$A = \begin{bmatrix} -\frac{J m_{tot}\omega_x^2 + \sin(\varphi)^2 L_e^2 m_{tot}^2 \omega_x^2}{J m_{tot}} & -\frac{\cos(\varphi)\sin(\varphi) L_e^2 m_{tot}\omega_y^2}{J} & \sin(\varphi) L_e \omega_\theta^2 \\ -\frac{\cos(\varphi)\sin(\varphi) L_e^2 m_{tot}\omega_x^2}{J} & -\omega_y^2 - \frac{\cos(\varphi)^2 L_e^2 m_{tot}\omega_y^2}{J} & \cos(\varphi) L_e \omega_\theta^2 \\ \frac{\sin(\varphi) L_e m_{tot}\omega_x^2}{J} & \frac{\cos(\varphi) L_e m_{tot}\omega_y^2}{J} & -\omega_\theta^2 \end{bmatrix} \tag{21}$$

$$B = \begin{bmatrix} \frac{\sin(\varphi) C_{\theta x} L_e}{J} - \frac{\sin(\varphi)^2 C_{xx} L_e^2}{J} - \frac{\cos(\varphi)\sin(\varphi) C_{yx} L_e^2}{J} - \frac{C_{xx}}{m_{tot}} \\ \frac{\cos(\varphi) C_{\theta x} L_e}{J} - \frac{\cos(\varphi)\sin(\varphi) C_{xx} L_e^2}{J} - \frac{\cos(\varphi)^2 C_{yx} L_e^2}{J} - \frac{C_{yx}}{m_{tot}} \\ -\frac{C_{\theta x}}{J} + \frac{\sin(\varphi) C_{xx} L_e}{J} + \frac{\cos(\varphi) C_{yx} L_e}{J} \end{bmatrix} \tag{22}$$

$$C = \begin{bmatrix} \frac{\sin(\varphi) C_{\theta y} L_e}{J} - \frac{\sin(\varphi)^2 C_{xy} L_e^2}{J} - \frac{\cos(\varphi)\sin(\varphi) C_{yy} L_e^2}{J} - \frac{C_{xy}}{m_{tot}} \\ \frac{\cos(\varphi) C_{\theta y} L_e}{J} - \frac{\cos(\varphi)\sin(\varphi) C_{xy} L_e^2}{J} - \frac{\cos(\varphi)^2 C_{yy} L_e^2}{J} - \frac{C_{yy}}{m_{tot}} \\ -\frac{C_{\theta y}}{J} + \frac{\sin(\varphi) C_{xy} L_e}{J} + \frac{\cos(\varphi) C_{yy} L_e}{J} \end{bmatrix} \tag{23}$$

$$D = \begin{bmatrix} \frac{\sin(\varphi) C_{\theta\theta} L_e}{J} - \frac{\sin(\varphi)^2 C_{x\theta} L_e^2}{J} - \frac{\cos(\varphi)\sin(\varphi) C_{y\theta} L_e^2}{J} - \frac{C_{x\theta}}{m_{tot}} \\ \frac{\cos(\varphi) C_{\theta\theta} L_e}{J} - \frac{\cos(\varphi)\sin(\varphi) C_{x\theta} L_e^2}{J} - \frac{\cos(\varphi)^2 C_{y\theta} L_e^2}{J} - \frac{C_{y\theta}}{m_{tot}} \\ -\frac{C_{\theta\theta}}{J} + \frac{\sin(\varphi) C_{x\theta} L_e}{J} + \frac{\cos(\varphi) C_{y\theta} L_e}{J} \end{bmatrix} \tag{24}$$

It is through solving the eigenvalue problem for this linearized system of equations that it is possible to estimate the aerodynamic stability of a bluff body subjected to aerodynamic forces. The system of equations is stable if all the roots of the eigenvalue problem are below zero. The eigenvalue problem for this system of equations results in a 6th order polynomial, which can be solved either by numerical means or analytically by applying the Routh-Hurwitz stability criterion to the 6th order polynomial. By using the Routh-Hurwitz stability criterion it is also possible to differentiate whether the instability is characterised as diverged or flutter, Ref. [8].

4 PREDICTION OF INSTABILITY

The following describes the results found by the new 3DOF model proposed in this paper. Due to the limited number of wind tunnel experiments providing input data for the new model, the presented analysis focuses only on aerodynamic phenomena for wind normal to the cable axis. Previously performed analysis of 2DOF response in the *x*-*y*-direction is reported by Gjelstrup *et al.* in Ref. [4]

4.1 Aerodynamic data

Figure 6 shows the aerodynamic input data, used by the new model, which are taken from wind tunnel test performed by Chabart *et al* in 1998, Ref. [2]. The aerodynamic data are used in calculating the instability ranges, which are shown in Figure 8.

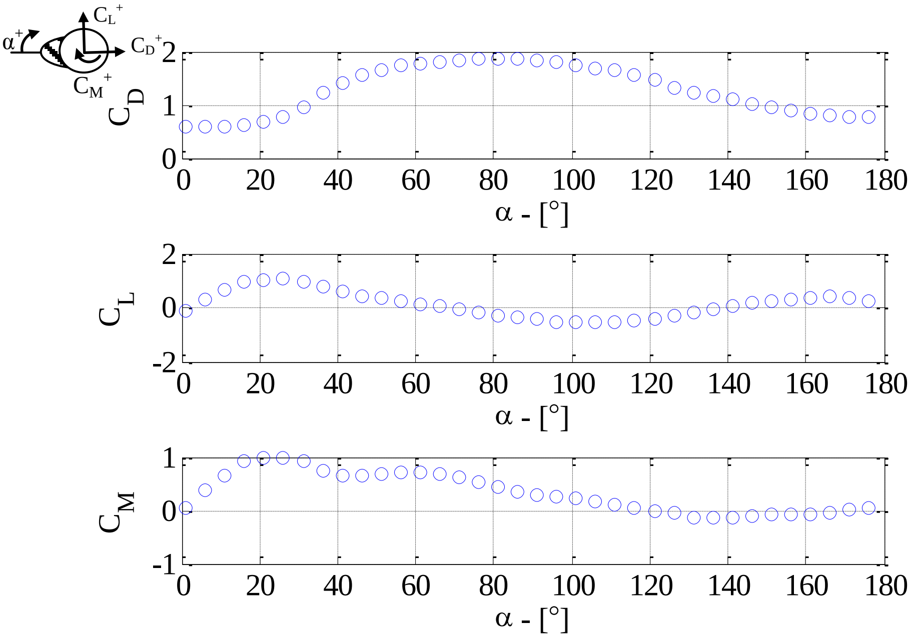

Figure 6. Aerodynamic coefficients taken from Ref. [2] and transformed into the model's coordinate system.

4.2 Calculated instability

Figure 7 shows a cross sectional view of the iced cable model from which the aerodynamic data were obtained. R_δ is the calculated individually for each angle of attack on the non-displaced body and used for the prediction of the instability range of the iced cable model.

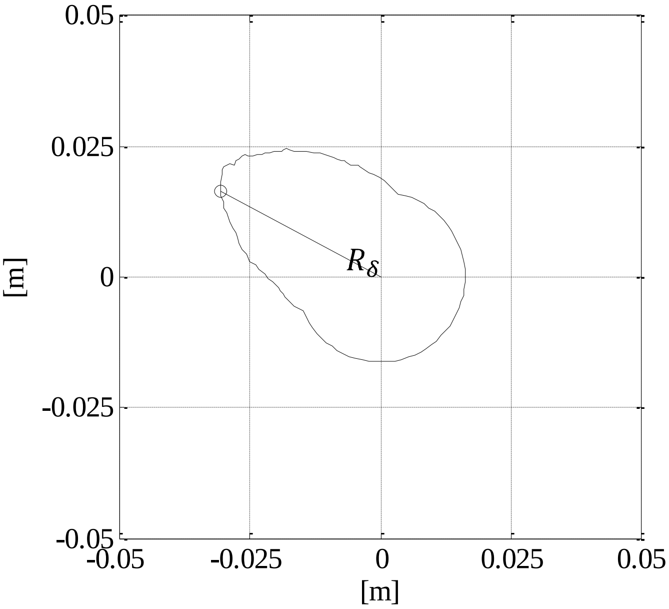

Figure 7. Iced cable with radial distance R_δ to the leading edge.

Figure 8a shows the calculated instability range found by using the aerodynamic data shown in Figure 6. Values less than zero indicate the ranges of instability predicted by the model. The unstable ranges are ~25° - ~45°, ~70° - ~135° and ~170° - 180°. Figure 8a also shows the Den Hartog criterion for instability, which states that galloping occurs, if $C_D + \partial C_L/\partial\alpha < 0$, where C_D and C_L are aerodynamic drag and lift coefficients and α is the wind angle of attack. The value of $C_D + \partial C_L/\partial\alpha$ is marked with a white line dotted with circles and the zero level for the Den Hartog criteria is marked with a straight white line, see Figure 8a. The Den Hartog criterion predicts instability in two ranges, 30° - 45° and 170° - 180°.

Comparing the results from these three approaches in Figure 8b it is demonstrated that the new model is capable of predicting instability over a wide range of wind angles of attack acting in a combined effect of drag lift and moment, which is not considered by previous models.

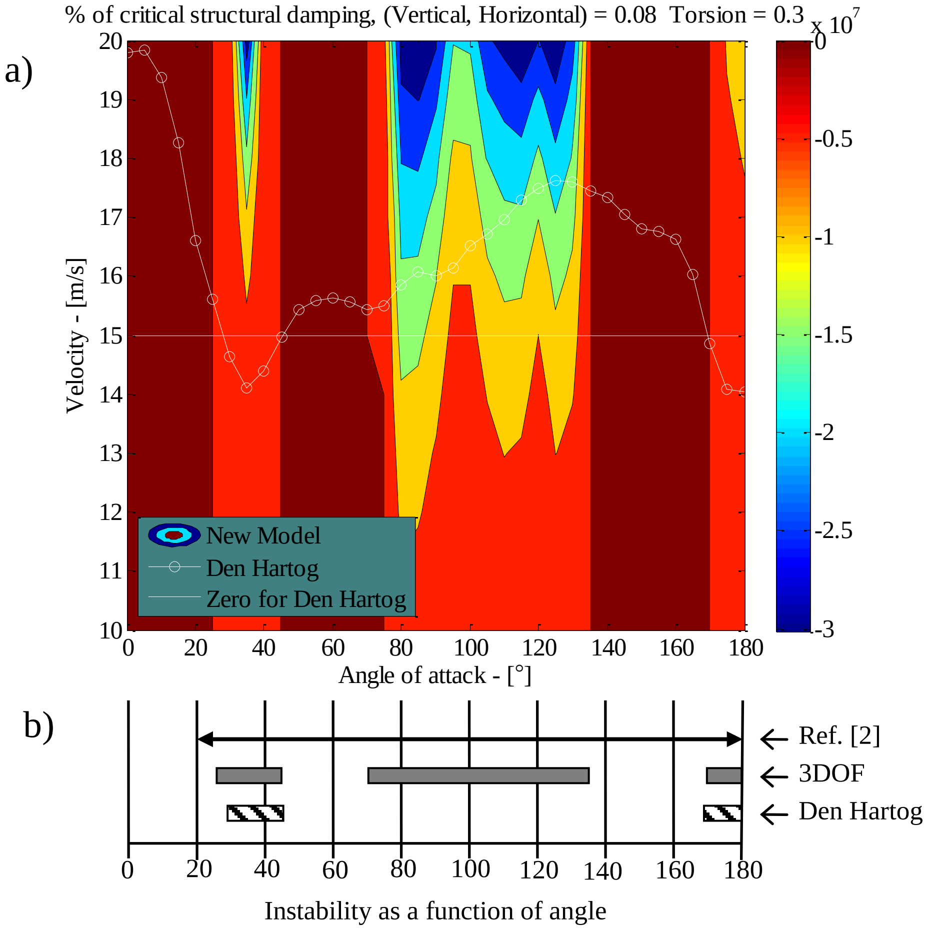

Figure 8. a) Range of predicted instability for the combined Drag, Lift and moment and $\gamma_0 = 0°$. b) Comparison of experimental found instability with Den Hartog and the 3DOF model

4.3 Discussion of results

Comparing the numerical found instability with results from previously made wind tunnel test, Ref. [2], good agreement between the experimental observed instability and the range predicted from the here presented model could be demonstrated. However the ranges from ~45° - ~70° and ~135° - ~170° are considered as stable in the numerical model, whereas the wind tunnel test, performed by Chabart *et al.* Ref. [2], shows that the model tested for different wind speeds and angles of attack was unstable in the entire range between 20° to 180°.

In comparison to older models designed with the aim to predict aerodynamic instability based on aerodynamic forces, this new model is able to predict instability over a wider range of wind angles.

REFERENCES

[1] R. D. Blevins. *Flow-Induced Vibration*, 2. Ed., Krieger, 1994.
[2] O. Chabart, and J. L. Lilien. "Galloping of electrical lines in wind tunnel facilities." *Journal of Wind Engineering and Industrial Aerodynamics*, 74-6, 967-976, 1998.
[3] A. G. Davenport. "Buffeting of suspension bridge by storm winds." *American Society of Civil Engineers -- Proceedings*, 88, 233-268, 1962.
[4] H. Gjelstrup, C. Georgakis, and A. Larsen. "A Preliminary Investigation of the Hanger Vibrations on the Great Belt East Bridge." Seventh International Symposium on Cable Dynamics, Vienna (Austria), 2007
[5] J. P. D. Hartog. "Transmission-Line Vibration Due to Sleet." *Institute of Electrical Engineers*, 51, 1074-1086, 1932.
[6] J. H. G. Macdonald, and G. L. Larose. "A unified approach to aerodynamic damping and drag/lift instabilities, and its application to dry inclined cable galloping." *Journal of Fluids and Structures*, 22,(2), 229-252, 2006.
[7] W. W. Martin, I. G. Currie, and E. Naudascher. "Streamwise oscillations of cylinders." *Journal of the Engineering Mechanics Division-Asce*, 107,(3), 589-607, 1981.
[8] J. J. Thomsen. *Vibrations and Stability*, Second Edition Ed., Springer, 2003.

Paper VI ([66])

“Aerodynamic Instability of a cylinder with thin ice accretion”

H. Gjelstrup & C.T. Georgakis

In proceedings: *8th International Symposium on Cable Dynamics, 2009*

AERODYNAMIC INSTABILITY OF A CYLINDER WITH THIN ICE ACCRETION

Henrik GJELSTRUP
COWI A/S, Parallelvej 2, 2800 Kgs. Lyngby, Denmark
hegj@cowi.dk/heg@byg.dtu.dk

Christos T. GEORGAKIS
Technical University of Denmark, Building 118, Brovej, 2800 Kgs. Lyngby , Denmark
cg@byg.dtu.dk

Introduction

The present work is motivated by a hanger vibration event on the Great Belt East Bridge, involving hanger ice accretion from March 27-31, 2001. The paper outlines a series of icing tests performed on a cylinder at the NRC Altitude Icing Wind Tunnel in March 2009 and the wind tunnel tests thereafter, leading to a description of the mechanism behind the hanger motional instability.

Transmission line vibrations due to ice accretion have received considerable interest in recent years [1-5]. *Although much work has been done on the wind-induced vibrations of bridge cables e.g.* [6-8], *little or no research on ice-accreted bridge cables exists.*

Figure 1 shows a typical section of ice accretion as has been found on a vertical hanger of the Great Belt East Bridge, with a diameter of approximately 115mm. This ice shape is not from the specific aforementioned vibration event, but it illustrates that a fairly uniform ice accretion can be generated on cylindrical cables. In order to investigate the nature of accretion, a set of wind tunnel tests were performed at varying temperatures and with varying levels of liquid water content.

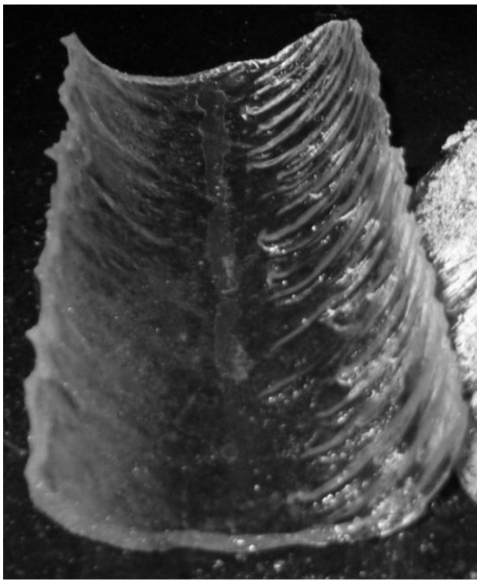

Figure 1 Ice accretion from a vertical hanger
Courtesy of Storebælt A/S

From these experiments, one ice shape similar to that of Figure 1 was selected. This was then used in the generation of a generalized ice profile. The generalized ice profile was selected so as to depict with a fair degree of representation the most commonly observed ice accretion on the Great Belt East Bridge. Subsequently, the generalized ice profile was manufactured by use of rapid prototyping.

Next, a series of static wind tunnel tests were undertaken to determine the aerodynamic force coefficients of the rapidly prototyped hanger sectional model.

Finally the aerodynamic force coefficients (drag, lift and moment), found from the static wind tunnel tests, were used to determine the potential for aerodynamic instability of the hanger through application of the quasi-steady theory developed by Gjelstrup et al. [9-10]. The application of the theoretical model yield regions of expected aerodynamic instability in which the observed vibrations of the Great Belt East Bridge hangers lie.

ICE ACCRETION WIND TUNNEL TESTS

As mentioned, a series of ice accretion tests on cylinders were performed by DTU at the NRC Institute for Aerospace Research Altitude Icing Wind Tunnel Facility (AIWT) in Ottawa, Canada in March 09'. The tests were performed with varying wind velocities and flow liquid water content (LWC). AIWT has a test section of 0.57mx0.57m, with the overall design and testing capabilities of the facility described by Oleskiw et.al [11]. As such, wind velocities of 10m/s, 20m/s and 30m/s, where chosen, so also as to lie within the velocity range observed during the aforementioned vibration event on the Great Belt East Bridge hangers.

Icing experiment setup

For the creation of the generalised ice accretion profile, a cylinder of diameter 89mm was chosen for the section model, as it is the section of closest diameter to that of the Great East Belt Bridge hanger that was available for testing. Other test parameters specific to the generalised ice profile are provided in Table 1.

TABLE 1 - Test parameters for generation of generalised ice accretion profile, section and flow

LWC [g/m^3]	Wind speed [m/s]	Droplet size [µm]	T_{air} [°C]	Test time [min.]	Diameter [m]	Orientation [-]
0.4	20	50	-3	10	0.089	Vertical

The LWC of 0.4 g/m^3 was chosen based on the experimental work of Lozowski [12] and the theoretical work on the thermodynamics of icing cylinders by Mazin et. al [13]. From the aforementioned works, it is possible to deduce that a LWC higher than 0.4 has no consequence on ice formation for temperatures just below zero. Furthermore, a value of LWC of 0.44 g/m^3 in strato-cumulus clouds has been reported by Hess et. al [14]. The strato-cumulus cloud belongs to a class of clouds which is characterized by large dark, rounded masses, usually in groups, lines, or waves. These clouds are often seen at either the front or tail end of worsening weather, often indicating approaching storms. For the icing tests it was assumed that the ice on the hangers form due to an aerosoled LWC in the air surrounding the cable similar that of a strato-cumulus cloud, as this fits the observation on the day of the specific vibration event on the Great Belt East Bridge hangers.

Figure 2 shows the weather data collected during the vibration event. A more detail description of the event is provided by Gjelstrup et al [7]. Note that the vibration event started at around 18m/s just before midnight, corresponding to a Reynolds number of approximately 1.32×10^5, and that the vibrations occurred for a fairly constant wind direction of 130°±10° from magnetic north.

Fig. 3c shows the generated ice accretion, similar to Fig. 1, which was chosen for the analysis herewith.

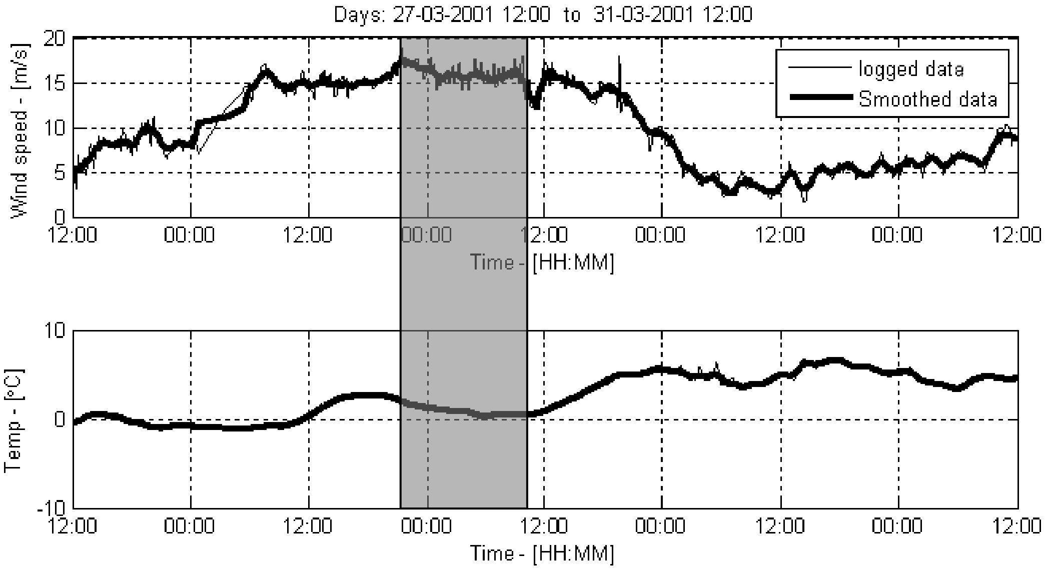

Figure 2 Collected weather data during vibration event on the Great Belt hangers. ■ marks the vibration event

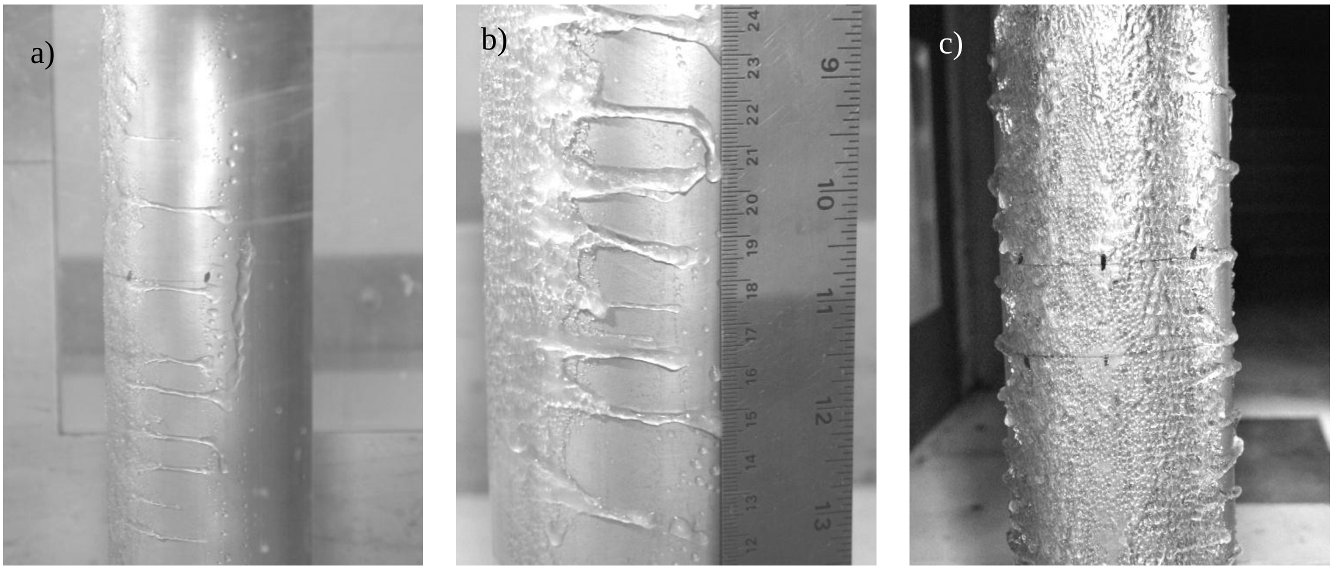

Figure 3a) - Side view of test cylinder with small water pathways and large drops running down at 100°, b) - Side view of test cylinder with arms of solid ice, c) Front view of iced test cylinder after 600sec.

Time-dependant ice accretion

For the specific ice accretion, the following observations were made during the tests. The first small ice droplets where visible around the stagnation point after approximately 30sec. Then, 20 secs later, the accumulated water started to generate small pathways (Figure 3a) of water in which the accumulated water flowed from about 25° to approximately 100° behind the stagnation point, where it again started to accumulate. In some locations this also happened at 110°. It was also observed that large drops of water were running along the cylinder at approximately the 100° line.

The core area of accretion started to show distinguishable features in comparison to the rest of the ice accretion after approximately 260sec from start. Here the core area is defined as ±20° (in average) and an outer area is defined to be between 20° and 45°. At this point, the small water pathways had grown into solid arms of ice, Figure 3b.

At the 600sec mark, the largest accumulation of ice was found at around the 30° to 35° line. At the stagnation point, a narrow area with a smooth surface had been generated. The arms of solid ice were at this point located between 50° and 100° on average. The end points of the arms were pointing downwards at angles ranging from 45° to 90°, where 0° is defined as horizontal. At some spots, relatively long water/ice rivulets were observed, but no continuous water/ice rivulet was created.

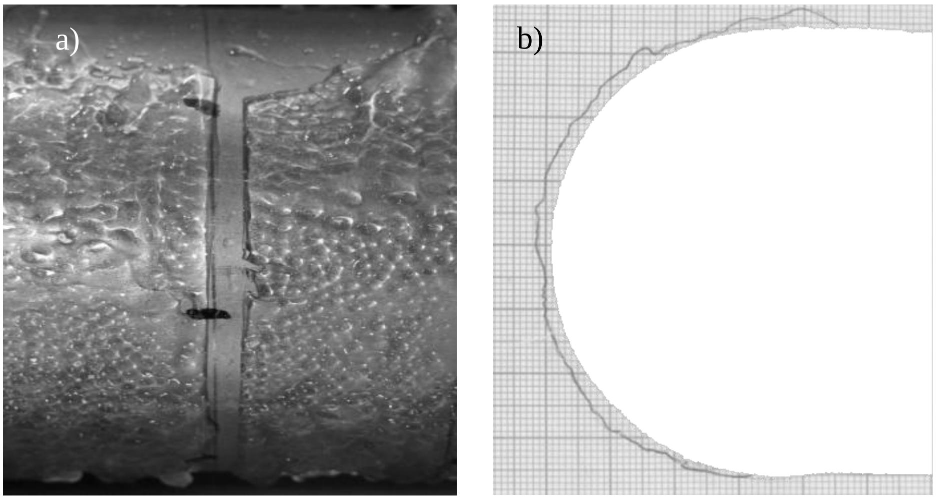

Figure 4a) - Close-up of front view of thin melted slice, picture is rotated 90°,
b) - Traced ice surface

At the end of the test, a thin slice of ice was melted at the centre of the cylinder (Figure 4a). The ice profile was traced by placing a piece of paper on a thin plate of metal which was cut to match the cylinder's diameter (Figure 4b). The thin metal plate was placed against the ice and the ice profile was traced using a specially formed pencil. The resulting trace is shown in Figure 4b. Note that the aforementioned tracing method does not allow for the accurate capture of the 3D surface changes.

The trace of the ice profile of Figure 4b has been digitized and can be seen in Figure 5a, where the mean ice thickness is shown in Figure 5b. This mean cross-sectional thickness of the ice shape corresponds to 5.2% of the cylinder radius and was used as a template for the generalized thin ice profile. The generalized ice profile was used in dry wind-tunnel tests for the determination of static force coefficients.

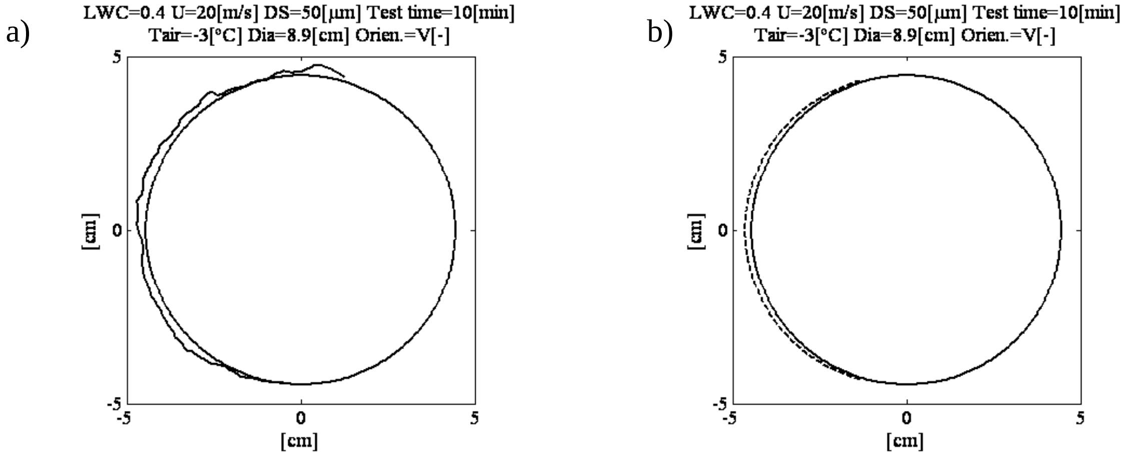

Figure 5a) Digitized ices shape on a cylinder, b) Mean ice shape thickness on a cylinder

GENERALIZED ICE PROFILE

A cross-sectional sketch of the cable with the generalized ice profile is shown in Figure 6a. A photograph of the simulated ice accretion, which is based on the experimentally determined profile, is shown in Figure 6b. The simulated ice accretion was produced through rapid prototyping and has a mid-point point thickness of 2mm.

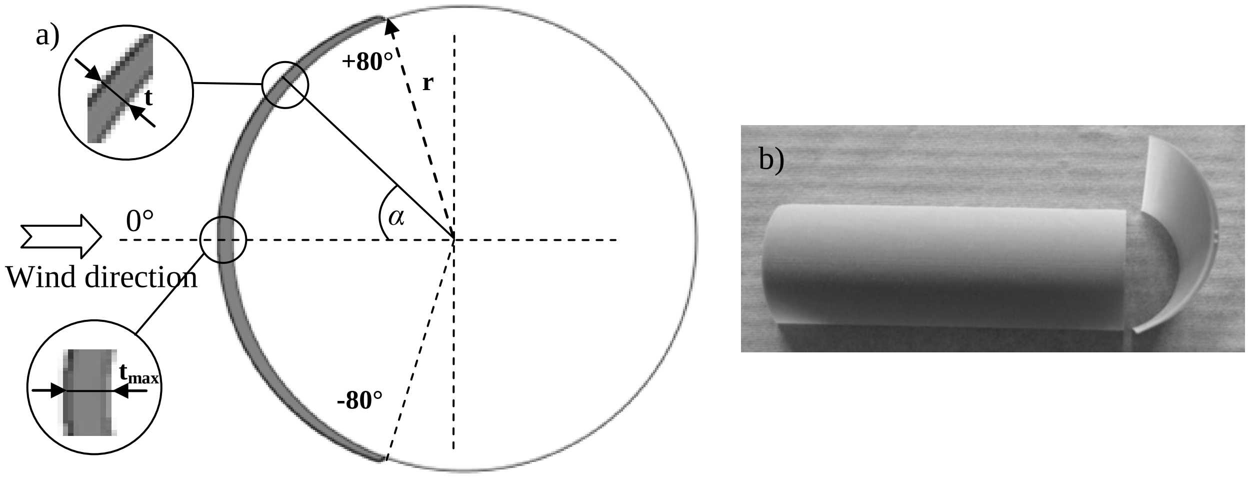

Figure 6a) Model with ice, b) ice produced by rapid prototyping

The thickness of the prototyped ice accretion zeroes at ±80° from the stagnation point, as shown in Figure 6a. An expression of the ice thickness as a function of angle from stagnation point is given by

Eq. (1), where t is the ice thickness, r is the test cylinder diameter, t_{max} is the mean ice stagnation thickness and α is the angle. The definition of the variables in Eq. (1) can also be seen in Figure 6a.

$$t = -r + t_{max} * \cos(\alpha) + \sqrt{(-t_{max}^2 + r^2 + t_{max}^2 * \cos(\alpha))} \tag{1}$$

The final dimensions of the tested sectional model and ice accretion are listed in Table 2.

TABLE 2: Dimensions of the test section, model and ice

Model	Diameter	0.07m
	Length	0.96 m
Simulated ice	0° thickness	2 mm
Simulated ice to cylinder dia. ratio		5.7%

AERODYNAMIC FORCE COEFFICIENTS

The static aerodynamic force coefficient wind tunnel tests were performed at the Closed Circuit Wind Tunnel (CCWT) at FORCE Technology in Lyngby, Denmark. The cross-sectional dimensions of the exchangeable working section of the Closed Circuit Wind-Tunnel are 1.00m × 0.70m. The definition of the wind tunnel coordinate system is shown in Figure 7a, where drag is measured in the x-direction, lift is measured in the z-direction and moment is measured about the y-direction.
The force coefficients were determined for wind velocities of 22, 27, 31, 37 and 41 m/s and are shown in Figure 7b,c,d.

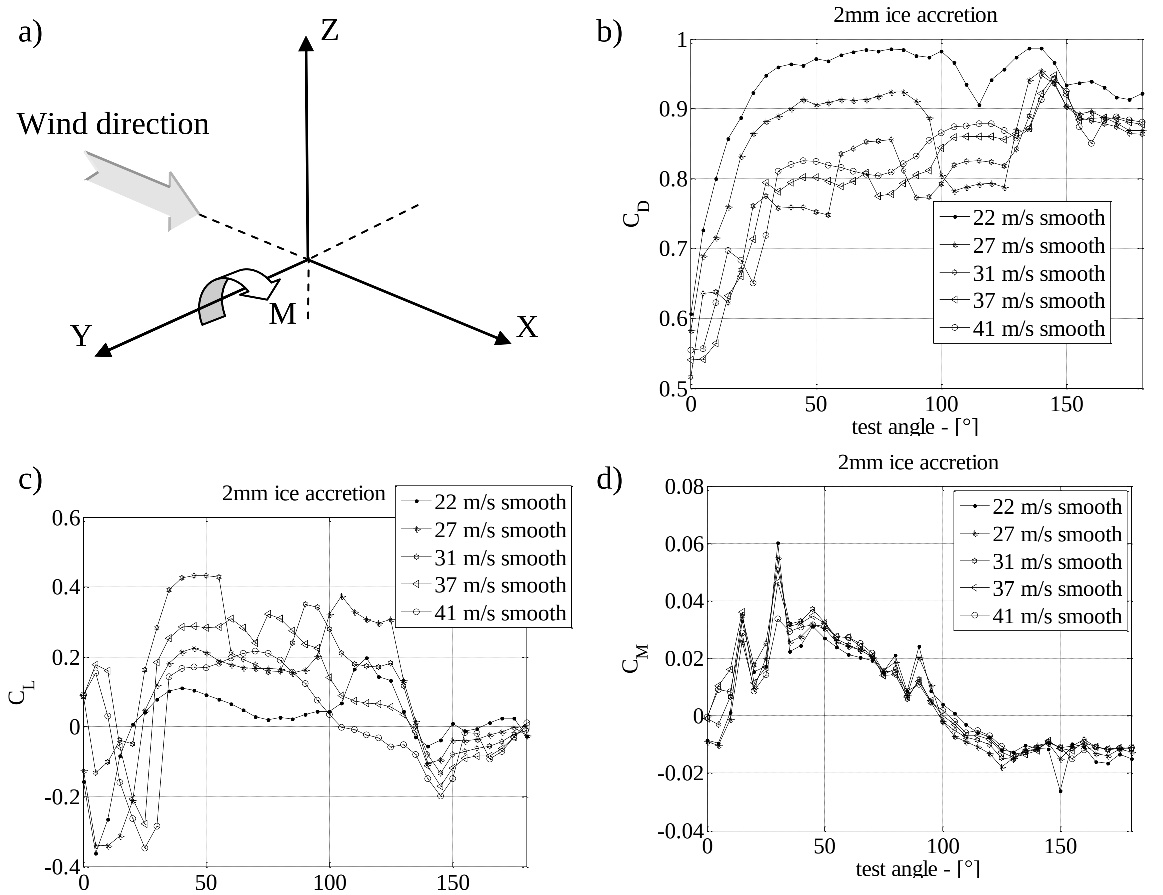

Figure 7a) Sign convention for test results, b) Aerodynamic Drag coefficients c) Aerodynamic Lift coefficients, d) Aerodynamic Moment coefficients

The tests were all performed in smooth flow (turbulence intensity below 1%) and the model was tested for wind angles between 0° and 180°, in steps of 5°. A wind direction of 0° in model scale is equivalent to a wind direction of 130° in full-scale (Southeastly wind).

By examining Figure 7b, 7c and 7d, it can be seen that the aerodynamic force coefficients are dependent on both wind velocity and angle of attack. This dependency is most significant for C_D and C_L. C_M has a relatively small dependency on wind velocity.

The Reynolds numbers achieved during the wind tunnel tests were between 1.0×10^5 to 1.9×10^5. In this range, a sharp drop in the lift force and the steep rise in the drag force was observed for a wind direction of 60° and a scaled wind velocity of 31m/s (Figure 7b-7c). It is believed that the separation bubble behind the specimen is relatively unstable at this angle. As a consequence, the bubble has the tendancy to change to a more stable position, generating in the process a lower lift but higher drag force. This has also been observed for other wind speeds and angles of attack.

PREDICTED INSTABILITY

Through use of the determined aerodynamic force coefficients, the potential for motional instability of the iced bridge hanger is estimated through use of the generalized three-degree-of-freedom (3-DOF) quasi-steady model presented by Gjelstrup et al. [9-10]. The result of this application can be seen in Figure 8, where the shaded areas indicate zones of instability. Here, the instability can occur in the range between 0° and 25° and between 175° and 180° for most wind velocities. A smaller zone of instability is also found between 50° and 65° for wind velocities of between 27m/s to 37m/s. Similarly, an additional zone of instability is found between 120° and 140° for wind velocities of about 22m/s to 37m/s.

The bold typed x's of Figure 8 represent the scaled values of wind velocity and angle of attack for the hanger vibration event on the Great Belt East Bridge. It should be observed that the predicted aerodynamic instability for the iced bridge hanger corresponds well with the observed aerodynamic instability on the Great Belt bridge hangers.

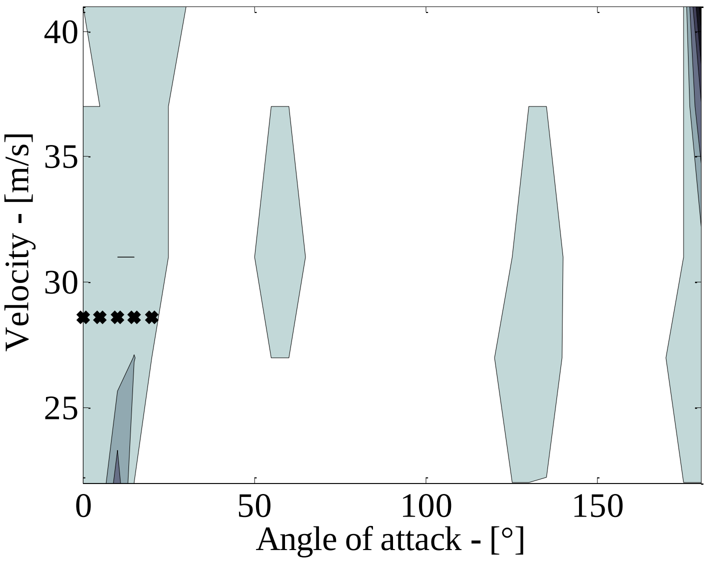

Figure 8 Predicted instability plot. Shaded zones are indicate regions of instability, where ✖ indicates the ranges in which hanger vibration was observed on the Great Belt East Bridge. The model-scale velocities presented above have been scaled using corresponding Reynolds numbers in full-scale.

ACKNOWLEDGEMENTS

The authors would like to thank Femern Bælt A/S and Storebælt A/S for their sponsorship of the icing tests at NRC, Ottawa, Canada. The authors would also like to additionally thank FORCE Technology A/S for use of their wind tunnel facilities for the determination of the aerodynamic force coefficients, as well as Storebælt A/S for the aforementioned vibration event data.

REFERENCES

[1] O. Nigol, and P. G. Buchan, 1981, "Conductor Galloping .1. Den Hartog Mechanism." *Ieee Transactions on Power Apparatus and Systems*, 100,(2), 699-707

[2] O. B. Nigol, P. G., 1981, "Conductor Galloping .2. Torsional Mechanism." *Ieee Transactions on Power Apparatus and Systems*, 100,(2), 708-720

[3] O. Chabart, and J. L. Lilien, 1998, "Galloping of electrical lines in wind tunnel facilities." *Journal of Wind Engineering and Industrial Aerodynamics*, 74-6, 967-976

[4] P. V. Phuc. (2005). "A wind tunnel study on unstady forces of ice accreted transmission lines." In: *BBAA V 5th international Colloquium on Bluff Body Aerodynamics and Applications*, p373-376.

[5] M. Shimizu. (2005). "A wind tunnel study on aerodynamic Characteristics of ice accreted transmission lines." In: *BBAA V 5th international Colloquium on Bluff Body Aerodynamics and Applications*, p369-372

[6] Y. Q. Ni, X. Y. Wang, Z. Q. Chen, and J. M. Ko, 2007, "Field observations of rain-wind-induced cable vibration in cable-stayed Dongting Lake Bridge." *Journal of Wind Engineering and Industrial Aerodynamics*, 95,(5), 303-328

[7] H. Gjelstrup, C. Georgakis, and A. Larsen. (2007). "A Preliminary Investigation of the Hanger Vibrations on the Great Belt East Bridge." In: *Seventh International Symposium on Cable Dynamics*, Vienna (Austria).

[8] M. Virlogeux, 1998, "Cable vibrations in cable-stayed bridges,." *A. Larsen, S. Esdahl (Eds.), Bridge Aerodynamics, Balkema, Rotterdam*, 213–233

[9] H. Gjelstrup, A. Larsen, C. Georgakis, and H. Koss. (2008). "A new general 3DOF quasi-steady aerodynamic instability model." In: *BBAA VI International Colloquium on: Bluff Bodies Aerodynamics & Applications*, Milano, Italy, .

[10] H. Gjelstrup, and C. Georgakis, 2009, "A 3DOF quasi-steady bluff-body instability model, submitted to Journal of Wind Engineering & Industrial Aerodynamics, Mar 02, 2009."

[11] M. M. Oleskiw, F. H. Hyde, and P. J. Penna. (2001). "In-flight Icing Simulation Capabilities of NRC's Altitude Icing Wind Tunnel " In: *39th AIAA Aerospace Science Meeting & Exhibit*, Reno, NV.

[12] E. P. S. Lozowski, J.R.; Hearty, P.F., 1983, "The icing of an unheated, nonrotating cylinder. II. Icing wind tunnel experiments." *Journal of Climate and Applied Meteorology*, 22,(12), 2063-2074

[13] I. P. Mazin, A. V. Korolev, A. Heymsfield, G. A. Isaac, and S. G. Cober, 2001, "Thermodynamics of icing cylinder for measurements of liquid water content in supercooled clouds." *Journal of Atmospheric and Oceanic Technology*, 18,(4), 543-558

[14] M. Hess, P. Koepke, and I. Schult, 1998, "Optical Properties of Aerosols and Clouds: The Software Package OPAC." *Bulletin of the American Meteorological Society*, 79,,(5), 831–844

Appendix A

Vibrations on the Great Belt East Bridge Hangers and Weather Data

Table A1 and Table A2 show a list over visually reported and measured vibration observations.

Table A1. Measured Hanger Vibration with Large Displacements. All Vibration is in 1st to 3rd Mode Shape.

Date of vibration event	Location in respect to pylon	Hanger	Maximal displacement [m]	Wind velocity [m/s]	Wind direction [°]	Air temperature [°C]	Humidity (%)	Damper type applied to hanger
Measured observations								
06-03-2001	free	147.1N	0,9	7.2	233	2,2	76	-
16-03-2001	free	147.1N+S	1,3	6.8	300	2,2	77	-
29-03-2001	free	all	2,0	16	130	1,3	78	-
07-10-2003	free	149.1N	0,8	12	230	9,5	81	Spiral
25-10-2003	free	149.1N	0,7	13	250	2,3	65	Spiral
22-12-2003	free	146.2N - 150.1N	1.5	12	350	-2,5	79	Spiral & Wind rope
22-10-2004	free	111.1 S	1.2	15	200	11,6	79	Tuned Liquid Damper
05-12-2004	lee	111.2 N	0,7	15	270	7,8	87	Tuned Liquid Damper
20-12-2004	free	147.1S	0.5	11	330	3,9	81	-
21-12-2004	lee	147.1N+S	0.5	9	230	2,2	78	Wind rope N
22-12-2004	lee	110.2 N	0.5	18	225	2,9	95	Tuned Liquid Damper
24-12-2004	lee	110.1 N	2.0	12	270	5,6	87	Tuned Liquid Damper
25-12-2004	free	147.1S	0.8	14	170	4.5	87	-
24-01-2005	free	149.1S	1.8	13	20	0.2	75	-
27-01-2005	free	147.1S	0.8	7	330	0.0	93	-
29-01-2005	lee	147.1S	1.0	4	300	0.7	89	-
02-03-2005	free	147.1S	1.5	12	80	-1.9	98	-
03-03-2005	free	147.1S	0.8	7	0	-4.8	74	-
04-03-2005	free	147.1S	1.3	6	180	-4.0	76	-
13-12-2005	free	147.1S	0.3	10	300	5,8	91	hydraulics
07-02-2006	free	147.1S+N	0.2	12	285	5,6	95	Wind rope N & hydraulics S

Table A2. Visually Observed Hanger Vibration with Large Displacements. All Vibration is in 1st to 3rd Mode Shape.

Date of vibration event	Location in respect to pylon	Hanger	Maximal displacement [m]	Wind velocity [m/s]	Wind direction [°]	Air temperature [°C]	Humidity (%)	Damper type applied to hanger
Visual observations								
31-10-2000	free	147.2 N	1,5 - 2,0	22 - 24	SW	4,7[2]		
14-12-2000	lee for hanger nearest to pylon	144.1 - 147.2 N	0,5 - 1,0	15 - 18	WSW	-0,7[2]		
14-12-2000		146.2 - 147.2 S	0,5 - 1,0	15 - 18	WSW	-0,7[2]		
05-02-2001	lee	113.1 - 114.1 S	0,0 - 0,4	15 - 20	E-ESE	-0,4[2]		
05-02-2001	free	111.2 - 110.2 S	0,0 - 0,3	15 - 20	E-ESE	-0,4[2]		
12-03-2001	free	111.2 S	0,0 - 0,3	10 - 12	SW	0,0[2]		
19-12-2005	-	147.2 - 146.1 S	0,3 - 0,5					
01-11-2006	lee	113.1S	0,5 - 1,0	19-22	N-NNE	?		
01-11-2006	maybe lee	113.1N	0,5 - 1,0	19-22	N-NNE	?		

---

[2] Temperature is found from the mean of all minimum temperature with in the week of the event. Icing can occur up to 4 °C.

The notation of the cable can been found in Figure A1

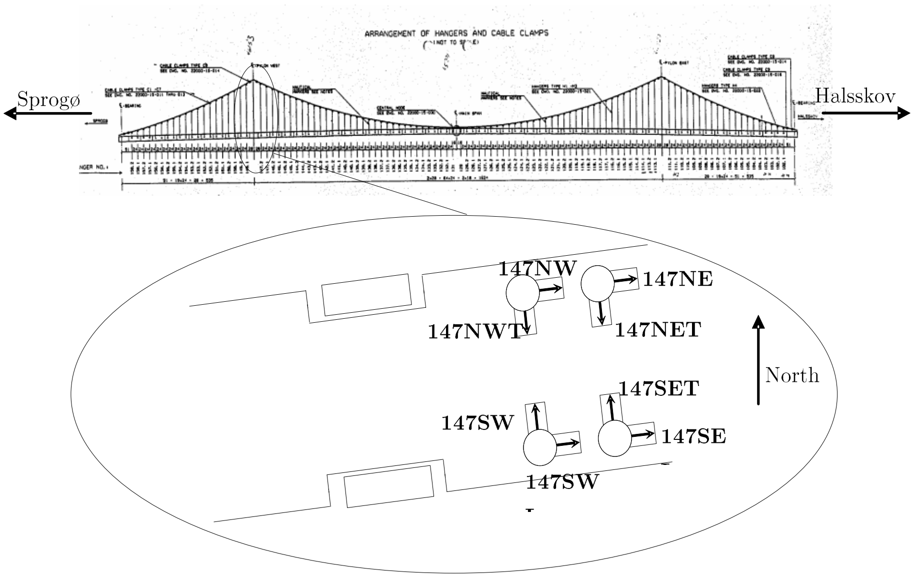
ARRANGEMENT OF HANGERS AND CABLE CLAMPS
Sprogø
Halsskov
147NW
147NE
147NWT
147NET
North
147SET
147SW
147SE
147SW

Figure A1. Hanger Notation for Table A1 and Table A2.

Figure A2 show summarized plots of all registered weather data for the winter periods October to April in the years 2000 to 2008. The individual data point in the data set is a 5 minute or 10 minute mean value. The data is registered at the mid of the Great Belt East Bridge. The x-axis in Figure A2 is divided into interval with respect to the x-axis title, where the number for the interval shows the upper limit of that particular interval. The left hand side y-axis in Figure A2 gives the number of events, which falls within the intervals of the different plots. The right hand side y-axis shows the accumulated data used to plot the different interval, starting from zero.

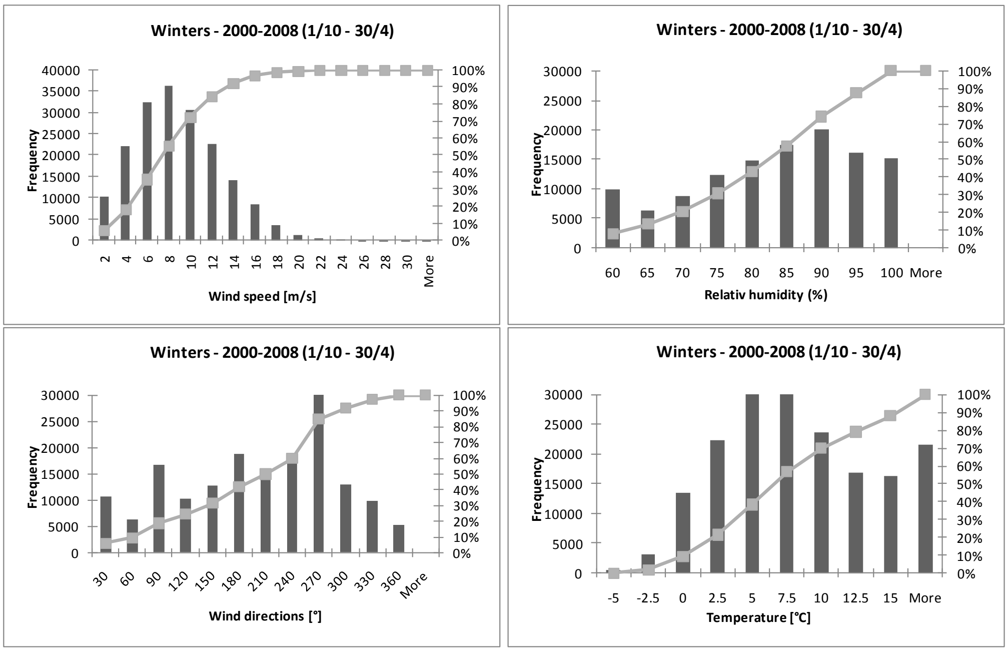

Figure A2. Weather Data for the Periods October to April in the Years 2000 to 2008.

Appendix B

Smooth and Turbulent Wind Velocity Profiles

Wind Profiles in Smooth Flow

In the following the wind tunnel profiles obtained from experiments in the CCWT at FORCE is presented.

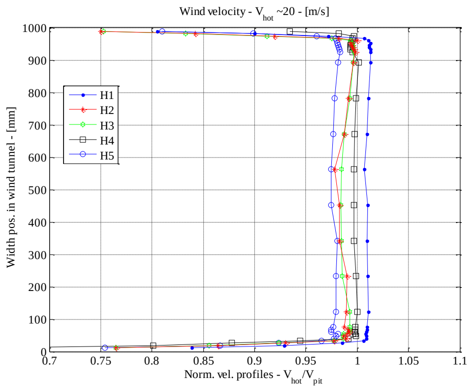

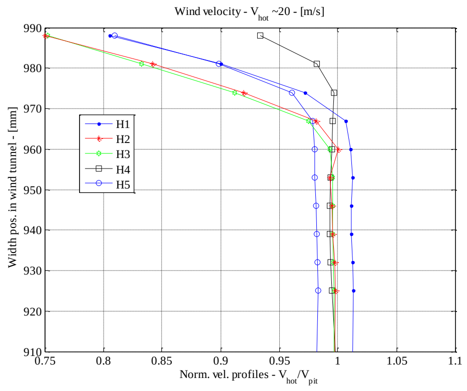

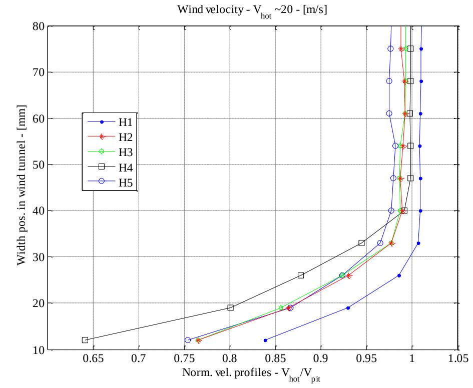

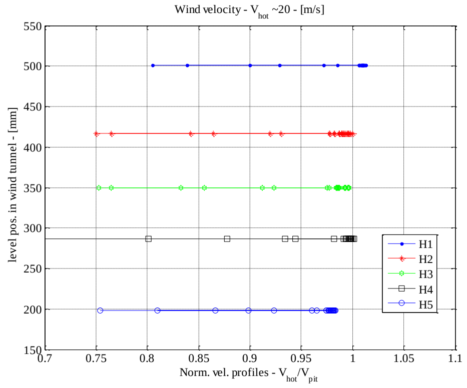

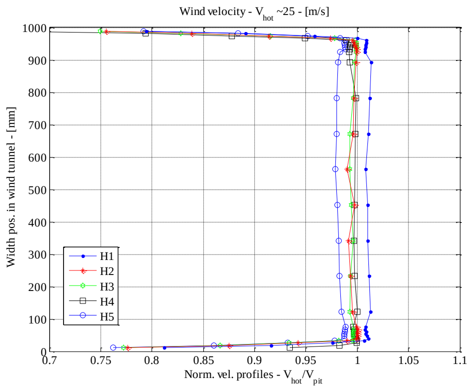

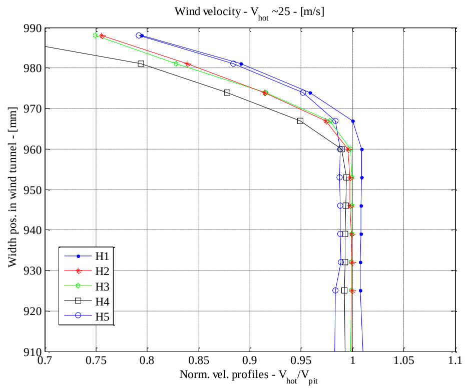

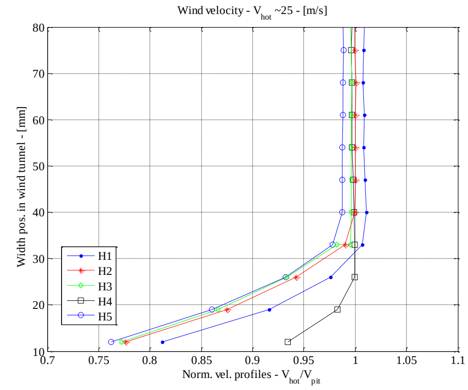

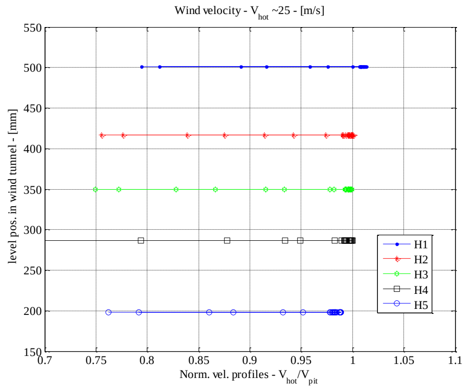

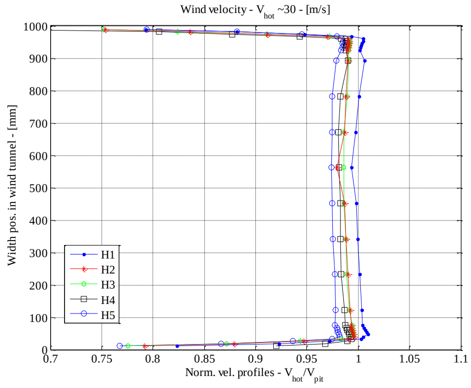
Wind velocity - V_{hot} ~30 - [m/s]
Width pos. in wind tunnel - [mm]
Norm. vel. profiles - V_{hot}/V_{pit}
0
100
200
300
400
500
600
700
800
900
1000
0.7
0.75
0.8
0.85
0.9
0.95
1
1.05
1.1
H1
H2
H3
H4
H5

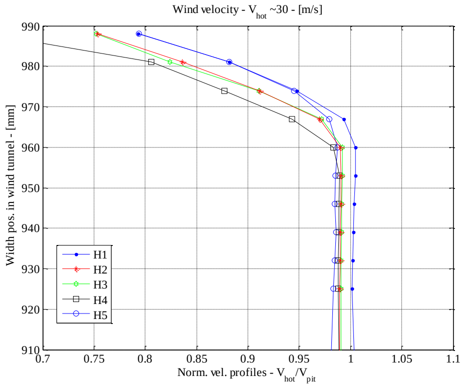
Wind velocity - V_{hot} ~30 - [m/s]
Width pos. in wind tunnel - [mm]
Norm. vel. profiles - V_{hot}/V_{pit}
910
920
930
940
950
960
970
980
990
0.7
0.75
0.8
0.85
0.9
0.95
1
1.05
1.1
H1
H2
H3
H4
H5

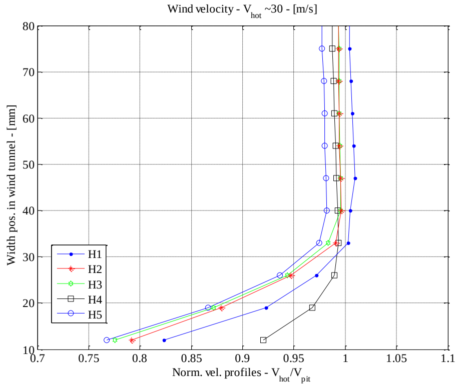
Wind velocity - V_{hot} ~30 - [m/s]
Width pos. in wind tunnel - [mm]
Norm. vel. profiles - V_{hot}/V_{pit}
10
20
30
40
50
60
70
80
0.7
0.75
0.8
0.85
0.9
0.95
1
1.05
1.1
H1
H2
H3
H4
H5

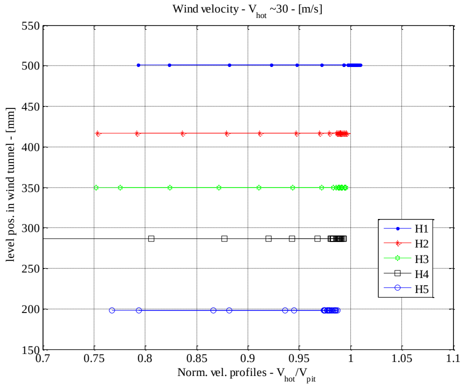
Wind velocity - V_{hot} ~30 - [m/s]
level pos. in wind tunnel - [mm]
Norm. vel. profiles - V_{hot}/V_{pit}
150
200
250
300
350
400
450
500
550
0.7
0.75
0.8
0.85
0.9
0.95
1
1.05
1.1
H1
H2
H3
H4
H5

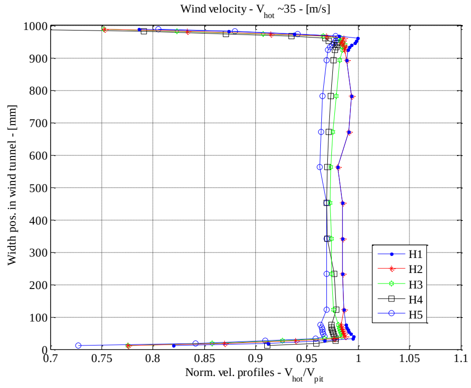
Wind velocity - V_{hot} ~35 - [m/s]
Width pos. in wind tunnel - [mm]
Norm. vel. profiles - V_{hot}/V_{pit}
0
100
200
300
400
500
600
700
800
900
1000
0.7
0.75
0.8
0.85
0.9
0.95
1
1.05
1.1
H1
H2
H3
H4
H5

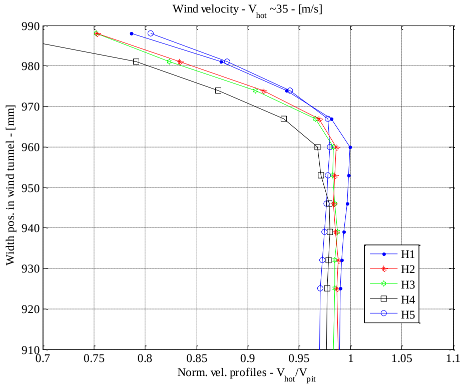
Wind velocity - V_{hot} ~35 - [m/s]
Width pos. in wind tunnel - [mm]
Norm. vel. profiles - V_{hot}/V_{pit}
910
920
930
940
950
960
970
980
990
0.7
0.75
0.8
0.85
0.9
0.95
1
1.05
1.1
H1
H2
H3
H4
H5

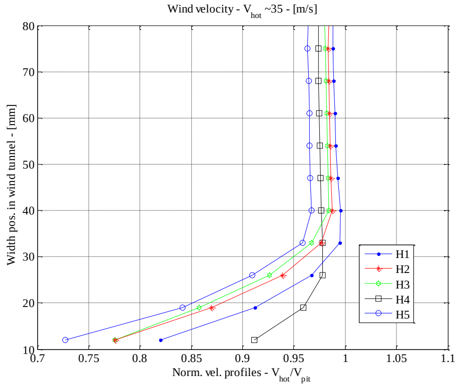
Wind velocity - V_{hot} ~35 - [m/s]
Width pos. in wind tunnel - [mm]
Norm. vel. profiles - V_{hot}/V_{pit}
10
20
30
40
50
60
70
80
0.7
0.75
0.8
0.85
0.9
0.95
1
1.05
1.1
H1
H2
H3
H4
H5

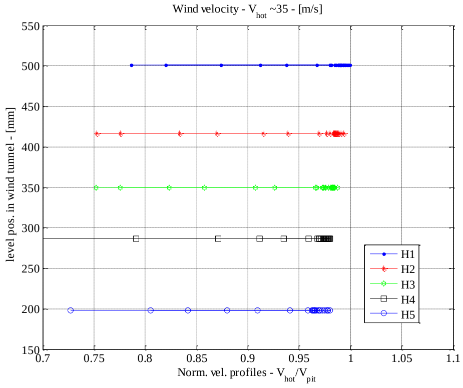
Wind velocity - V_{hot} ~35 - [m/s]
level pos. in wind tunnel - [mm]
Norm. vel. profiles - V_{hot}/V_{pit}
150
200
250
300
350
400
450
500
550
0.7
0.75
0.8
0.85
0.9
0.95
1
1.05
1.1
H1
H2
H3
H4
H5

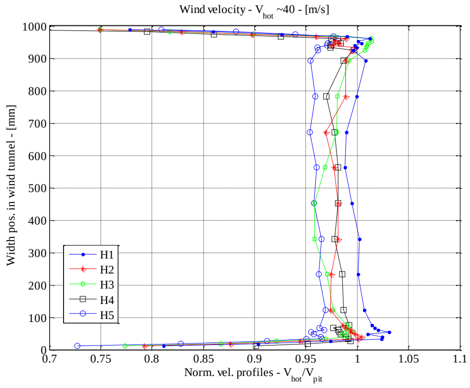
Wind velocity - V hot ~40 - [m/s]
Width pos. in wind tunnel - [mm]
Norm. vel. profiles - V hot /V pit
0.7
0.75
0.8
0.85
0.9
0.95
1
1.05
1.1
0
100
200
300
400
500
600
700
800
900
1000
H1
H2
H3
H4
H5

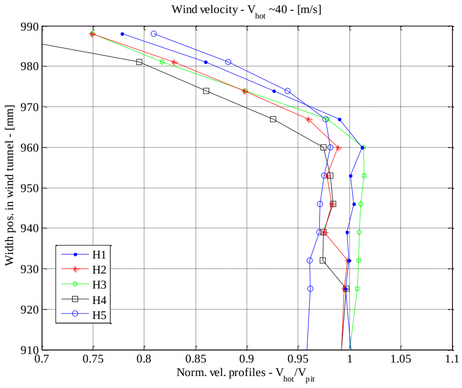
Wind velocity - V hot ~40 - [m/s]
Width pos. in wind tunnel - [mm]
Norm. vel. profiles - V hot /V pit
0.7
0.75
0.8
0.85
0.9
0.95
1
1.05
1.1
910
920
930
940
950
960
970
980
990
H1
H2
H3
H4
H5

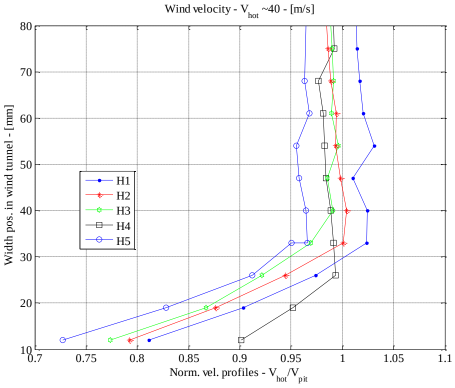
Wind velocity - V hot ~40 - [m/s]
Width pos. in wind tunnel - [mm]
Norm. vel. profiles - V hot /V pit
0.7
0.75
0.8
0.85
0.9
0.95
1
1.05
1.1
10
20
30
40
50
60
70
80
H1
H2
H3
H4
H5

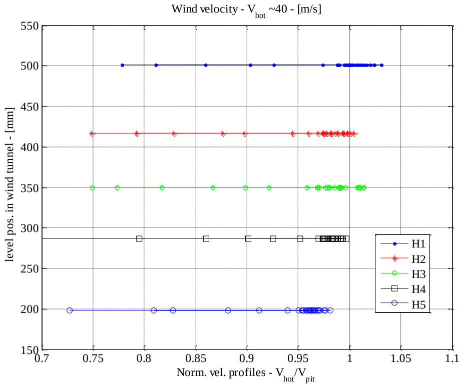
Wind velocity - V hot ~40 - [m/s]
level pos. in wind tunnel - [mm]
Norm. vel. profiles - V hot /V pit
0.7
0.75
0.8
0.85
0.9
0.95
1
1.05
1.1
150
200
250
300
350
400
450
500
550
H1
H2
H3
H4
H5

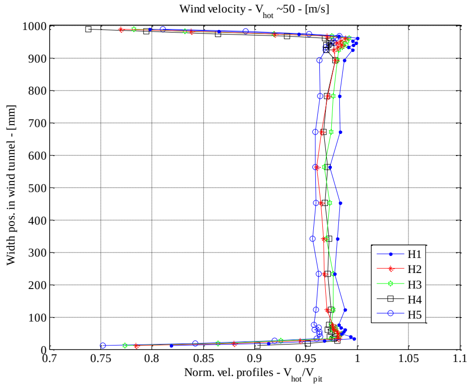
Wind velocity - V hot ~50 - [m/s]
Width pos. in wind tunnel - [mm]
Norm. vel. profiles - V hot /V pit
0.7
0.75
0.8
0.85
0.9
0.95
1
1.05
1.1
0
100
200
300
400
500
600
700
800
900
1000
H1
H2
H3
H4
H5

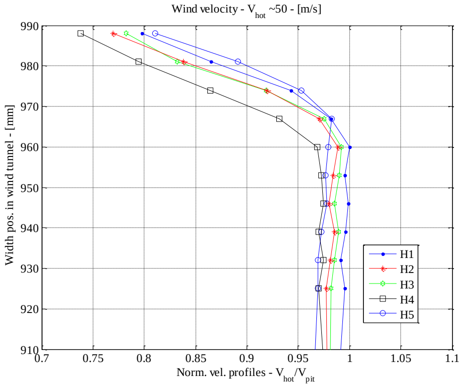
Wind velocity - V hot ~50 - [m/s]
Width pos. in wind tunnel - [mm]
Norm. vel. profiles - V hot /V pit
0.7
0.75
0.8
0.85
0.9
0.95
1
1.05
1.1
910
920
930
940
950
960
970
980
990
H1
H2
H3
H4
H5

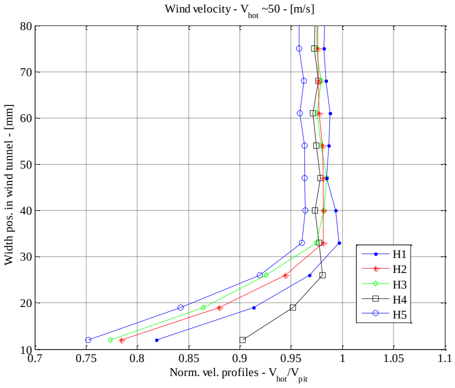
Wind velocity - V hot ~50 - [m/s]
Width pos. in wind tunnel - [mm]
Norm. vel. profiles - V hot /V pit
0.7
0.75
0.8
0.85
0.9
0.95
1
1.05
1.1
10
20
30
40
50
60
70
80
H1
H2
H3
H4
H5

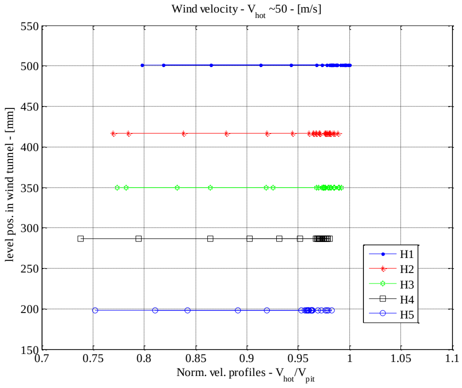
Wind velocity - V hot ~50 - [m/s]
level pos. in wind tunnel - [mm]
Norm. vel. profiles - V hot /V pit
0.7
0.75
0.8
0.85
0.9
0.95
1
1.05
1.1
150
200
250
300
350
400
450
500
550
H1
H2
H3
H4
H5

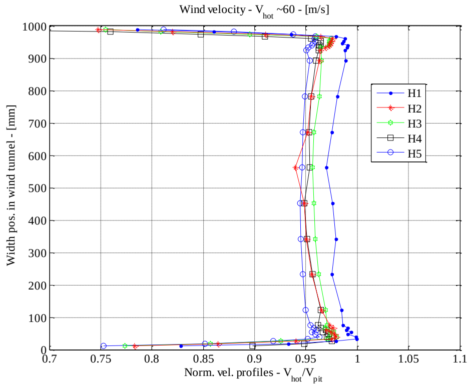
Wind velocity - V_{hot} ~60 - [m/s]
Width pos. in wind tunnel - [mm]
Norm. vel. profiles - V_{hot}/V_{pit}
0
100
200
300
400
500
600
700
800
900
1000
0.7
0.75
0.8
0.85
0.9
0.95
1
1.05
1.1
H1
H2
H3
H4
H5

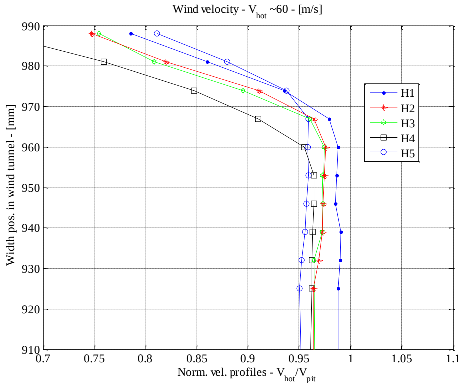
Wind velocity - V_{hot} ~60 - [m/s]
Width pos. in wind tunnel - [mm]
Norm. vel. profiles - V_{hot}/V_{pit}
910
920
930
940
950
960
970
980
990
0.7
0.75
0.8
0.85
0.9
0.95
1
1.05
1.1
H1
H2
H3
H4
H5

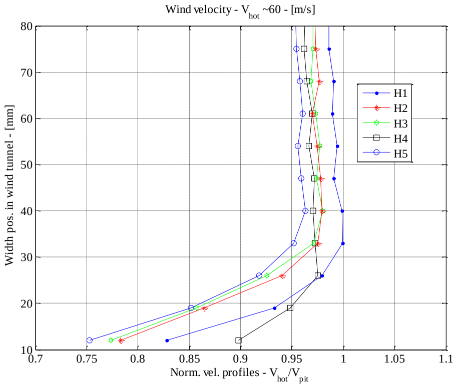
Wind velocity - V_{hot} ~60 - [m/s]
Width pos. in wind tunnel - [mm]
Norm. vel. profiles - V_{hot}/V_{pit}
10
20
30
40
50
60
70
80
0.7
0.75
0.8
0.85
0.9
0.95
1
1.05
1.1
H1
H2
H3
H4
H5

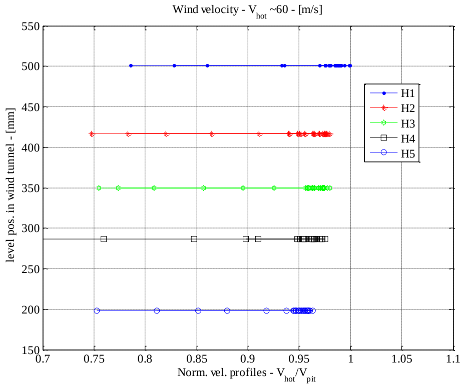
Wind velocity - V_{hot} ~60 - [m/s]
level pos. in wind tunnel - [mm]
Norm. vel. profiles - V_{hot}/V_{pit}
150
200
250
300
350
400
450
500
550
0.7
0.75
0.8
0.85
0.9
0.95
1
1.05
1.1
H1
H2
H3
H4
H5

Profiles and Angles as a Function of Height Positions

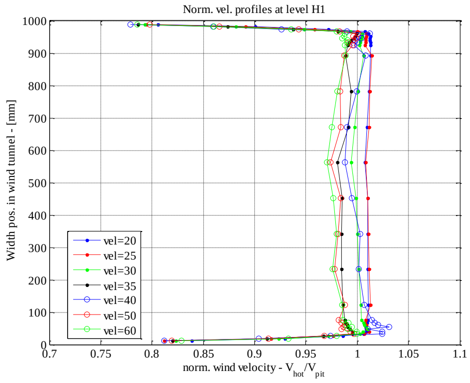

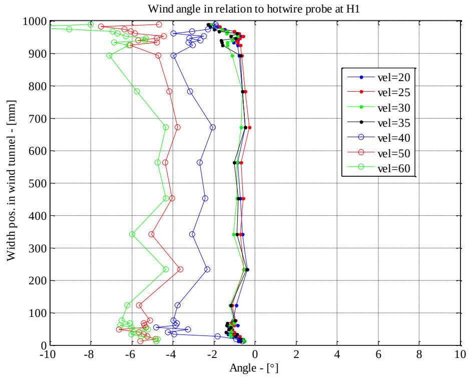

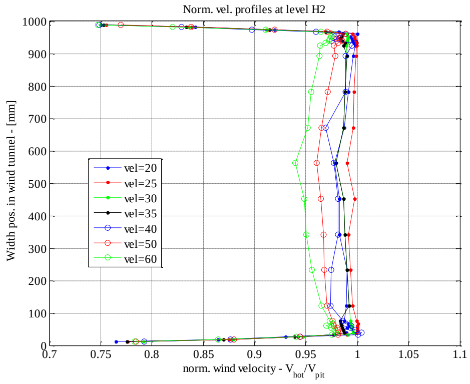

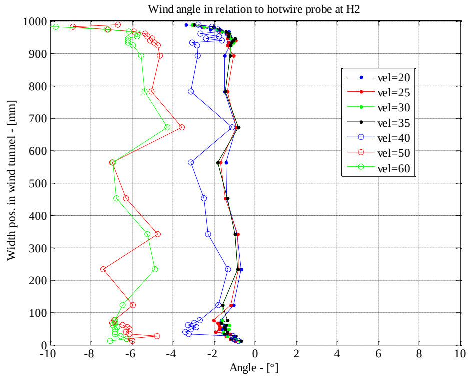

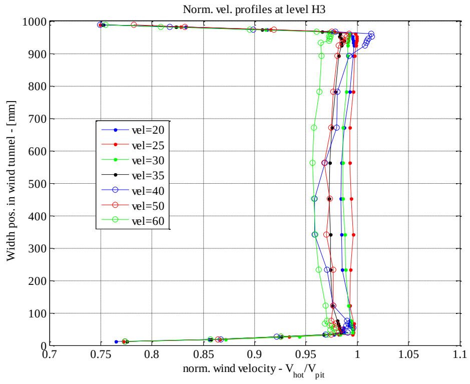

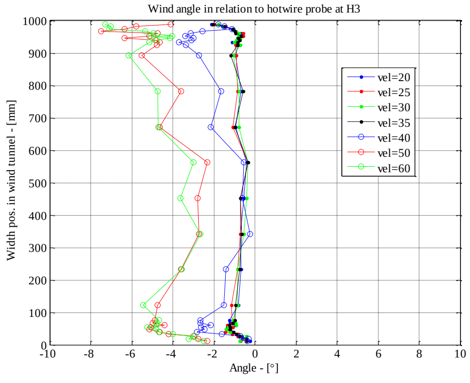

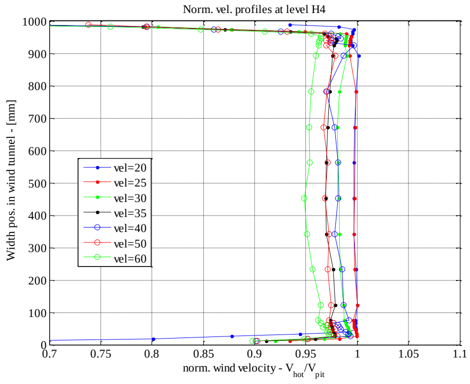

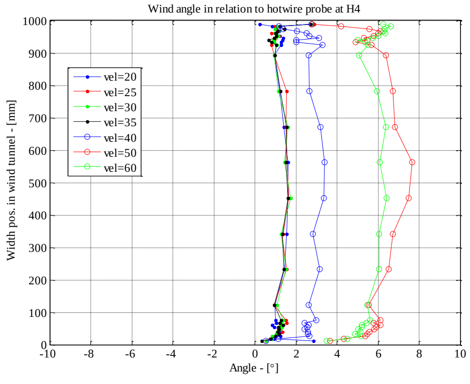

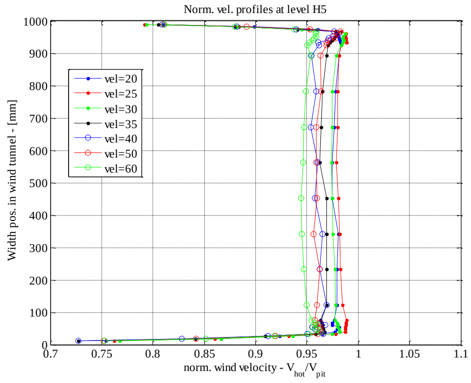

Norm. vel. profiles at level H5

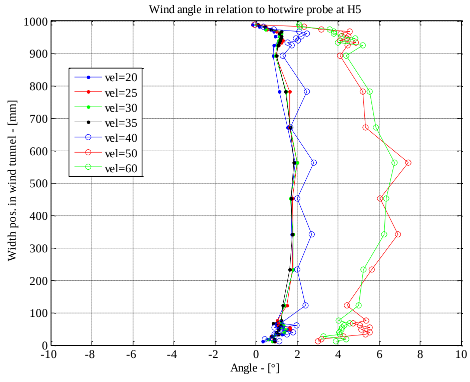

Wind angle in relation to hotwire probe at H5

Wind Angle as a Function of Velocity.

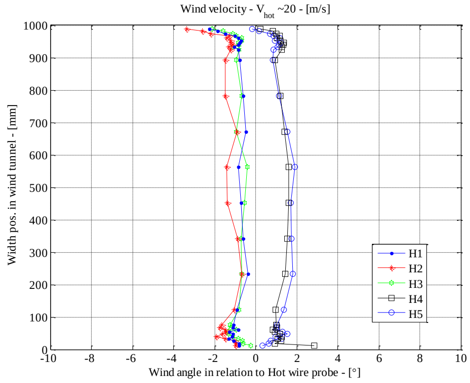

Wind velocity - V_{hot} ~20 - [m/s]

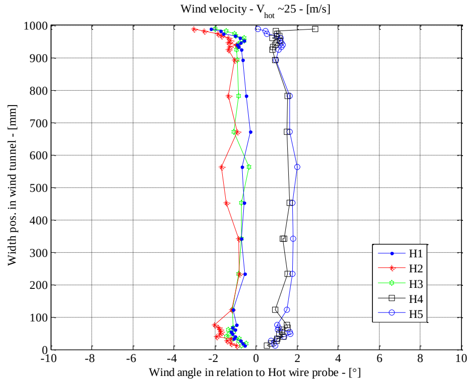

Wind velocity - V_{hot} ~25 - [m/s]

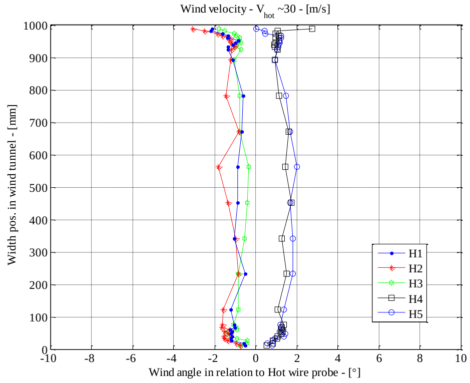

Wind velocity - V_{hot} ~30 - [m/s]

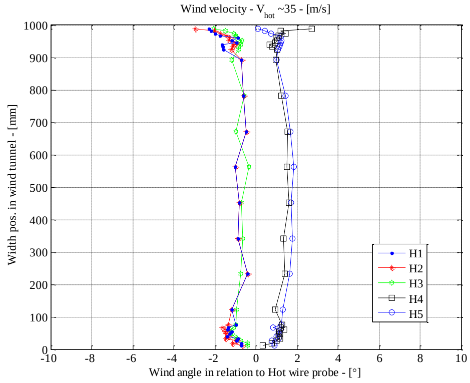

Wind velocity - V_{hot} ~35 - [m/s]

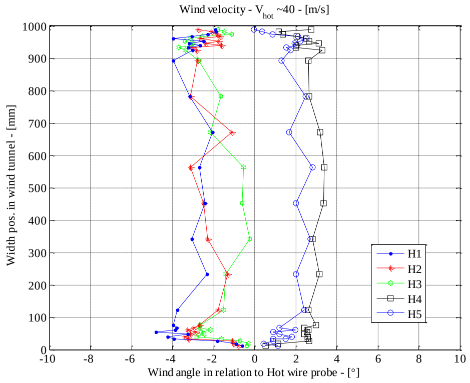

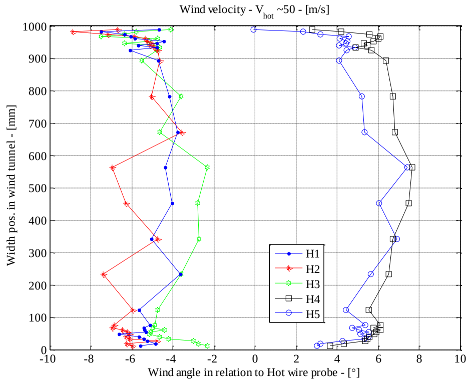

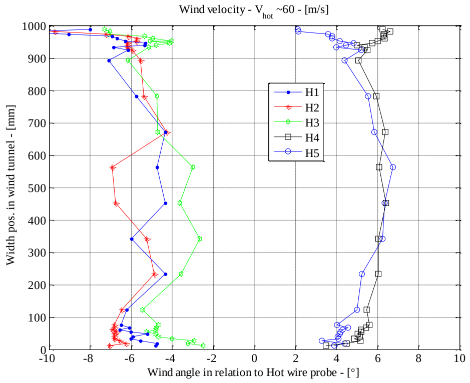

Plots of Skew Velocity Profiles

Below are shown velocity profiles in absolute velocities. It is seen that the skewness of the profiles increase with wind speed.

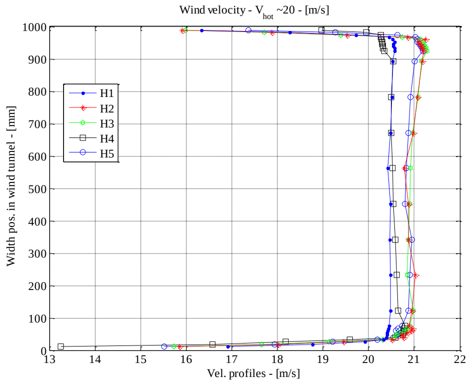

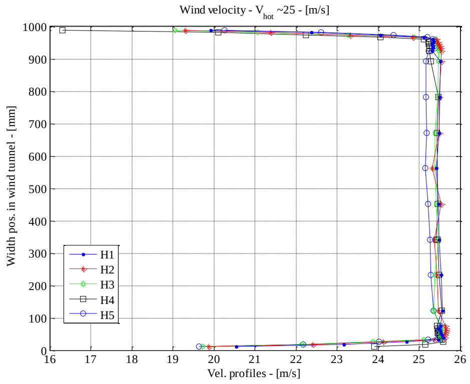

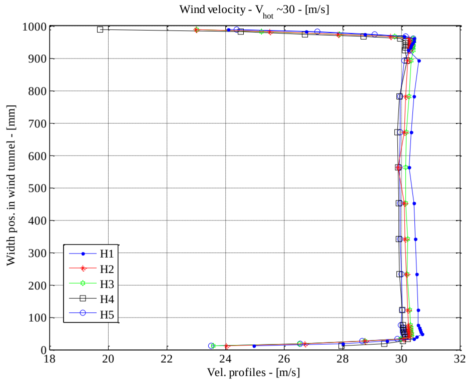
Wind velocity - V_{hot} ~30 - [m/s]

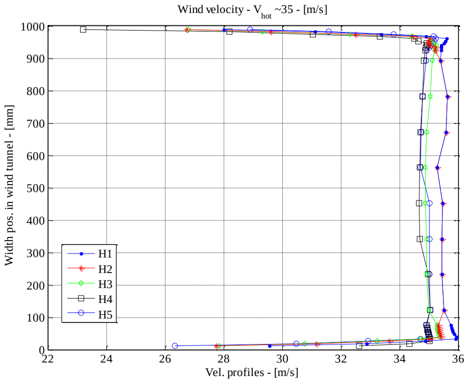
Wind velocity - V_{hot} ~35 - [m/s]

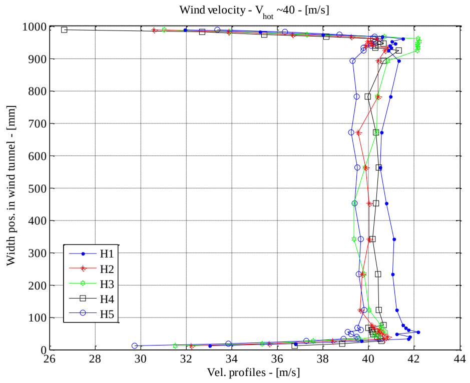
Wind velocity - V_{hot} ~40 - [m/s]

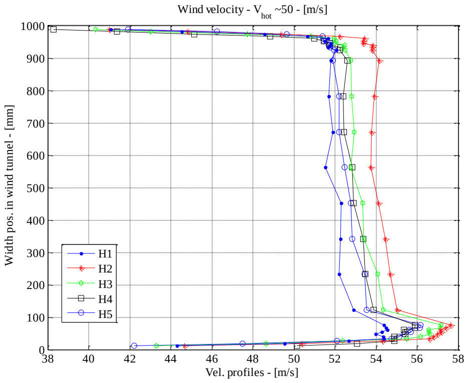
Wind velocity - V_{hot} ~50 - [m/s]

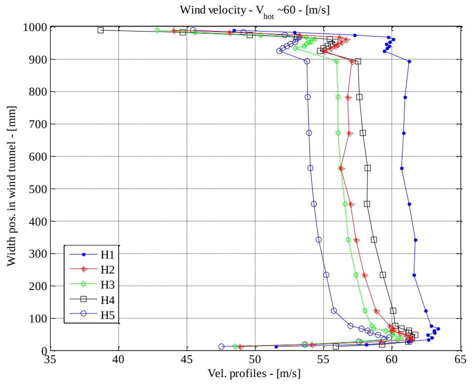
Wind velocity - V_{hot} ~60 - [m/s]

Wind Profiles in Turbulent flow (I_X~7%)

Wind velocity - V_{hot} ~20 - [m/s]

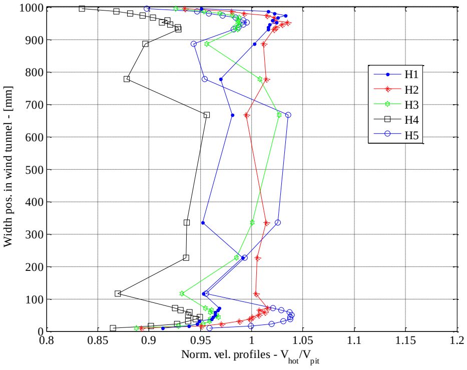

Wind velocity - V_{hot} ~20 - [m/s]

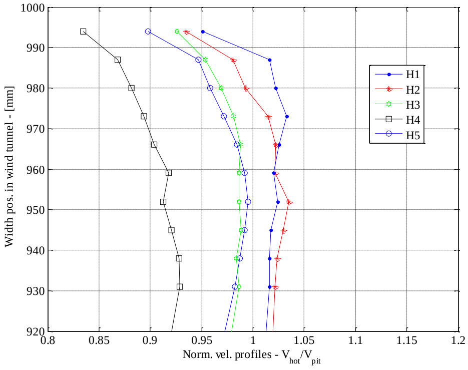

Wind velocity - V_{hot} ~20 - [m/s]

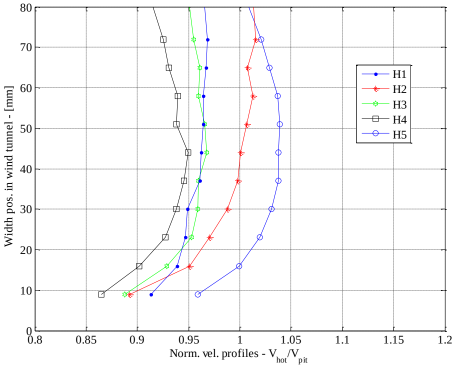

Wind velocity - V_{hot} ~20 - [m/s]

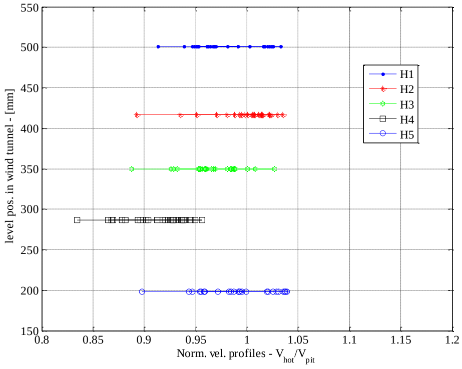

Wind velocity - V_{hot} ~25 - [m/s]

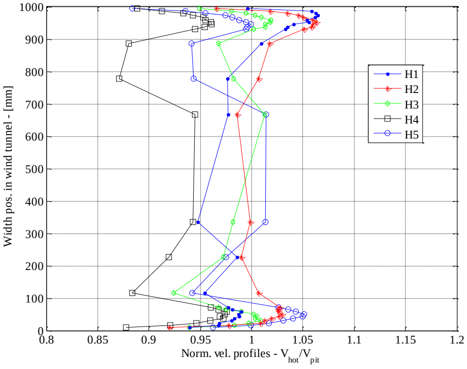

Wind velocity - V_{hot} ~25 - [m/s]

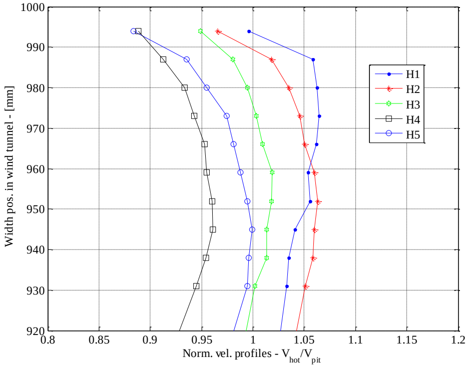

Wind velocity - V_{hot} ~25 - [m/s]

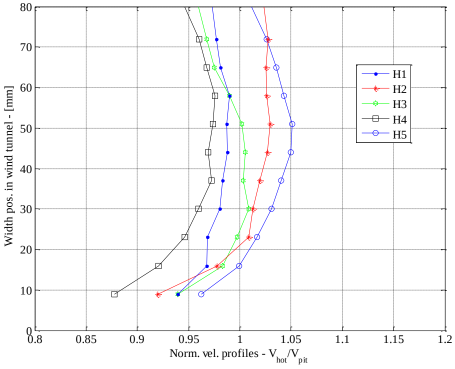

Wind velocity - V_{hot} ~25 - [m/s]

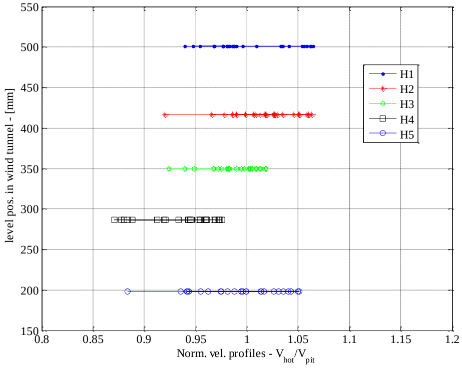

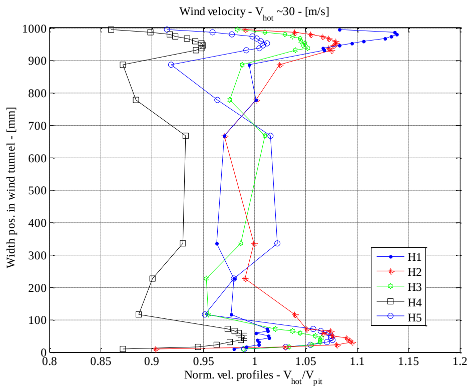
Wind velocity - V_{hot} ~30 - [m/s]
Width pos. in wind tunnel - [mm]
Norm. vel. profiles - V_{hot}/V_{pit}
0
100
200
300
400
500
600
700
800
900
1000
0.8
0.85
0.9
0.95
1
1.05
1.1
1.15
1.2
H1
H2
H3
H4
H5

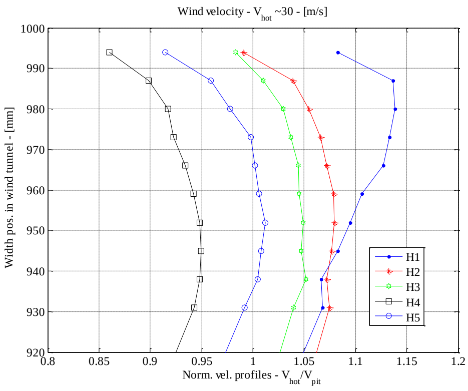
Wind velocity - V_{hot} ~30 - [m/s]
Width pos. in wind tunnel - [mm]
Norm. vel. profiles - V_{hot}/V_{pit}
920
930
940
950
960
970
980
990
1000
0.8
0.85
0.9
0.95
1
1.05
1.1
1.15
1.2
H1
H2
H3
H4
H5

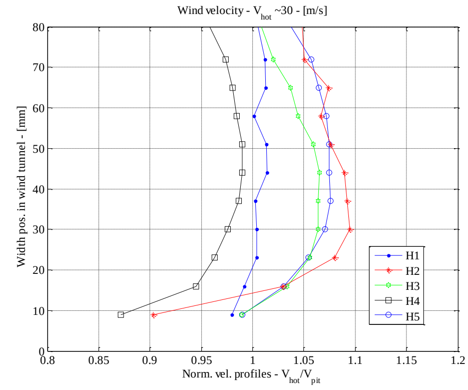
Wind velocity - V_{hot} ~30 - [m/s]
Width pos. in wind tunnel - [mm]
Norm. vel. profiles - V_{hot}/V_{pit}
0
10
20
30
40
50
60
70
80
0.8
0.85
0.9
0.95
1
1.05
1.1
1.15
1.2
H1
H2
H3
H4
H5

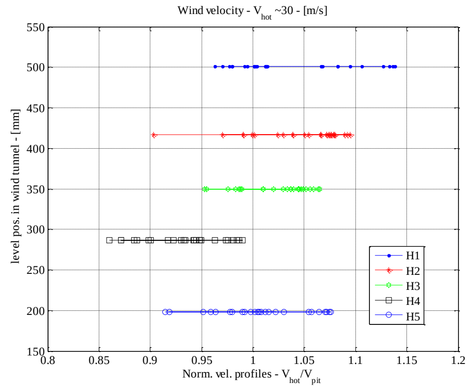
Wind velocity - V_{hot} ~30 - [m/s]
level pos. in wind tunnel - [mm]
Norm. vel. profiles - V_{hot}/V_{pit}
150
200
250
300
350
400
450
500
550
0.8
0.85
0.9
0.95
1
1.05
1.1
1.15
1.2
H1
H2
H3
H4
H5

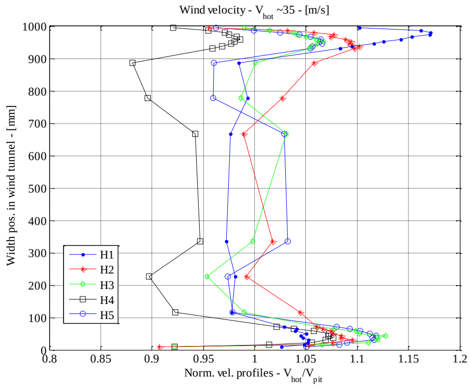
Wind velocity - V_{hot} ~35 - [m/s]
Width pos. in wind tunnel - [mm]
Norm. vel. profiles - V_{hot}/V_{pit}
0
100
200
300
400
500
600
700
800
900
1000
0.8
0.85
0.9
0.95
1
1.05
1.1
1.15
1.2
H1
H2
H3
H4
H5

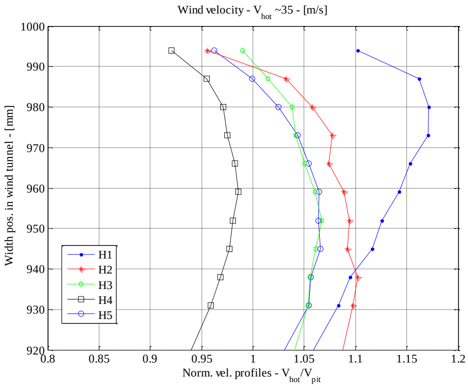
Wind velocity - V_{hot} ~35 - [m/s]
Width pos. in wind tunnel - [mm]
Norm. vel. profiles - V_{hot}/V_{pit}
920
930
940
950
960
970
980
990
1000
0.8
0.85
0.9
0.95
1
1.05
1.1
1.15
1.2
H1
H2
H3
H4
H5

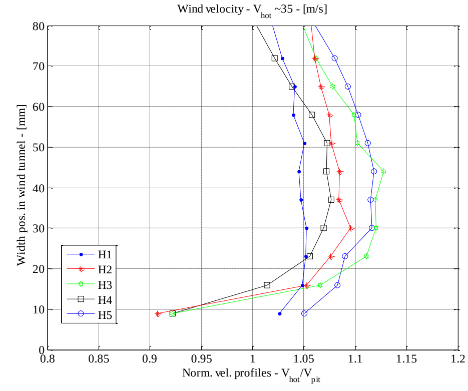
Wind velocity - V_{hot} ~35 - [m/s]
Width pos. in wind tunnel - [mm]
Norm. vel. profiles - V_{hot}/V_{pit}
0
10
20
30
40
50
60
70
80
0.8
0.85
0.9
0.95
1
1.05
1.1
1.15
1.2
H1
H2
H3
H4
H5

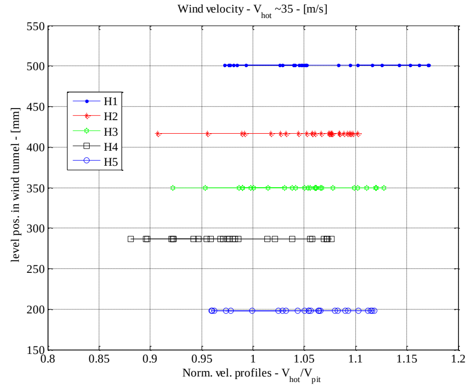
Wind velocity - V_{hot} ~35 - [m/s]
level pos. in wind tunnel - [mm]
Norm. vel. profiles - V_{hot}/V_{pit}
150
200
250
300
350
400
450
500
550
0.8
0.85
0.9
0.95
1
1.05
1.1
1.15
1.2
H1
H2
H3
H4
H5

Profiles as a Function of Height Positions

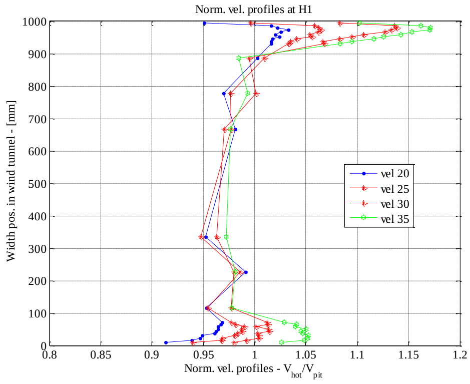

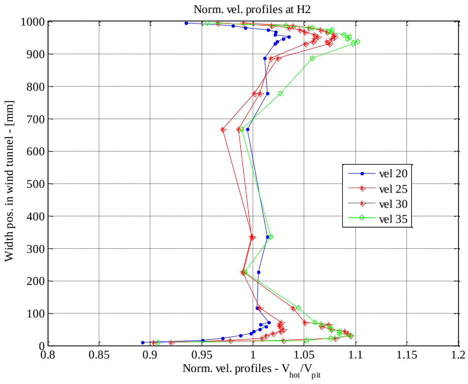

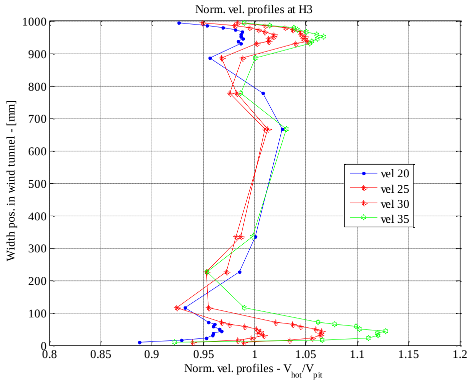

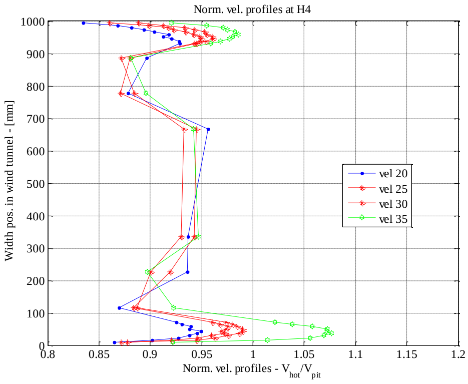

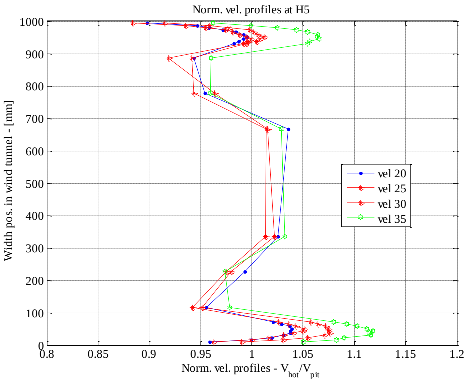

Wind Angle as a Function of Velocity and Height Positions.

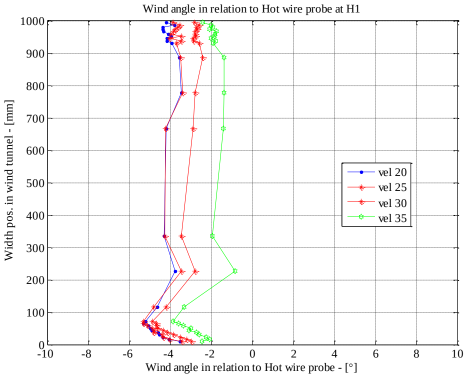

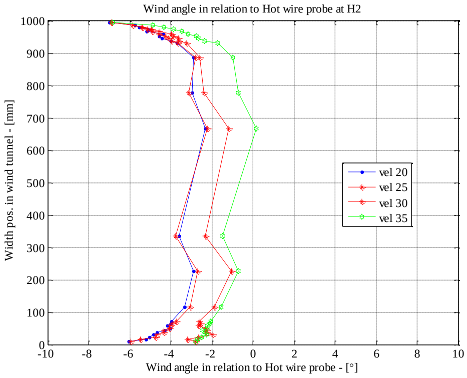

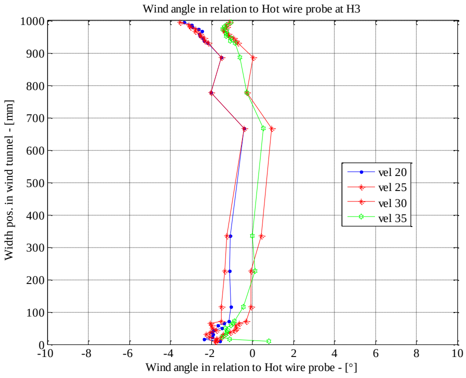

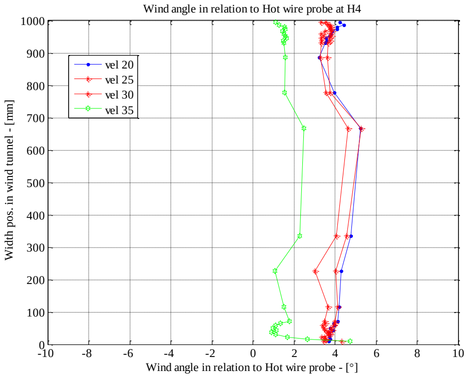

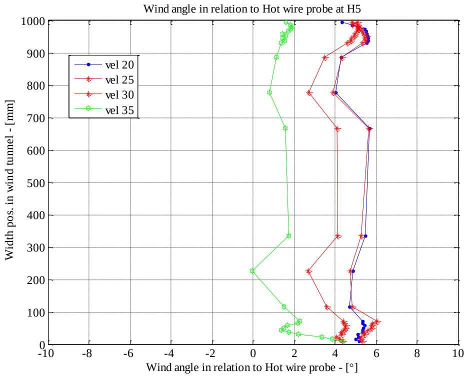

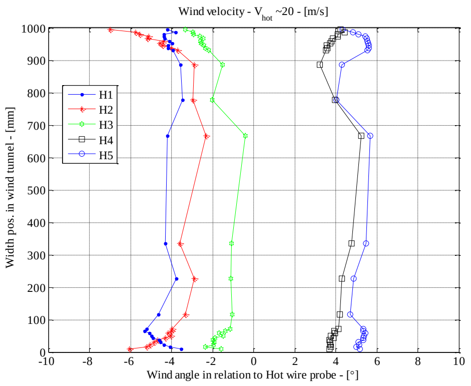

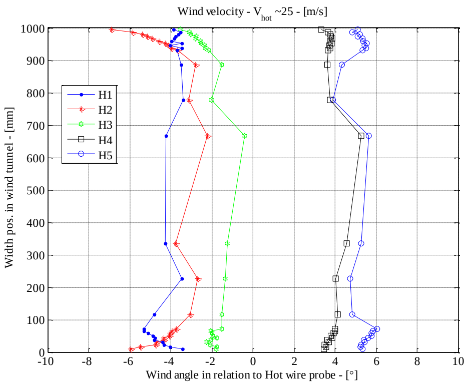

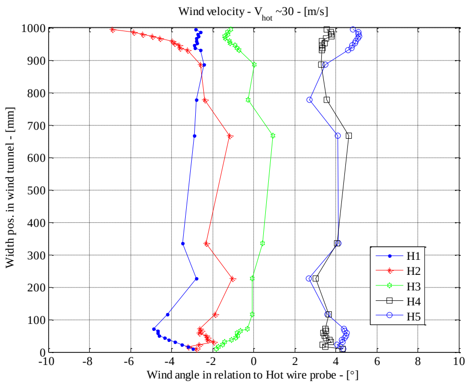

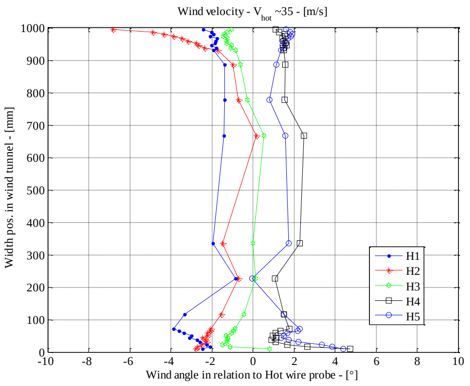

Plots of Velocity Profiles Skewness

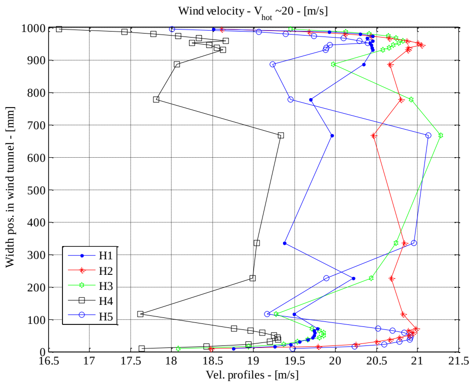

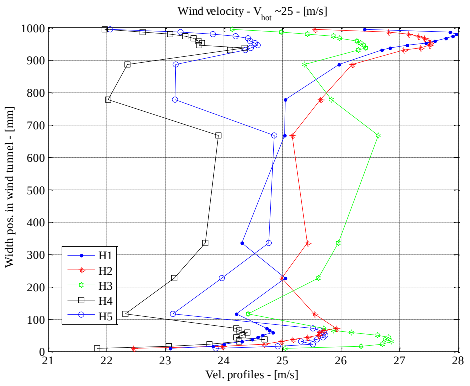

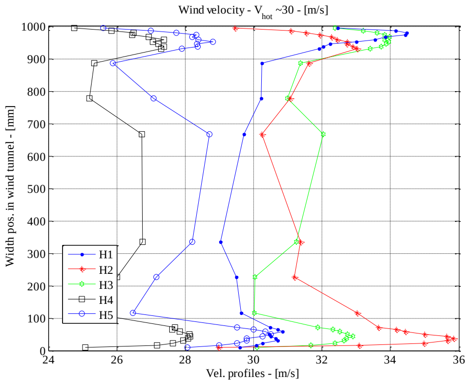

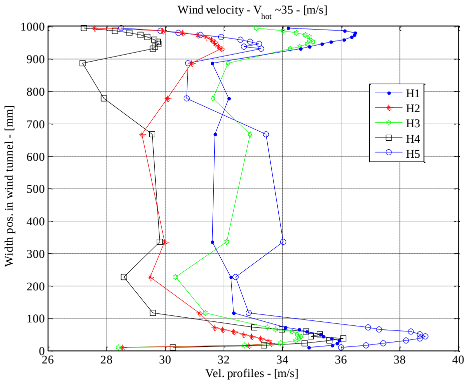

Appendix C

Displacements of D-Section in Smooth and Turbulent Flow (I_X~7%)

Smooth Flow Tuned Frequencies

$\mathrm{f}_{\mathrm{torsional}} = 6.50 \ \mathrm{f}_{\mathrm{heave}} = 6.48$

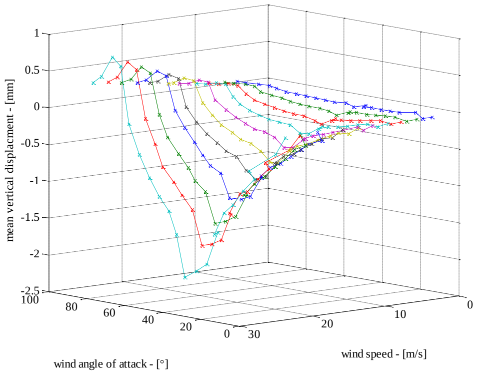

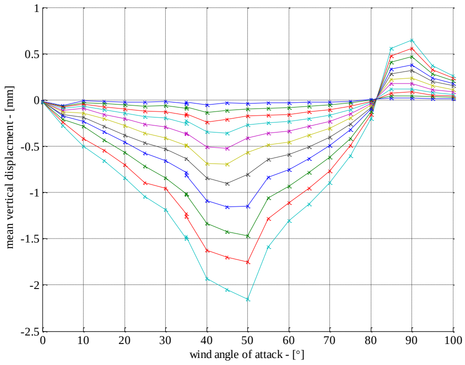

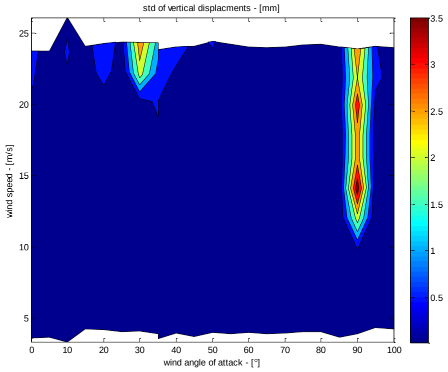

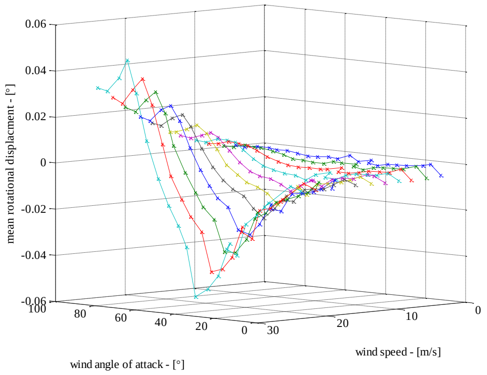

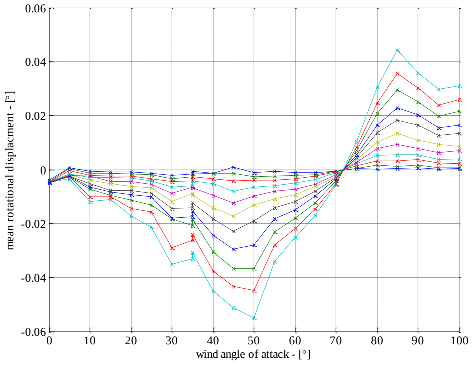

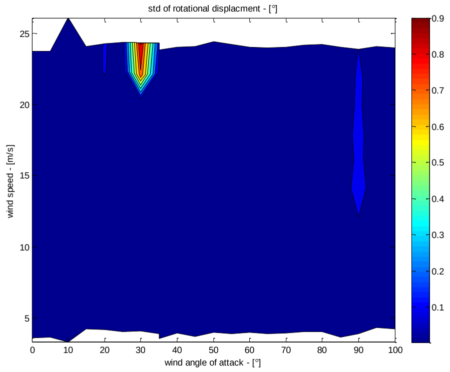

Turbulent Flow (I_X~7%) Tuned Frequencies

$f_{torsional} = 6.50$ $f_{heave} = 6.48$

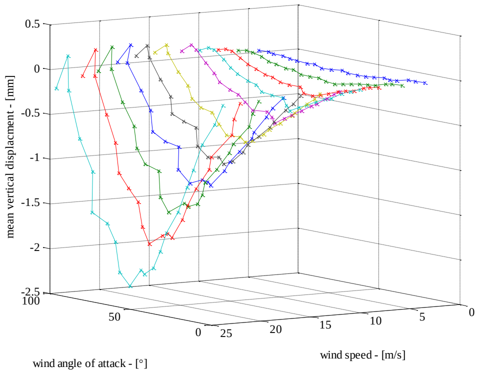

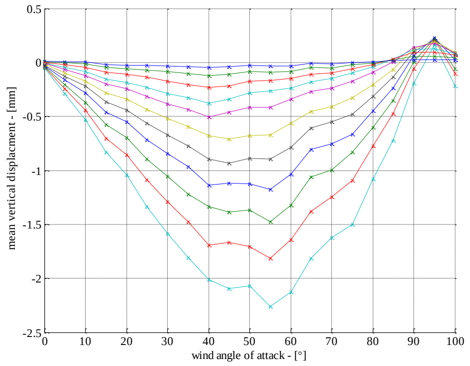

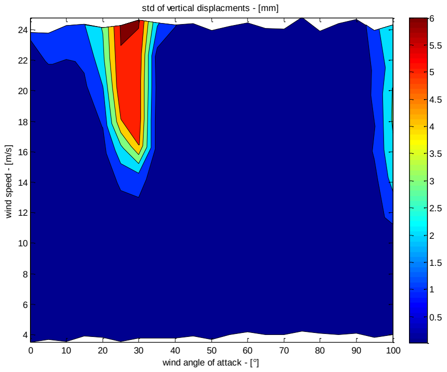

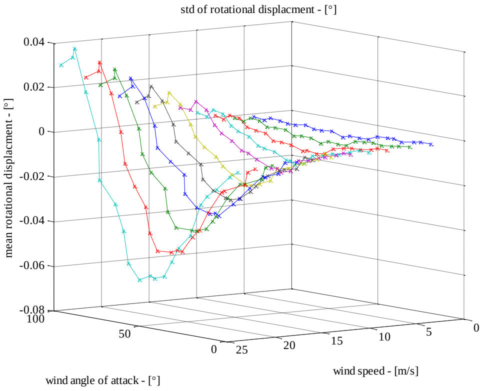

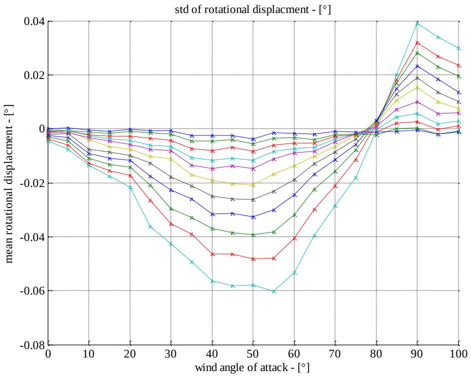

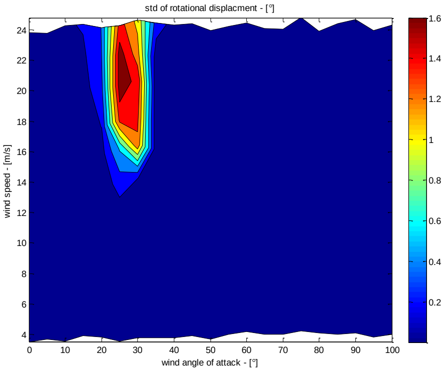

Smooth Detuned Frequencies

$f_{\text{torsional}} = 11.8$ $f_{\text{heave}} = 6.44$

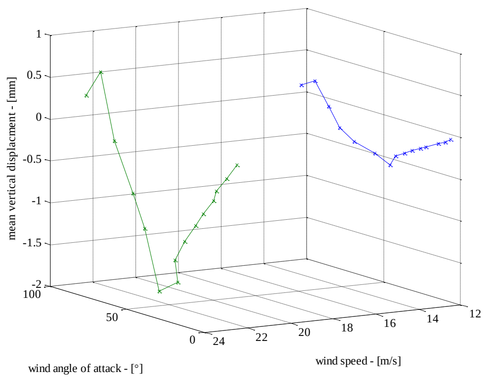

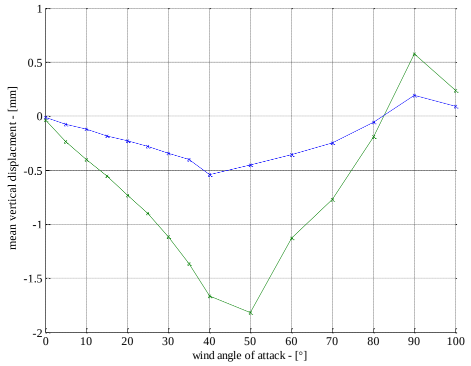

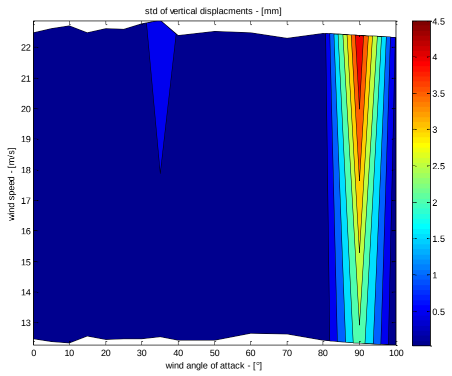

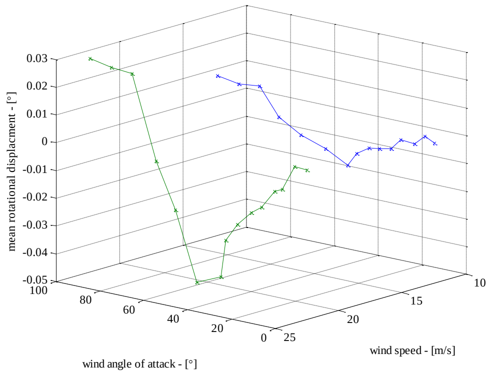

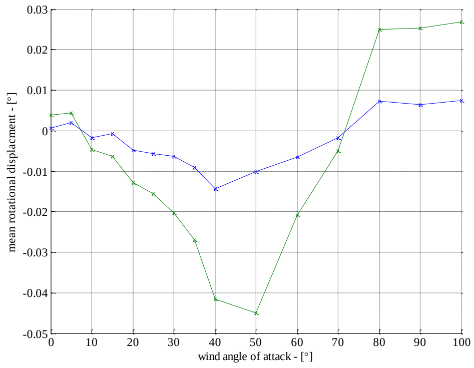

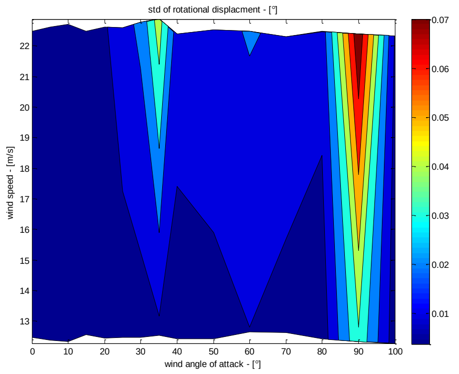

$f_{\text{torsional}} = 4.66\ f_{\text{heave}} = 6.44$

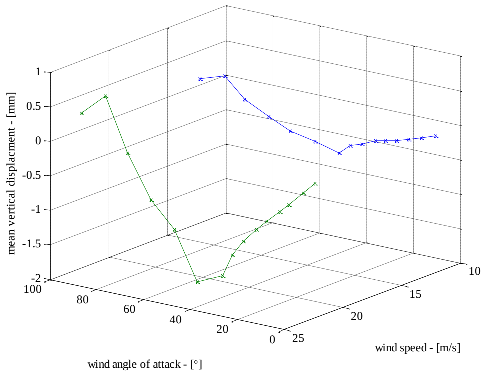

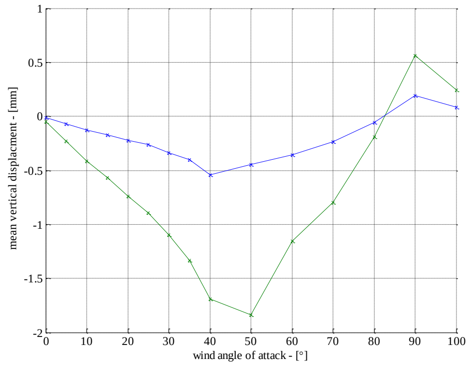

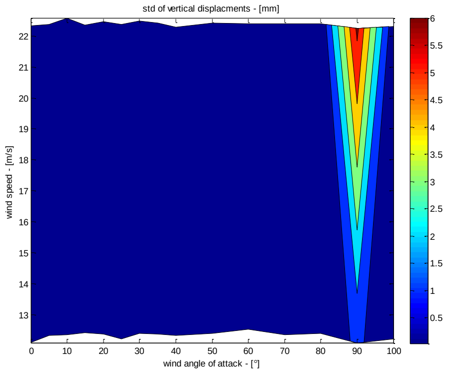

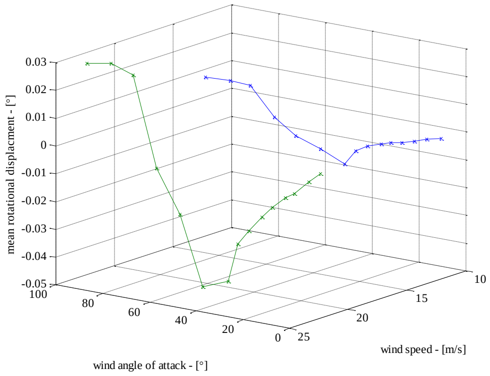

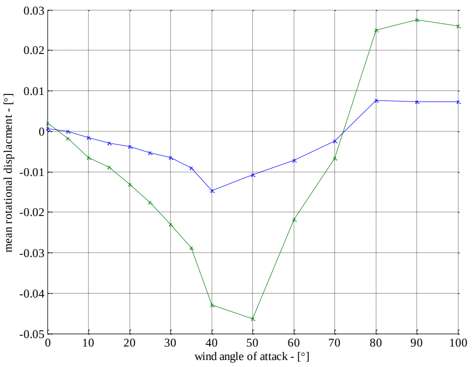

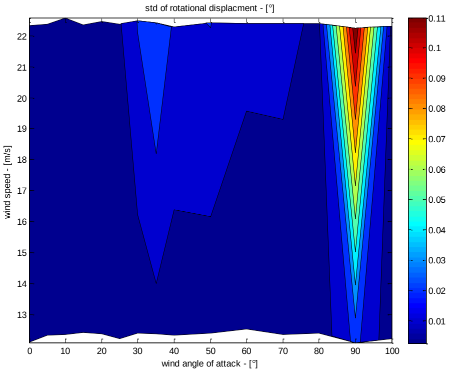

Appendix D

Ice Shapes Obtained from Experiments at NRC

Ice Shapes Obtained at NRC

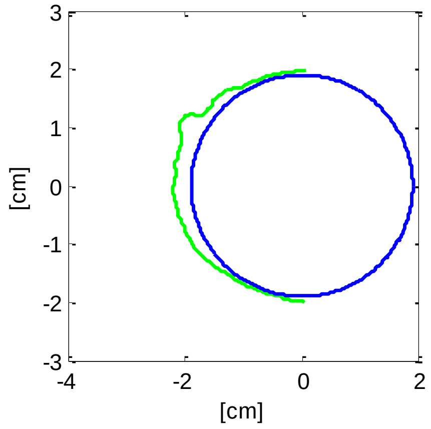
Mean(ice)/R=10% run=1a LWC=0.4 U=10[m/s] DS=50[µm]
Tair=-5[ºC] Ttest=15[min] Dia=3.81[cm] Pos.=H[-]

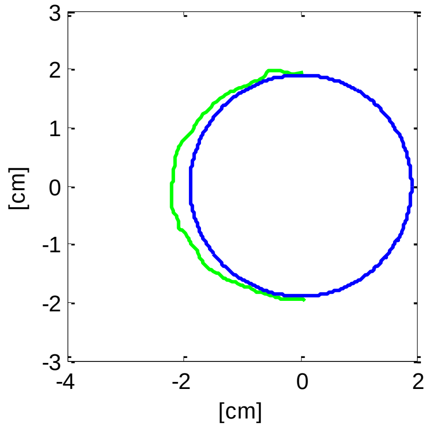
Mean(ice)/R=9% run=1b LWC=0.4 U=10[m/s] DS=50[µm]
Tair=-5[ºC] Ttest=15[min] Dia=3.81[cm] Pos.=H[-]

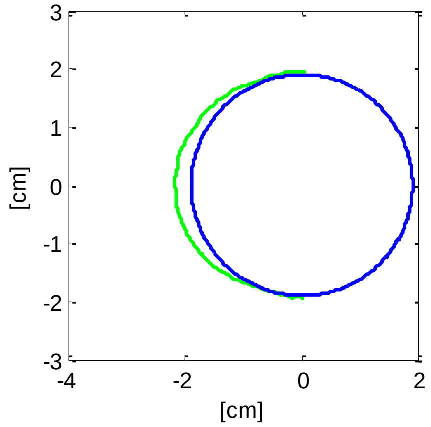
Mean(ice)/R=8% run=2a LWC=0.4 U=10[m/s] DS=50[µm]
Tair=-5[ºC] Ttest=10[min] Dia=3.81[cm] Pos.=H[-]

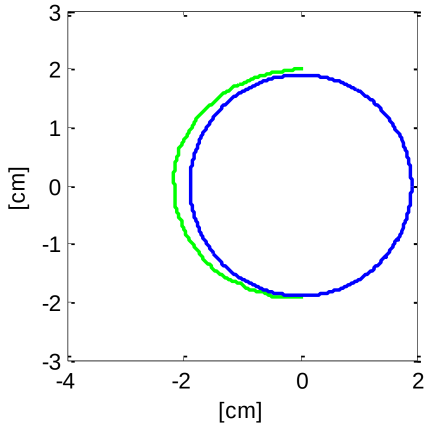
Mean(ice)/R=9% run=2b LWC=0.4 U=10[m/s] DS=50[µm]
Tair=-5[ºC] Ttest=10[min] Dia=3.81[cm] Pos.=H[-]

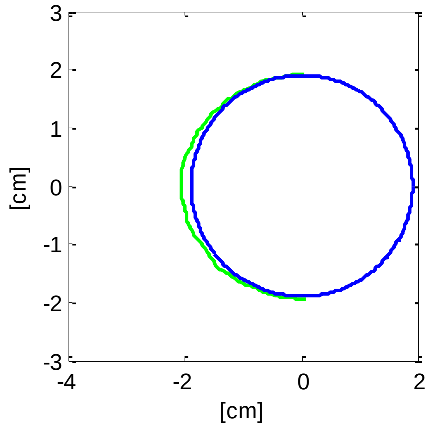
Mean(ice)/R=4% run=3a LWC=0.4 U=10[m/s] DS=30[µm]
Tair=-5[ºC] Ttest=10[min] Dia=3.81[cm] Pos.=H[-]

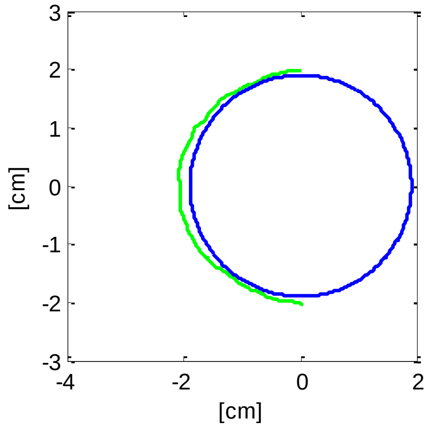
Mean(ice)/R=6% run=3b LWC=0.4 U=10[m/s] DS=30[µm]
Tair=-5[ºC] Ttest=10[min] Dia=3.81[cm] Pos.=H[-]

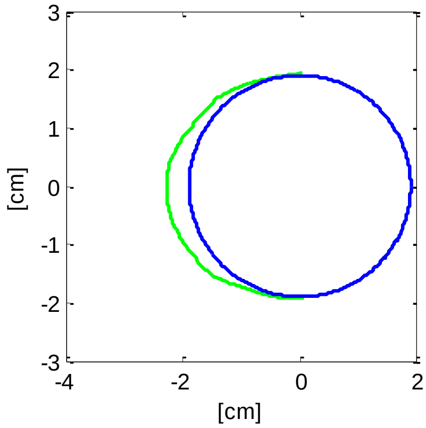
Mean(ice)/R=10% run=5a LWC=0.4 U=10[m/s] DS=50[µm]
Tair=-5[ºC] Ttest=15[min] Dia=3.81[cm] Pos.=H[-]

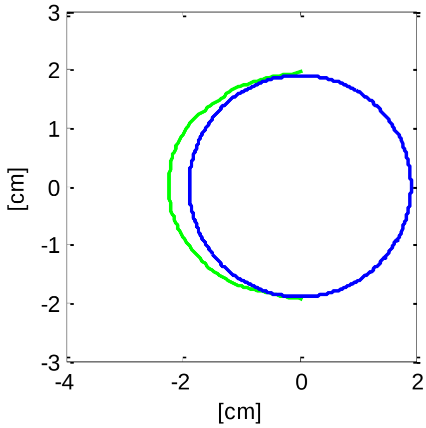
Mean(ice)/R=10% run=5b LWC=0.4 U=10[m/s] DS=50[µm]
Tair=-5[ºC] Ttest=15[min] Dia=3.81[cm] Pos.=H[-]

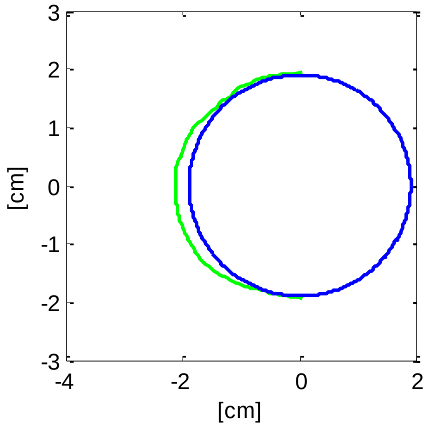
Mean(ice)/R=7% run=6a LWC=0.4 U=10[m/s] DS=50[µm]
Tair=-4[ºC] Ttest=10[min] Dia=3.81[cm] Pos.=H[-]

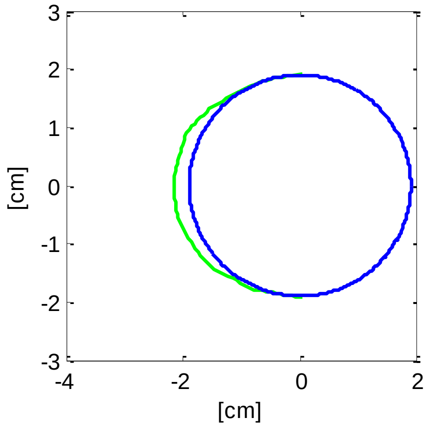
Mean(ice)/R=7% run=6b LWC=0.4 U=10[m/s] DS=50[µm]
Tair=-4[ºC] Ttest=10[min] Dia=3.81[cm] Pos.=H[-]

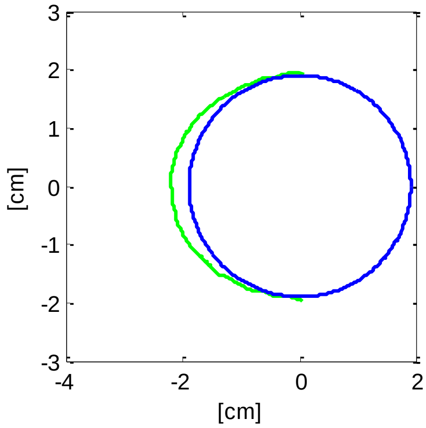
Mean(ice)/R=9% run=7a LWC=0.4 U=10[m/s] DS=50[µm]
Tair=-3[ºC] Ttest=10[min] Dia=3.81[cm] Pos.=H[-]

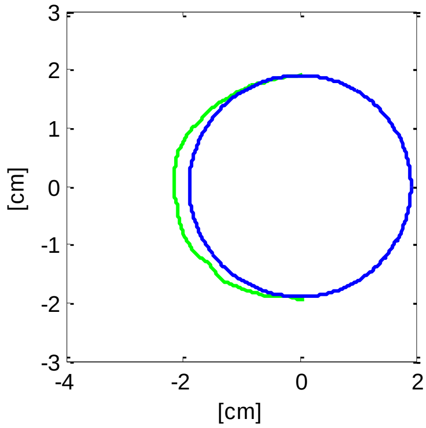
Mean(ice)/R=8% run=7b LWC=0.4 U=10[m/s] DS=50[µm]
Tair=-3[ºC] Ttest=10[min] Dia=3.81[cm] Pos.=H[-]

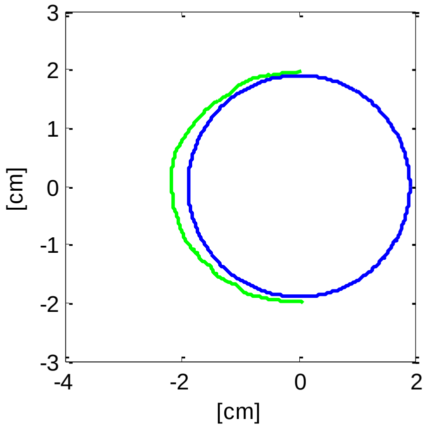
Mean(ice)/R=9% run=8a LWC=0.4 U=10[m/s] DS=50[µm]
Tair=-2[ºC] Ttest=10[min] Dia=3.81[cm] Pos.=H[-]

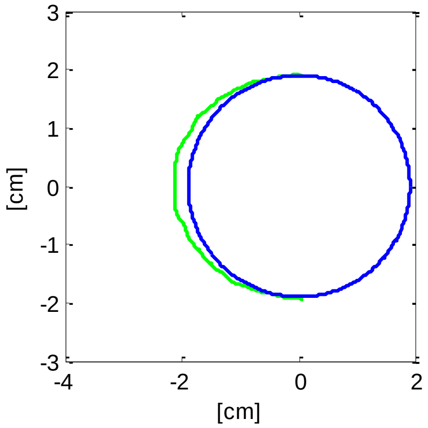
Mean(ice)/R=7% run=8b LWC=0.4 U=10[m/s] DS=50[µm]
Tair=-2[ºC] Ttest=10[min] Dia=3.81[cm] Pos.=H[-]

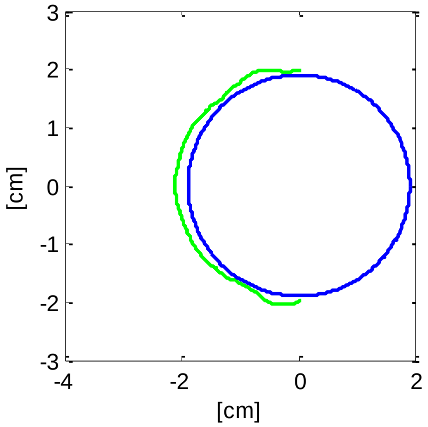
Mean(ice)/R=8% run=9a LWC=0.4 U=10[m/s] DS=50[µm]
Tair=-1[ºC] Ttest=10[min] Dia=3.81[cm] Pos.=H[-]

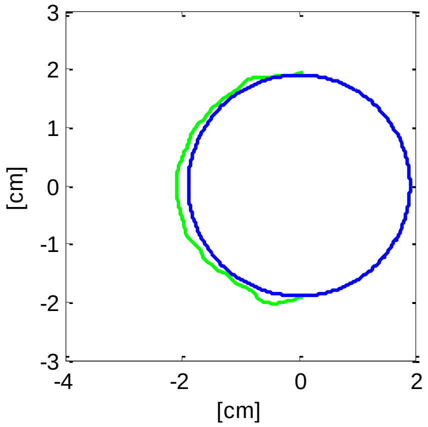
Mean(ice)/R=7% run=9b LWC=0.4 U=10[m/s] DS=50[µm]
Tair=-1[ºC] Ttest=10[min] Dia=3.81[cm] Pos.=H[-]

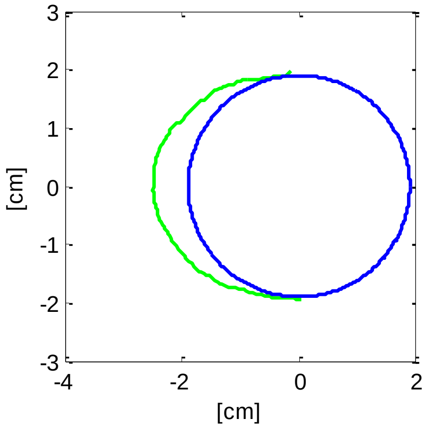
Mean(ice)/R=17% run=10a LWC=0.4 U=10[m/s] DS=50[µm]
Tair=-5[ºC] Ttest=30[min] Dia=3.81[cm] Pos.=H[-]

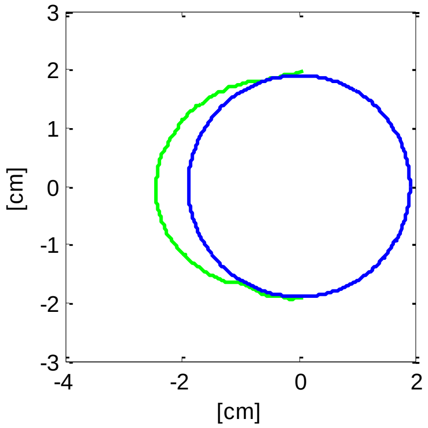
Mean(ice)/R=15% run=10b LWC=0.4 U=10[m/s] DS=50[µm]
Tair=-5[ºC] Ttest=30[min] Dia=3.81[cm] Pos.=H[-]

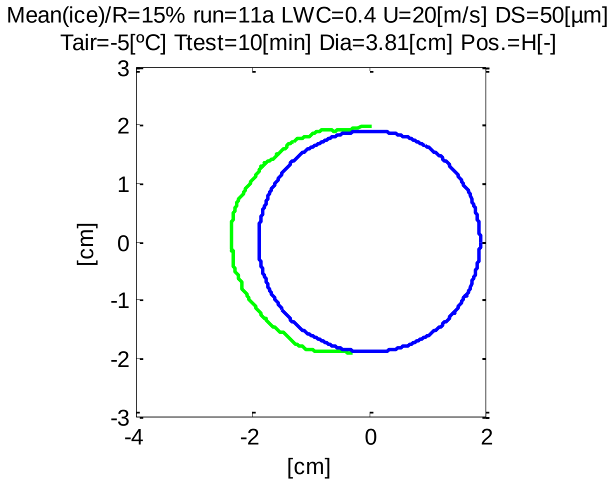

Mean(ice)/R=15% run=11a LWC=0.4 U=20[m/s] DS=50[µm]
Tair=-5[ºC] Ttest=10[min] Dia=3.81[cm] Pos.=H[-]

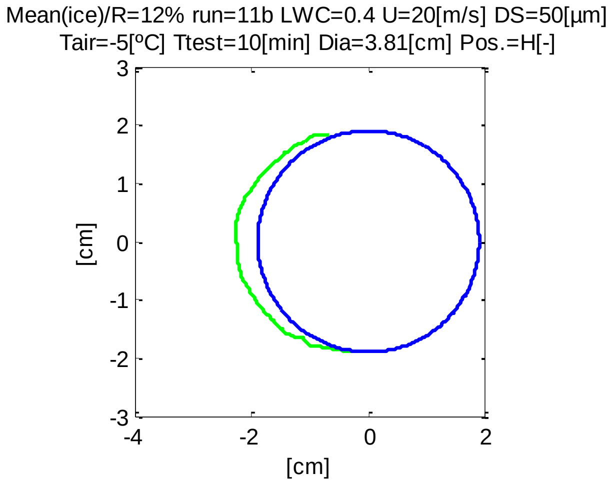

Mean(ice)/R=12% run=11b LWC=0.4 U=20[m/s] DS=50[µm]
Tair=-5[ºC] Ttest=10[min] Dia=3.81[cm] Pos.=H[-]

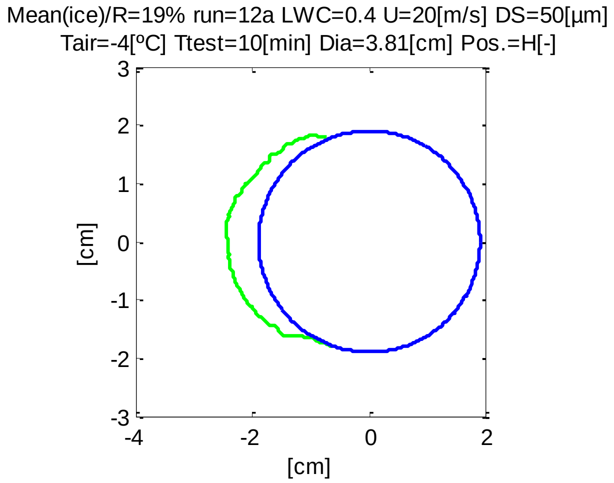

Mean(ice)/R=19% run=12a LWC=0.4 U=20[m/s] DS=50[µm]
Tair=-4[ºC] Ttest=10[min] Dia=3.81[cm] Pos.=H[-]

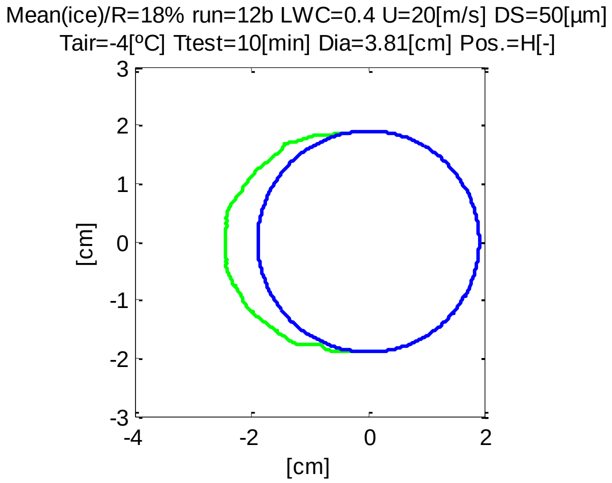

Mean(ice)/R=18% run=12b LWC=0.4 U=20[m/s] DS=50[µm]
Tair=-4[ºC] Ttest=10[min] Dia=3.81[cm] Pos.=H[-]

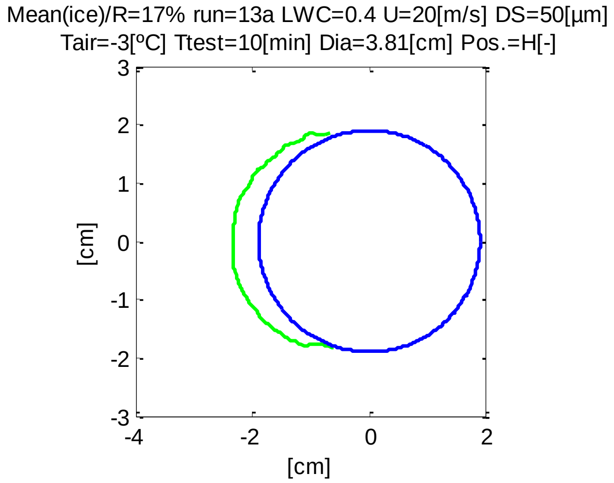

Mean(ice)/R=17% run=13a LWC=0.4 U=20[m/s] DS=50[µm]
Tair=-3[ºC] Ttest=10[min] Dia=3.81[cm] Pos.=H[-]

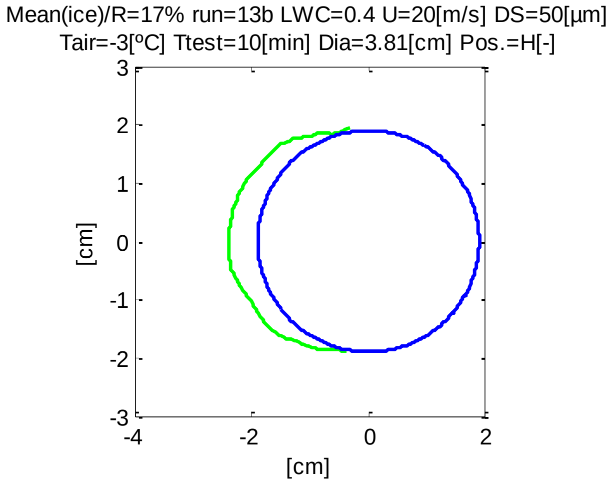

Mean(ice)/R=17% run=13b LWC=0.4 U=20[m/s] DS=50[µm]
Tair=-3[ºC] Ttest=10[min] Dia=3.81[cm] Pos.=H[-]

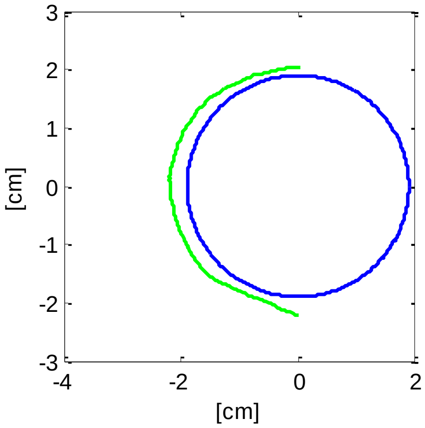

Mean(ice)/R=12% run=14a LWC=0.4 U=20[m/s] DS=50[µm]
Tair=-2[ºC] Ttest=10[min] Dia=3.81[cm] Pos.=H[-]

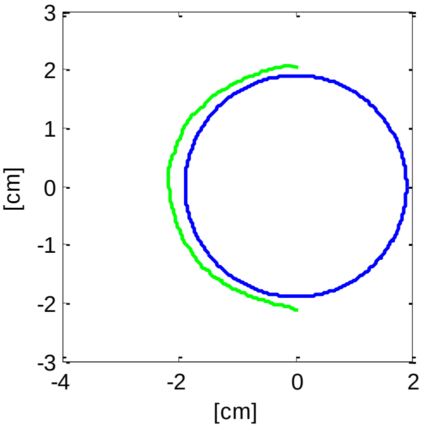

Mean(ice)/R=11% run=14b LWC=0.4 U=20[m/s] DS=50[µm]
Tair=-2[ºC] Ttest=10[min] Dia=3.81[cm] Pos.=H[-]

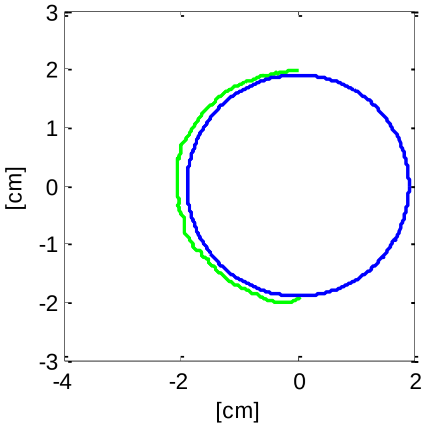

Mean(ice)/R=7% run=15a LWC=0.4 U=20[m/s] DS=50[µm]
Tair=-1[ºC] Ttest=10[min] Dia=3.81[cm] Pos.=H[-]

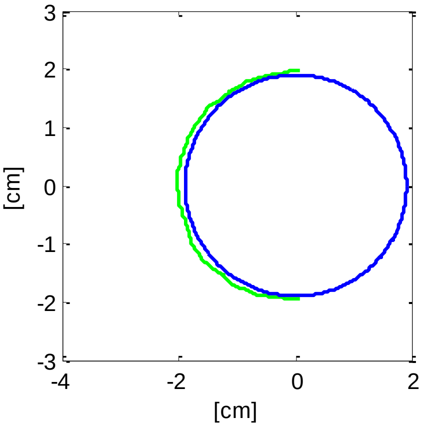

Mean(ice)/R=5% run=15b LWC=0.4 U=20[m/s] DS=50[µm]
Tair=-1[ºC] Ttest=10[min] Dia=3.81[cm] Pos.=H[-]

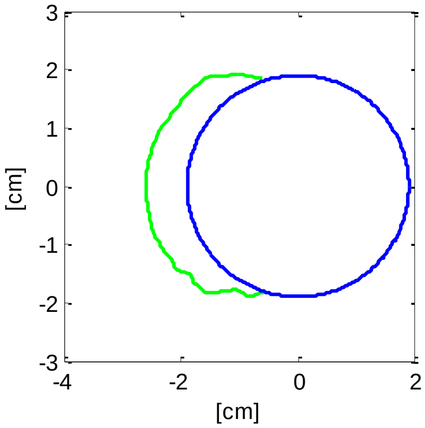

Mean(ice)/R=27% run=16a LWC=0.4 U=30[m/s] DS=50[µm]
Tair=-5[ºC] Ttest=10[min] Dia=3.81[cm] Pos.=H[-]

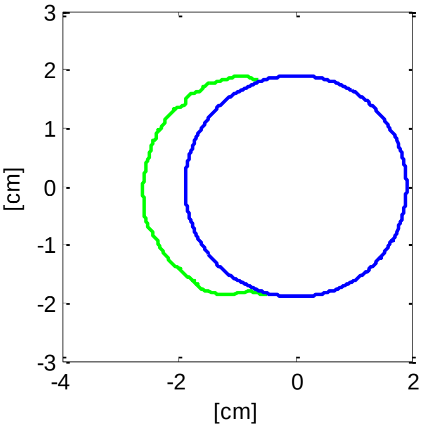

Mean(ice)/R=27% run=16b LWC=0.4 U=30[m/s] DS=50[µm]
Tair=-5[ºC] Ttest=10[min] Dia=3.81[cm] Pos.=H[-]

Mean(ice)/R=21% run=17a LWC=0.4 U=30[m/s] DS=50[µm]
Tair=-4[ºC] Ttest=10[min] Dia=3.81[cm] Pos.=H[-]

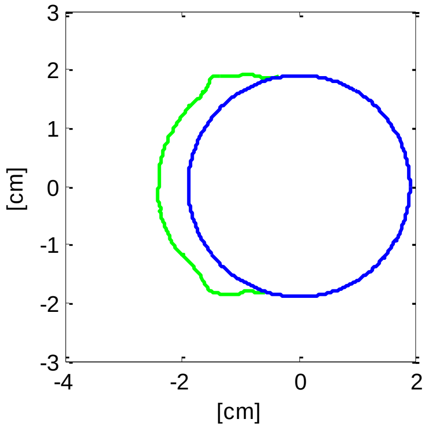

Mean(ice)/R=17% run=17b LWC=0.4 U=30[m/s] DS=50[µm]
Tair=-4[ºC] Ttest=10[min] Dia=3.81[cm] Pos.=H[-]

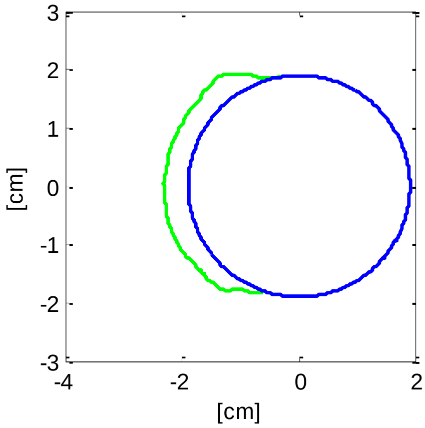

Mean(ice)/R=20% run=18a LWC=0.4 U=30[m/s] DS=50[µm]
Tair=-3[ºC] Ttest=10[min] Dia=3.81[cm] Pos.=H[-]

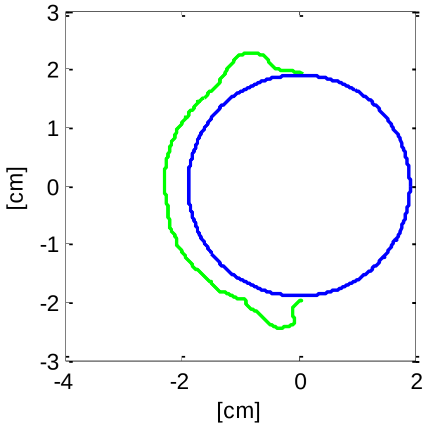

Mean(ice)/R=15% run=18b LWC=0.4 U=30[m/s] DS=50[µm]
Tair=-3[ºC] Ttest=10[min] Dia=3.81[cm] Pos.=H[-]

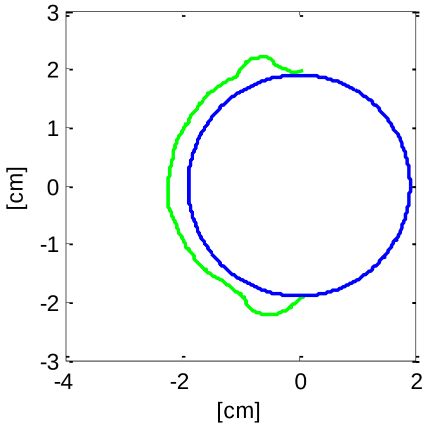

Mean(ice)/R=14% run=19a LWC=0.4 U=30[m/s] DS=50[µm]
Tair=-2[ºC] Ttest=10[min] Dia=3.81[cm] Pos.=H[-]

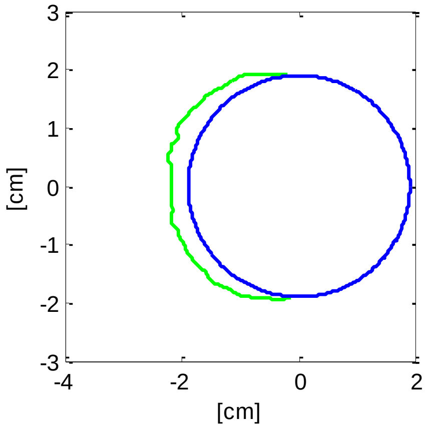

Mean(ice)/R=11% run=19b LWC=0.4 U=30[m/s] DS=50[µm]
Tair=-2[ºC] Ttest=10[min] Dia=3.81[cm] Pos.=H[-]

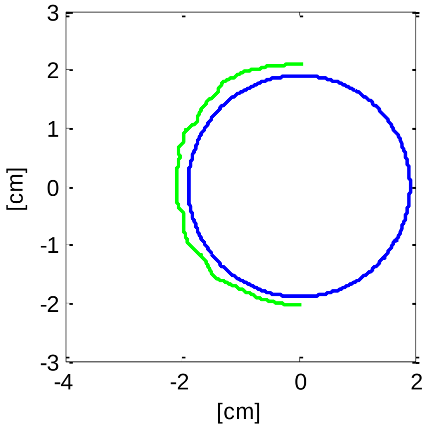

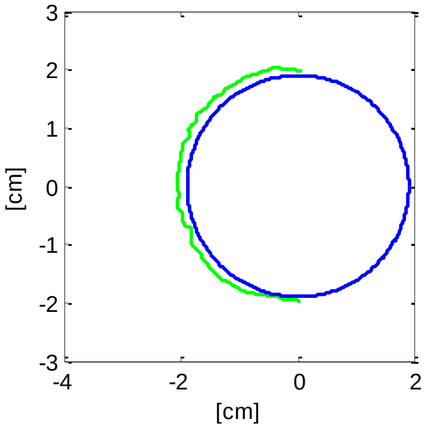
Mean(ice)/R=8% run=20a LWC=0.4 U=30[m/s] DS=50[µm]
Tair=-1[ºC] Ttest=10[min] Dia=3.81[cm] Pos.=H[-]

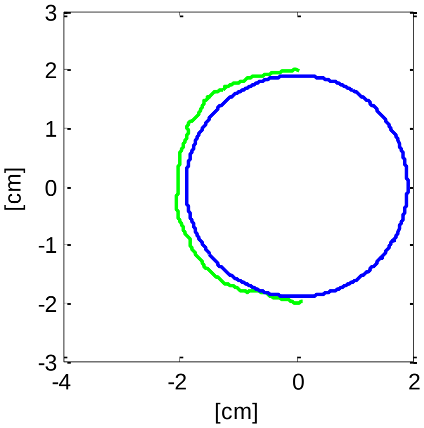
Mean(ice)/R=8% run=20b LWC=0.4 U=30[m/s] DS=50[µm]
Tair=-1[ºC] Ttest=10[min] Dia=3.81[cm] Pos.=H[-]

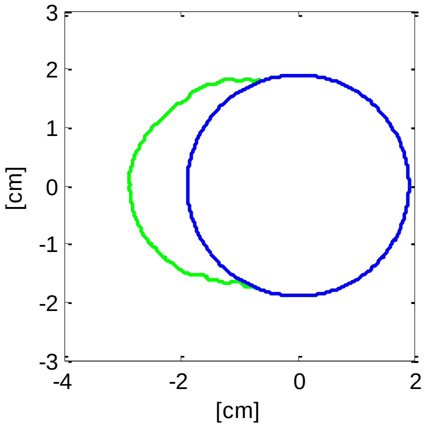
Mean(ice)/R=32% run=21a LWC=0.4 U=10[m/s] DS=50[µm]
Tair=-5[ºC] Ttest=60[min] Dia=3.81[cm] Pos.=H[-]

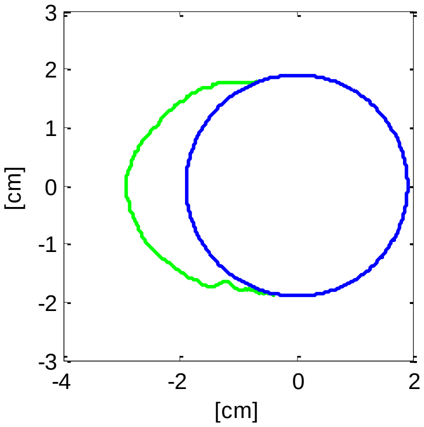
Mean(ice)/R=29% run=21b LWC=0.4 U=10[m/s] DS=50[µm]
Tair=-5[ºC] Ttest=60[min] Dia=3.81[cm] Pos.=H[-]

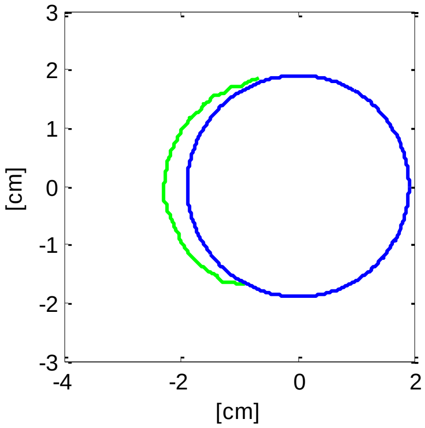
Mean(ice)/R=14% run=22a LWC=0.4 U=30[m/s] DS=20[µm]
Tair=-5[ºC] Ttest=5[min] Dia=3.81[cm] Pos.=H[-]

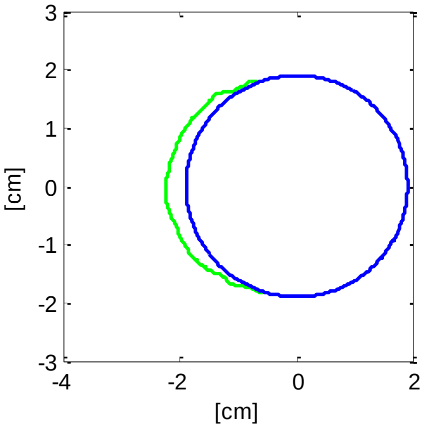
Mean(ice)/R=11% run=22b LWC=0.4 U=30[m/s] DS=20[µm]
Tair=-5[ºC] Ttest=5[min] Dia=3.81[cm] Pos.=H[-]

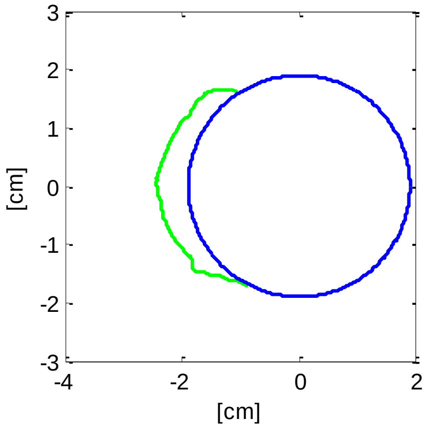
Mean(ice)/R=18% run=23a LWC=0.4 U=30[m/s] DS=20[µm]
Tair=-5[ºC] Ttest=10[min] Dia=3.81[cm] Pos.=H[-]

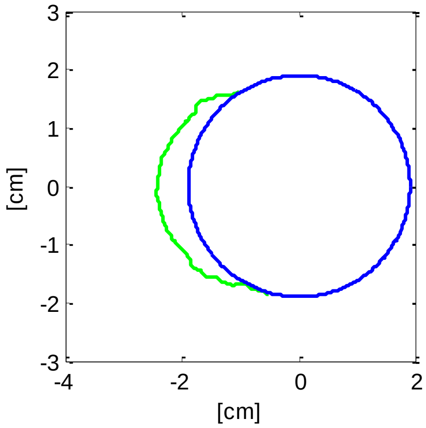
Mean(ice)/R=18% run=23b LWC=0.4 U=30[m/s] DS=20[µm]
Tair=-5[ºC] Ttest=10[min] Dia=3.81[cm] Pos.=H[-]

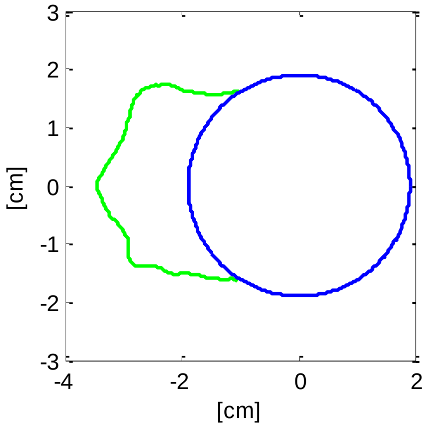
Mean(ice)/R=49% run=24a LWC=0.4 U=30[m/s] DS=20[µm]
Tair=-5[ºC] Ttest=30[min] Dia=3.81[cm] Pos.=H[-]

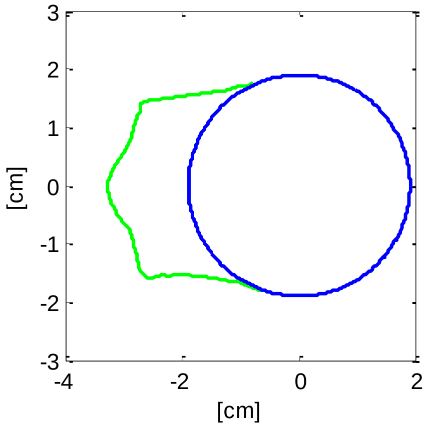
Mean(ice)/R=43% run=24b LWC=0.4 U=30[m/s] DS=20[µm]
Tair=-5[ºC] Ttest=30[min] Dia=3.81[cm] Pos.=H[-]

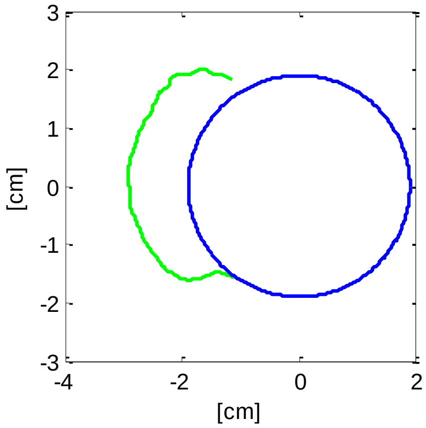
Mean(ice)/R=42% run=25a LWC=0.4 U=20[m/s] DS=50[µm]
Tair=-3[ºC] Ttest=30[min] Dia=3.81[cm] Pos.=H[-]

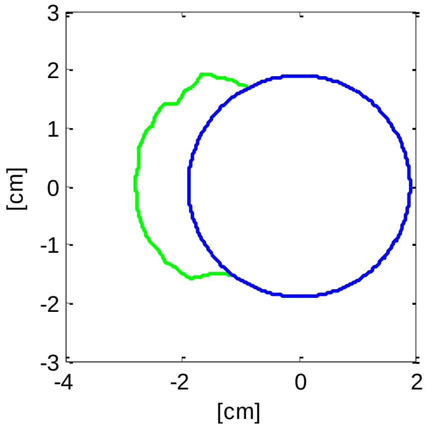
Mean(ice)/R=35% run=25b LWC=0.4 U=20[m/s] DS=50[µm]
Tair=-3[ºC] Ttest=30[min] Dia=3.81[cm] Pos.=H[-]

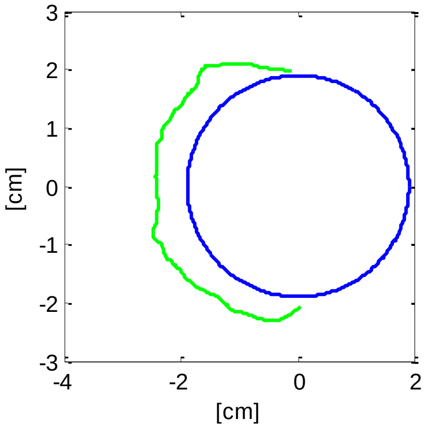
Mean(ice)/R=27% run=26a LWC=0.4 U=20[m/s] DS=50[µm]
Tair=-2[ºC] Ttest=30[min] Dia=3.81[cm] Pos.=H[-]

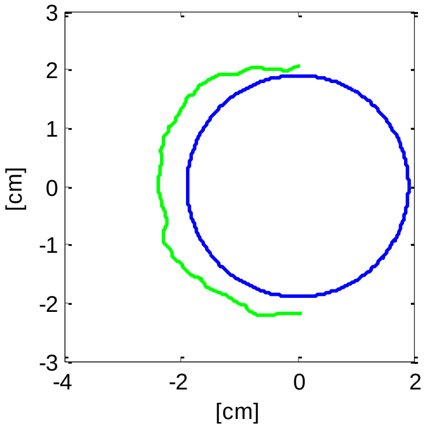
Mean(ice)/R=22% run=26b LWC=0.4 U=20[m/s] DS=50[µm]
Tair=-2[ºC] Ttest=30[min] Dia=3.81[cm] Pos.=H[-]

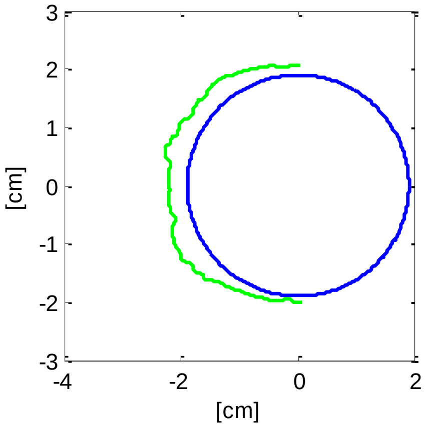
Mean(ice)/R=16% run=27a LWC=0.4 U=20[m/s] DS=50[µm]
Tair=-1[ºC] Ttest=30[min] Dia=3.81[cm] Pos.=H[-]

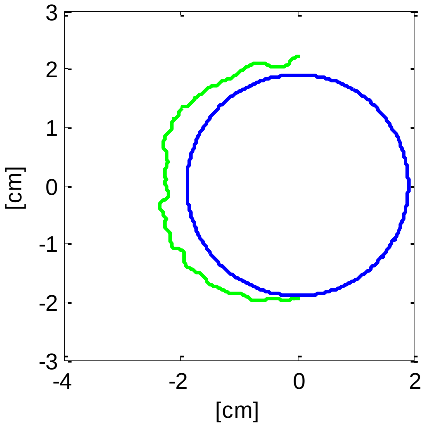
Mean(ice)/R=19% run=27b LWC=0.4 U=20[m/s] DS=50[µm]
Tair=-1[ºC] Ttest=30[min] Dia=3.81[cm] Pos.=H[-]

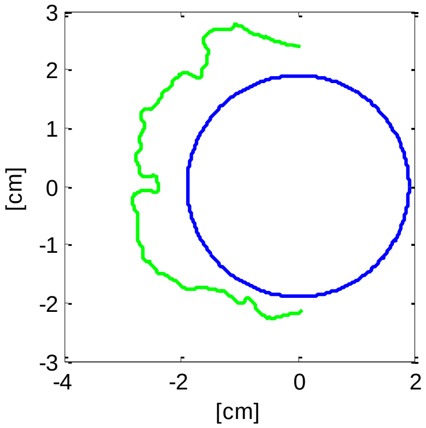
Mean(ice)/R=37% run=28a LWC=0.4 U=20[m/s] DS=50[µm]
Tair=-1[ºC] Ttest=60[min] Dia=3.81[cm] Pos.=H[-]

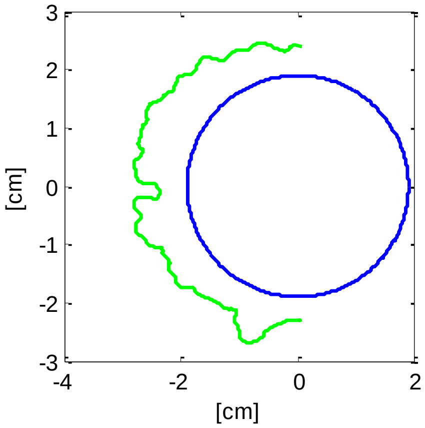
Mean(ice)/R=38% run=28b LWC=0.4 U=20[m/s] DS=50[µm]
Tair=-1[ºC] Ttest=60[min] Dia=3.81[cm] Pos.=H[-]

Mean(ice)/R=4% run=29 LWC=0.4 U=20[m/s] DS=50[µm]
Tair=-3[ºC] Ttest=10[min] Dia=8.9[cm] Pos.=H[-]

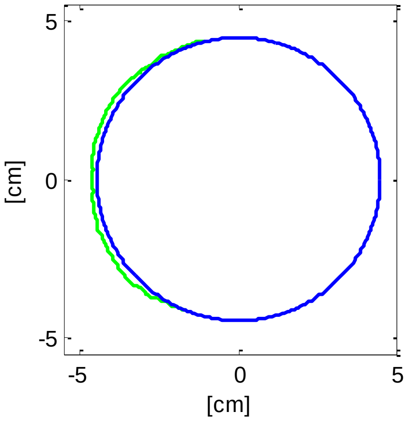

Mean(ice)/R=9% run=30 LWC=0.4 U=20[m/s] DS=50[µm]
Tair=-3[ºC] Ttest=30[min] Dia=8.9[cm] Pos.=H[-]

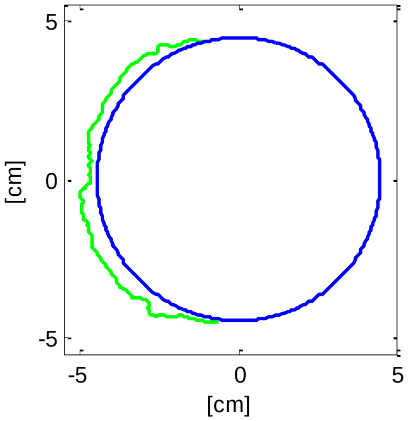

Mean(ice)/R=4% run=31 LWC=0.4 U=20[m/s] DS=50[µm]
Tair=-2[ºC] Ttest=10[min] Dia=8.9[cm] Pos.=H[-]

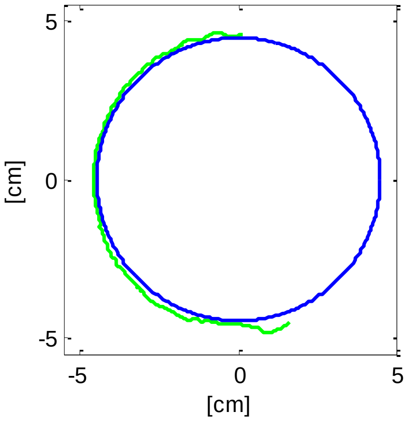

Mean(ice)/R=6% run=32 LWC=0.4 U=20[m/s] DS=50[µm]
Tair=-2[ºC] Ttest=30[min] Dia=8.9[cm] Pos.=H[-]

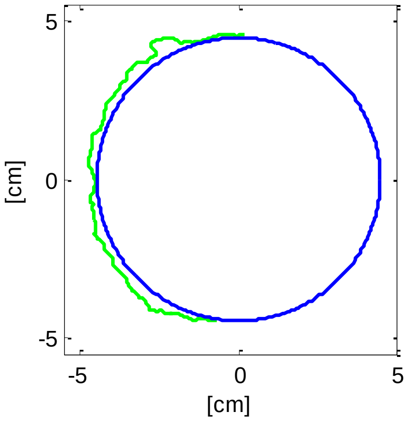

Mean(ice)/R=4% run=33 LWC=0.4 U=20[m/s] DS=50[µm]
Tair=-1[ºC] Ttest=30[min] Dia=8.9[cm] Pos.=H[-]

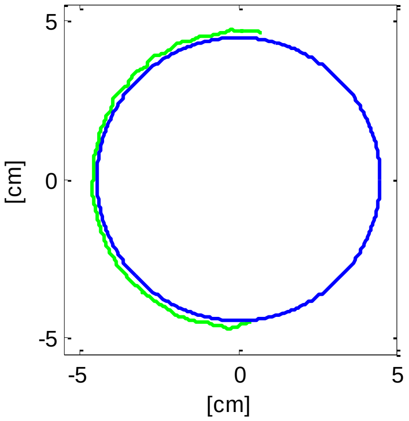

Mean(ice)/R=5% run=34 LWC=0.4 U=20[m/s] DS=50[µm]
Tair=-3[ºC] Ttest=10[min] Dia=8.9[cm] Pos.=V[-]

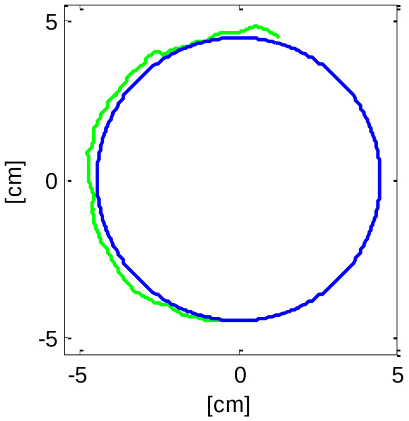

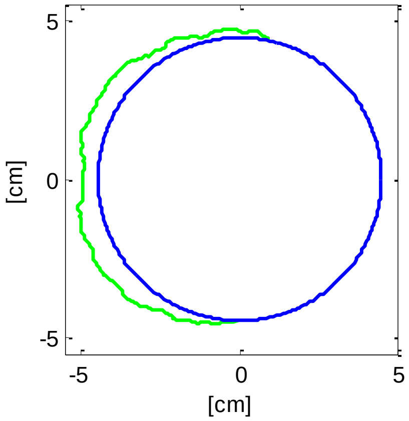

Mean(ice)/R=11% run=35 LWC=0.4 U=20[m/s] DS=50[µm]
Tair=-3[ºC] Ttest=30[min] Dia=8.9[cm] Pos.=V[-]

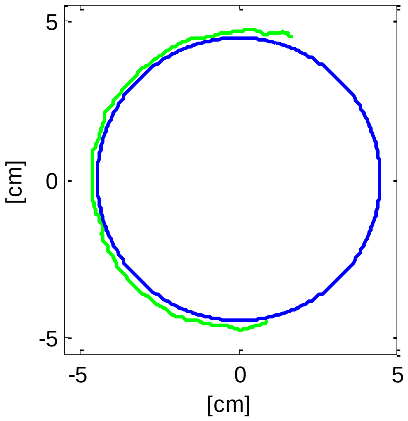

Mean(ice)/R=5% run=36 LWC=0.4 U=20[m/s] DS=50[µm]
Tair=-2[ºC] Ttest=10[min] Dia=8.9[cm] Pos.=V[-]

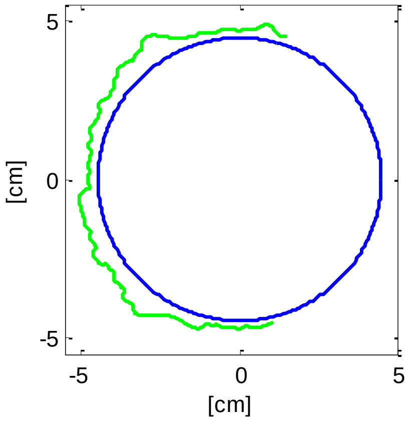

Mean(ice)/R=11% run=37 LWC=0.4 U=20[m/s] DS=50[µm]
Tair=-2[ºC] Ttest=30[min] Dia=8.9[cm] Pos.=V[-]

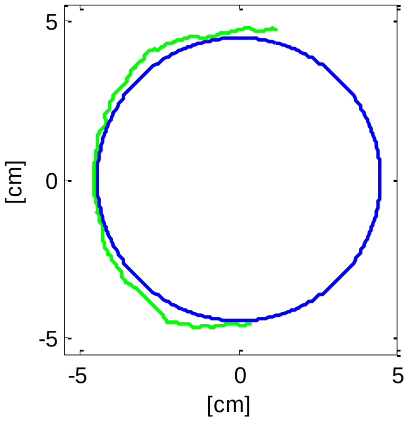

Mean(ice)/R=6% run=38 LWC=0.4 U=20[m/s] DS=50[µm]
Tair=-1[ºC] Ttest=30[min] Dia=8.9[cm] Pos.=V[-]

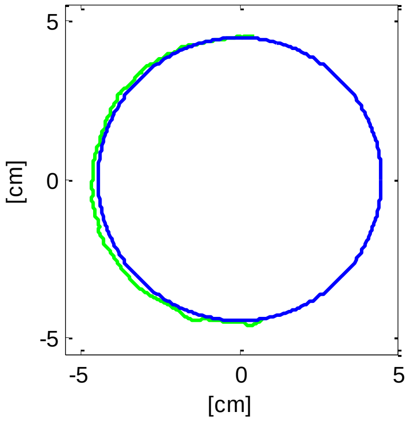

Mean(ice)/R=3% run=39 LWC=0.4 U=10[m/s] DS=50[µm]
Tair=-1[ºC] Ttest=30[min] Dia=8.9[cm] Pos.=V[-]

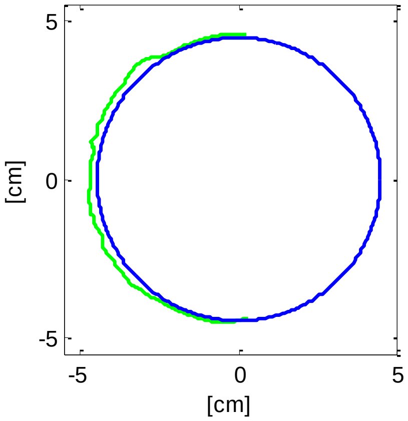

Mean(ice)/R=4% run=40 LWC=0.4 U=10[m/s] DS=50[µm]
Tair=-2[ºC] Ttest=30[min] Dia=8.9[cm] Pos.=V[-]

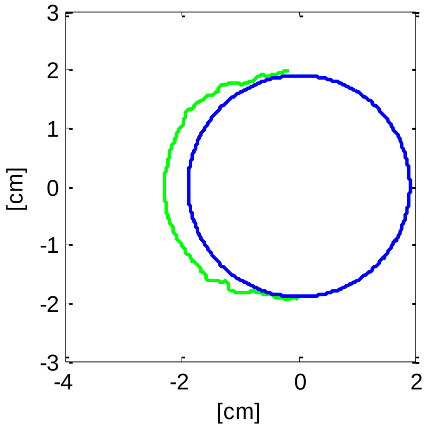
Mean(ice)/R=13% run=41 LWC=0.4 U=20[m/s] DS=50[µm]
Tair=-3[ºC] Ttest=10[min] Dia=3.81[cm] Pos.=V[-]

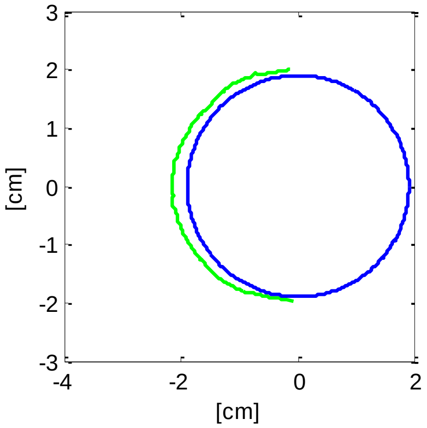
Mean(ice)/R=9% run=42 LWC=0.4 U=10[m/s] DS=50[µm]
Tair=-3[ºC] Ttest=10[min] Dia=3.81[cm] Pos.=V[-]

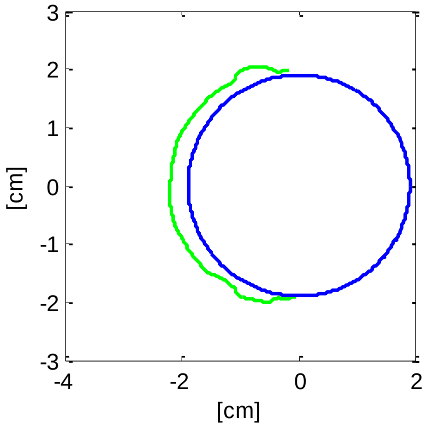
Mean(ice)/R=13% run=43 LWC=0.4 U=20[m/s] DS=50[µm]
Tair=-2[ºC] Ttest=10[min] Dia=3.81[cm] Pos.=V[-]

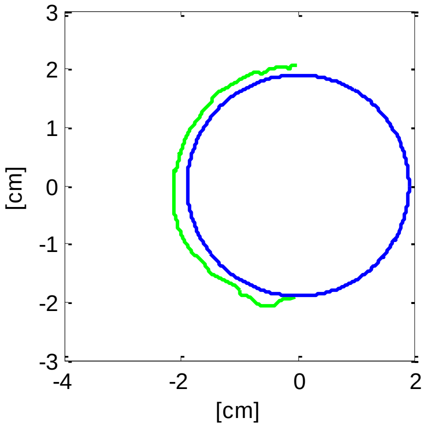
Mean(ice)/R=10% run=44 LWC=0.4 U=20[m/s] DS=50[µm]
Tair=-1[ºC] Ttest=10[min] Dia=3.81[cm] Pos.=V[-]

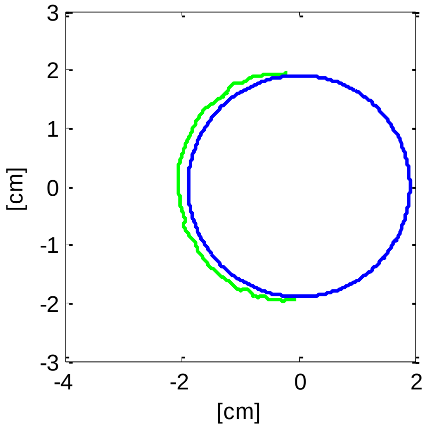
Mean(ice)/R=7% run=45 LWC=0.4 U=10[m/s] DS=50[µm]
Tair=-1[ºC] Ttest=10[min] Dia=3.81[cm] Pos.=V[-]

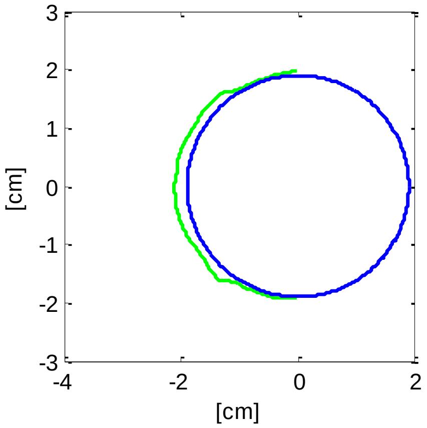
Mean(ice)/R=7% run=46 LWC=0.4 U=10[m/s] DS=50[µm]
Tair=-2[ºC] Ttest=10[min] Dia=3.81[cm] Pos.=V[-]

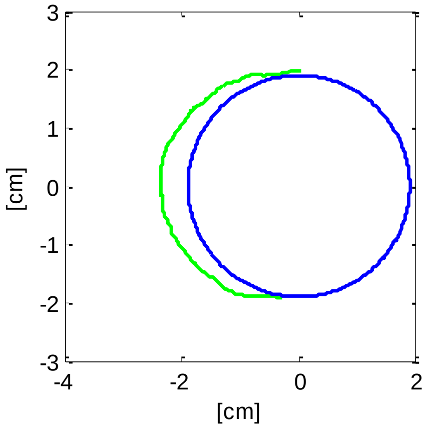
Mean(ice)/R=15% run=11a LWC=0.4 U=20[m/s] DS=50[µm]
Tair=-5[ºC] Ttest=10[min] Dia=3.81[cm] Pos.=H[-]

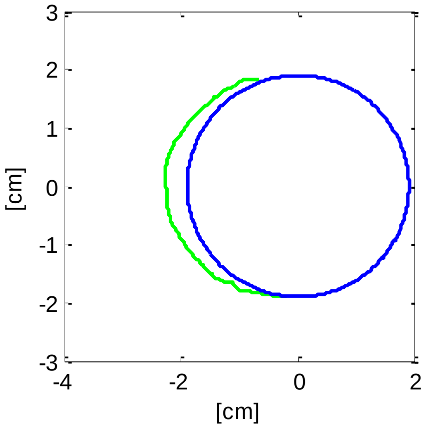
Mean(ice)/R=12% run=11b LWC=0.4 U=20[m/s] DS=50[µm]
Tair=-5[ºC] Ttest=10[min] Dia=3.81[cm] Pos.=H[-]

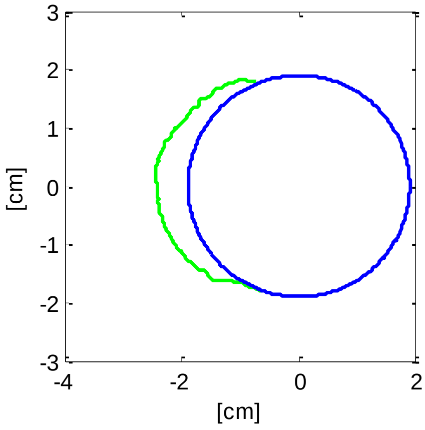
Mean(ice)/R=19% run=12a LWC=0.4 U=20[m/s] DS=50[µm]
Tair=-4[ºC] Ttest=10[min] Dia=3.81[cm] Pos.=H[-]

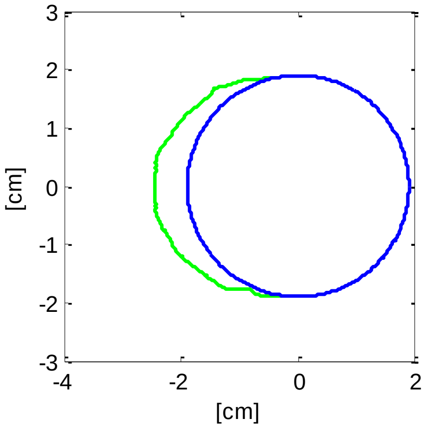
Mean(ice)/R=18% run=12b LWC=0.4 U=20[m/s] DS=50[µm]
Tair=-4[ºC] Ttest=10[min] Dia=3.81[cm] Pos.=H[-]

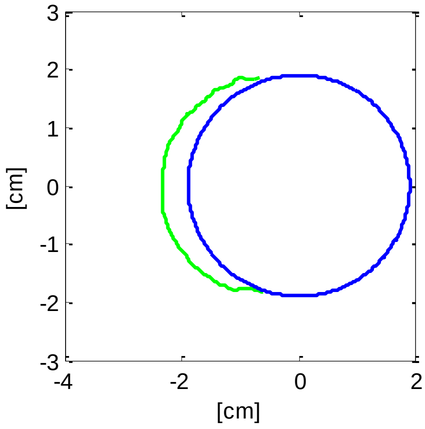
Mean(ice)/R=17% run=13a LWC=0.4 U=20[m/s] DS=50[µm]
Tair=-3[ºC] Ttest=10[min] Dia=3.81[cm] Pos.=H[-]

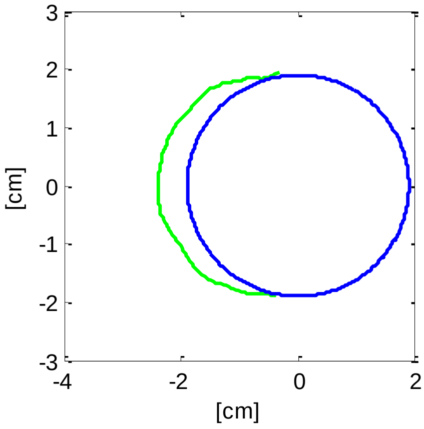
Mean(ice)/R=17% run=13b LWC=0.4 U=20[m/s] DS=50[µm]
Tair=-3[ºC] Ttest=10[min] Dia=3.81[cm] Pos.=H[-]

Appendix E

Subtest Programs from Icing Tests performed at NRC

Subtest programs from icing test performed at NRC

Table E1

Listing of test sorted by Variation of Time

No.	Umean	Tair	D	DS	LWC	Pos.	Variation
	[m/s]	[°C]	[cm]	[µm]	[g/m³]	[-]	Run#(t[min])
A1	10	-5	3.81	50	0.4	H	2(10) ; 5(15) ; 10(30) ; 21(60)
A2	30	-5	3.81	20	0.4	H	22(5) ; 23(10) ; 24(30)
A3	20	-1	3.81	50	0.4	H	15(10) ; 27(30) ; 28(60)
A4	20	-2	3.81	50	0.4	H	14(10) ; 26(30)
A5	20	-3	3.81	50	0.4	H	13(10) ; 25(30)
A6	20	-2	8.9	50	0.4	H	31(10) ; 32(30)
A7	20	-3	8.9	50	0.4	V	34(10) ; 35(30)
A8	20	-2	8.9	50	0.4	V	36(10) ; 37(30)
A9	20	-3	8.9	50	0.4	H	29(10) ; 30(30)

Table E2

Listing of test sorted by Influence of Temperature

No.	Umean	Time	D	DS	LWC	Pos.	Variation
	[m/s]	[min]	[cm]	[µm]	[g/m³]	[-]	Run#(T[°C])
B1	10	10	3.81	50	0.4	H	2(-5) ; 6(-4) ; 7(-3) ; 8(-2) ; 9(-1)
B2	20	10	3.81	50	0.4	H	11(-5) ; 12(-4) ; 13(-3) ; 14(-2) ; 15(-1)
B3	30	10	3.81	50	0.4	H	16(-5) ; 17(-4) ; 18(-3) ; 19(-2) ; 20(-1)
B4	20	30	3.81	50	0.4	H	25(-3) ; 26(-2) ; 27(-1)
B5	20	30	8.9	50	0.4	H	30(-3) ; 32(-2) ; 33(-1)
B6	20	10	8.9	50	0.4	H	29(-3) ; 31(-2)
B7	20	30	8.9	50	0.4	V	35(-3) ; 37(-2) ; 38(-1)
B8	20	10	8.9	50	0.4	V	34(-3) ; 36(-2)
B9	10	30	8.9	50	0.4	V	40(-2); 39(-1)
B10	20	10	3.81	50	0.4	V	41(-3) ; 43(-2) ; 44(-1)
B11	10	10	3.81	50	0.4	V	42(-3) ; 46(-2) ; 45(-1)

Table E3

Listing of test sorted by Variation of Droplet size

No.	Umean	Tair	Time	D	LWC	Pos.	Variation
	[m/s]	[°C]	[min]	[cm]	[g/m³]	[-]	Run#(DS[µm])
C1	10	-5	10	3.81	0.4	H	2(50) ; 3(30)
C2	10	-5	10	3.81	0.4	H	16(50) ; 23(20)

Table E4

Listing of test sorted by Variation of Velocity

No.	Tair	Time	D	DS	LWC	Pos.	Variation
	[°C]	[min]	[cm]	[µm]	[g/m^3]	[-]	Run#(U[m/s])
D1	-1	10	3.81	50	0.4	V	44(20) ; 45(10)
D2	-2	10	3.81	50	0.4	V	43(20) ; 46(10)
D3	-3	10	3.81	50	0.4	V	41(20) ; 42(10)
D4	-2	30	8.9	50	0.4	V	37(20) ; 40(10)
D5	-1	30	8.9	50	0.4	V	38(20) ; 39(10)
D6	-1	10	3.81	50	0.4	H	9(10) ; 15(20) ; 20(30)
D7	-2	10	3.81	50	0.4	H	8(10) ; 14(20) ; 19(30)
D8	-3	10	3.81	50	0.4	H	7(10) ; 13(20) ; 18(30)
D9	-4	10	3.81	50	0.4	H	6(10) ; 12(20) ; 17(30)
D10	-5	10	3.81	50	0.4	H	2(10) ; 11(20) ; 16(30)

Table E5

Listing of test sorted by Variation of Diameter

No.	Umean	Tair	Time	DS	LWC	Pos.	Variation
	[m/s]	[°C]	[min]	[µm]	[g/m^3]	[-]	Run#(D[cm])
E1	20	-3	10	50	0.4	V	41(3.81) ; 34(8.9)
E2	20	-2	10	50	0.4	V	43(3.81) ; 36(8.9)
E3	20	-3	10	50	0.4	H	13(3.81) ; 29(8.9)
E4	20	-2	10	50	0.4	H	14(3.81) ; 31(8.9)
E5	20	-3	30	50	0.4	H	25(3.81) ; 30(8.9)
E6	20	-2	30	50	0.4	H	26(3.81) ; 32(8.9)
E7	20	-1	30	50	0.4	H	27(3.81) ; 33(8.9)

Table E6

Listing of test sorted by Influence of Position

No.	Umean	Tair	Time	D	DS	LWC	Variation
	[m/s]	[°C]	[min]	[cm]	[µm]	[g/m^3]	Run#(Pos.)
F1	20	-3	10	8.9	50	0.4	29(H) ; 34(V)
F2	20	-3	30	8.9	50	0.4	30(H) ; 35(V)
F3	20	-2	10	8.9	50	0.4	31(H) ; 36(V)
F4	20	-2	30	8.9	50	0.4	32(H) ; 37(V)
F5	20	-1	30	8.9	50	0.4	33(H) ; 38(V)
F6	20	-3	10	3.81	50	0.4	13(H) ; 41(V)
F7	10	-3	10	3.81	50	0.4	7(H) ; 42(V)
F8	20	-2	10	3.81	50	0.4	14(H) ; 43(V)
F9	20	-1	10	3.81	50	0.4	15(H) ; 44(V)
F10	10	-1	10	3.81	50	0.4	9(H) ; 45(V)
F11	10	-2	10	3.81	50	0.4	8(H) ; 46(V)

The main focus of thesis is to understanding and simulating wind-induced vibrations of iced vertical cables. This has been approach by the development of a new 3 degree-of-freedom instability model, which can predict instability and estimate the needed damping to avoid instability. The instability model has been validated through wind tunnel experiments, which consist of three experimental series. One experimental series concentrating on ice formation on cables, the second and third looking at static force coefficients and dynamic responses of selected ice shapes.

Finally, the static force coefficients and dynamic responses have been used in a comparison to the predicted values from the instability model.

DTU Civil Engineering
Department of Civil Engineering
Technical University of Denmark

Brovej, Building 118
2800 Kgs. Lyngby
Telephone 45 25 17 00

www.byg.dtu.dk

ISBN: 9788778773159
ISSN: 1601-2917